

# **The design and application of luminescent thermometers**

A closer look at biases and uncertainties



# The design and application of luminescent thermometers

A closer look at biases and uncertainties

Het ontwerp en de toepassing van luminescente thermometers

Afwijkingen en onzekerheden nader bekeken

(met een samenvatting in het Nederlands)

Proefschrift

ter verkrijging van de graad van doctor aan de Universiteit Utrecht op gezag van  
de rector magnificus, prof.dr. H.R.B.M. Kummeling, ingevolge het besluit van het  
college voor promoties in het openbaar te verdedigen op

woensdag 25 januari 2023 des middags te 12.15 uur

door

Thomas Pieter van Swieten

geboren op 10 september 1993 te Rotterdam

**Promotoren:**

Prof. dr. A. Meijerink

Prof. dr. ir. B.M. Weckhuysen

**Copromotor:**

Dr. F.T. Rabouw

Dit werk maakt deel uit van het onderzoeksprogramma 'Future methodologies in catalysis and solar fuels production' van the Netherlands Center for Multiscale Catalytic Energy Conversion (MCEC), een Zwaartekracht-programma dat wordt gefinancierd door de Nederlandse Organisatie voor Wetenschappelijk Onderzoek (NWO).

# Contents

- Chapter 1. Introduction
- Chapter 2. The impact of noise and background on measurement uncertainties in luminescence thermometry
- Chapter 3. Extending the dynamic temperature range of Boltzmann thermometers
- Chapter 4. A Ho<sup>3+</sup>-based luminescent thermometer for sensitive sensing over a wide temperature range
- Chapter 5. Mapping elevated temperatures with a micrometer resolution using the luminescence of chemically stable upconversion nanoparticles
- Chapter 6. Enormous photonic artifacts in luminescence nanothermometry
- Chapter 7. Summary and outlook

References

Appendix

Samenvatting in het Nederlands

Acknowledgments

List of publications and presentations

Curriculum vitae



---

# Chapter 1

## Introduction

## 1.1 Luminescent materials as a new type of thermometers

Temperature plays a critical role in society. In our daily lives, temperature is for instance important for the preparation of our food, it serves as a measure for our physical health, and it affects the climate that we live in. A large variety of thermometers have been developed over the last centuries to measure temperature and give insight into the generation and dissipation of heat. The first thermometers worked via the expansion and contraction of a liquid or a gas that is confined to a tube.<sup>1,2</sup> The addition of a scale to the tube and the standardization of thermometer response made it possible to perform calibrated temperature measurements.<sup>3</sup> Today, these conventional liquid-based thermometers are more and more replaced either by metals with a linear relation between the electrical resistance and temperature or by thermocouples, in which a temperature difference at a junction between different metals creates an electric potential.<sup>4,5</sup> These thermometers can be applied to a large variety of systems, especially on the macroscopic scale.

Continuous developments in science and technology however push the size requirements of thermometers to increasingly smaller dimensions. In some cases, thermocouples or resistance thermometers can fulfil this demand.<sup>6</sup> State-of-the-art examples include: micrometer-sized thermocouples designed for measurements in single biological cells,<sup>7,8</sup> microelectromechanical systems (MEMS) with thermoresistive components, and scanning probe microscopy techniques that use a thermoresistive tip or one with a built-in thermocouple.<sup>9–11</sup> However, these techniques require thermal contact between the studied system and the sensing element that often consists of bulky components. In addition, the sensing element needs to be connected to a device that records the temperature-sensitive signal. These disadvantages make contact thermometers only suited for a limited number of microscopic systems.

Techniques that rely on temperature-dependent emission of light are a promising alternative to existing microscopic thermometers, because the acquisition of emission occurs remotely without physical connection between the sensing element and the detector. One example is infrared thermography. In this technique, blackbody radiation emitted by an object is recorded by an infrared detector, which allows for the conversion of the total radiant power to temperature using Planck's law.<sup>12</sup> However, the diffraction limit imposes poor spatial resolutions of several micrometers for infrared thermography. Temperature measurements based on photoluminescence offer a solution because here the emission wavelengths can range from the UV to the near-infrared, resulting in

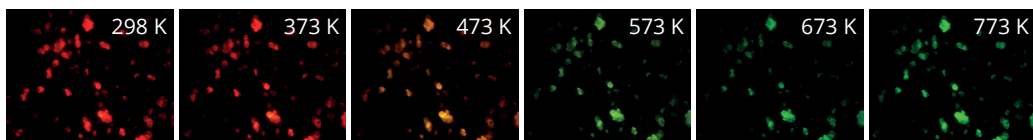


**Figure 1.1.** Microscope images of luminescent  $\text{Na}(\text{Y,Gd})\text{F}_4:\text{Ho}^{3+}(12\%)$  crystals upon 445 nm excitation at various temperatures. The dimensions of the field-of-view are  $90 \times 110 \mu\text{m}$ . With increasing temperature, the luminescence of the crystals changes from red to green, which makes it an interesting material for thermometry.



enhanced spatial resolutions down to a few hundred nanometers.<sup>13</sup> Such experiments typically involve the insertion of a photoluminescent material into a sample of interest followed by the excitation and detection of the temperature-dependent emission (Fig. 1.1). This already enabled measurements of heat distributions in complex and dynamic systems such as biological tissue of living animals and catalyst particles during chemical reactions.

## 1.2 Photoluminescence of the lanthanides

Photoluminescent materials can absorb and emit light. Many different systems are photoluminescent, including atoms, molecules, and semiconductor crystals. In this thesis, we focus on inorganic crystals in which part of the cations is substituted by trivalent lanthanide ions, a procedure called doping. Materials from this class show unique optical properties, like narrow-line emission in different wavelength regimes and insensitivity for the chemical environment, which is particularly useful in luminescence thermometry. Thanks to modern synthesis techniques it is also possible to reduce the size of these materials to the nanoscale. Application of these nanocrystals as luminescent (nano)thermometers has become widespread in the fields of biology, chemistry, and engineering.

The lanthanides are generally displayed as a series of elements at the bottom of the periodic table ranging from La to Lu. The electronic configuration of the metallic lanthanides is  $[\text{Xe}]4f^{0-14}5d^{0-1}6s^2$ , but the most common form is the 3+ oxidation state, where the 5d and 6s electrons have been removed. Except for  $\text{La}^{3+}$  and  $\text{Lu}^{3+}$ , the trivalent lanthanides have partially filled 4f orbitals. Electronic transitions within the partially filled 4f subshell are responsible for their interesting optical properties, such as narrow-line emission, which originates from chemical shielding of the 4f electrons. More specifically, the 4f electrons are strongly localized close to the nucleus and they only weakly interact with the ligands. Therefore, the emission energy of a specific f–f transitions is almost independent of the inorganic crystal that hosts the trivalent lanthanide

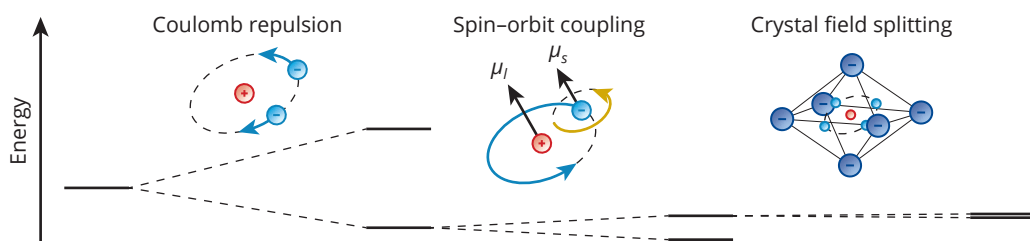


**Figure 1.2.** Schematic illustration of the interactions that split the energy levels of trivalent lanthanides. Coulomb repulsion affects the movement (light blue arrows) of the negatively charged 4f electrons (light blue spheres). Spin-orbit coupling describes the interaction between an electron's orbital angular momentum  $\mu_l$  due to the movement around the nucleus and the spin angular momentum  $\mu_s$  due to the intrinsic spin (yellow arrow). Crystal-field splitting involves the weak interaction between the 4f electrons with the negatively charged ligands (dark blue spheres).

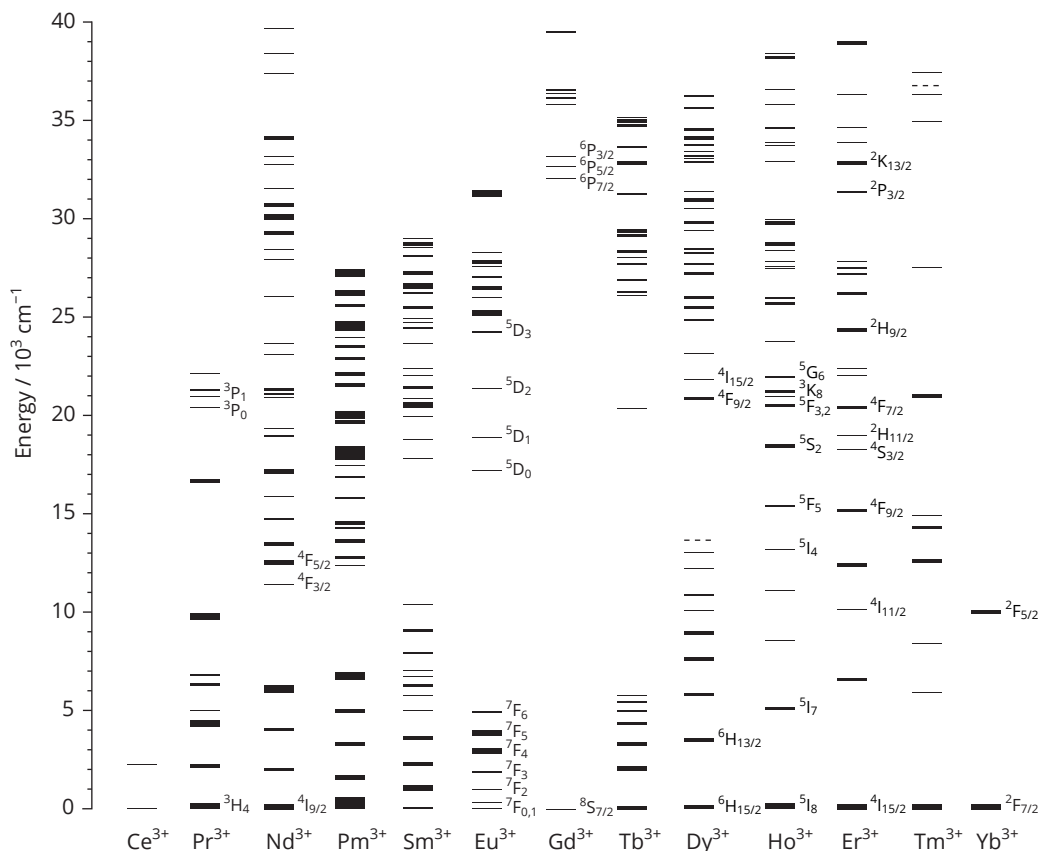


**Figure 1.3.** Dieke's diagram. The horizontal bars represent the 4f energy levels of the trivalent lanthanides. Each energy levels further splits in the presence of a crystal field. The width of the bars corresponds to energy differences caused by crystal field splitting.<sup>14</sup> The energy levels relevant for this thesis are labeled by their term symbol.

ion.

The f–f transitions are accompanied by a redistribution of electrons over the 4f orbitals. Each of the seven 4f orbitals can be occupied by two electrons. Consequently, the number of possible electronic configurations ranges from 14 for Ce<sup>3+</sup> and Yb<sup>3+</sup> to 3432 for Gd<sup>3+</sup>. The energy of the configurations is partially determined by the electrostatic interactions between the negatively charged electrons (Coulomb repulsion, Fig. 1.2). This causes energy differences between the configurations of 10<sup>4</sup>–10<sup>5</sup> cm<sup>-1</sup>. In addition, each electron experiences a magnetic interaction between its intrinsic spin angular momentum and the angular momentum induced by its orbital movement (spin–orbit coupling, Fig. 1.2). The relative orientation of these magnetic moments depends on the distribution of the 4f electrons over the orbitals and determines the strength of their interaction, resulting in additional energy differences of 10<sup>3</sup>–10<sup>4</sup> cm<sup>-1</sup>. After taking Coulomb repulsion and spin–orbit coupling into account, some of the configurations still have equal

energies and form degenerate groups that we call energy levels, where the ground state is the level with the lowest energy. The energy levels are generally labeled by the corresponding term symbol  $^{2S+1}L_J$ , where  $S$  is the total spin angular momentum,  $L$  is the total orbital angular momentum, and  $J$  is the total magnetic momentum. As discussed above, the crystal field surrounding the ion weakly interacts with the chemically shielded 4f electrons, and this causes an additional splitting of only  $\sim 10^2 \text{ cm}^{-1}$ . It is thus possible to construct a diagram of all 4f levels, almost irrespective of the host crystal, which was first performed by Dieke (Fig. 1.3).<sup>14</sup> This diagram shows that the trivalent lanthanides have a rich energy-level structure, which explains the generally large number of lines in their absorption and emission spectrum.

The transitions between the 4f levels are induced by the absorption and emission of light. Some of the transitions have dominant electric-dipole character. For electric-dipole transitions the electric field of light mixes the initial with the final state. In principle, electric-dipole transitions within the 4f shell are forbidden, because the initial and final state have the same symmetry with respect to the inversion center, *i.e.* they are of equal parity and the transition dipole moment vanishes. However, placing the ion into an asymmetric crystal field enables admixture of opposite-parity states by odd-parity crystal-field components. This partially lifts the parity selection rule and makes electric-dipole f–f transitions slightly allowed.<sup>15</sup> Selection rules also apply to magnetic-dipole transitions that couple to the magnetic field of light, but they do not require a difference in parity between the initial and final state. Many magnetic-dipole f–f transitions are therefore fully allowed, but the transition probabilities are typically 3–4 orders of magnitude weaker than the ones with electric-dipole character. However, magnetic-dipole emissions can be relatively strong when the parity selection rule for electric-dipole transitions is barely lifted. A well-known example is  $\text{Eu}^{3+}$  in a crystal field with inversion symmetry that shows intense magnetic-dipole  $^5\text{D}_0 \rightarrow ^7\text{F}_1$  emission and weak electric-dipole  $^5\text{D}_0 \rightarrow ^7\text{F}_2$  emission.<sup>16</sup>

Besides the f–f absorptions, other transitions can also excite the luminescence of lanthanide-doped materials. For instance, electrons can be also promoted from the 4f to the 5d orbitals, which in some lanthanides, like  $\text{Ce}^{3+}$ , occurs already at relatively low absorption energies in the UV or visible.<sup>17</sup> The absorption (and emission) bands of 4f–5d transitions are strong as they are parity allowed and they are broad because the 5d orbitals participate in chemical bonding with the surrounding ligands. The latter causes an offset between the potential energy curves of the ground and the excited state, which enables coupling of the electronic transition to vibrations, resulting in broad absorption and emission bands. Another type of broad-band absorption involves transfer of an electron from the ligands to the lanthanide ion.<sup>18</sup> These charge-transfer transitions are fully allowed, which generally results in bright luminescence from the lanthanide ions already at low excitation intensities and dopant concentrations.

Once an ion is in an excited state, it can spontaneously release its energy via the emission of a photon. This is accompanied by relaxation to one of the lower energy levels, although decay to the ground state is generally dominant. The probability of each transition is quantified by the spontaneous emission rate, where the radiative decay rate of a specific level is the sum of all spontaneous

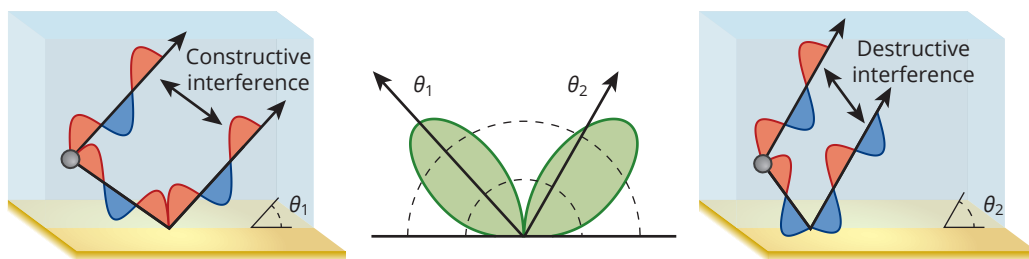


**Figure 1.4.** Emission of an electric dipole that interacts with a mirror. Depending on the emission direction, the mirror causes either constructive (left panel) or destructive (right panel) interference. This determines the angular distribution of spontaneous emission as illustrated by the radiation pattern (center panel).

emission rates from this level. The radiative decay rate of most 4f levels, having parity forbidden transitions, is on the order of  $1 \text{ ms}^{-1}$ , while  $\text{Ce}^{3+}$  and other luminescent materials with allowed transitions typically have radiative rates of  $10^3\text{--}10^5 \text{ ms}^{-1}$ .<sup>18</sup> As discussed for  $\text{Eu}^{3+}$ , the parity selection rule is partially lifted by host lattices with asymmetric sites, which makes f–f transitions with electric-dipole character more allowed and can therefore increase the radiative decay rates of the 4f levels.

The spontaneous emission rate is further influenced by the optical environment of the emitter, which is defined by the refractive index of the dielectric materials within a few emission wavelengths. This concerns, for instance, the dielectric interfaces close to a luminescent nanocrystal or the refractive index of the solvent, in which it is dispersed.<sup>19,20</sup> Drexhage demonstrated the effect of the optical environment using an illustrative experiment: he placed  $\text{Eu}^{3+}$ -based molecules near a mirror and measured the decay rate at various emitter–mirror distances.<sup>21</sup> As a function of the distance, he observed variations in the decay rate and in the angular distribution of luminescence, which he explained as self-interference between direct and reflected emission that modifies the spontaneous emission rate in certain directions (Fig. 1.4). An equivalent interpretation is that the optical environment determines the local density of optical states (LDOS), which, according to Fermi's golden rule, controls the spontaneous emission rate.<sup>22–24</sup> This photonic effect is highly wavelength dependent. Therefore, the luminescence intensity of f–f emissions not only depends on the local crystal field but also on the optical environment. We investigate the impact of the optical environment on the performance of luminescent thermometers in Chapters 5 and 6.

The excited-state population can also change via energy transfer from an excited emitter, the donor, to a nearby absorber, the acceptor. In this process, the donor loses (part of) its excited-state energy to bring the acceptor to a (higher) excited level. Given that these transitions are in resonance, the rate of energy transfer increases for stronger transition dipoles and for shorter donor–acceptor distances ( $R$ ). When the transition dipole on both the donor and acceptor have electric-dipole character, the energy-transfer rate scales with  $R^{-6}$ , as described by Förster.<sup>25</sup> Fig. 1.5 shows the three different energy-transfer mechanisms that are relevant for this thesis. In the conventional type of energy transfer, as presented in Fig. 1.5a, the acceptor is in the ground state and it receives

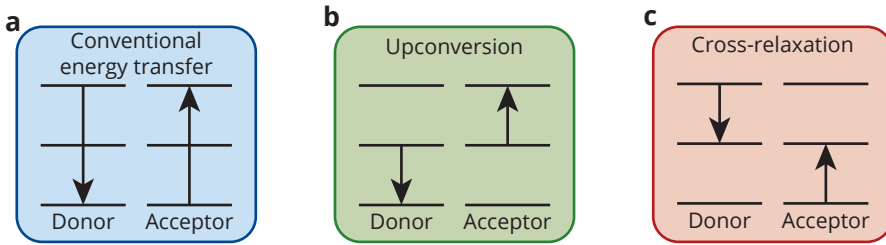


**Figure 1.5.** A selection of energy-transfer mechanisms relevant for this thesis. Conventional energy transfer (a) brings the donor to the ground state by exciting the acceptor from the ground state to an excited state. In upconversion energy transfer (b), the acceptor is already in an intermediate excited state and it thus reaches an even higher excited state when it accepts energy. Cross-relaxation (c) involves partial energy transfer, which leaves both the acceptor and the donor in an intermediate excited state.

all the excited-state energy from the donor. This can take place in many luminescent materials. Other interesting energy-transfer processes are also possible between trivalent lanthanides.<sup>26,27</sup> One of them is upconversion, in which the acceptor is already in an excited state and is brought to an even higher state by the donor (Fig. 1.5b). In Chapters 2, 5, and 6, we use nanocrystals that are co-doped with  $\text{Er}^{3+}$  and  $\text{Yb}^{3+}$  to obtain bright green upconversion luminescence upon infrared (980 nm) excitation. Upconversion nanocrystals are popular in thermometry but also find applications as luminescent labels in bio-imaging due to the high penetration depth of infrared excitation and the absence of background fluorescence. The third energy-transfer mechanism involves cross-relaxation (Fig. 1.5c). Here, the acceptor is in the ground state and receives a part of the excited-state energy from the donor. Cross-relaxation quenches the luminescence of many excited lanthanide ions at higher dopant concentrations. In Chapter 4, we exploit cross-relaxation to design a new thermometer based on the luminescence of  $\text{Ho}^{3+}$ .

Energy transfer can also take place between an excited ion and local vibrations in the host crystal or surrounding molecules. This either populates a lower energy level via the emission of phonons, commonly referred to as multi-phonon relaxation, or it excites the emitter to a higher energy level via the absorption of phonons.<sup>28,29</sup> The rate of these processes depends on the occupation of phonon modes

$$n = \frac{1}{\exp(\hbar\omega/k_B T) - 1}, \quad (1.1)$$

which increases with temperature  $T$  and decreases with vibrational energy  $\hbar\omega$ . The phonon emission rate scales as  $(1 + n)^p$ , where  $p$  is the number of required phonons to bridge the energy gap to the lower level. For one part, phonon emission is thus spontaneous and temperature-independent, while it also involves a stimulated temperature-dependent component. In contrast, phonon absorption is a purely stimulated process and scales as  $n^p$ . These relations illustrate that the response of lanthanide-doped materials to temperature heavily relies on the vibrational energies of the host

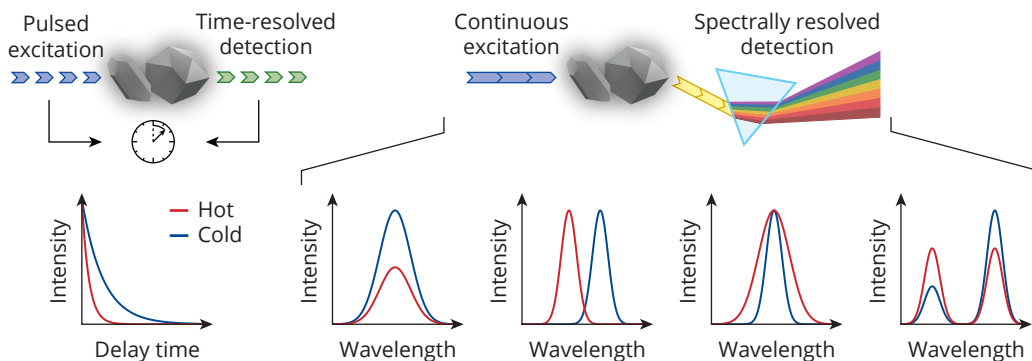


**Figure 1.6.** How to extract the temperature from a luminescent thermometer? In general, either luminescence decay curves or emission spectra are analyzed to quantify temperature. Luminescence decay experiments require pulsed excitation and a single-photon counting detector. At every pulse, the excitation source sends a synchronization signal to the time-to-digital converter (clock), while the detector does the same at each photon detection event. This enables the registration of the delay time, that is the difference in time between pulse and detection events. Making a histogram of all delay times constructs a decay curve, which contains the dynamics of luminescence. Many luminescent materials show faster decay at elevated temperatures. Spectrally resolved measurements typically use continuous excitation and record the emission intensity in each wavelength interval during a specific acquisition time. Prisms and gratings (blue triangle) are the most common optical elements to separate the emission wavelengths, while charge-coupled devices (CCDs) are convenient to detect the emission spectrum in one capture. In luminescence thermometry, the absolute intensity, peak position, peak width, and relative intensity in the emission spectrum are commonly used as measures for temperature.

crystal and the energy differences between the 4f levels, which are therefore important parameters to optimize in the design of luminescent thermometers.

### 1.3 What makes a good luminescent thermometer?

Different spectroscopic techniques can be used to extract the temperature from luminescent materials (Fig. 1.6). Some of them rely on luminescence decay curves obtained via time-resolved measurements and they exploit temperature-dependent decay channels, like multi-phonon relaxation or thermally activated crossover to a charge-transfer state. However, these measurements typically require long acquisition times in the order of minutes, which make this method mainly suited for experiments in static samples. Other methods use the emission spectrum of the thermometer, because it is fast and simple to record and it contains multiple temperature-dependent features. For instance, the intensity of a single emission band can be a measure for temperature. The intensity of a single band is however not often used, because it is also sensitive to experimental factors like instabilities in the excitation source and changes in sample alignment. Thermometers that use the spectral width or the peak energy of an emission band do not have these issues, but they typically have larger measurement uncertainties and strongly depend on the spectral reso-

lution. In this thesis, we study luminescent thermometers based on the luminescence intensity ratio (*LIR*) between two emission bands. The *LIR* is extracted from the emission spectrum, it is independent of experimental factors that reduce the absolute signal, and, in many materials, it sensitively responds to temperature, resulting in reliable temperature measurements. This makes the *LIR* the preferred choice for luminescence thermometry.

The reliability of a ratiometric thermometer depends on the potential to minimize systematic and random measurement errors, also called biases and uncertainties, respectively. One common source of systematic errors stems from the calibration procedure, which generally involves the acquisition of emission spectra at specific set temperatures using an externally controlled heater, followed by fitting of the intensity ratios to some analytical model. Poor thermal contact between the sample and the heater could result in an inaccurate calibration. More importantly, the lack of a physically realistic model for the intensity ratio forces the user to resort to arbitrary fitting procedures, which obscures the systematic errors introduced by the calibration. This last consideration has made lanthanide-doped materials with two closely separated energy levels a popular type of thermometer.<sup>29</sup> Namely, once the nonradiative coupling rates between these levels are much faster than radiative decay, the system is in thermal equilibrium and the *LIR* approximately follows Boltzmann statistics, serving as a simple and reliable calibration model.

Many other systematic errors may arise in the course of a luminescence thermometry experiment. The first error is already encountered at absorption of the excitation light. Namely, high excitation intensities can generate heat and this may increase the temperature of the sample.<sup>30</sup> Heat dissipation may additionally vary for different thermometer environments, which makes sample temperature not only dependent on the excitation intensity but also on the thermal properties of the medium. Once the thermometer is excited, the wavelength-dependent refractive index of the medium can further affect temperature readout via modification of the spontaneous emission rate.<sup>31,32</sup> After emission of a photon, self-absorption might distort the luminescence spectrum when the concentration of thermometer particles is sufficiently high. Similarly, part of the spectrum can be selectively absorbed, scattered, or reflected in the emission path from the thermometer to the detector, for example by the sample medium or by the optics of the equipment.<sup>33</sup> Finally, data-analysis procedures like background subtraction or the removal of overlapping emissions may be inaccurate, resulting in additional distortions of the spectrum. Reliable thermometry experiments require awareness of all possible systematic errors. In this way, these errors could be minimized by the optimized design of the thermometer and the spectroscopy setup.

Random errors in luminescence measurements are caused by the statistical nature of photon detection and can be recognized as noise in the emission spectrum. The conversion of intensity ratio to temperature is also subject to this noise and this is generally quantified by the temperature uncertainty ( $\sigma_T$ ). Assuming that the noise follows the Poisson distribution, the temperature uncertainty simplifies to

$$\sigma_T = \frac{1}{S_r} \frac{\sigma_{LIR}}{LIR} = \frac{1}{S_r} \sqrt{\frac{1}{I_A} + \frac{1}{I_B}}. \quad (1.2)$$

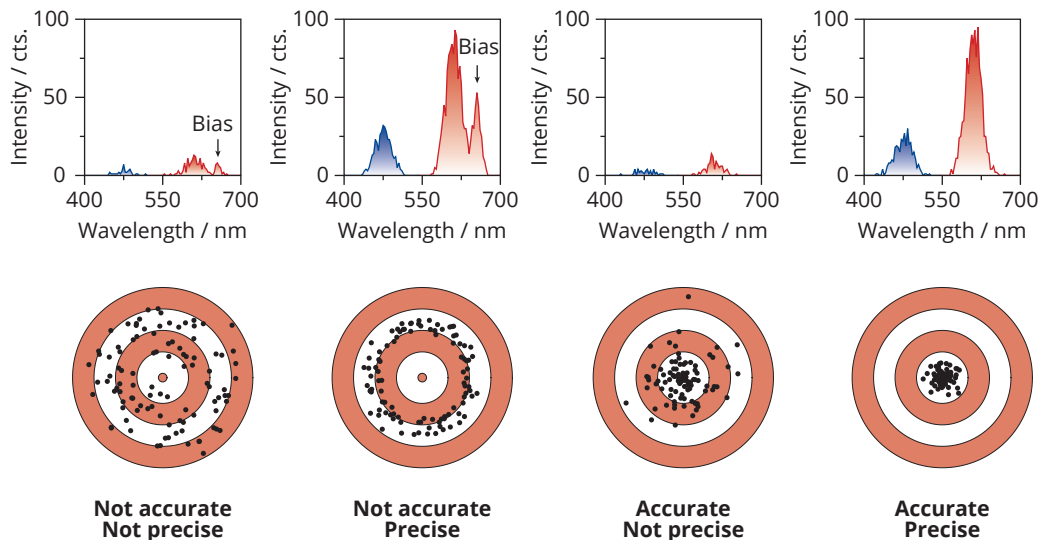


**Figure 1.7.** Biases and uncertainties in LIR thermometry. The upper row of panels shows simulated luminescence spectra that consist of two Gaussian emission bands A (red) and B (blue) with Poissonian detection noise. The first two spectra additionally contain a third emission band that represents a bias. The bottom row of panels displays the measured temperatures calculated using the intensity ratio B/A in a series of 100 simulated spectra and a relative sensitivity of  $1\% \text{ K}^{-1}$ . Each data point was placed at a random angle on a circle with a radius that scales with the deviation from the true temperature (the bulls eye).

Here,  $\sigma_{LIR}$  is the noise on the  $LIR$  and the square-root term is the total noise-to-signal ratio on emissions A and B, where  $I_{A,B}$  is the corresponding integrated photon counts. The temperature uncertainty also depends on the relative sensitivity

$$S_r = \frac{1}{LIR} \left| \frac{dLIR}{dT} \right|, \quad (1.3)$$

which quantifies how strongly the  $LIR$  responds to temperature (with units in  $\% \text{ K}^{-1}$ )—division by the absolute value of the  $LIR$  makes comparison with other thermometers possible. Eq. 1.2 shows that thermometers with bright luminescence have lower temperature uncertainties. To reduce quenching of the luminescence by multi-phonon relaxation most Boltzmann thermometers therefore rely on thermally coupled levels with a large energy gap to the next lower-lying level, typically above  $3000 \text{ cm}^{-1}$ .

Fig. 1.7 summarizes the impact of random and systematic errors on the accuracy and precision of radiometric thermometers. To this end, we have simulated series of luminescence spectra at different luminescence intensities with and without an overlapping emission line, *i.e.* a bias. The overlapping emission causes a shift of the measured temperatures, which leads to inaccurate values. As indicated by Eq. 1.2, random errors decrease with increasing luminescence intensity,



which we also observe in Fig. 1.7. In the presence of a bias, increasing the luminescence intensity also decreases the random errors, although the measurement remains inaccurate. Reliable thermometry experiments thus not only require a sensitive response to temperature and high luminescence intensities but also the absence of systematic errors.

## 1.4 Motivation and outline of the PhD thesis

Luminescence thermometry is a rapidly expanding field that has the potential to give insight into temperature profiles and heat distributions with sub-micrometer resolution. Thermometry research is nowadays focused on the development of new materials with increasingly higher relative sensitivities, but it is often unclear how these materials perform in the actual application. In this thesis, we systematically study the random and systematic errors of luminescent thermometers to better understand what affects the reliability of temperature readout and to find methods that improve thermometer design.

The random errors of thermometer materials are typically characterized by the temperature uncertainty. However, this quantity strongly depends on the spectroscopic setup and the measurement conditions, making it unsuited for comparison of thermometers. In **Chapter 2**, we provide the theoretical background of photon-detection statistics and use this to predict the temperature uncertainty of luminescent thermometers in actual experimental conditions. To verify these predictions we experimentally determine the uncertainty from thermometer emission that is acquired with different spectroscopic settings and background levels, introducing various sources of photon and detection noise. Our findings elucidate which intrinsic thermometer properties determine the temperature uncertainty and this enables us to propose alternative guidelines for fair thermometer comparison.

Although materials with new mechanisms of temperature-dependent luminescence are continuously developed, thermometers that rely on Boltzmann equilibrium remain the most popular type. The relative sensitivity of Boltzmann thermometers follows the simple expression  $\Delta E/k_B T^2$ , but this puts an upper limit on the dynamic temperature range, in which these thermometers can be reliably used. At low temperatures, the relative sensitivity is high, but the sustainment of Boltzmann equilibrium is no longer given due to slow nonradiative coupling, putting a lower limit on the dynamic range. In **Chapter 3**, we fundamentally study the onset of thermal equilibrium and find strategies to shift the onset temperature to lower values. Our experimental results on  $\text{Eu}^{3+}$ -doped materials show that host lattices with high vibrational energies and short lanthanide-ligand distances have low onset temperatures. We compare these results with materials based on other lanthanide ions, which indicates that selection rules further control the onset of thermal equilibrium. These insights enable more accurate measurements in an extended temperature range.

In **Chapter 4**, we introduce a novel thermometer based on the colorful luminescence of  $\text{Ho}^{3+}$  (Fig. 1.1). The luminescence not only responds to temperature, but it is also sensitive to the  $\text{Ho}^{3+}$

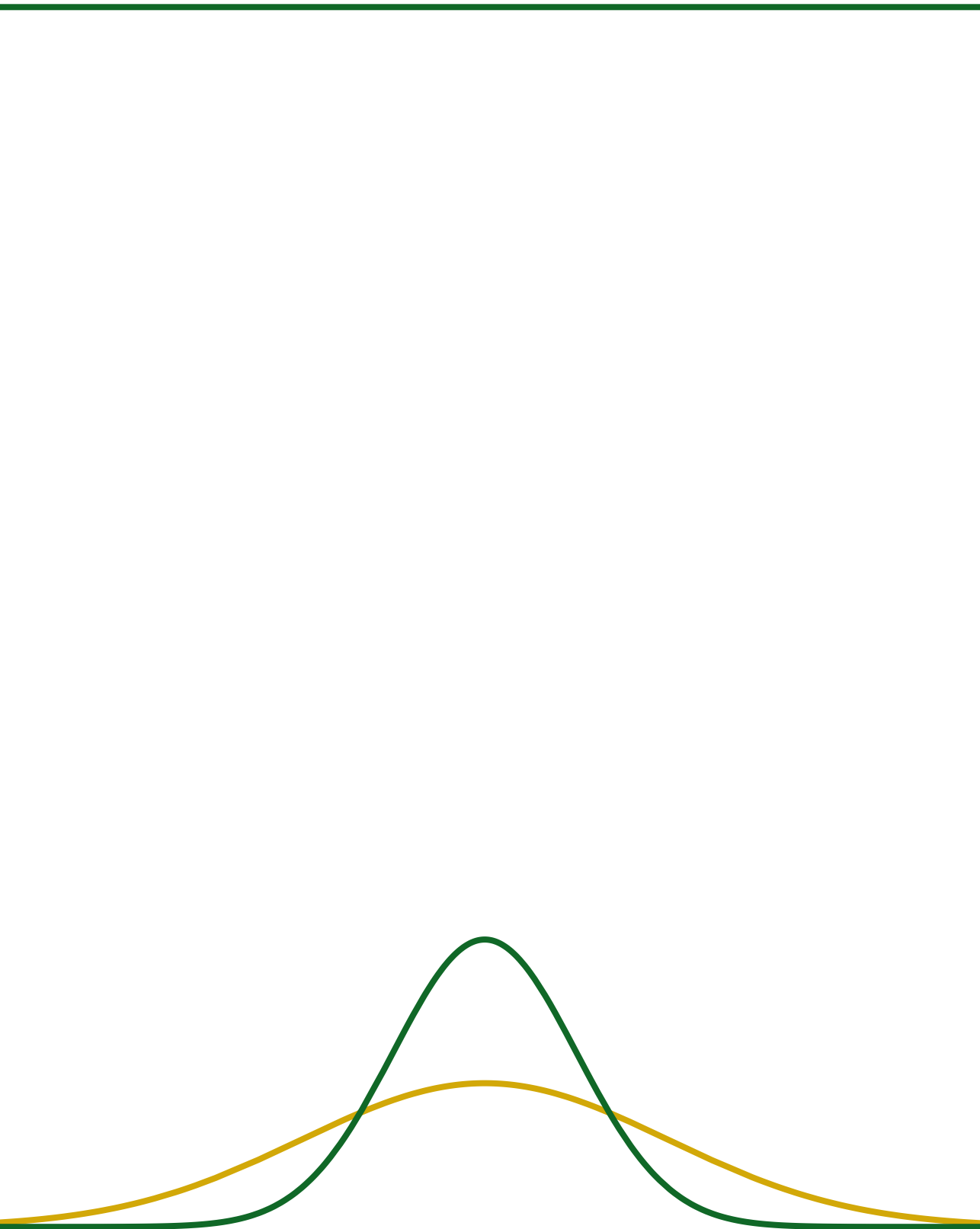
concentration. This makes it possible to tune the sensitivity and precision of the thermometer by variation of the  $\text{Ho}^{3+}$  concentration. We carefully measure the excited-state dynamics of the thermometer to model the light output and find the  $\text{Ho}^{3+}$  concentration with minimal temperature uncertainty for a specific temperature window.

A few studies have examined the performance of thermometers in realistic experimental conditions and they reported systematic errors in temperature readout caused by experimental factors like wavelength-dependent absorption of light by the sample medium. As a result, the community started to realize that control over systematic errors is important for reliable measurements. In **Chapter 5**, we study two other sources of systematic errors. As a model experiment, we map the temperature on a microelectronic heater using the upconversion luminescence of  $\text{Er}^{3+}$ -/ $\text{Yb}^{3+}$ -co-doped nanocrystals and acquire the luminescence with confocal microscopy, achieving a spatial resolution of  $\sim 1 \mu\text{m}$ . Our results reveal that high-resolution thermometry is vulnerable to interfering emissions from higher excited states, caused by high excitation intensities. Moreover, we observe systematic deviations of the readout temperature at the reflective metal of the heater, which we explain as self-interference between reflected and direct thermometer emission. Both the interfering emissions and the photonic distortions introduce biases in temperature readout. Although our static samples allow for the correction of these errors, this is more challenging or even impossible in dynamic systems.

**Chapter 6** further investigates the photonic distortions using substrates that systematically vary the distance between a Au mirror and  $\text{Er}^{3+}$ - or  $\text{Ho}^{3+}$ -based thermometers. The average energy  $\bar{\omega}$  of the temperature-sensitive emissions is similar for both thermometers, while the difference in emission energy  $\Delta\omega$  of  $\text{Ho}^{3+}$  is larger by a factor 7. We observe readout errors of 100 K for  $\text{Er}^{3+}$  and much higher errors of 250 K for  $\text{Ho}^{3+}$ . Our self-interference model reveals that not only the emission energies of the thermometer ( $\Delta\omega/\bar{\omega}$ ), but also the numerical aperture of the microscope objective and the sample geometry determine the photonic artifacts. These results serve as an important guideline to minimize errors in temperature readout caused by the optical environment.

**Chapter 7** summarizes the work of this thesis and gives several future research directions to further reduce systematic and random errors in luminescence thermometry.





---

# Chapter 2

## The impact of noise and background on measurement uncertainties in luminescence thermometry

### Abstract

Materials with temperature-dependent luminescence can be used as local thermometers when incorporated in, for example, a biological environment or chemical reactor. Researchers continuously develop new materials aiming for the highest sensitivity of the luminescence to temperature. Although the comparison of luminescent materials based on their temperature sensitivity is convenient, this parameter gives an incomplete description of the potential performance of the materials in applications. In this Chapter, we demonstrate how the precision of a temperature measurement with luminescent nanocrystals depends not only on the temperature sensitivity of the nanocrystals, but also on their luminescence strength compared to measurement noise and background signal. After first determining the noise characteristics of our instrumentation, we show how the uncertainty of a temperature measurement can be predicted quantitatively. Our predictions match the temperature uncertainties that we extract from repeated measurements, over a wide temperature range (303–473 K), for different CCD readout settings, and for different background levels. The work presented here is the first study that incorporates all these practical issues to accurately calculate the uncertainty of luminescent nanothermometers. This method will be important for the optimization and development of luminescent nanothermometers.

### Based on:

T.P. van Swieten, A. Meijerink and F.T. Rabouw, The Impact of Noise and Background on Measurement Uncertainties in Luminescence Thermometry, *ACS Photonics* **9**, 1366–1374 (2022).

---

## 2.1 Introduction

Nanomaterials with temperature-dependent luminescence are one of the most versatile thermometers on the microscopic scale with applications in biology, electronics, and catalysis.<sup>34–36</sup> The temperature of a nanothermometer is determined by recording its emission spectrum or its luminescence lifetime. The intensity ratio between two emission bands is most frequently considered, because this parameter is insensitive to fluctuations in the excitation intensity, changes in alignment, and scattering of the luminescence. The relative sensitivity,  $S_r$  (in %  $K^{-1}$ ), expresses how strongly the intensity ratio changes with temperature and is thus a measure for the measurement accuracy.  $S_r$  is an intrinsic property of a thermometer material (which however depends on temperature) and is easily determined by measuring emission spectra over a range of temperatures. Newly developed thermometer materials are therefore often characterized and compared in terms of this parameter.<sup>13,37</sup>

In practice, the reliability of temperature readout relies not only on the relative sensitivity but also on the signal-to-noise ratio of a measurement. These parameters together determine the temperature uncertainty,  $\sigma_T$ . Current methods to determine  $\sigma_T$  are diverse. The most direct method is experimentally recording a series of luminescence spectra and calculating the standard deviation of the extracted temperatures.<sup>38</sup> Alternatively, the noise level on a single spectrum may be estimated from fluctuations in the baseline. The latter method underestimates the temperature uncertainty, because it fails to take the noise on detected photons into account.<sup>39</sup> More importantly, both methods are often used in idealized circumstances where background signal is minimal, a large amount of thermometer material is measured, luminescence is efficiently collected, and/or long measurement times are used. The extracted values of  $\sigma_T$  depend strongly on these circumstances. In contrast to  $S_r$ ,  $\sigma_T$  is not an intrinsic property of a (nano)thermometer material. Consequently, user-to-user differences have caused variations in reported uncertainties of several orders of magnitude for the same thermometer, while some measurement conditions such as environment of the thermometer were similar.<sup>13</sup> It is not clear to what extent these reported values of  $\sigma_T$  are relevant for actual applications of the (nano)thermometers, which may put restrictions on the measurement procedure and/or introduce background fluorescence and black-body radiation.<sup>33</sup> In addition, undesired emissions from the thermometer itself, for example from higher-excited levels, can interfere with temperature measurements.<sup>30</sup> Although subtracting a reference spectrum of any background signal removes the systematic error,<sup>40</sup> the influence on the temperature uncertainty remains. It is currently unclear how these practical complications affect the performance of luminescent (nano)thermometers. This makes a fair comparison of potential thermometer materials impossible.

In this Chapter, we use the statistics of photon detection to quantify how noise and background signal affect the temperature uncertainty of a luminescence (nano)thermometry experiment. Not only the properties of the thermometer material are important, but also the characteristics of the detector and the sample. We first measure the background-free upconversion luminescence of  $\text{NaYF}_4:\text{Er}^{3+}(2\%),\text{Yb}^{3+}(18\%)$  nanocrystals using a conventional CCD and characterize the diffe-

rent types of detector noise. Using error propagation, we quantitatively explain the temperature uncertainties determined by recording a series of spectra, which increase with set temperature. We study the impact of detector noise by recording upconversion luminescence with electron multiplication gain using an electron multiplying CCD (EMCCD). An increase in gain boosts the signal to overcome readout noise and thus reduces the temperature uncertainty. Finally, we examine the effect of background signal. Even if we subtract the background signal, the experimental temperature uncertainty increases with higher background levels as predicted from the larger error on the number of detected photons. These new methods to calculate the uncertainty show that not only the relative sensitivity  $S_r$  of a thermometer determines its performance, but also the achievable signal-to-noise ratio. The temperature uncertainty  $\sigma_T$  depends strongly on measurement conditions and is therefore a poor parameter to compare the potential of thermometer materials. We propose alternative metrics that could be considered.

## 2.2 Results

We first discuss the uncertainty achieved with a model thermometer based on two emissive excited levels A and B (Fig. 2.1a). An increase in temperature affects the relative intensities emitted by these levels, resulting in a change of the intensity ratio in the emission spectrum. In a typical experiment, these emissions are spectrally separated by a grating and captured by a CCD, photo-multiplier tube, or photodiode array. The photosensitive material in the detector converts the incident photons to photoelectrons. The number of photoelectrons  $k$  recorded in one exposure will follow the Poisson distribution:

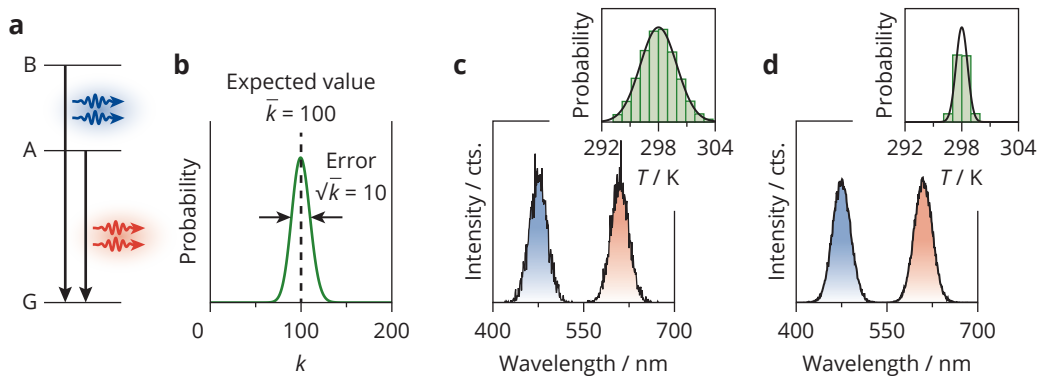


**Figure 2.1.** The temperature uncertainty achieved with a model thermometer. **(a)** Energy level diagram of the model thermometer. The solid black arrows represent the radiative decay pathways. **(b)** The Poisson distribution with mean  $\bar{k} = 100$  and standard deviation  $\sqrt{\bar{k}} = 10$ . **(c)** Simulated luminescence spectrum comprising two Gaussian emission bands with Poissonian detection noise. The inset shows a histogram of the temperatures that are extracted from 10000 simulated spectra using the ratio of integrated counts, a physical temperature of 298 K, and a relative sensitivity of  $1\% \text{ K}^{-1}$ . The black line is a normal distribution with a mean of 298 K and a standard deviation that is calculated via Eq. 2.3. **(d)** Same as in **(c)** but for a total luminescence intensity that is 10 times higher.

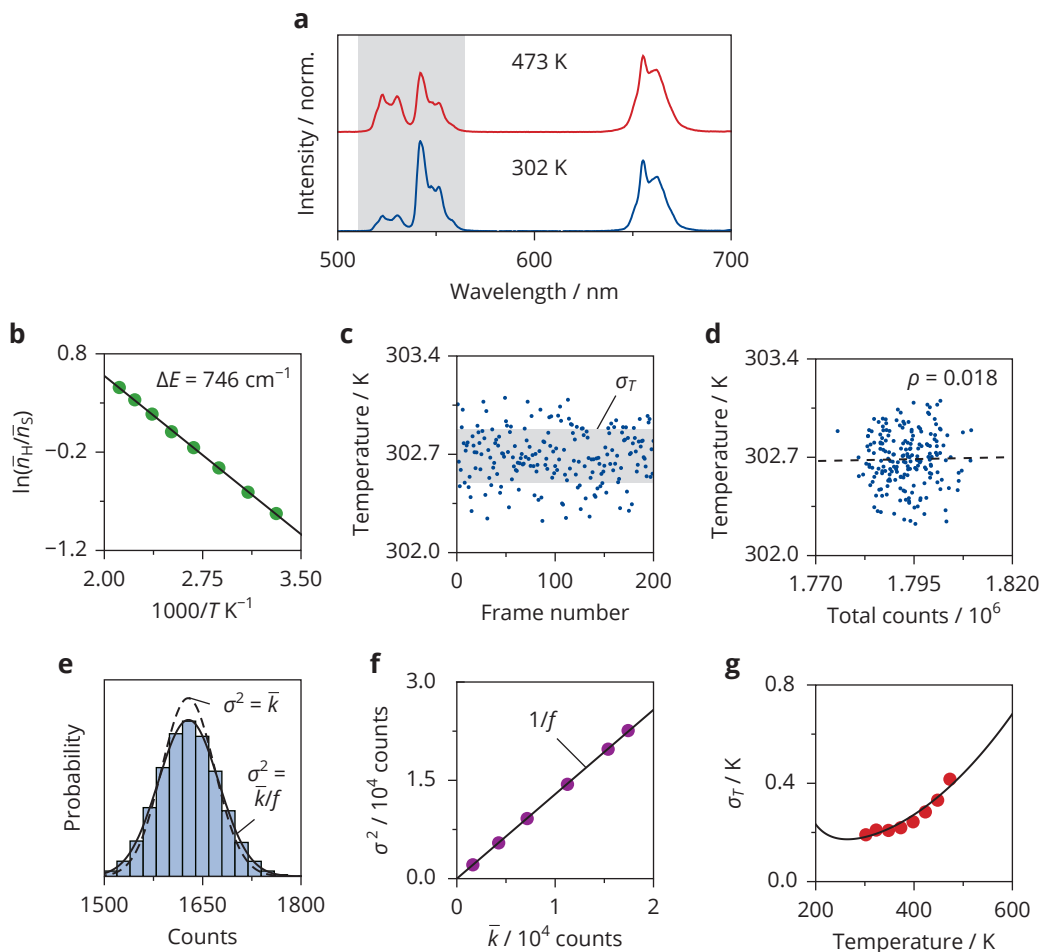


**Figure 2.2.** The experimental temperature uncertainty. **(a)** Upconversion luminescence of dried  $\text{NaYF}_4:\text{Er}^{3+}(2\%),\text{Yb}^{3+}(18\%)$  nanocrystals upon 980-nm excitation at 302 K (blue) and 473 K (red). **(b)** The logarithm of the ratio between the  ${}^2\text{H}_{11/2}$  and  ${}^4\text{S}_{3/2}$  emission with integration ranges 516–534 nm and 538–545 nm (green dots), respectively. The black line is a fit of the experimental ratios to Boltzmann's distribution (Eq 2.4), yielding values of  $746 \text{ cm}^{-1}$  for  $\Delta E$  and 15.2 for  $C$ . **(c)** Temperatures extracted from 200 experimental spectra using the calibration in **(b)**. The thermocouple in our heating stage measured a temperature of 302 K during the acquisition of spectra, showing a small deviation with the mean of the temperatures extracted from the spectra, likely caused by a systematic error in the calibration. The grey shaded area covers the temperature range of the mean  $\pm$  standard deviation. **(d)** Correlation between the measured temperature and the total counts within the integration ranges of the  ${}^2\text{H}_{11/2}$  and  ${}^4\text{S}_{3/2}$  emissions. The correlation coefficient  $\rho$  is close to zero, indicating that measured temperature and total counts are uncorrelated. **(e)** The distribution of counts per 1000-ms frame, for pixels on our CCD camera showing an average of 1629 counts / 1000 ms when measured over 200 frames. The camera recorded the reflection of a white lamp on a microscopy slide. The solid line is a fit of the experimental data to the normal distribution ( $\bar{k} = 1629$ ,  $\sigma^2 = 2112$ ) and the dashed line shows the Poisson distribution with  $\bar{k} = 1629$ . **(f)** Plot of the variance against the mean (purple dots) measured via the procedure in **(e)** for different intensities of the white lamp. The black line is a fit of the experimental data to the model



$\sigma^2 = \bar{k}f + \sigma_r^2$ , where  $f = 0.78$  is the analog-to-digital conversion factor and  $\sigma_r^2 = 57$  is the readout variance of one pixel. **(g)** Temperature uncertainties at various physical temperatures obtained via the procedure in **(c)** (red dots). The black line is the temperature uncertainty calculated using Eq. 2.3, with no fit parameters.

$$p_{\text{poisson}}(k, \bar{k}) = \frac{\bar{k}^k e^{-\bar{k}}}{k!}, \quad (2.1)$$

where  $\bar{k}$  is the expected number of photoelectrons, which is proportional to the product of the photon flux and the acquisition time, and is in general different for levels A and B. An interesting property of the Poisson distribution is that the standard deviation is equal to the square root of the expected value (Fig. 2.1b). The next step in the detection process is the translation of photoelectrons to digital counts for each pixel, which enables construction of the emission spectrum. For a luminescence thermometry experiment, the observables of interest in the spectrum are the integrated counts of the emissions from levels A and B:  $n_A$  and  $n_B$ , respectively. As  $n_A$  and  $n_B$  are independent random variables, the measurement error on the intensity ratio  $R = n_B/n_A$  follows from error propagation:<sup>41</sup>

$$\sigma_R = \sqrt{\left(\frac{\partial R}{\partial \bar{n}_A}\right)^2 \sigma_A^2 + \left(\frac{\partial R}{\partial \bar{n}_B}\right)^2 \sigma_B^2} = \frac{\bar{n}_B}{\bar{n}_A} \sqrt{\left(\frac{\sigma_A}{\bar{n}_A}\right)^2 + \left(\frac{\sigma_B}{\bar{n}_B}\right)^2}. \quad (2.2)$$

Here,  $\bar{n}_{A,B}$  are the expected counts of A and B with corresponding variances  $\sigma_{A,B}^2$  and  $\bar{n}_{A,B}/\sigma_{A,B}$  are the signal-to-noise ratios on  $n_A$  and  $n_B$ . Assuming that the errors and expected counts are related as described by the Poisson distribution, we expect lower  $\sigma_R$  for higher counts.

Conversion of  $R$  to a temperature value requires knowledge of the relative sensitivity. This is often obtained by calibrating the spectral response of the thermometer over a range of temperatures. Any error in the calibrated relative sensitivity leads to a systematic difference between the measured and physical temperature. However, the random error  $\sigma_T$  on the measured temperature only depends on the probability distribution function of the measured  $R$  and on the relative sensitivity of the thermometer:<sup>41</sup>

$$\sigma_T = \sqrt{\left(\frac{\partial T}{\partial R}\right)^2 \sigma_R^2} = \frac{1}{S_r} \sqrt{\left(\frac{\sigma_A}{\bar{n}_A}\right)^2 + \left(\frac{\sigma_B}{\bar{n}_B}\right)^2} \quad (2.3)$$

This shows that, as expected, the temperature uncertainty decreases with increasing signal-to-noise ratio. An alternative approach of luminescence thermometry relies on the shift of an emission band at varying temperature. We use a similar analysis as above to determine the temperature uncertainty of measurements based on a spectral shift (Eqs. A2.1–A2.2). Finally, we verify Eq. 2.3 by simulating luminescence spectra with two emissions bands and determine the temperature from the ratio of the simulated counts (Fig. 2.1c). These simulated temperatures follow a normal distribution with a standard deviation that matches  $\sigma_T$  calculated using Eq. 2.3. The distribution

of temperatures would deviate from normal if  $\bar{n}_{A,B}$  becomes of order unity, rather than  $\gg 1$  as we consider in Fig. 2.1 and is typical in experiments. An increase in counts results in a narrower distribution of measured temperatures, consistent with Eq. 2.3 (Fig. 2.1d). We thus understand quantitatively how experiments with higher counts, performed with, for example, longer acquisition times or brighter thermometers, have a lower temperature uncertainty.

In Fig. 2.2, we experimentally study the temperature uncertainty of thermometry measurements at elevated temperatures. We acquired spectra with a CCD camera, because this is the most frequently used detector in the luminescence thermometry community. The CCD camera conveniently records an entire spectrum within one capture. In contrast, step-wise acquisition of a spectrum with a scanning monochromator and single-point detector such as a photo-multiplier tube leads to additional temperature errors if the excitation intensity fluctuates during the measurement. We use  $\text{NaYF}_4:\text{Er}^{3+}(2\%),\text{Yb}^{3+}(18\%)$  nanocrystals as thermometers, because green upconversion emission from this popular thermometer material can be excited with 980-nm light, preventing background fluorescence.<sup>42</sup> Fig. 2.2a shows the luminescence spectra, in which the two emission bands at 540 nm and 520 nm are due to radiative decay from the thermally coupled levels in  $\text{Er}^{3+}$ ,  $^4\text{S}_{3/2}$  and  $^2\text{H}_{11/2}$ , respectively. An increase in temperature ( $T$ ) changes the ratio of the expected counts within the emission bands of  $^4\text{S}_{3/2}$  and  $^2\text{H}_{11/2}$ ,  $\bar{n}_S$  and  $\bar{n}_H$ , respectively, following Boltzmann's distribution

$$\frac{\bar{n}_H}{\bar{n}_S} = C \exp\left(-\frac{\Delta E}{k_B T}\right), \quad (2.4)$$

where  $\Delta E$  is the energy gap between these levels,  $k_B$  is Boltzmann's constant, and  $C$  is the pre-exponential factor that includes the degeneracies and radiative decay rates from the two levels to the ground state. To use this relation as a calibration of our thermometer, we average 200 spectra and obtain  $\bar{n}_S$  and  $\bar{n}_H$  by summing the counts of all pixels within the integration boundaries of the corresponding emission bands. We then fit the ratio measured at various temperatures to Eq. 2.4 and find a value of  $746 \text{ cm}^{-1}$  for  $\Delta E$  and 15.2 for  $C$  (Fig. 2.2b).<sup>43</sup> We use this calibration to convert the measured intensity ratios from spectra with different levels of noise to readout temperatures.

Fig. 2.2c shows the temperatures that we extracted from a series of spectra using the calibration of Fig. 2.2b.<sup>44</sup> These values are evenly distributed around the mean, which is a sign of a stable physical temperature during the measurement. Correlations between the extracted temperature and the total green luminescence counts could indicate that the laser heats the sample as variations in laser intensity would result in higher count rates coinciding with more laser heating. Experiments at higher laser powers do show such correlations (Fig. A2.2), which indicates that increasing the excitation intensity to reduce the uncertainty can induce a systematic error on temperature readout. This is not observed in our experiments shown in Fig. 2.2d. We therefore used the standard deviation of the measured temperatures as the experimental temperature uncertainty at a fixed sample temperature. Fluctuations in excitation intensity below the heating threshold

do not affect the intensity ratio nor the signal-to-noise ratio (Fig. A2.3).

To understand the magnitude of the variations in measured temperature (Fig. 2.2c), we must consider the noise generated by our detector. The main noise sources in a CCD measurement are counting noise due to the statistics of incident photons and readout noise due to the translation of photoelectrons to digital counts by the analog-to-digital converter (ADC).<sup>45</sup> We characterize these by acquiring a large set of 200 reference images on our CCD camera, illuminating it with a white lamp, and histogramming the digital counts of pixels with the same mean (Fig. 2.2e). The distribution of digital counts approximates a normal distribution with a variance that is, in our case, slightly larger than the corresponding Poisson distribution would have, taking the single-pixel readout variance into account. This difference is due to the conversion of photoelectrons to digital counts, which changes the variance on the output counts by the ADC factor,  $f$ .<sup>46,47</sup> Fig. 2.2f shows a fit of the experimental variances to a model that includes the ADC factor and the readout noise:

$$\sigma^2 = \frac{\bar{n}}{f} + \sigma_r^2. \quad (2.5)$$

We find a value of 0.78 for the ADC factor, which is specific to our camera in the used settings. If an emission band is integrated over  $N$  camera pixels, the variance of the total readout noise on this band is  $N$  times larger than the single-pixel readout variance  $\sigma_r^2 = 57$ . We can now insert this expression and the relative sensitivity of a Boltzmann thermometer,  $\Delta E/k_B T^2$ ,<sup>29</sup> into Eq. 2.3 to calculate the expected temperature uncertainty from a luminescence spectrum.

Fig. 2.2g shows the temperature dependence of the uncertainty by comparing experiments with the theoretical trend (Eqs. 2.3–2.5). Using the method presented in Fig. 2.2c, we determine the temperature uncertainty at various physical temperatures and find values of 0.2 K at room temperature increasing to more than 0.4 K at 473 K.<sup>48,49</sup> Between the different physical temperatures of the experiment, the total counts within the spectrum varied slightly—a decrease is likely due to thermal quenching and an increase could indicate water desorption from the surface of the dried nanocrystals.<sup>50</sup> This affects the signal-to-noise ratio and thus obscures the impact of the intensity ratio on the temperature uncertainty. We therefore kept the sum of  $\bar{n}_S$  and  $\bar{n}_H$  roughly constant at  $2 \times 10^6$  counts, which allows us to separately calculate  $\bar{n}_S$  and  $\bar{n}_H$  using Eq. 2.4 in a range of physical temperatures. We can therefore use Eq. 2.4 to calculate  $\bar{n}_S$  and  $\bar{n}_H$  separately, depending on the physical temperature. Inserting these values, along with the detector characteristics (Eq. 2.5), into Eq. 2.3 yields the theoretical uncertainty (black line in Fig. 2.2g). The calculated uncertainties agree well with the experimental values, without using any fit parameters. We therefore conclude that after proper characterization of the photodetector, error propagation correctly predicts the experimental uncertainty and its temperature dependence.

As a further illustration of the effect of the detector noise characteristics on a temperature measurement, we consider the effect of electron multiplication (EM) in an EMCCD. Emerging applications of luminescent nanomaterials, such as single-particle thermometry, require photodetectors that are able to record extremely weak signals.<sup>51,52</sup> EMCCDs could offer a solution

as they enhance the signal by orders of magnitude, compared to conventional CCDs, but the electron multiplication process causes additional noise.<sup>45,46</sup> We start by considering the detection of photons and generation of photoelectrons, which in both a conventional CCD and an EMCCD follows Poisson statistics. Both types of cameras then transfer the photoelectrons to the ADC via the serial readout register and convert them to digital counts. In an EMCCD camera, the readout register is extended with additional registers that, depending on the applied voltage, multiply the number of photoelectrons and thus boost the signal. In practice, the output electrons pass through hundreds of multiplication registers, resulting in a total EM gain  $G$ . The number of output electrons  $n_{\text{out}}$  follows the gamma distribution

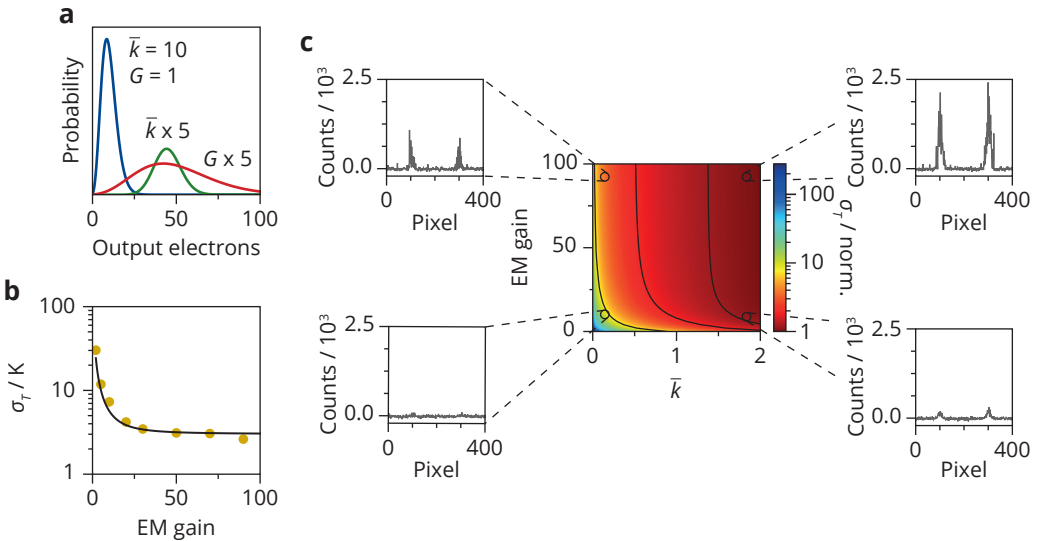


**Figure 2.3.** The effect of electron multiplication on the temperature uncertainty. **(a)** The distribution of output electrons for different input photoelectrons  $\bar{k}$  and EM gains  $G$ . This distribution is obtained by convolution of the gamma distribution with the Poisson distribution. **(b)** The experimental temperature uncertainties obtained from 200 upconversion spectra for various levels of EM gain ranging from 2 to 90 (yellow dots). The average numbers of photoelectrons generated by a pixel are 5 and 30 for the  $^2\text{H}_{11/2}$  and  $^4\text{S}_{3/2}$  emissions, respectively. The solid black line is the temperature uncertainty calculated via Eqs. 2.3 and 2.7, with no fit parameters. **(c)** Color map of the temperature uncertainty as a function of the expected photoelectrons  $\bar{k}$  per pixel and the EM gain. The temperature uncertainties in the color map were calculated via the expected value of the output electrons, excluding spurious electrons, and the variance of all output electrons (Eq. A2.3). All uncertainties were normalized to the minimum value within the map. The contour lines correspond to  $\sigma_T$  values of 1.2, 2.0, and 8.0 K. We obtain the simulated spectra in Fig. 2.3c by drawing random numbers of output electrons from the distribution of Eq. A2.3, with as an input a spectrum consisting of two peaks with Gaussian shape of equal amplitude covering a total of 400 pixels. The four insets show example spectra simulated for the experimental settings to which they are linked in the color map. We set the readout noise for each pixel to  $\sigma_r = 26$ , matching that of our EMCCD detector at a 30-MHz readout rate and pre-amplifier gain 2. We assume a probability of spurious charges of  $p_s = 0.0004$  to give the simulated spectra the characteristic background noise of electron multiplication.

$$p_{\text{gamma}}(n_{\text{out}}, k, G) = n_{\text{out}}^{k-1} \frac{e^{-n_{\text{out}}/G}}{G^k (k-1)!}. \quad (2.6)$$

Here  $k$  is the number of photoelectrons generated by a CCD pixel, which enter the multiplication registers. Fig. 2.3a shows the probability distribution of  $n_{\text{out}}$  as a function of expected number of input photoelectrons  $\bar{k}$  and the EM gain  $G$ . EM produces an expected number of counts of  $\bar{n}_{\text{out}} = \bar{k}G$  with a variance that approximates  $\sigma_n^2 = 2\bar{k}G^2/f$  (Eq. A2.3 and Fig. A2.4). The signal-to-EM-counting-noise ratio  $\bar{n}_{\text{out}}/\sigma_n = \sqrt{kf/2}$ , where readout noise is excluded, is thus independent of the gain factor. This derivation shows that EMCCD measurements have an additional counting noise of  $\sqrt{2}$ , commonly referred to as the excess noise factor. Therefore, EM gain can only improve a temperature measurement if  $n_{\text{out}}$  is small with respect to other noise sources.

In Fig. 2.3b, we compare the experimental temperature uncertainty at various levels of EM gain with theoretical predictions. First, we acquired 200 experimental spectra with an EM gain of only a factor 2, while keeping the number of incident photons per pixel low. This resulted in an extremely high uncertainty of 30 K. Applying EM gain to values of 25 causes a sharp decline of the uncertainty to 3 K. The effect of even higher EM gains is weak. We again explain this trend using Eqs. 2.3 and 2.5 (solid line) by realizing that the variance of the  $^4\text{S}_{3/2}$  and  $^2\text{H}_{11/2}$  counts is due to a combination of Poissonian counting noise amplified by the ADC factor  $f$  and the EM gain factor  $G^2$  and readout noise. [For photon fluxes relevant for luminescence thermometry, we can neglect noise due to spurious electrons created during shifting of charges through the multiplication register (Fig. A2.5).<sup>45,46</sup>] EM gain increases the signal (as well as the counting noise) with respect to the readout noise:

$$\frac{\bar{n}_{\text{out}}}{\sigma_n} = \frac{\bar{k}G}{\sqrt{2\bar{k}G^2/f + \sigma_r^2}}. \quad (2.7)$$

Fig. 2.3c illustrates the effect of EM gain for a range of expected photoelectrons. We observe the highest uncertainty in the bottom left of the map, where both the EM gain and the number of expected photoelectrons are low—the corresponding simulated spectrum barely shows emission. For all numbers of expected photoelectrons, we observe a rapid decrease of the uncertainty with increasing gain, although this effect becomes negligible once readout noise is overcome (Fig. A2.6). Indeed, the signal-to-total-noise ratio (Eq. 2.7) approaches a constant value of  $\sqrt{kf/2}$  for large  $G$  and EM cannot improve it further (Fig. A2.7). In practice, EM gain is thus useful if and only if the signal is weak compared to readout noise.

Besides the photodetector, background emission by the surroundings of the thermometer can be another source of uncertainty, which is relevant when the thermometer is used in realistic experimental conditions.<sup>53</sup> We discuss how such a distortion of the spectrum affects the temperature uncertainty even after subtraction of the background. Fig. 2.4a shows how we have mimicked this experimental issue: we have measured the upconversion luminescence with and without additional broadband background signal from a white lamp. Subtracting a reference measurement of the

lamp recovers a clean thermometer spectrum from the experiment with background. However, the noise on the background signal cannot be removed. The corrected spectrum therefore contains more noise compared to the background-free upconversion emission spectrum (Fig. 2.4b).

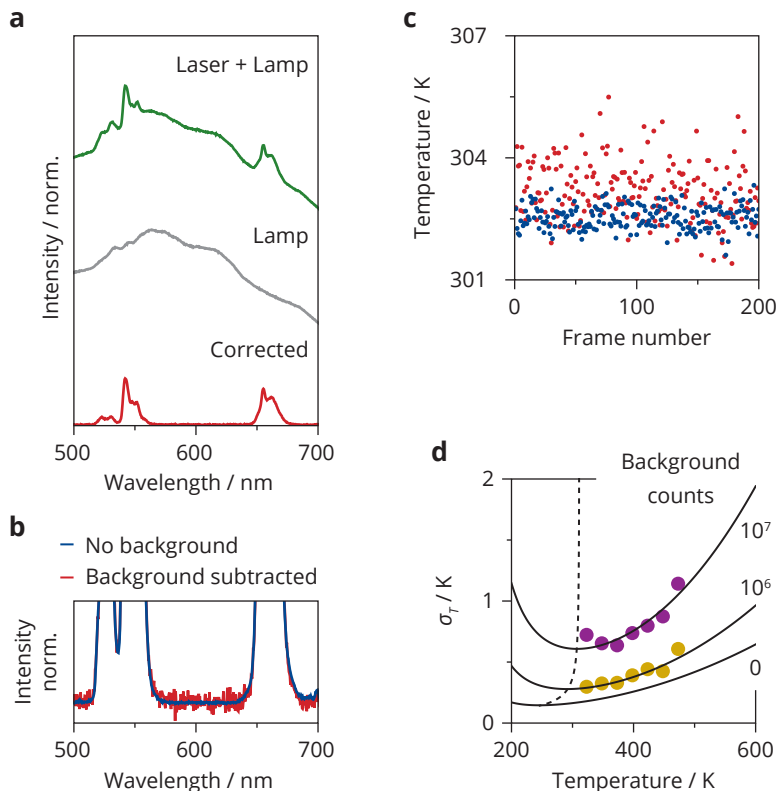


**Figure 2.4.** The influence of background subtraction on the temperature uncertainty. **(a)** Reflection spectrum of the white lamp illuminating dried  $\text{NaYF}_4:\text{Er}^{3+}(2\%),\text{Yb}^{3+}(18\%)$  nanocrystals without (grey) and with simultaneous 980 nm excitation (green). Subtraction of the grey spectrum from the green spectrum yields the corrected upconversion spectrum (red). The total signal (thermometer) and background (lamp) counts within the integration ranges of the  ${}^2\text{H}_{11/2}$  and  ${}^4\text{S}_{3/2}$  emission are  $2 \times 10^6$  and  $2 \times 10^7$ , respectively. **(b)** Zoom-in on the noise of a spectrum acquired without background (blue) and with broadband background that is subsequently subtracted (red). **(c)** The calibration curve of Fig. 2.2b was used to convert a series of 200 spectra with no background (blue) and with lamp background subtracted (red) to temperatures. The red and blue dots show a systematic difference of the mean, which we attribute to an error introduced by recording and subtracting the reference spectrum, for example because the lamp spectrum fluctuated slightly over time. **(d)** Temperature uncertainties as a function of set temperature, measured by comparing the readout temperature of 200 background-subtracted spectra. The solid black lines are the expected temperature uncertainties for  $2 \times 10^6$  (yellow dots) and  $2 \times 10^7$  (purple dots) subtracted background counts, calculated using Eq. 2.4. The expected background counts on the  ${}^2\text{H}_{11/2}$  and  ${}^4\text{S}_{3/2}$  emissions are obtained by taking the sum of the counts in the subtracted spectrum between 516–534 nm and 538–545 nm, respectively, averaged over 200 spectra. The dashed black line marks the minimum of the temperature uncertainty for all subtracted background counts.

This translates to an increased temperature uncertainty (Fig. 2.4c). We can further understand this from the expression for the variance  $\sigma_{b,i}^2$  in the counts from emitting state  $i$  after background removal

$$\sigma_{b,i}^2 = \frac{\bar{n}_i + \bar{n}_{b,i}}{f} + \sigma_r^2, \quad (2.8)$$

where  $\bar{n}_{b,i}$  is the expected number of background counts removed. Additional counts from dark current in the photodetector have equivalent impact on the temperature uncertainty as background emissions. Again, inserting this expression into Eq. 2.3 gives the theoretical temperature uncertainty after background removal.

The measured uncertainties as a function of physical temperature match the predicted values for a range of different background levels (Fig. 2.4d). We observe higher absolute values of the uncertainty with increasing background. This effect is as large as a factor of three for the background level in Fig. 2.4a, even though we could subtract the background using a reference measurement. We further observe that the minimum of the temperature uncertainty (dashed line) shifts to higher set temperatures with increasing background counts. In practice, low levels of background are challenging to completely avoid, especially at elevated temperatures where black-body radiation becomes an issue. Fig. 2.4 shows how this affects the absolute value of temperature uncertainty as well as the optimal operating temperature of a thermometer compared to idealized measurement conditions without background signal.

Our work clearly demonstrates how the precision of a temperature measurement depends not only on the relative sensitivity of the thermometer, but also on the measurement conditions. As these measurement conditions will be different for different applications, this raises the question of how to define a relevant metric to compare thermometers. Currently, the achieved temperature uncertainty is frequently reported in the literature. However, our results show that the temperature uncertainty is not a fundamental property of the thermometer. Temperature uncertainties measured under idealized experimental conditions are difficult to compare and may not be relevant for applications. In particular, different experimental settings can yield wildly different contributions of various noise sources. However, whatever the specific experimental noise contributions are, the temperature uncertainty is always minimal for a high relative sensitivity  $S_r$  and for a strong luminescence signal (Eq. 2.3). Although  $S_r$  of newly developed thermometer materials is commonly reported,<sup>54</sup> the potential signal strength is hardly considered.

The realization that signal strength is essential for precise temperature measurement makes it possible to identify relevant parameters, in addition to  $S_r$ , that define a good thermometer. The expected counts on emissions A and B can be written as

$$\bar{n}_{A,B} = N_C P_{\text{exc}} \sigma_{\text{abs}} \eta_{\text{PL}} \varphi_{A,B} \eta_{\text{det}} t G. \quad (2.9)$$

Here, absorption of excitation light is determined by the number of luminescent centers in the excitation volume ( $N_C$ ) and the absorption cross section  $\sigma_{\text{abs}}$  per luminescent center. The lumi-

nescence further scales with the photoluminescence quantum yield  $\eta_{\text{PL}}$  of the relevant thermometer emission lines and the temperature-dependent populations that define the fractions  $\varphi_{\text{A,B}}$  of emission coming from A or B. The spectroscopic equipment sets the detection efficiency  $\eta_{\text{det}}$ . The integration time  $t$ , the excitation power used  $P_{\text{exc}}$ , and the EM gain  $G$  can be chosen by the experimentalist.

In Eq. 2.9, we can distinguish the experimental factors ( $\eta_{\text{det}}$ ,  $P_{\text{exc}}$ ,  $t$ ,  $N_{\text{C}}$ , and  $G$ ) from the thermometers properties ( $\sigma_{\text{abs}}$ ,  $\eta_{\text{PL}}$ , and  $\varphi_{\text{A,B}}$ ). The experimental factors will depend on the available equipment and the type of sample. The freedom to choose a long  $t$ , high  $N_{\text{C}}$ , or high  $P_{\text{exc}}$  may be restricted if the sample is not static, if the sample volume is small, or if strong excitation induces laser heating (which also depends on heat dissipation in the sample). The values of these parameters are not intrinsic thermometer properties but depend strongly on the application. Another factor that affects the temperature uncertainty is the emission wavelength of the thermometer, because it determines the required type of detector and therefore the amount of dark current. Infrared detectors typically have a high dark current due to the small band gap of the photo-sensitive material, resulting in a relatively high uncertainty for infrared-emitting thermometers. Eq. 2.9 also contains some intrinsic properties that can vary by orders of magnitude between different materials. We propose that a fair comparison between potential thermometer materials should consider these intrinsic parameters. For practical applications, high  $\sigma_{\text{abs}}$  and  $\eta_{\text{PL}}$  for a given doping content  $N_{\text{C}}$  and excitation power  $P_{\text{exc}}$  are as important as a high thermal sensitivity of  $\varphi_{\text{A,B}}$ .<sup>55</sup> These intrinsic properties of the thermometer determine the achievable signal compared to various application-related issues, like background fluorescence or blackbody radiation.

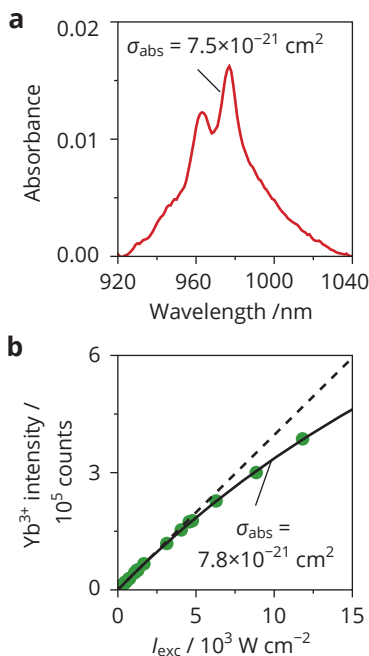


**Figure 2.5.** Experimental methods to determine the absorption cross-section. **(a)** Absorption spectrum of  $\text{NaYF}_4:\text{Yb}^{3+}$  (18%) nanocrystals dispersed in cyclohexane. The spectrum shows a clear absorption band due to the  ${}^2\text{F}_{7/2} \rightarrow {}^2\text{F}_{5/2}$  transition of  $\text{Yb}^{3+}$ . Rayleigh scattering caused a background of roughly 0.0015 absorbance units, which was subtracted from the spectrum. The concentration of the bare nanocrystals without ligands is 10 mg/mL, which corresponds to a concentration of  $\text{Yb}^{3+}$  ions of  $5.4 \times 10^{18} \text{ cm}^{-3}$ . Taking the inhomogeneous dielectric surroundings of the  $\text{Yb}^{3+}$  ions inside the dispersed nanocrystal into account,<sup>19</sup> this translates into an absorption cross-section of  $\sigma_{\text{abs}} = 7.5 \times 10^{-21} \text{ cm}^2$  at 977 nm. **(b)** Intensity of the  $\text{Yb}^{3+}$  luminescence measured on microcrystalline  $\text{NaYF}_4:\text{Yb}^{3+}$  (18%) for various excitation intensities  $I_{\text{exc}}$  of 980 nm light (green dots). The solid black line is a fit of the experimental data to Eq. 2.10, which yields a  $\sigma_{\text{abs}}$  value of  $7.8 \times 10^{-21} \text{ cm}^2$  at 980 nm. The dashed line is a linear fit to the low-excitation-intensity data to clearly visualize the nonlinear trend of the high-excitation-intensity data.



Studies of new thermometers often include measurements of the sensitivity, but experimental values of  $\eta_{\text{PL}}$  and  $\sigma_{\text{abs}}$  are rare. Depending on the doping concentration, the synthesis procedure, and the excitation power,  $\eta_{\text{PL}}$  can vary over a few orders of magnitude and it is therefore an important parameter to report. A well-established method to measure  $\eta_{\text{PL}}$  is to determine the number of absorbed and emitted photons of a sample using an integrating sphere. This has already improved the design and synthesis of thermometer materials. For example, recent studies on  $\text{NaYF}_4:\text{Er}^{3+}, \text{Yb}^{3+}$  nanocrystals have optimized the quantum yield of  $\text{NaYF}_4:\text{Er}^{3+}, \text{Yb}^{3+}$  in a range of excitation powers, reaching values comparable to bulk material.<sup>56</sup>

Characterizing  $\sigma_{\text{abs}}$  can be more challenging, especially for microcrystalline samples where strong light scattering prevents measuring optical absorption over a well-defined path length. We study a clear dispersion of  $\text{Yb}^{3+}$ -doped  $\text{NaYF}_4$  nanocrystals with absorption spectroscopy to show that for a specific ion–host combination  $\sigma_{\text{abs}}$  simply follows from Lambert-Beer's law (Fig. 2.5a).<sup>57–59</sup> We find a maximum value of  $7.5 \times 10^{-21} \text{ cm}^2$  at 977 nm, which matches literature values obtained from absorption measurements of single crystals<sup>60,61</sup> and from the kinetics of upconversion luminescence.<sup>62</sup> These values are an order of magnitude lower than the value that Sui *et al.* obtain from Judd-Ofelt parameters and an experimental photoluminescence decay rate.<sup>63,64</sup> Non-radiative processes, indicated by the multi-exponential decay curve, have likely resulted in an overestimation of the spontaneous emission rate and, thus, of the absorption cross section. Another method has recently been developed by our group, which extracts  $\sigma_{\text{abs}}$  from the luminescence saturation characteristics.<sup>65,66</sup> In contrast to absorption measurements, it works well on microcrystalline samples and is thus a suitable alternative for samples that cannot be synthesized in nanocrystalline form. This method requires standard spectroscopic equipment, a continuous-wave laser, a lens to achieve sufficiently high excitation intensities, and careful characterization of the excitation spot on the sample (Fig. 2.6). We used this method to acquire the luminescence of  $\text{Yb}^{3+}$ -doped  $\text{NaYF}_4$  microcrystals at various excitation intensities ( $I_{\text{exc}}$ ), revealing clear signs of saturation at  $5 \text{ kW cm}^{-2}$  (Fig. 2.5b).<sup>67</sup> We fit this trend to the steady-state emission intensity of an excited two-level system that suffers from ground-state depletion.

$$I_{\text{ss}} = A \frac{\sigma_{\text{abs}} I_{\text{exc}} / h\nu}{\sigma_{\text{abs}} I_{\text{exc}} / h\nu + k_{\text{decay}}}. \quad (2.10)$$

Where  $A$  is a scaling constant,  $h\nu$  is the energy of an excitation photon, and  $k_{\text{decay}}$  is the total decay rate of the excited ion.<sup>68</sup> We find a  $\sigma_{\text{abs}}$  value of  $7.8 \times 10^{-21} \text{ cm}^2$  at 980 nm, which perfectly matches the result of Fig. 2.5a. This demonstrates that the methods presented here provide a reliable  $\sigma_{\text{abs}}$ . Together with existing methods to determine  $\eta_{\text{PL}}$  and  $S_{\text{p}}$ , it should now be possible to predict the uncertainty of temperature measurements for any particular experimental setting. This shows how valuable it is to consider absorption cross sections and the quantum yields in the design of future and existing thermometers.

## 2.3 Conclusions

We have characterized how experimental conditions affect the uncertainty of temperature measurements through (nano)thermometry based on luminescence intensity ratios. We first measured all noise sources associated with photon detection and developed statistical models to quantitatively predict the temperature uncertainty in a wide range of temperatures and for various experimental settings. We observed that enhancement of the luminescence signal by applying EM gain significantly reduces the uncertainty until readout noise is overcome. In addition, we studied the impact of background emissions, which is a realistic practical issue. Background increases the uncertainty of a temperature measurement even if it is properly subtracted from the measurement. Our work demonstrates that the temperature uncertainty is not an intrinsic property of a luminescent (nano)thermometer, but instead strongly depends on the photodetector and measurement conditions. We propose a guideline of how to compare different thermometers in a way that is relevant irrespective of the spectroscopic equipment used or of the sample under consideration. Such new ways of comparing luminescent (nano)thermometers are essential to develop and choose the ideal thermometer for the desired application.

## 2.4 Methods

**Sample preparation.**  $\text{NaYF}_4:\text{Er}^{3+}(2\%),\text{Yb}^{3+}(18\%)$  and  $\text{NaYF}_4:\text{Yb}^{3+}(18\%)$  nanocrystals with a spherical shape and a diameter of roughly 30 nm were synthesized using the method of Geitenbeek *et al.*<sup>43</sup> The nanocrystals were dispersed in cyclohexane. A droplet of the dispersion of upconversion nanocrystals was dried on a cover slip and this was attached to a microscopy slide for mechanical strength. For the measurements at elevated temperatures, a droplet of dispersion was dried directly on a microscopy slide. For the absorption measurements, the dispersion of  $\text{NaYF}_4:\text{Yb}^{3+}(18\%)$  nanocrystals was further purified with one additional washing step. Residual NaF from the synthesis was removed by sedimentation without the addition of anti-solvent.

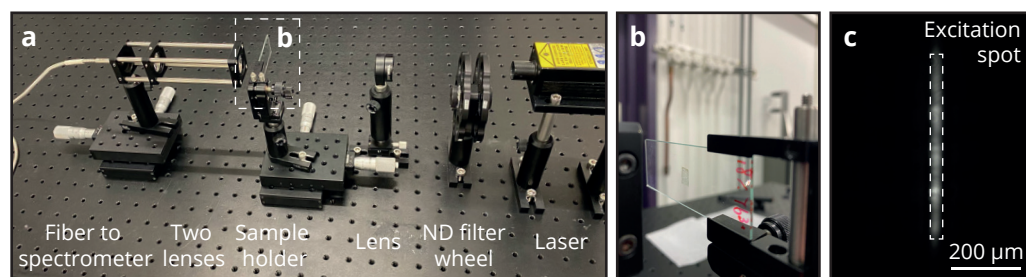


**Figure 2.6.** Luminescence saturation setup. (a) Photograph of the setup. (b) Zoom-in of the microcrystalline  $\text{NaYF}_4:\text{Yb}^{3+}(18\%)$  sample attached to microscopy slide in (b) using double-sided scotch tape. (c) Image of the 980 nm excitation spot on the glass slide near the sample. The divergence of the laser was larger in one direction, which resulted in an elongated shape of the focused laser spot. The white dashed line indicates the spot size from which the excitation intensity was determined.

**Spectroscopy experiments.** Acquisition of the luminescence was performed on a Nikon Ti-U inverted microscope, on which the sample was placed. The microscope contains two levels of filter cube wheels. A 50/50 beam splitter was placed in both the upper and the lower level to reflect 980 nm excitation light (Coherent OBIS LX, 150 mW) and white lamp light (Halogen Lamp 12V–100W), respectively. The excitation laser was used at full power to minimize laser instabilities. The excitation light passed through neutral density filters with an optical density of 4. These light sources were directed to the sample via an air objective (Nikon CFI S Plan Fluor ELWD 60XC) to focus the excitation light on the sample. The upconversion luminescence and reflection of the lamp light was then guided through both beam splitters and a 775 nm shortpass filter (Edmund Optics) towards a spectrograph (Andor Kymera 193i) equipped with an EMCCD detector (Andor iXon Ultra 888). The measurements in conventional CCD and EMCCD modes were acquired with a readout rate of 1 MHz and 30 MHz, respectively. The spectral acquisition times were 1000 ms and 500 ms for the CCD and EMCCD measurements, respectively. The pre-amplifier gain was set to 2 for all measurements. A heating stage (Linkam THMS600) was used to perform the measurements at elevated temperatures. The microscopy slide was pressed against the heating element to ensure good thermal contact. The front window of the stage was replaced by a home-made piece of glassware that enables a working distance of down to 2 mm. A continuous flow of nitrogen gas was directed through the stage.

The absorption spectrum was acquired on a double-beam PerkinElmer Lambda 950 UV/vis/NIR spectrometer. After the measurement, the dispersion was dried to determine the nanocrystal concentration. Thermogravimetric analysis (Q50, TA Instruments) was performed to determine the mass fraction of the ligands (4.4%), which was subtracted from the dried mass to obtain the NaYF<sub>4</sub>:Yb<sup>3+</sup>(18%) concentration. A home-built setup, shown in Fig. 2.6a, was used to determine the absorption cross section from the saturation characteristics of NaYF<sub>4</sub>:Yb<sup>3+</sup>. Microcrystalline NaYF<sub>4</sub>:Yb<sup>3+</sup>(18%) was prepared via the procedure of Krämer *et al.*<sup>67</sup> A thin layer of powder was attached to a microscopy slide using double-sided scotch tape (Fig. 2.6b). To control the excitation intensity on the sample, the light output from a continuous wave 2W 980-nm laser (MDL-III) was directed through neutral-density filters and a lens. A 1000 nm shortpass filter (Thorlabs FESH1000) was used to clean the laser spectrum. Two lenses were used to guide the emission to a fiber that was connected to a spectrometer (Andor Kymera 193i) equipped with a water-cooled CCD detector (Andor iDus 1.7μm InGaAs). A 1000 nm longpass filter (Thorlabs FESH1000) was used to reject the excitation light. The excitation intensity at the sample was determined by measuring the output power of the laser (2.16 W) and characterizing the spot size with a simple CCD camera (Thorlabs DCU223C) (Fig. 2.6c).

## 2.5 Appendix

**Spectral shift thermometers.** To predict the uncertainty of thermometers based on a spectral shift  $\Delta\lambda$  we consider an emission band with a Gaussian shape, which has mean value  $\bar{\lambda}$  and width  $\delta$ . A recorded photon constitutes a measurement of the emission wavelength  $\bar{\lambda}$  with an

uncertainty of  $\delta$ . If we use  $\bar{n}$  photons to estimate  $\bar{\lambda}$ , we achieve an uncertainty of the peak position of  $\delta/\sqrt{\bar{n}}$ . The uncertainty of a measurement based on the spectral shift thus depends on both the spectral width and the signal strength. Similar to Eq. 2.3, we can write the temperature uncertainty of these measurements as

$$\sigma_T = \sqrt{\left(\frac{\partial T}{\partial \bar{\lambda}}\right)^2} \sigma_{\bar{\lambda}} = \frac{1}{S_r} \frac{\delta}{\bar{\lambda} \sqrt{\bar{n}}}, \quad (\text{A2.1})$$

where

$$S_r = \frac{1}{\bar{\lambda}} \left| \frac{\partial \bar{\lambda}}{\partial T} \right|. \quad (\text{A2.2})$$

This allows us to compare the temperature uncertainty as a function of signal strength for measurements based on intensity ratio and spectral shift (Fig. A2.1). We observe that the temperature uncertainties of both methods show the same scaling with signal strength—the only difference is the absolute value. In practice, experimental factors such as the spectral resolution increase the absolute uncertainty of spectral-shift thermometers. The above equations thus only give qualitative insight in the relation between spectral width, signal strength, and the temperature uncertainty.

**Statistics of electron multiplication.** We used the work of Harpsøe *et al.* to calculate the distribution of output electrons after the electron multiplication registers of our EMCCD camera<sup>45</sup>

$$p_{\text{EM}}(\bar{k}, n_{\text{out}}) = \left( (1 - mp_s) \mathcal{N}(n_{\text{out}}, \sigma_r) + p_s \sum_{l=1}^m p_{\text{gamma}}(n_{\text{out}}, 1, G^{(m-l)/m}) \right) p_{\text{poisson}}(0, \bar{k}) + \sum_{k=1}^{\infty} p_{\text{gamma}}(n_{\text{out}}, k, G) p_{\text{poisson}}(k, \bar{k}). \quad (\text{A2.3})$$

Here, the first term describes readout noise with a Gaussian distribution  $\mathcal{N}(n_{\text{out}}, \sigma_r)$  and noise

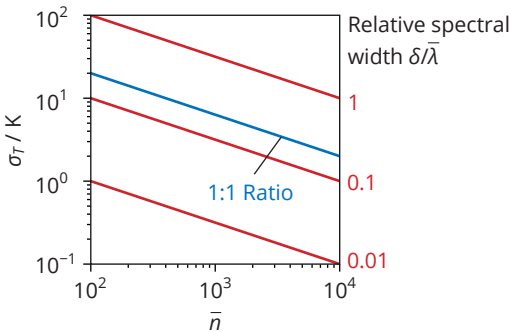


**Figure A2.1.** Calculated temperature uncertainty for intensity-ratio (blue line) and spectral-shift thermometers (red lines) with relative sensitivities of  $1\% \text{ K}^{-1}$  and  $0.1\% \text{ K}^{-1}$ , respectively. In both cases,  $\bar{n}$  is the total counts within the entire spectrum. The uncertainty of the ratiometric thermometer is calculated with a 1:1 intensity ratio and assuming Poissonian counting noise. Different values of the relative spectral width  $\delta/\bar{\lambda}$  were used to demonstrate the effect of this parameter on the temperature uncertainty.

due to spurious electrons, which are the unwanted electrons created during shifting of charges through the multiplication register with an overall probability  $p_s$  per readout. This process can occur in any of the  $m$  multiplication registers ( $m = 604$  for our camera). After creation of such an electron in the  $l^{\text{th}}$  register, it is amplified  $m-l$  times. Eq. A2.3 approximates that readout and spurious noise are relevant only if zero photoelectrons enter the multiplication register [which has a probability  $p_{\text{poisson}}(0, \bar{k})$ ], because amplified photoelectrons otherwise dominate the probability distribution  $p_{\text{EM}}$ . The second term calculates the distribution of output electrons after multiplication of at least one photoelectron. The probability of obtaining the specific number of photoelectrons  $k$  is given by the Poisson distribution.

We derive the expected value ( $\bar{n}_{\text{out}}$ ) and the variance ( $\sigma_n$ ) of the multiplied photoelectrons as follows

$$\bar{n}_{\text{out}} = \int_0^\infty n_{\text{out}} \sum_{k=1}^\infty p_{\text{gamma}}(n_{\text{out}}, k, G) p_{\text{poisson}}(k, \bar{k}) dn = \bar{k}G, \quad (\text{A2.4})$$

$$\sigma_n = \int_0^\infty (n_{\text{out}} - \bar{k}G)^2 \sum_{k=1}^\infty p_{\text{gamma}}(n_{\text{out}}, k, G) p_{\text{poisson}}(k, \bar{k}) dn = 2\bar{k}G^2 - \bar{k}^2 G^2 e^{-\bar{k}}. \quad (\text{A2.5})$$

When  $\bar{k}$  is much smaller or much larger than one, the second term of the variance is negligible and the expression simplifies to  $2\bar{k}G^2$ . For  $\bar{k}$  values around 1, this simplification no longer holds, leading to a deviation from the full expression of at most 23%. The experimental uncertainties in Fig. 2.3b are therefore determined with  $\bar{k}$  values that are much larger than one.

---

### Laser-induced heating.

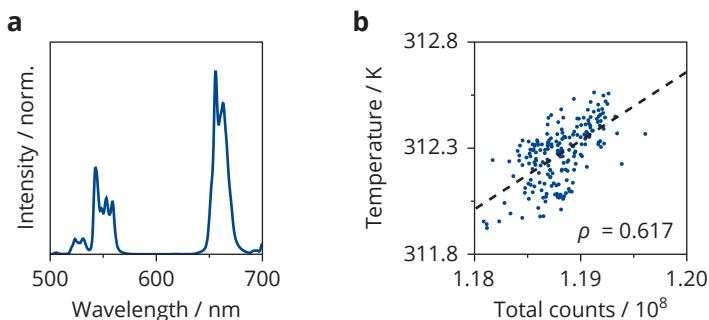


**Figure A2.2.** (a) Upconversion luminescence of dried NaYF<sub>4</sub>:Er<sup>3+</sup>(2%),Yb<sup>3+</sup>(18%) nanocrystals upon 980-nm excitation. The excitation laser was used at full power without neutral density filters in the optical path. The laser was focused on the back focal plane of the objective to achieve wide-field excitation. (b) Correlation between the measured temperature and the total counts within 516–534 nm and 538–545 nm for the <sup>2</sup>H<sub>11/2</sub> and <sup>4</sup>S<sub>3/2</sub> emission, respectively. The correlation coefficient ( $\rho$ ) of the linear regression is much larger than zero, indicating that measured temperature and total counts are correlated. This is likely due to fluctuations in the intensity of the excitation laser, which cause fluctuations in laser-induced heating of the nanocrystals. In our experiments, we prevented such effects by setting the excitation intensity four orders of magnitude lower.

### An unstable excitation source.

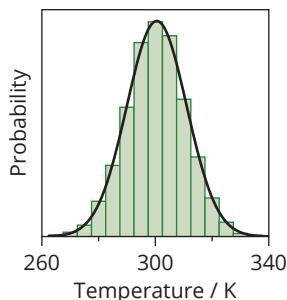


**Figure A2.3.** Histogram of temperatures extracted from 10<sup>4</sup> simulated spectra constituting two emission lines. The expected number of photons in a spectrum was assumed to follow a Gaussian distribution with a standard deviation of 25% reflecting fluctuations in excitation intensity. The average expected number of photons was set to  $(\bar{n}_A + \bar{n}_B) = 500$  counts and Poissonian noise was added to each spectrum. The solid line corresponds to the temperature distribution that is calculated using Eq. 2.3 by simply replacing the expected photon counts  $\bar{n}_{A,B}$  with the averaged expected photon counts  $(\bar{n}_{A,B})$ . The match between the simulation and the model indicates that, in the absence of laser-induced heating, the temperature distribution is unaffected by an unstable excitation source.

**Analog-to-digital conversion factor in electron multiplication mode.**

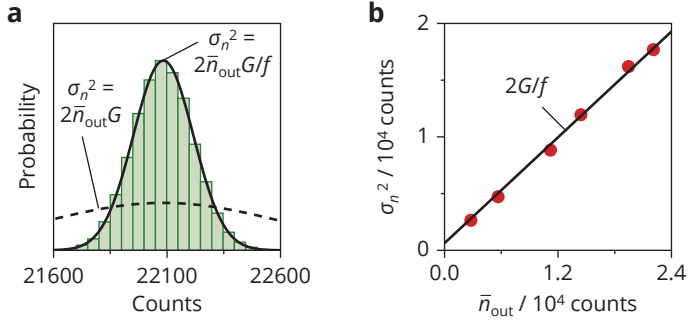


**Figure A2.4.** (a) The distribution of counts per 100-ms frame, for pixels on our EMCCD camera showing an average of 22085 counts / 100 ms when measured over 200 frames. The camera recorded the reflection of a white lamp on a microscopy slide at an EM gain level of 2. The solid line is a fit of the experimental data to the normal distribution ( $\bar{k} = 22085$ ,  $\sigma^2 = 17690$ ) and the dashed line shows the distribution of output electrons according to Eqs. A2.4-A2.5 with  $\bar{k} = 22085$ . (b) Plot of the variance against the mean (red dots) measured via the procedure in panel (a). The black line is a fit of the experimental data to the model  $\sigma_n^2 = 2\bar{n}_{out}G/f + \sigma_r^2$ , where  $f = 5.14$  is the analog-to-digital conversion factor and  $\sigma_r^2 = 630$  is the readout variance of one pixel.

**The probability of generating spurious electrons.**

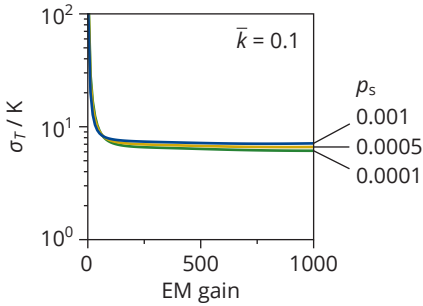


**Figure A2.5.** Temperature uncertainty for a range of total EM gains and various probabilities of generating spurious electrons  $p_s$ , covering the range that we expect to encounter in our EMCCD. We estimate that these probabilities are 2 to 3 orders of magnitude lower than the probability of multiplying a real photoelectron at an EM gain of 1000. The uncertainties are calculated from the expected value of the output electrons, excluding spurious electrons, and from the variance of all output electrons. We use an extremely low value of expected photoelectrons  $\bar{k} = 0.1$  as input and observe only a very weak effect of spurious charges on the temperature uncertainty. This indicates that for more realistic values of  $\bar{k}$  the impact of spurious charges on the temperature uncertainty is negligible.

**Readout noise versus peak ratio.** Fig. A2.6 considers the effect of significantly differing emission intensities in the two emission bands. Of particular interest is the scenario in which the signal in one emission band is weaker than the readout noise, while the other band exceeds the readout noise. To understand the impact on the temperature uncertainty we simulate two emission bands as Gaussians (Fig. A2.6a). We then calculate the temperature uncertainty of these scenarios using Eqs. 2.3 and 2.7 (Fig. A2.6b). EM gain has a stronger beneficial effect on the temperature uncertainty if the emission spectrum is asymmetric (solid lines) and if the readout noise is higher (blue lines).

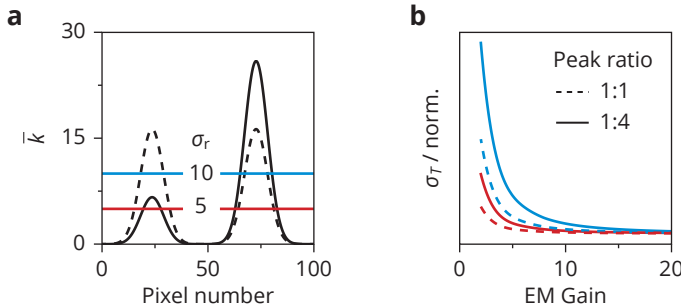


**Figure A2.6.** (a) Two bands with Gaussian shape and a peak ratio of 1:4 (solid black line) and 1:1 (dashed black line). The integrated area below the dashed and solid black lines is equal. The red and blue line correspond to readout noise levels of 5 and 10, respectively. (b) Calculated temperature uncertainty for the different scenarios in (a). The blue curves show the uncertainty for a readout noise level of 10 and a peak ratio of 1:4 (solid line) and 1:1 (dashed line). Same for the red curves but for a readout noise level of 5. The uncertainties are calculated from the single-pixel expected values of output electrons, excluding spurious electrons, and from the single-pixel variances of all output electrons, followed by summing the values for the individual pixels within each emission band. Each curve is individually normalized to its minimum uncertainty, which in each case occurs at the highest EM gain.

### Conventional CCD versus electron-multiplication CCD.

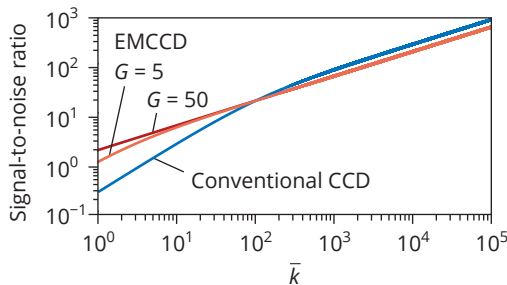
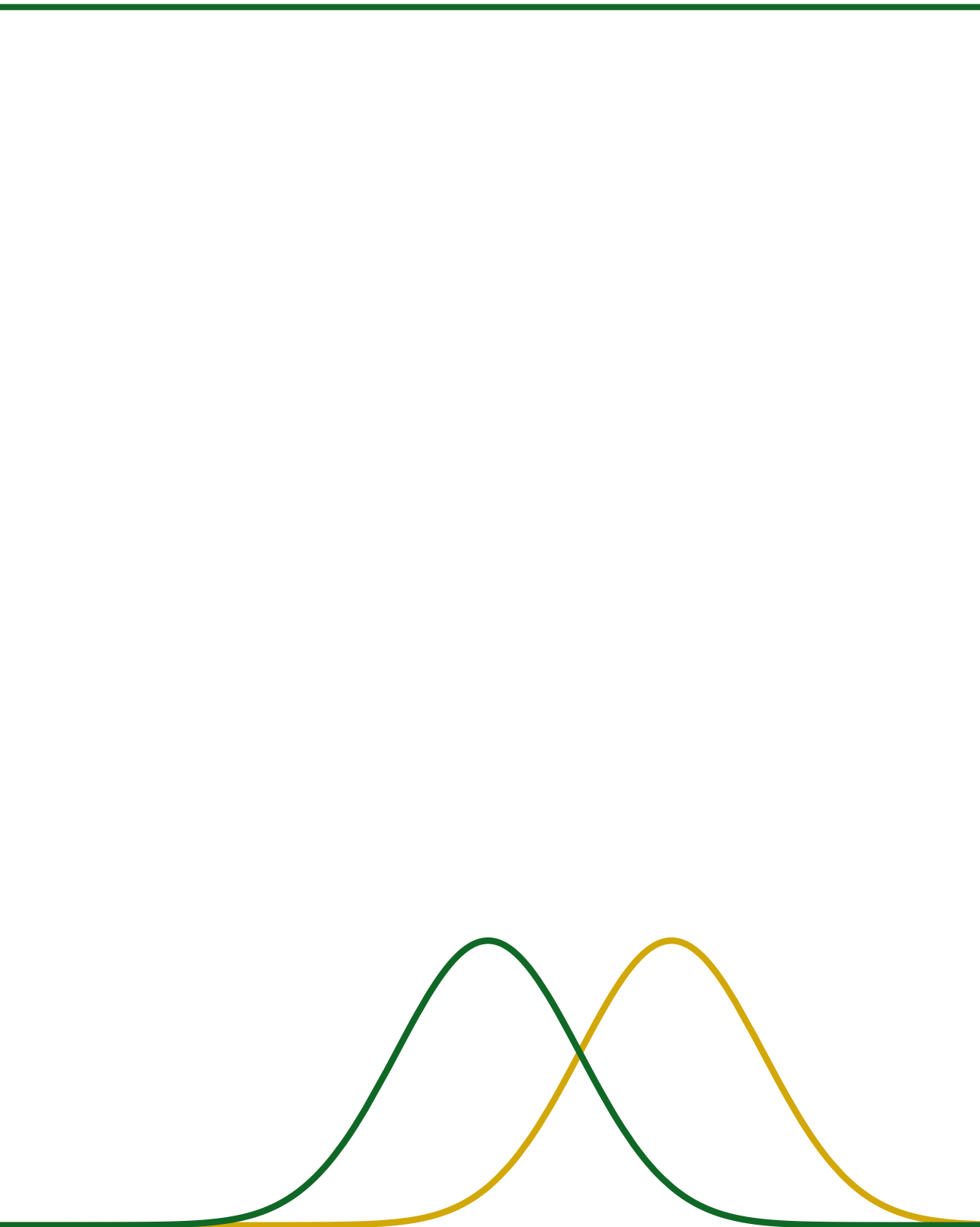


**Figure A2.7.** Signal-to-noise ratio for a conventional CCD and an EMCCD with a multiplication gain  $G$  of 5 and 50. In all cases, the readout variance  $\sigma_r^2$  was set to 100 and the ADC factor was set to 1. Compared to the EMCCD, the signal-to-noise ratio of a conventional CCD is poor at a low number of expected photoelectrons  $\bar{k}$ , but it outperforms the EMCCD above 100 photoelectrons.







---

# Chapter 3

## Extending the dynamic temperature range of Boltzmann thermometers

### Abstract

Lanthanide-doped (nano)crystals are an important class of materials in luminescence thermometry. The working mechanism of these thermometers is diverse but most often relies on variation of the ratio of emission intensities from two thermally coupled excited states with temperature. At low temperatures, nonradiative coupling between the states can be slow compared to radiative decay, but, at higher temperatures, the two states reach thermal equilibrium due to faster nonradiative coupling. In thermal equilibrium, the intensity ratio follows Boltzmann statistics, which gives a convenient model to calibrate the thermometer. In this Chapter, we investigate multiple strategies to shift the onset of thermal equilibrium to lower temperatures, which enables Boltzmann thermometry in a wider dynamic range. We use  $\text{Eu}^{3+}$ -doped microcrystals as a model system and find that the nonradiative coupling rates increase for host lattices with higher vibrational energies and shorter lanthanide–ligand distances, which reduces the onset temperature of thermal equilibrium by more than 400 K. We additionally reveal that thermometers with excited states coupled by electric-dipole transitions have lower onset temperatures than those with magnetic-dipole-coupled states due to selection rules. These insights provide essential guidelines for the optimization of Boltzmann thermometers to operate in an extended temperature range.

### Based on:

T.P. van Swieten, J.M. Steenhoff, A. Vlasblom, R. de Berg, S.P. Mattern, F.T. Rabouw, M. Suta and A. Meijerink, Extending the dynamic temperature range of Boltzmann thermometers, *Light: Science and Applications*, in press.

---

### 3.1 Introduction

Over the last two decades, materials with temperature-sensitive luminescence have been developed as probes for remote thermometry. In particular, crystals doped with trivalent lanthanide ( $\text{Ln}^{3+}$ ) ions have received great interest. The luminescence of these ions is characterized by narrow emission lines that cover the deep ultraviolet until the near-infrared regions of the electromagnetic spectrum, making them suitable optical probes in various research fields.<sup>20,49,69</sup> The emission spectra of  $\text{Ln}^{3+}$  ions can strongly depend on temperature, which makes  $\text{Ln}^{3+}$ -doped materials promising candidates for optical thermometry. The intensity ratio between two emission lines is most commonly used as measure for temperature because it is often insensitive to experimental factors that affect the integrated intensity such as alignment and the excitation intensity and it allows for the use of a simple measurement setup. How strongly the intensity ratio responds to temperature is governed by nonradiative transitions between excited states within the thermometer material.

An important class of ratiometric thermometers is based on two thermally coupled excited states within a single  $\text{Ln}^{3+}$  ion. Thermal coupling involves the interaction with one or multiple phonons to bridge the energy gap between the two states, which enables exchange of their populations. At elevated temperatures, these nonradiative transitions become faster than any other decay or feeding pathway and, as a result, the populations of the two states reach thermal equilibrium.<sup>29</sup> In host lattices with similar phonon energies, excited states with smaller energy gaps thermally equilibrate at lower temperatures, because fewer phonons are required to bridge the gap resulting in faster nonradiative coupling. The luminescence intensity ratio (*LIR*) of two states in thermal equilibrium follows Boltzmann statistics, which serves as a reliable calibration model. The performance of Boltzmann thermometers is further quantified by the relative sensitivity  $\Delta E/k_{\text{B}}T^2$  and, in some cases, by the absolute sensitivity  $dLIR/dT$ . Suta and Meijerink used these parameters to propose an optimum temperature window for thermometry experiments based on the energy gap ( $\Delta E = 2-3.41 k_{\text{B}}T$ ), assuming the two emitting states are in thermal equilibrium.<sup>29</sup> A stricter definition of the dynamic temperature range, in which Boltzmann thermometers have reliable performance, should additionally consider the onset temperature of thermal equilibrium. Especially at the lower temperature limit, Boltzmann equilibrium is not always realized.

Recent studies have shown that at elevated dopant concentrations cross-relaxation between nearby thermometer ions can affect the establishment of thermal equilibrium. For instance, the  ${}^4\text{F}_{3/2}$  and  ${}^4\text{F}_{5/2}$  levels of  $\text{Nd}^{3+}$  experience strong cross-relaxation providing an additional depopulation path that competes with nonradiative coupling and thus causes an undesired increase of the onset temperature of thermal equilibrium.<sup>70</sup> Cross-relaxation from the  ${}^5\text{D}_1$  and  ${}^5\text{D}_0$  levels of  $\text{Eu}^{3+}$  lead to a desirable opposite effect.<sup>71</sup> Coupling with  ${}^7\text{F}_0-{}^7\text{F}_3$  and  ${}^7\text{F}_2-{}^7\text{F}_4$  transitions in nearby  $\text{Eu}^{3+}$  ions that are resonant with the  ${}^5\text{D}_1-{}^5\text{D}_0$  energy gap accelerates nonradiative coupling between the states, which shifts the onset of Boltzmann equilibrium to lower temperatures. However, only for specific Boltzmann thermometers can cross-relaxation extend the dynamic range and, so far, a positive impact is only reported for  $\text{Eu}^{3+}$ . Universal methods to extend the dynamic temperature range of all Boltzmann thermometers are still lacking, which hampers their optimization for spe-

cific applications.

In this Chapter, we investigate how the host crystal and selection rules affect the dynamic range of Boltzmann thermometers. We prepare microcrystalline materials doped with low concentrations of  $\text{Eu}^{3+}$ , serving as a model system for Boltzmann thermometry, and acquire the steady-state luminescence spectra and time-resolved luminescence from  ${}^5\text{D}_1$  and  ${}^5\text{D}_0$  to understand the impact of the host crystal on the nonradiative coupling rates between these levels. Our results show that the coupling rates increase with the maximum vibrational energy of the host crystal, which is in qualitative agreement with the energy-gap law. This reduces the onset of thermal equilibrium from 750 K for fluorides with maximum vibrational energies of  $450\text{ cm}^{-1}$  to 450 K for complex oxides with  $1200\text{--}1400\text{ cm}^{-1}$  vibrations. Secondly, we demonstrate that even within a series of isostructural fluorides it is possible to control the nonradiative rates via the lanthanide–fluoride distance and exploit the distance dependence of energy transfer between vibrational modes and the  $\text{Eu}^{3+}$  ion to shift the onset temperature by more than 100 K. Thirdly, we compare the onset temperature of  $\text{Eu}^{3+}$ -doped materials with other  $\text{Ln}^{3+}$ -based Boltzmann thermometers, which reveals an important role of selection rules: thermometers that rely on coupling between the emitting states by magnetic-dipole transitions, like  $\text{Eu}^{3+}$  and  $\text{Nd}^{3+}$ , tend to have higher onset temperatures than thermometers with electric-dipolar nonradiative transitions. Finally, our results on  $\text{Y}_2\text{O}_2\text{S}:\text{Eu}^{3+}$  showed a surprising effect of additional nonradiative pathways on temperature-dependent luminescence. The new insights presented are essential for a better understanding of the performance of Boltzmann thermometers and for the design of thermometers with an optimized dynamic temperature range for specific applications.

### 3.2 Results

We investigated the luminescence of  $\text{Eu}^{3+}$  in various host lattices to understand how the onset of thermal equilibrium between  ${}^5\text{D}_0$  and  ${}^5\text{D}_1$  can be controlled. The dopant concentration in each host ( $\text{LaBO}_3$ ,  $\text{LaPO}_4$ ,  $\text{Y}_2\text{O}_3$ ,  $\text{Y}_2\text{O}_2\text{S}$ ,  $\text{NaREF}_4$  ( $RE = \text{La}, \text{Y}, \text{Lu}$ )) was below 0.5% to prevent an influence (lowering) of the onset temperature by cross-relaxation between  $\text{Eu}^{3+}$  ions. Fig. 3.1 shows the luminescence spectra of  $\text{Eu}^{3+}$  in all these materials acquired at room temperature. The spectra show characteristic  $\text{Eu}^{3+}$  luminescence with bright emission lines at 585–630 nm due to the  ${}^5\text{D}_0 \rightarrow {}^7\text{F}_{1-2}$  transitions.<sup>71</sup> The spectra show additional lines at 520–570 nm and 510 nm which are assigned to  ${}^5\text{D}_1 \rightarrow {}^7\text{F}_{0-2}$  and  ${}^5\text{D}_2 \rightarrow {}^7\text{F}_3$  transitions, respectively.<sup>20</sup> The intensity of  ${}^5\text{D}_1$  and  ${}^5\text{D}_2$  emissions decreases as the maximum vibrational energy of the host lattice increases going from  $\beta\text{-NaREF}_4$  ( $450\text{ cm}^{-1}$ ),  $\text{Y}_2\text{O}_2\text{S}$  ( $550\text{ cm}^{-1}$ ),  $\text{Y}_2\text{O}_3$  ( $600\text{ cm}^{-1}$ ),  $\text{LaPO}_4$  ( $1200\text{ cm}^{-1}$ ), to  $\text{LaBO}_3$  ( $1400\text{ cm}^{-1}$ ).<sup>72</sup> This indicates that nonradiative relaxation becomes faster when less phonons are required to bridge the gap to the first lower excited state, which is in agreement with the energy-gap law.<sup>73–75</sup> Comparing the spectra of the  $\beta\text{-NaREF}_4$ , which all have similar vibrational energies, the  ${}^5\text{D}_1$  and  ${}^5\text{D}_2$  emissions show an increasing trend in emission intensity going from a shorter ( $\beta\text{-NaLuF}_4$ ) to a longer ( $\beta\text{-NaLaF}_4$ ) lanthanide–ligand distance. This hints towards an inverse scaling of nonradiative coupling rates with the lanthanide–ligand distance, which is the expected

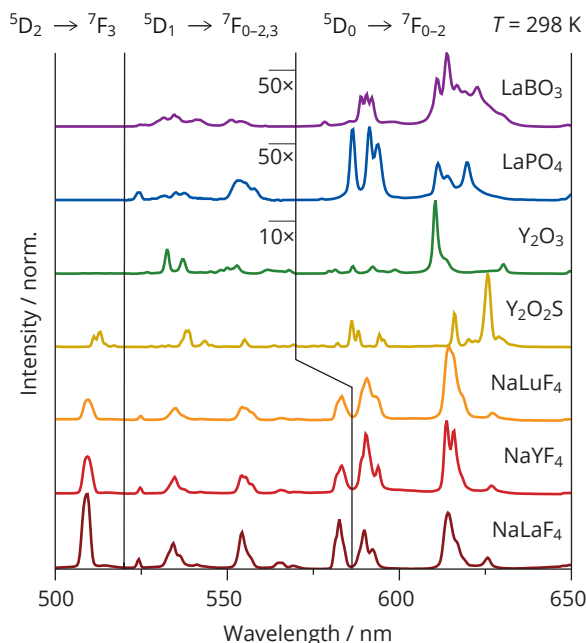


**Figure 3.1.** Luminescence of  $\text{Eu}^{3+}$ . (a) Emission spectra of various  $\text{Eu}^{3+}$ -doped host lattices acquired at room temperature (Fig. 1.3 shows a detailed energy-level diagram of  $\text{Eu}^{3+}$ ). The luminescence of  $\beta\text{-NaREF}_4\text{:Eu}^{3+}$  ( $RE = \text{La, Y, Lu}$ ) was excited at 395 nm into the  $^5\text{L}_6$  level, while  $\text{Eu}^{3+}$  in the other samples was excited into the ligand-to-metal charge-transfer band at 250–310 nm. To prevent cross-relaxation low  $\text{Eu}^{3+}$  concentrations of 0.4–0.5% were used in  $\text{LaBO}_3$ ,  $\text{LaPO}_4$ ,  $\text{NaLuF}_4$ ,  $\text{NaYF}_4$ , and  $\text{NaLaF}_4$ , while this required even lower dopant concentrations of 0.1% and 0.05% for  $\text{Y}_2\text{O}_2\text{S}$  and  $\text{Y}_2\text{O}_3$ , respectively. The vertical lines mark the wavelength range of the  $^5\text{D}_1 \rightarrow ^7\text{F}_{0-3}$  emissions of  $\beta\text{-NaREF}_4\text{:Eu}^{3+}$  and the  $^5\text{D}_1 \rightarrow ^7\text{F}_{0-2}$  emissions of the other materials. The emissions were magnified by a factor 10 for  $\text{Y}_2\text{O}_3$  and by a factor 50 for  $\text{LaBO}_3$  and  $\text{LaPO}_4$ .

trend for energy transfer to lattice vibrations.<sup>73,76</sup> Remarkably, the  $^5\text{D}_1$  and  $^5\text{D}_2$  emissions in  $\text{Y}_2\text{O}_2\text{S}$  are much stronger compared to  $\text{Y}_2\text{O}_3$ , while the vibrational energies are similar. A plausible explanation is the enhanced admixture of the low-energy  $\text{Eu}^{3+} \leftarrow \text{S}^{2-}$  charge-transfer state in  $\text{Y}_2\text{O}_2\text{S}$  with the energy levels of  $\text{Eu}^{3+}$ , which increases the radiative rates for forced electric-dipole transitions from  $^5\text{D}_1$  and  $^5\text{D}_2$  but not for nonradiative magnetic-dipole transitions between  $^5\text{D}_1$  and  $^5\text{D}_0$ . In the following sections, we analyze the time- and spectrally-resolved luminescence acquired at 7–873 K to further study these observations and, more importantly, determine the influence of the host lattice and selection rules on the onset of thermal equilibrium.

**The required number of phonons.** First, we study the relation between the maximum phonon energy of the host lattice and the onset of thermal equilibrium, where we focus on  $\text{Y}_2\text{O}_3$ ,  $\text{LaPO}_4$ , and  $\text{LaBO}_3$ . Fig. 3.2a shows the luminescence decay curves of the  $^5\text{D}_1$  emission for these materials at various temperatures. We observe single-exponential decay at 78 K, which confirms that cross-relaxation is negligible as this would cause highly multi-exponential decay.<sup>71</sup> At elevated temperatures, decay from  $^5\text{D}_1$  becomes faster, because the rate of multi-phonon relaxation to  $^5\text{D}_0$  increases as phonon modes are thermally occupied. The measurements at elevated temperatures additionally show a slow component—in  $\text{LaPO}_4$  and  $\text{LaBO}_3$ , this is barely distinguishable from background signal due to the low amplitude of this component. Fig. A3.1 shows decay curves for  $\text{Y}_2\text{O}_3\text{:Eu}^{3+}$  on an extended time scale, in which the slow component is clearly visible and which demonstrate that the decay rate of the slow component matches the population-weighted average

radiative decay rate of the thermally coupled  ${}^5D_1$  and  ${}^5D_0$  levels, in agreement with the work of Geitenbeek *et al.*<sup>71</sup> The fast component contains the information on the temperature dependence of multi-phonon relaxation and is used to further analyze nonradiative coupling.

The decay rate of the fast component  $k_2$  is described as the sum of temperature-independent radiative decay with rate  $k_{r,2}$  and a temperature dependent multi-phonon relaxation term<sup>29,77</sup>

$$k_2 = k_{r,2} + k_{nr}(0)g_1(1+n)^p, \quad (3.1)$$

where  $k_{nr}(0)$  is the intrinsic nonradiative rate,  $g_1$  is the degeneracy of the lower excited state,  $p$  is the number of phonons needed to bridge the gap,  $n$  is phonon occupation number of the involved phonon mode with energy  $\hbar\omega$  (Eq. 1.1). Multi-phonon relaxation is thus governed by spontane-

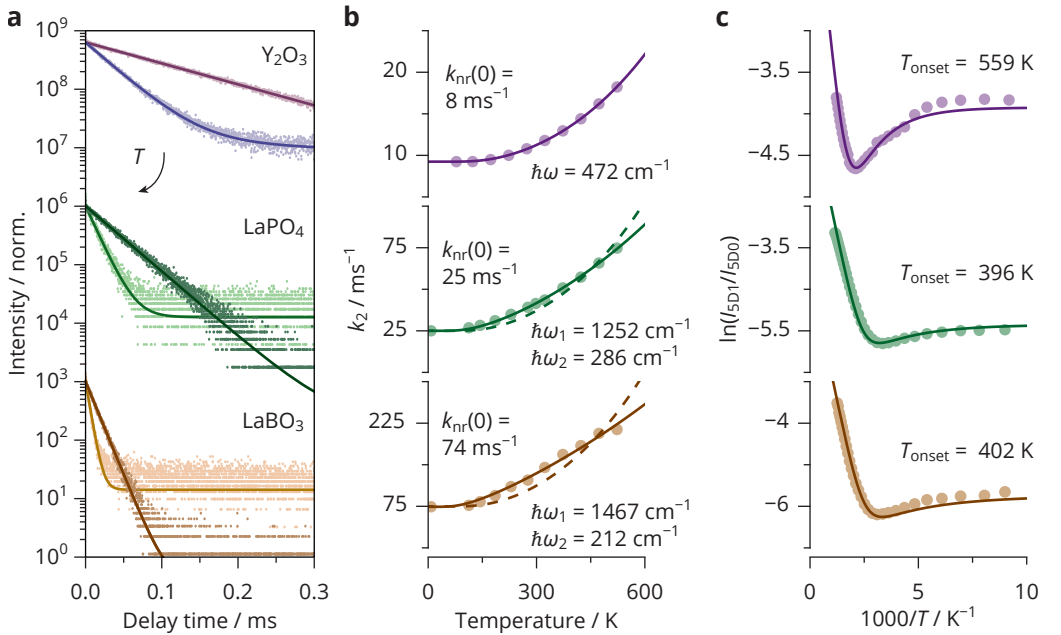


**Figure 3.2.** Relation between the maximum phonon energy and the onset of thermal equilibrium. **(a)** Luminescence decay curves of the  ${}^5D_1$  emission for  $Y_2O_3$  (top),  $LaPO_4$  (middle), and  $LaBO_3$  (bottom). The luminescence was excited at  ${}^7F_0 \rightarrow {}^5D_1$  and the decay curves were measured at 78 K (dark color, slower decay) and 523 K (light color, faster decay). **(b)** Decay rates of the  ${}^5D_1$  emission at various temperatures. The solid line in the top plot and the dashed lines in the middle and bottom plots are fits of the experimental rates (dots) to Eq. 3.1, while the solid lines in the middle and bottom plots are fits to Eq. 3.3. **(c)** Intensity ratios of the  ${}^5D_1$  and  ${}^5D_0$  emissions for various temperatures determined from luminescence spectra upon excitation into the charge-transfer states. The solid lines are fits of the experimental ratios (dots) to the model of Eq. 3.4 for  $Y_2O_3$  and of Eq. 3.5 for  $LaBO_3$  and  $LaPO_4$  (lines). The onset temperatures for thermal equilibrium ( $T_{onset}$ ) were calculated using Eq. 3.6 for  $Y_2O_3:Eu^{3+}$  and a numerical solution was used for  $LaPO_4:Eu^{3+}$  and  $LaBO_3:Eu^{3+}$  (see text for further details).

ous phonon emission that is independent of temperature and by stimulated phonon emission that increases with temperature as phonon modes are thermally occupied. We determine  $k_{r,2}$  and  $k_{nr}(0)$  using luminescence measurements at low temperatures with negligible stimulated phonon emission. Specifically, we determine  $k_2$  from the  ${}^5D_1$  decay curve using a single exponential fit and then determine  $k_{r,2}$  and  $k_{nr}(0)$  using the intensity ratio between the  ${}^5D_1$  and  ${}^5D_0$  emissions in the low-temperature luminescence spectrum excited at  ${}^7F_0 \rightarrow {}^5D_1$  (Eq. A3.1). This yields values for  $k_{nr}(0)$  of 8, 25, and  $74 \text{ ms}^{-1}$  for  $Y_2O_3$ ,  $LaPO_4$ , and  $LaBO_3$ , respectively, which shows an increasing trend with the maximum vibrational energy of the host. This is in agreement with the energy-gap law, formulated by van Dijk and Schuurmans<sup>73-75</sup>

$$k_{nr}(0) = A \exp(-\gamma p), \quad (3.2)$$

where constants  $A$  and  $\gamma$  depend on the host lattice and on the dipole moment of the nonradiative coupling transition. This indicates that host lattices with higher vibrational energies have faster nonradiative coupling, which can lower the onset temperatures of thermal equilibrium. The energy-gap law as discussed by Van Dijk and Schuurmans also shows that the nonradiative rates scale with the (electric-)dipole transition probability between the two levels.

Next, we determine the rates of the fast component from  ${}^5D_1$  decay curves recorded at various temperatures (Fig. 3.2b). At low temperatures, we used a single-exponential fit, while a biexponential fit was necessary to match the experiments at elevated temperatures. The decay rates increase with temperature, as we observed before in Fig. 3.2a. We first analyze this trend for  $Y_2O_3$  by fitting the experimental rates (dots) to Eq. 3.1 (solid line), where we optimized the phonon energy  $\hbar\omega$  and order  $p$  of the phonon process while keeping  $k_{r,2}$  and  $k_{nr}(0)$  fixed. For all  $Eu^{3+}$ -based thermometers of this study, we fixed the energy gap between  ${}^5D_1$  and  ${}^5D_0$  to  $1750 \text{ cm}^{-1}$ . The fit is in excellent agreement with the experiment and yields values of  $\hbar\omega = 472 \text{ cm}^{-1}$  and  $p = 3.7$ . In this case, multi-phonon relaxation is best described by a non-integer number of phonons, which indicates that the process is in reality more complex than described by Eq. 3.1. Where in the simple multi-phonon relaxation picture a vibrational overtone of a single phonon mode is considered to bridge the energy gap, in reality multiple combinations of vibrational modes with different energies can be used to bridge the gap in parallel processes. It is impossible to capture and model all these different combinations of vibrational modes that contribute to multi-phonon relaxation. We therefore approximate that nonradiative transitions take place via an effective non-integer number of phonons.

To analyze the  ${}^5D_1$  decay rates of  $Eu^{3+}$ -doped  $LaPO_4$  and  $LaBO_3$ , we again fit the experimental data (dots) to Eq. 3.1 (dashed lines). In this case, the model poorly matches the experiment, so multi-phonon relaxation likely involves more than one effective phonon mode. We therefore adjust the model to allow one phonon with higher energy  $\hbar\omega_1$  and occupation  $n_1$  and a non-integer number of phonons  $p_2$  with lower energy  $\hbar\omega_2$  and occupation  $n_2$ :

$$k_2 = k_{r,2} + k_{nr}(0)g_1(1 + n_1)(1 + n_2)^{p_2}. \quad (3.3)$$



We fit the experimental decay rates to Eq. 3.3 and find for both  $\text{LaPO}_4$  and  $\text{LaBO}_3$  an excellent match between model and experiment. For  $\text{LaPO}_4$ , we find that the transition takes place via one phonon of  $1252 \text{ cm}^{-1}$  and 1.7 phonons of  $286 \text{ cm}^{-1}$ , while in  $\text{LaBO}_3$  one phonon of  $1467 \text{ cm}^{-1}$  and 1.3 phonons of  $212 \text{ cm}^{-1}$  give the best fit. At temperatures relevant for thermometry ( $< 1000 \text{ K}$ ), the occupation of these high-energy modes is negligible compared to the occupation of the low-energy modes. The high-energy modes that participate in the transition are thus spontaneously emitted, while the temperature dependence is determined by the increasing population of the low-energy modes.

To monitor and understand the onset temperature for thermal equilibrium we study the luminescence intensity ratio between the  ${}^5\text{D}_1$  and  ${}^5\text{D}_0$  emission, which is the relevant metric for  $\text{Eu}^{3+}$ -based thermometry. Fig. 3.2c shows the  ${}^5\text{D}_1/{}^5\text{D}_0$  ratios for various temperatures, which presents a similar trend for the three studied materials. At low temperatures, the ratio remains constant when thermal occupation of phonon modes is still negligible. At higher temperatures, the phonon occupation increases, which initially enhances relaxation from  ${}^5\text{D}_1$  to  ${}^5\text{D}_0$  via stimulated phonon emission, and later also boosts excitation from  ${}^5\text{D}_0$  to  ${}^5\text{D}_1$  via (stimulated) phonon absorption—the latter depends on temperature as  $n(T)^p$ . In the region between these regimes, we observe a minimum in the intensity ratios, because the phonon emission rate increases faster with temperature than the phonon absorption rate (Eqs. A3.2–A3.3). At temperatures beyond the minimum, the intensity ratio increases and thermal equilibrium is established, which causes the typical Boltzmann behavior: a linear relation between the logarithm of intensity ratio and reciprocal temperature.

To further understand the observations in Fig. 3.2c, we consider the analytical intensity ratio of two excited states that can decay radiatively and that are thermally coupled via phonon emission and absorption pathways. The system is excited into a higher-energy auxiliary state from which feeding to the two thermally coupled levels takes place. Assuming that one effective phonon mode participates in the coupling pathway, the steady-state solution of the rate equations gives the following expression for the intensity ratio<sup>29,71</sup>

$$\frac{I_2}{I_1} = C \frac{k_{r,1} \alpha + k_{nr}(0) g_2 n^p}{k_{r,2} (1 - \alpha) + k_{nr}(0) g_1 (1 + n)^p}, \quad (3.4)$$

where  $k_{r,1}$  and  $k_{r,2}$  are the radiative decay rates from the lower ( ${}^5\text{D}_0$ ) and higher ( ${}^5\text{D}_1$ ) thermally coupled levels, respectively, and pre-factor  $C$  is the ratio between the Einstein coefficients for spontaneous photon emission from these states ( $A_2/A_1$ ) to lower states involved in the determination of intensity ratio ( $I_2/I_1$ ). Feeding factor  $\alpha$  gives the fraction of the auxiliary-state population that feeds directly into the higher thermally coupled state, while the remaining part ( $1 - \alpha$ ) populates the lower thermally coupled state. In the three oxide host lattices, feeding is dominated by multi-phonon relaxation indicated by the absence of  ${}^5\text{D}_2$  emissions, which sets  $\alpha$  to 1. We fit the experimental ratios of  $\text{Y}_2\text{O}_3:\text{Eu}^{3+}$  to Eq. 3.4, where we separately determined  $k_{r,1}$  from a decay curve of  ${}^5\text{D}_0$  at 7 K, leaving  $C$  as the only fitting parameter. For  $\text{LaPO}_4:\text{Eu}^{3+}$  and  $\text{LaBO}_3:\text{Eu}^{3+}$ , we

need a modified expression for the intensity ratio to account for the participation of two different phonon modes in the thermal coupling transition

$$\frac{I_2}{I_1} = C \frac{k_{r,1} \alpha + k_{nr}(0) g_2 n_1 n_2^{p_2}}{k_{r,2} (1 - \alpha) + k_{nr}(0) g_1 (1 + n_1) (1 + n_2)^{p_2}}. \quad (3.5)$$

We fit the experimental intensity ratios of  $\text{LaPO}_4:\text{Eu}^{3+}$  and  $\text{LaBO}_3:\text{Eu}^{3+}$  to Eq. 3.5 with again  $C$  as the only fitting parameter. For all three materials, we find an excellent agreement between model and experiment, which confirms that, in  $\text{Eu}^{3+}$ -doped  $\text{Y}_2\text{O}_3$ ,  $\text{LaPO}_4$ , and  $\text{LaBO}_3$ , thermal coupling determines the temperature-dependence of the intensity ratio between  ${}^5\text{D}_1$  and  ${}^5\text{D}_0$ .

To compare the dynamic range of these thermometer materials we determine the onset of

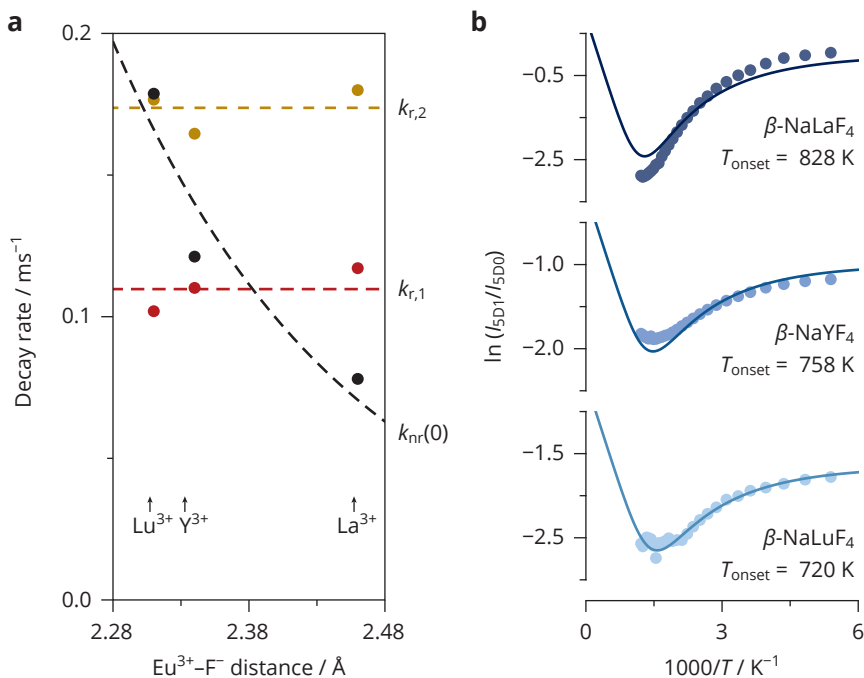


**Figure 3.3.** Tuning the intrinsic nonradiative rate via the lanthanide–ligand distance. **(a)** Radiative rates of  ${}^5\text{D}_0$  ( $k_{r,1}$ ) and  ${}^5\text{D}_1$  ( $k_{r,2}$ ) and the intrinsic nonradiative rate between these levels  $k_{nr}(0)$  for  $\text{Eu}^{3+}$  in  $\beta\text{-NaLuF}_4$ ,  $\beta\text{-NaYF}_4$ , and  $\beta\text{-NaLaF}_4$ . Similar to the procedure described in Eq. A3.1, luminescence measurements at 7 K were used to determine these rates. The dashed lines serve as guide to the eye. **(b)** Intensity ratios between the  ${}^5\text{D}_1$  and  ${}^5\text{D}_0$  emissions for various temperatures determined from luminescence spectra upon excitation at 395 nm in  ${}^5\text{L}_6$ . The solid lines are the result of a global fit of the experimental ratios (dots) to the model of Eq. 3.4 (lines), where one value of pre-factor  $C$ , one value of the vibrational energy  $\hbar\omega$ , and three different values of feeding factor  $\alpha$  were used as fitting parameters. The onset temperatures were calculated using Eq. 3.6.

thermal equilibrium. In the absence of additional nonradiative transitions like cross-relaxation, thermal equilibrium starts when phonon emission and absorption become faster than radiative decay. Since phonon absorption is a purely stimulated process and contains no spontaneous contribution, its rate is always lower than the phonon emission rate. Assuming that the radiative rates of the thermally coupled levels are of the same order of magnitude, thermal equilibrium is therefore limited by the competition between phonon absorption and radiative decay within the lower level. If one effective phonon mode is involved, we can thus derive the expected onset temperature from the condition  $k_{r,1} = k_{nr}(0)g_2n^p$ :

$$T_{\text{onset}} = \frac{\Delta E/p}{k_B \ln \left[ 1 + \left( \frac{g_2 k_{nr}(0)}{k_{r,1}} \right)^{1/p} \right]}. \quad (3.6)$$

We find an onset temperature of 559 K for  $\text{Eu}^{3+}$  in  $\text{Y}_2\text{O}_3$ . The above condition changes to  $k_{r,1} = k_{nr}(0)g_2n_1n_2^{p_2}$  for  $\text{LaPO}_4:\text{Eu}^{3+}$  and  $\text{LaBO}_3:\text{Eu}^{3+}$ , which has no simple solution for  $T_{\text{onset}}$  but can be solved numerically, giving onset temperatures of 396 K and 402 K, respectively. Clearly, the onset temperature is lower in host lattices with higher vibrational energies, which is thus an important parameter to control and optimize the dynamic range of Boltzmann thermometers.

**The lanthanide–ligand distance.** We further investigate the impact of the lanthanide–ligand distance on the nonradiative transitions using  $\text{Eu}^{3+}$ -doped  $\beta\text{-NaLuF}_4$ ,  $\beta\text{-NaYF}_4$ , and  $\beta\text{-NaLaF}_4$ . In these materials the  $\text{Eu}^{3+}\text{-F}^-$  distance varies without a change in their hexagonal crystal structure.<sup>78,79</sup> We use crystal structure data (acquired at room temperature) to determine the average  $\text{Eu}^{3+}\text{-F}^-$  distances in  $\beta\text{-NaLuF}_4$  (2.31 Å),  $\beta\text{-NaYF}_4$  (2.34 Å), and  $\beta\text{-NaLaF}_4$  (2.46 Å). Similar to the procedure described in Eq. A3.1, we record the luminescence of these materials at 7 K and determine  $k_{nr}(0)$  and  $k_{r,2}$  using the decay curve of the  ${}^5\text{D}_1$  emission and the  ${}^5\text{D}_1/{}^5\text{D}_0$  intensity ratio in the luminescence spectrum excited at  ${}^7\text{F}_0 \rightarrow {}^5\text{D}_1$  (Fig. 3.3a). In addition, we extract  $k_{r,1}$  from the decay curve of the  ${}^5\text{D}_0$  emission. The analysis clearly reveals that the radiative rates are insensitive to the  $\text{Eu}^{3+}\text{-F}^-$  distances in this series of isostructural host lattices. This is also expected as the  $\text{Eu}^{3+}$  ions share the same local site symmetries in  $\beta\text{-NaREF}_4$  and selection rules therefore have similar impact although slight variations in the crystal field strength could explain small differences in the radiative rates. In contrast, the intrinsic nonradiative rate  $k_{nr}(0)$  strongly decreases with increasing  $\text{Eu}^{3+}\text{-F}^-$  distance from  $0.18 \text{ ms}^{-1}$  for  $\beta\text{-NaLuF}_4$  to  $0.08 \text{ ms}^{-1}$  for  $\beta\text{-NaLaF}_4$ . Ermolaev and Sveshnikova observed a qualitatively similar distance dependence for coupling of excited lanthanide and transition-metal ions to solvent vibrations, which they interpreted as dipole–dipole energy transfer between the electronic transition dipole moment and the dipole moment of the vibrational mode.<sup>73,76</sup> If the transitions involved are two localized electric dipoles with a distance between the dipoles that is much larger than their spatial extension, the nonradiative rate can be described as Förster-type energy-transfer that scales inversely with distance to the sixth power. This is a valid approximation for coupling with distant solvent vibrations, which was

demonstrated by the analysis of solvent quenching in  $\text{Er}^{3+}$ -doped  $\text{NaYF}_4$  nanocrystals.<sup>68</sup> However, the nonradiative transitions between  $^5\text{D}_1$  and  $^5\text{D}_0$  have dominant magnetic-dipole character and the lattice vibrations spatially overlap with the transition of the  $\text{Eu}^{3+}$  ion. The decreasing trend of the intrinsic nonradiative rate with increasing lanthanide–ligand distance is evident and may be qualitatively understood as follows: the oscillating charge density due the surrounding lattice motion induces an electromagnetic field, which has a gradually weaker amplitude at the position of the  $\text{Eu}^{3+}$  ions for larger  $\text{Eu}^{3+}$ –ligand distances. However, further work is required to quantitatively understand the observed distance dependence.

Fig. 3.3b presents the  $^5\text{D}_1/^5\text{D}_0$  intensity ratios of the three  $\text{Eu}^{3+}$ -doped fluorides at various temperatures and shows a similar trend as observed in the oxides (Fig. 3.2c). In Fig. 3.1, we noted intense  $^5\text{D}_2$  emissions in the luminescence spectra of the fluorides acquired at room temperature. A long-lived  $^5\text{D}_2$  state does not exclusively relax to the  $^5\text{D}_1$  state by multi-phonon relaxation but allows for substantial radiative feeding from  $^5\text{D}_2$  to both  $^5\text{D}_1$  and  $^5\text{D}_0$  and, thus, no longer allows us to set  $\alpha$  to 1.<sup>80</sup> In addition, we can assume that nonradiative coupling in the three  $\beta$ - $\text{NaREF}_4$  hosts takes place via one effective vibrational mode with equal energy, since the effective mass of the  $\text{Eu}^{3+}$ – $\text{F}^-$  units is the same.<sup>79</sup> Furthermore, Fig. 3.3a demonstrates that the radiative rates of  $\text{Eu}^{3+}$  in the  $\beta$ - $\text{NaREF}_4$  hosts are very similar and we thus expect that one value of pre-factor  $C$  describes all intensity ratios. We therefore perform a global fit on the experimental ratios of all three materials to Eq. 3.4 to find one value of  $\hbar\omega$  and one value of  $C$ , where we use three different feeding factors  $\alpha$  as additional fitting parameters and the values of  $k_{r,1}$  and  $k_{\text{nr}}(0)$  from Fig. 3.3a as input parameters. This yields a value for  $\hbar\omega$  of  $414\text{ cm}^{-1}$  and values for  $\alpha$  of 0.76, 0.75, and 0.83 for  $\beta$ - $\text{NaLuF}_4$ ,  $\beta$ - $\text{NaYF}_4$ , and  $\beta$ - $\text{NaLaF}_4$ , respectively, showing no clear trend in  $\alpha$  with  $\text{Eu}^{3+}$ – $\text{F}^-$  distance. However, we would expect a decrease of  $\alpha$  with increasing distance due to reduced multi-phonon relaxation rates and, therefore, a long-lived  $^5\text{D}_2$  state with a stronger contribution of radiative feeding to  $^5\text{D}_0$  bypassing the  $^5\text{D}_1$  state. The absence of this trend and the poor quality of the fits indicate that the description of feeding by a constant  $\alpha$  is not completely correct. Instead,  $\alpha$  should likely depend on temperature, since feeding of the  $^5\text{D}_1$  state by multi-phonon relaxation is also temperature-dependent. Designing a model that includes the temperature dependence of feeding is complex and beyond the scope of this study. Nevertheless, we can still determine an approximate onset temperature using the obtained  $k_{\text{nr}}(0)$ ,  $k_{r,1}$ , and  $\hbar\omega$ , which are reliable and yield values for  $T_{\text{onset}}$  of 720 K, 758 K, and 828 K for  $\beta$ - $\text{NaLuF}_4$ ,  $\beta$ - $\text{NaYF}_4$ , and  $\beta$ - $\text{NaLaF}_4$ , respectively. As expected from the lower  $k_{\text{nr}}(0)$  and  $\hbar\omega$ , the onset temperatures in the fluorides are much higher than in the oxides. Moreover, these results demonstrate that reducing the  $\text{Eu}^{3+}$ – $\text{F}^-$  distance by only  $0.15\text{ \AA}$  lowers the onset temperature by more than 100 K, which confirms the importance of the lanthanide–ligand distance in controlling the dynamic range of Boltzmann thermometers.

**Selection rules.** So far, we have demonstrated how the host lattice affects nonradiative coupling for one specific transition, but a more generalized insight requires comparison of different thermometer ions and different pairs of thermally coupled levels. Besides the  $^5\text{D}_1$ – $^5\text{D}_0$  pair in  $\text{Eu}^{3+}$ ,

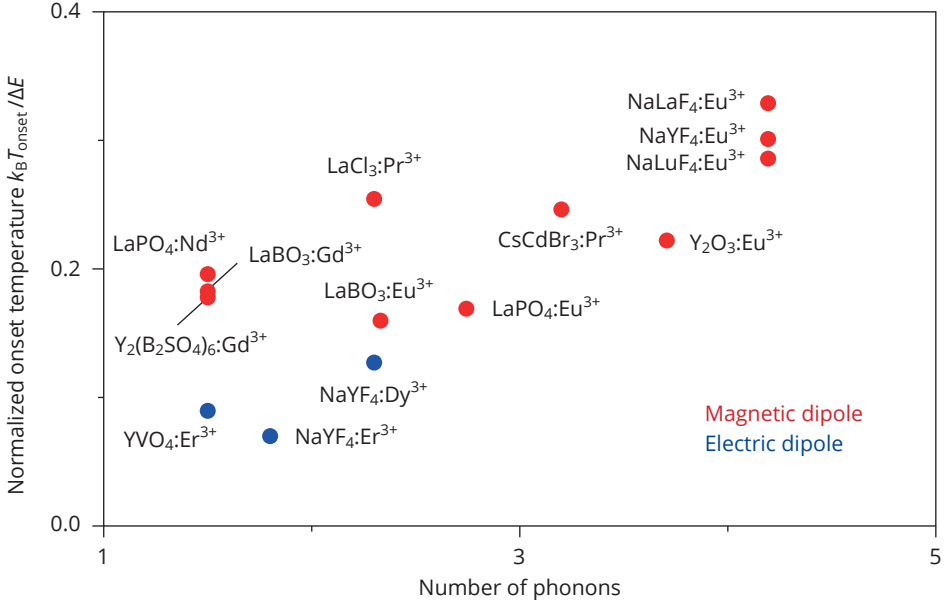


**Figure 3.4.** Normalized onset temperatures for various Boltzmann thermometers. All onset temperatures were calculated using Eq. 3.6 and normalized to  $\Delta E/k_B$ . The results of Figs. 3.2–3.3 were used to calculate the onset temperatures of the Eu<sup>3+</sup>-based thermometers. Decay rates were extracted from literature to calculate the onset temperatures of CsCdBr<sub>3</sub>:Pr<sup>3+</sup> ( $k_{nr}(0) = 1.5 \times 10^2 \text{ ms}^{-1}$ ,  $k_{1,r} = 51 \text{ ms}^{-1}$ )<sup>81</sup>, LaCl<sub>3</sub>:Pr<sup>3+</sup> ( $k_{nr}(0) = 3.1 \times 10^2 \text{ ms}^{-1}$ ,  $k_{1,r} = 68 \text{ ms}^{-1}$ )<sup>82,83</sup>, LaPO<sub>4</sub>:Nd<sup>3+</sup> ( $k_{nr}(0) = 57 \text{ ms}^{-1}$ ,  $k_{1,r} = 2.3 \text{ ms}^{-1}$ )<sup>70</sup>, LaBO<sub>3</sub>:Gd<sup>3+</sup> ( $k_{nr}(0) = 11 \text{ ms}^{-1}$ ,  $k_{1,r} = 0.29 \text{ ms}^{-1}$ )<sup>84</sup>, Y<sub>2</sub>(B<sub>2</sub>SO<sub>4</sub>)<sub>6</sub>:Gd<sup>3+</sup> ( $k_{nr}(0) = 8.9 \text{ ms}^{-1}$ ,  $k_{1,r} = 0.21 \text{ ms}^{-1}$ )<sup>84</sup>, YVO<sub>4</sub>:Er<sup>3+</sup> ( $k_{nr}(0) = 3.0 \times 10^4 \text{ ms}^{-1}$ ,  $k_{1,r} = 5.1 \text{ ms}^{-1}$ )<sup>85</sup>. Decay rates were measured to calculate the onset temperatures of NaYF<sub>4</sub>:Er<sup>3+</sup> ( $k_{nr}(0) = 1.9 \times 10^5 \text{ ms}^{-1}$ ,  $k_{1,r} = 1.4 \text{ ms}^{-1}$ ) and NaYF<sub>4</sub>:Dy<sup>3+</sup> ( $k_{nr}(0) = 2.0 \times 10^2 \text{ ms}^{-1}$ ,  $k_{1,r} = 1.3 \text{ ms}^{-1}$ ). In principle, the energy gap of LaPO<sub>4</sub>:Nd<sup>3+</sup>, LaBO<sub>3</sub>:Gd<sup>3+</sup>, Y<sub>2</sub>(B<sub>2</sub>SO<sub>4</sub>)<sub>6</sub>:Gd<sup>3+</sup>, and YVO<sub>4</sub>:Er<sup>3+</sup> could be bridged by one phonon mode, but Fig. 3.2b suggested that more than one mode is typically necessary to realize resonance, when the gap is small compared to the phonon energy. We therefore determine the onset temperature inserting both 1 and 2 phonons in Eq. 3.6 and use the average  $\rho$  and  $T_{\text{onset}}$ .

other popular Boltzmann thermometers use the  ${}^4F_{3/2}$ – ${}^4F_{5/2}$  pair in Nd<sup>3+</sup> ( $\Delta E \approx 1000 \text{ cm}^{-1}$ ), the  ${}^6P_{7/2}$ – ${}^6P_{5/2}$  pair in Gd<sup>3+</sup> ( $\Delta E \approx 600 \text{ cm}^{-1}$ ), the  ${}^3P_0$ – ${}^3P_1$  pair in Pr<sup>3+</sup> ( $\Delta E \approx 600 \text{ cm}^{-1}$ ), the  ${}^4S_{3/2}$ – ${}^2H_{11/2}$  pair in Er<sup>3+</sup> ( $\Delta E \approx 700 \text{ cm}^{-1}$ ), and the  ${}^4F_{9/2}$ – ${}^4I_{15/2}$  pair in Dy<sup>3+</sup> ( $\Delta E \approx 1000 \text{ cm}^{-1}$ ). One may expect relatively low nonradiative coupling rates between the emitting states in Eu<sup>3+</sup>, Nd<sup>3+</sup>, Gd<sup>3+</sup>, and Pr<sup>3+</sup>, because the transitions have dominant magnetic-dipole character as  $\Delta J = 1$  and the reduced matrix elements  $\langle \langle \|U^{(2)}\| \rangle \rangle^2$ ,  $\langle \langle \|U^{(4)}\| \rangle \rangle^2$ , and  $\langle \langle \|U^{(6)}\| \rangle \rangle^2$  describing electric-dipole transitions are small for these transitions. In those cases, the reduced matrix element  $\langle \langle \|L + g_S S\| \rangle \rangle^2$  describing magnetic dipolar transitions (with  $L$  as orbital and  $S$  as spin angular momentum) are relatively large.<sup>80</sup> In contrast, selection rules predict high coupling rates in Er<sup>3+</sup>- and Dy<sup>3+</sup>-based thermometers that rely on electric-dipole transitions as is evident from the large,  $\langle \langle \|U^{(2)}\| \rangle \rangle^2$ ,  $\langle \langle \|U^{(4)}\| \rangle \rangle^2$ , and  $\langle \langle \|U^{(6)}\| \rangle \rangle^2$  values for the transition between the  ${}^4S_{3/2}$ – ${}^2H_{11/2}$  levels in Er<sup>3+</sup>, and the  ${}^4F_{9/2}$ – ${}^4I_{15/2}$  levels in Dy<sup>3+</sup>. For thermometers with similar energy gaps, it was previously demonstrated that the nonradiative

rates of magnetic-dipole transitions are typically two to three orders of magnitude lower than of electric-dipole transitions.<sup>29</sup>

To understand how selection rules affect the onset of thermal equilibrium we extract  $k_{nr}(0)$ ,  $k_{r,1}$ ,  $\Delta E$ , and  $p$  from studies on various Boltzmann thermometers and determine the onset temperature using Eq. 3.6. These parameters are available in literature for multiple thermometers with magnetic-dipole transitions, but only for one thermometer with electric-dipole transitions ( $\text{YVO}_4:\text{Er}^{3+}$ ,  $k_{nr}(0) = 3.0 \times 10^4 \text{ ms}^{-1}$ ). To ensure reliable comparison we measured the luminescence of two additional thermometers with electric-dipole transitions:  $\beta\text{-NaYF}_4:\text{Er}^{3+}$  and  $\beta\text{-NaYF}_4:\text{Dy}^{3+}$ . At cryogenic temperatures, nonradiative decay from  ${}^2\text{H}_{11/2}$  in  $\text{Er}^{3+}$  and  ${}^4\text{I}_{15/2}$  in  $\text{Dy}^{3+}$  is already much faster than radiative decay, allowing extraction of  $k_{nr}(0)$  directly from the corresponding decay curves as  $k_{nr}(0) \gg k_{r,2}$  (Table A3.1). We find  $k_{nr}(0)$  values of  $1.9 \times 10^5 \text{ ms}^{-1}$  and  $2.0 \times 10^2 \text{ ms}^{-1}$  and onset temperatures of 75 K and 174 K for  $\text{Er}^{3+}$  and  $\text{Dy}^{3+}$ , respectively. Compared to  $\beta\text{-NaYF}_4:\text{Eu}^{3+}$ , the obtained value of  $k_{nr}(0)$  for  $\beta\text{-NaYF}_4:\text{Dy}^{3+}$  is indeed three orders of magnitude higher. Interestingly, the value of  $k_{nr}(0)$  for  $\beta\text{-NaYF}_4:\text{Er}^{3+}$  is higher than expected. We speculate that in addition to a large effect of selection rules also stronger electron–phonon coupling may contribute to the high  $k_{nr}(0)$  value in  $\text{Er}^{3+}$ .<sup>86</sup> To enable fair comparison of different thermometers we normalized the obtained onset temperatures to  $\Delta E/k_B$ . Fig. 3.4 reveals that the normalized onset temperature generally increases with  $p$  as expected from the energy-gap law. More importantly, the normalized onset temperature of thermometers with magnetic-dipole transitions is much higher than for thermometers with electric-dipole transitions. For a specific energy gap, experiments at low

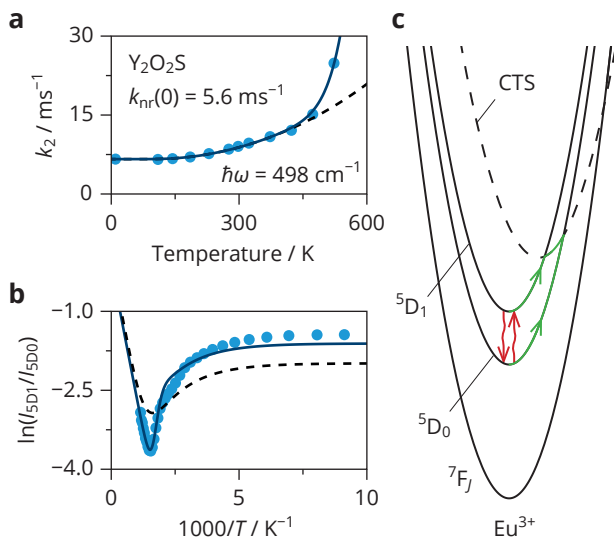


**Figure 3.5.** The impact of charge-transfer quenching on the onset of thermal equilibrium. **(a)** Decay rates of the  ${}^5\text{D}_1$  emission at various temperatures. The dashed black line is a fit of the experimental rates (blue dots) up to 423 K to Eq. 3.1, while the solid blue line is a fit to Eq. 3.7. **(b)** Intensity ratios between the  ${}^5\text{D}_1$  and  ${}^5\text{D}_0$  emissions for various temperatures extracted from luminescence spectra. The dashed black line is a fit of the experimental ratios (blue dots) to Eq. 3.4, while the solid blue line is a fit to Eq. 3.8. **(c)** Configurational coordinate diagram of the  ${}^5\text{D}_{0-1}$  and  ${}^7\text{F}_j$  levels of  $\text{Eu}^{3+}$  including the charge-transfer state (CTS) of  $\text{Y}_2\text{O}_2\text{S}$ . Coupling between  ${}^5\text{D}_1$  and  ${}^5\text{D}_0$  takes place directly via phonon emission and absorption (red arrows) and indirectly via crossover to the CTS (green arrows).

temperatures thus benefit from thermometers with electric-dipole transitions.

**An additional quenching pathway.** Besides modification of thermal coupling, the host lattice can also introduce additional nonradiative relaxation pathways via a higher excited state. Mostly, this is studied in relation to luminescence quenching caused by, for instance, thermally activated crossover.<sup>87</sup> To investigate how this affects thermal equilibrium we acquired the temperature-dependent luminescence of  $\text{Eu}^{3+}$  in  $\text{Y}_2\text{O}_2\text{S}$ , which has a low lying  $\text{S}^{2-}$ -to- $\text{Eu}^{3+}$  charge transfer state (CTS) due to the soft, polarizable nature of the  $\text{S}^{2-}$  ligands.<sup>88</sup> The temperature-dependent behavior is remarkably different from the other studied materials. This is already demonstrated by the decay rate of the  ${}^5\text{D}_1$  emission, which above 423 K drastically increases with temperature, more than expected for multi-phonon relaxation (Fig. 3.5a). We attribute this to thermally activated crossover from the  ${}^5\text{D}_1$  level to the CTS of the host.<sup>87</sup> We account for crossover to the CTS by the addition of a Mott-Seitz term to the total decay rate of  ${}^5\text{D}_1$ :

$$k_2 = k_{r,2} + k_{\text{CT}} \exp(-E_{a,2}/k_{\text{B}}T) + k_{\text{nr}}(0)g_1(1+n)^p, \quad (3.7)$$

where  $E_{a,2}$  is the activation barrier for crossover from  ${}^5\text{D}_1$  to the CTS and  $k_{\text{CT}}$  is the rate constant.<sup>89,90</sup> We again acquire the luminescence at 7 K and find an intrinsic nonradiative rate  $k_{\text{nr}}(0)$  of  $5.6 \text{ ms}^{-1}$  that is similar to  $\text{Y}_2\text{O}_3$  as expected from the comparable vibrational energies.<sup>72</sup> In contrast, the obtained radiative rates  $k_{r,1}$  of  $2.3 \text{ ms}^{-1}$  and  $k_{r,2}$  of  $1.0 \text{ ms}^{-1}$  are relatively high, which is explained by mixing of the CTS into the  ${}^5\text{D}_j$  states. Admixture of opposite-parity states into  $4f^n$  states induces forced electric-dipole transitions and is strongly enhanced if the energy difference is reduced, resulting in large Judd-Ofelt parameters  $\Omega_2$ ,  $\Omega_4$  and  $\Omega_6$ .<sup>91</sup> This can explain the high radiative decay rates. Note that a low-energy opposite-parity state can also enhance the nonradiative coupling rates if the transition has electric-dipole character. However, no enhancement is expected for the  ${}^5\text{D}_1$ - ${}^5\text{D}_0$  transitions due to the magnetic-dipole nature of this transition. Using  $k_{\text{nr}}(0)$  and  $k_{r,2}$  as input, we fit the experimental decay rates up to 423 K to Eq. 3.1 and obtain a  $\hbar\omega$  value of  $498 \text{ cm}^{-1}$  (black dashed line). Then, we fit the full range of decay rates to Eq. 3.7 with the obtained value for  $\hbar\omega$  and the reported value for  $E_{a,2}$  ( $6100 \text{ cm}^{-1}$ ) as additional input to find  $k_{\text{CT}}$  ( $1.6 \times 10^8 \text{ ms}^{-1}$ ).<sup>88</sup> The excellent agreement between the data and the model (solid blue line) indicates that thermally activated crossover to the CTS is an additional nonradiative path from  ${}^5\text{D}_1$  for  $\text{Eu}^{3+}$  in  $\text{Y}_2\text{O}_2\text{S}$ .

Fig. 3.5b shows the temperature-dependent intensity ratios of  $\text{Y}_2\text{O}_2\text{S}:\text{Eu}^{3+}$ , in which we observe a much sharper minimum than in the other studied materials. Similar to the fluorides, we also observed strong  ${}^5\text{D}_2$  emissions in the luminescence spectra of  $\text{Y}_2\text{O}_2\text{S}:\text{Eu}^{3+}$  (Fig. 3.1), indicating substantial feeding via radiative decay. We fit the experimental ratios (blue dots) to Eq. 3.4 (black dashed line) with  $\alpha$  and  $C$  as free parameters. The poor quality of the fit demonstrates that thermal coupling in this material cannot be solely described by phonon emission and absorption. Instead, the CTS can introduce a second indirect nonradiative coupling pathway. Specifically, the CTS can be fed from  ${}^5\text{D}_1$  and  ${}^5\text{D}_0$ , after which it relaxes back to one of these states (Fig. 3.5c). The

steady-state solution to the rate equations of this extended system is

$$\frac{I_2}{I_1} = C \frac{k_{r,1}\alpha + k_{CT} \exp(-E_{a,1}/k_B T) + k_{nr}(0)g_2 n^p}{k_{r,2}(1 - \alpha) + k_{CT} \exp(-E_{a,2}/k_B T) + k_{nr}(0)g_1(1 + n)^p}. \quad (3.8)$$

Here,  $E_{a,1}$  is the activation barrier for crossover from  ${}^5D_0$ , which we fix to  $E_{a,2} + \Delta E$ , leaving only  $\alpha$  and  $C$  as free parameters. A fit of the experimental ratios to this extended model (blue solid line) perfectly captures the sharp minimum, which confirms that indirect coupling via the CTS modifies the thermal equilibration between  ${}^5D_1$  and  ${}^5D_0$ .<sup>88,92</sup> At lower temperatures, the quality of the fit decreases, which we again attribute to temperature-dependence of the feeding term  $\alpha$ . Fig. A3.2 shows that nonradiative coupling via the CTS dominates over phonon emission and absorption, which makes our definition of the onset temperature no longer valid. If we do determine the onset temperature using Eq. 3.6, it gives a value of 707 K. This is much higher than the onset in  $Y_2O_3$ , because the low-lying CTS causes faster radiative decay from  ${}^5D_0$ . An additional disadvantage of the low-lying CTS is quenching of the luminescence via crossover to the  ${}^7F_7$  states, which reduces the brightness of the thermometer resulting in low measurement precisions.<sup>93</sup> These considerations imply that the CTS in  $Y_2O_2S:Eu^{3+}$  has a negative impact on the performance of  $Eu^{3+}$  as a luminescent thermometer.

### 3.3 Discussion and conclusions

The dynamic temperature range is one of the most important considerations for the selection of a thermometer for a specific application. For luminescent Boltzmann thermometers, there has been a strong focus on realizing high relative sensitivities, which can be controlled via the energy gap. The highest sensitivities are however found for thermometers with large energy gaps, but they inherently suffer from high onset temperatures of thermal equilibrium putting a lower limit on the dynamic temperature range. This is not always realized and can lead to deviations and systematic errors in the lower temperature regime if Boltzmann equilibrium is assumed but not yet established.

Our work highlights three methods to lower the onset temperature and extend the dynamic temperature range of Boltzmann thermometers by: i) decreasing the number of required phonons to bridge the energy gap, ii) reducing the lanthanide–ligand distances within the host, and iii) selecting a thermometer with excited states coupled by electric-dipolar nonradiative transitions. All methods rely on maximizing the intrinsic coupling rates between the emitting states, which mainly determine the onset of thermal equilibrium. The lanthanide–ligand distance has the smallest, but still significant, effect on this rate, showing an increase of a factor two from  $\beta$ -NaLaF<sub>4</sub> to  $\beta$ -NaLuF<sub>4</sub> resulting in a reduction of  $T_{onset}$  by 100 K. In contrast, the intrinsic coupling rates increased by three orders of magnitude with a decrease in the average number of required phonons from 4.2 to 2.3. This caused a difference in the onset temperature of more than 400 K between  $\beta$ -NaLaF<sub>4</sub>:Eu<sup>3+</sup> (823 K) and LaBO<sub>3</sub>:Eu<sup>3+</sup> (402 K). We further observed that the intrinsic nonradi-



ative rate is two to three orders of magnitudes higher in luminescent thermometers, in which the excited states are coupled by electric-dipole transitions compared to thermometers with magnetic-dipole transitions, indicating an important and so far underestimated role of selection rules.

We find the lowest onset temperatures for  $\text{Er}^{3+}$ , as expected from the small energy gap of  $700\text{ cm}^{-1}$  and the electric-dipole character of the nonradiative transitions.  $\text{Er}^{3+}$ -based thermometers further benefit from a high oscillator strength of the  ${}^4\text{I}_{15/2} \leftrightarrow {}^2\text{H}_{11/2}$  transition, which leads to strong emission from the  ${}^2\text{H}_{11/2}$  state at relatively low thermal population and thus guarantees high measurement precisions.<sup>93</sup> An additional advantage of  $\text{Er}^{3+}$ -based thermometers is the possibility of co-doping with  $\text{Yb}^{3+}$  to allow for efficient generation of upconversion luminescence. This makes  $\text{Er}^{3+}$  the preferred Boltzmann thermometer in many cases. Some specific applications however require thermometers with different emission energies or higher sensitivities at elevated temperatures. For instance, experiments in biological tissue are preferably performed with  $\text{Nd}^{3+}$  due to the high penetration depth of its infrared emissions, while the large energy gap of  $\text{Eu}^{3+}$  makes it the preferred thermometer for accurate measurements of elevated temperatures. However, the magnetic-dipole character of the nonradiative transitions and the large energy gap inherently restrict such experiments to elevated temperatures. The experiments and considerations discussed in this work can aid in the selection of the best host materials to improve the dynamic range of these ions for specific applications when no thermometers with electric-dipole transitions are available.

We have experimentally demonstrated how the host lattice impacts nonradiative coupling between  ${}^5\text{D}_1$  and  ${}^5\text{D}_0$  in  $\text{Eu}^{3+}$ -based thermometers and how it controls the onset temperature of thermal equilibrium. Higher vibrational energies and shorter lanthanide–ligand distances help to lower the onset temperature of thermal equilibrium. Comparing onset temperatures of thermometers based on different lanthanide ions revealed that selection rules modify the intrinsic non-radiative rate and result in wider dynamic ranges for thermometers with excited states coupled by electric-dipolar transitions. These findings not only offer a fundamental understanding of thermal equilibrium but also provide design rules for the rational optimization of Boltzmann thermometers.

### 3.4 Materials and methods

**Chemicals.** Sodium fluoride (98%, NaF), ammonium fluoride (99.8%,  $\text{NH}_4\text{F}$ ), yttrium fluoride (99.9%,  $\text{YF}_3$ ), yttrium nitrate hexahydrate (99.8%,  $\text{Y}(\text{NO}_3)_3 \cdot 6\text{H}_2\text{O}$ ), lanthanum nitrate hexahydrate (99.999%,  $\text{La}(\text{NO}_3)_3 \cdot 6\text{H}_2\text{O}$ ), and europium nitrate pentahydrate (99.9%,  $\text{Eu}(\text{NO}_3)_3 \cdot 5\text{H}_2\text{O}$ ) were obtained from Sigma-Aldrich. Dysprosium fluoride (99.9%,  $\text{DyF}_3$ ) and europium fluoride (99.99%,  $\text{EuF}_3$ ) were purchased from Strem Chemicals. Lanthanum fluoride (99.99%,  $\text{LaF}_3$ ) and lutetium oxide (99.99%,  $\text{Lu}_2\text{O}_3$ ) were acquired from ChemPUR. Ammonium oxalate monohydrate (99.7%,  $(\text{NH}_4)_2\text{C}_2\text{O}_4 \cdot \text{H}_2\text{O}$ ) was obtained from Baker chemicals. Ammonium phosphate monohydrate (99%,  $(\text{NH}_4)_2\text{HPO}_4 \cdot \text{H}_2\text{O}$ ) was acquired from Merck. Boric acid (99.8%,  $\text{H}_3\text{BO}_3$ ) was

purchased from Merck. MilliQ water (H<sub>2</sub>O) was used for washing and the preparation of aqueous solutions.

**Synthesis.** Cubic Y<sub>2</sub>O<sub>3</sub>:Eu<sup>3+</sup>(0.05%) was prepared via a co-precipitation procedure. Solutions of 0.9995 eq. of Y(NO<sub>3</sub>)<sub>3</sub>·6H<sub>2</sub>O and 0.0005 eq. of Eu(NO<sub>3</sub>)<sub>3</sub>·5H<sub>2</sub>O in 10 mL H<sub>2</sub>O and 3 eq. (NH<sub>4</sub>)<sub>2</sub>C<sub>2</sub>O<sub>4</sub>·H<sub>2</sub>O in 50 mL H<sub>2</sub>O were mixed to form a white precipitate, which was washed with H<sub>2</sub>O and placed in a drying oven at 373 K. The dried precipitate was heated in air at 1673 K for 8 hours.

Monoclinic LaPO<sub>4</sub>:Eu<sup>3+</sup>(0.5%) was prepared via a co-precipitation procedure. Solutions of 0.995 eq. of La(NO<sub>3</sub>)<sub>3</sub>·6H<sub>2</sub>O and 0.005 eq. of Eu(NO<sub>3</sub>)<sub>3</sub>·5H<sub>2</sub>O in 15 mL H<sub>2</sub>O and 1 eq. (NH<sub>4</sub>)<sub>2</sub>HPO<sub>4</sub>·H<sub>2</sub>O in 15 mL H<sub>2</sub>O were mixed to form a white precipitate, which was washed with H<sub>2</sub>O and placed in a drying oven at 373 K. The dried precipitate was heated in air at 1273 K for 12 hours.

Orthorhombic LaBO<sub>3</sub>:Eu<sup>3+</sup>(0.5%) was prepared via a two-step procedure. First, La<sub>2</sub>O<sub>3</sub>:Eu<sup>3+</sup>(0.5%) was obtained by a co-precipitation procedure, similar to the synthesis of Y<sub>2</sub>O<sub>3</sub>:Eu<sup>3+</sup>(0.05%) but with 0.995 eq. of La(NO<sub>3</sub>)<sub>3</sub>·6H<sub>2</sub>O and 0.005 eq. of Eu(NO<sub>3</sub>)<sub>3</sub>·5H<sub>2</sub>O as reactants. The product was thoroughly mixed with 2 eq. of H<sub>3</sub>BO<sub>3</sub> and heated in air at 1123 K for 12 hours.

Hexagonal β-NaLuF<sub>4</sub>:Eu<sup>3+</sup>(0.5%) was prepared via a solid-state reaction. First, LuF<sub>3</sub> was synthesized by dissolution of Lu<sub>2</sub>O<sub>3</sub> in concentrated hydrogen chloride and precipitation with a concentrated aqueous NH<sub>4</sub>F solution in a Teflon beaker. The precipitated raw fluoride was isolated, washed with H<sub>2</sub>O and ethanol, dried at 393 K, and crystallized at 973 K in a bed of NH<sub>4</sub>F. A mixture of 0.995 eq. of LuF<sub>3</sub>, 0.005 eq. of EuF<sub>3</sub>, and 1 eq. of NaBF<sub>4</sub> was thoroughly ground and heated in N<sub>2</sub> atmosphere at 648 K for 3 hours. Hexagonal β-NaLaF<sub>4</sub>:Eu<sup>3+</sup>(0.5%) was obtained using the same procedure but with 0.995 eq. of LaF<sub>3</sub> and 2 eq. of NaBF<sub>4</sub> as reactants and a heating step at 898 K for 6 hours.

Hexagonal β-NaYF<sub>4</sub>:Dy<sup>3+</sup>(0.4%) was prepared via a solid-state reaction, based on the work of Geitenbeek *et al.*<sup>71</sup> A mixture of 0.996 eq. of YF<sub>3</sub>, 0.004 eq. of DyF<sub>3</sub>, 1 eq. of NaF, and 0.9 eq. of NH<sub>4</sub>F was thoroughly ground. The ground mixture was placed in the oven in N<sub>2</sub> atmosphere with a flux of NH<sub>4</sub>F and it was heated at 573 K for 3 hours followed by a second heating step at 823 K for 8 hours.

Hexagonal β-NaYF<sub>4</sub>:Eu<sup>3+</sup>(0.4%)<sup>71</sup>, hexagonal Y<sub>2</sub>O<sub>2</sub>S:Eu<sup>3+</sup>(0.1%)<sup>88</sup>, and hexagonal β-NaYF<sub>4</sub>:Er<sup>3+</sup>(0.1%)<sup>67</sup> were obtained from previously reported procedures.

**Structural characterization and spectroscopic experiments.** The crystal structure of the materials was confirmed with a Philips PW1700 X-ray powder diffractometer equipped with a Cu K<sub>α1</sub> (λ = 1.5418 Å) radiation source. All materials were found to be phase pure. The luminescence

spectra, from which the data is shown in Fig. 3.1, 3.2c, 3.3b, and 3.5b, were recorded using an Ocean Optics QE Pro010451 CCD detector and a 450 W Xe lamp as excitation source. The white light from the Xe lamp was passed through the TMS300 double monochromator of an Edinburgh Instruments FLS920 spectrofluorometer to select the excitation wavelength. The luminescence spectra that were used to determine  $k_{nr}(0)$  and  $k_{r,2}$  were acquired using a Triax 550 monochromator equipped with a Hamamatsu R928 photomultiplier tube and an Ekspla NT342B OPO laser (10 Hz) as excitation source. The line width of the laser was  $6 \text{ cm}^{-1}$ , which enabled highly selective excitation of the  ${}^7F_0 \rightarrow {}^5D_1$  transition. Luminescence decay measurements were performed using the same Triax monochromator and Ekspla laser, but with a Hamamatsu H7422 photomultiplier tube as a single-photon counting detector. The laser synchronization and detection signals were recorded with a PicoQuant Timeharp 260 time-correlated single-photon counting module. The temperature of the samples was controlled between 78 K and 873 K using a Linkam THMS600 heating stage. Measurements at 7 K were performed with an Oxford Instruments liquid-He cold-finger cryostat.

### 3.5 Appendix

**Analysis of the temperature-dependent luminescence.** We analyze the temperature dependence of the  $\text{Eu}^{3+}$  luminescence using decay curves and emission spectra. The goal of this analysis is to verify if the thermometer behaves as a system of two thermally coupled levels by fitting the experimental intensity ratios to Eq. 3.4 or 3.5. The number of unknown variables in Eq. 3.4 and 3.5 is however too large to use all of them as fitting parameters. We therefore separately determine  $k_{r,1}$ ,  $k_{r,2}$ , and  $k_{nr}(0)$  from luminescence measurements at 7 K, where the low temperatures suppress stimulated phonon emission and absorption or other undesired nonradiative processes. We use the decay rate of the  ${}^5D_0$  emission as value for  $k_{r,1}$ , while the decay rate of the  ${}^5D_1$  emission  $k_2$  is the sum of  $k_{r,2}$  and  $k_{nr}(0)$ , as  $g_1 = 1$ . Since decay from  ${}^5D_0$  is purely radiative, we can assume that at 7 K all  ${}^5D_0$  emission upon excitation into  ${}^5D_1$  is the sole result of spontaneous phonon emission from  ${}^5D_1$ . It is therefore possible to determine  $k_{r,2}$  and  $k_{nr}(0)$  from  $k_2$  using the emission spectrum covering all possible  ${}^5D_{0-1}$  emissions upon excitation in  ${}^7F_0 \rightarrow {}^5D_1$ :

$$\begin{aligned} k_{r,2} &= \frac{k_2 I_2}{I_2 + I_1}, \\ k_{nr}(0) &= \frac{k_2 I_1}{I_2 + I_1}. \end{aligned} \tag{A3.1}$$

Where  $I_2$  and  $I_1$  are the integrated intensities of the  ${}^5D_1$  and  ${}^5D_0$  emissions, respectively.

There are a few exceptions to this procedure. For  $\text{Y}_2\text{O}_3$ , we record the decay curve of the emission  ${}^5D_1$  and the full-range spectrum at 78 K, because in this case the  ${}^5D_1$  decay rate was slightly higher than the rate at 7 K, possibly due to differences in the decay rates of the crystal-field levels within  ${}^5D_1$ . For  $\text{LaBO}_3$ , the decay curve of  ${}^5D_0$  is multi-exponential at both 7 K and 78 K. We fit the decay curve measured at 78 K to three exponentials and used the average decay rate as  $k_{r,1}$ .

**The minimum in the temperature dependence of the intensity ratios.** Assuming that the feeding factor  $\alpha$  is one and  $p > 1$ , the temperature at which Eq. 3.5 goes through a minimum simplifies to

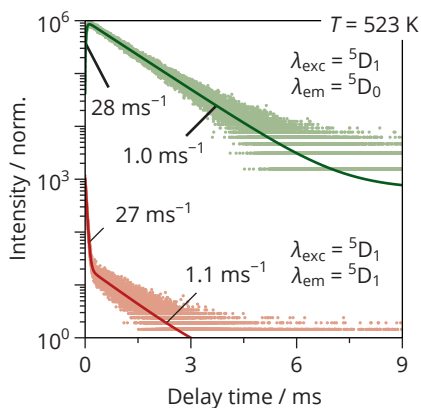
$$T_{\min} = \frac{\Delta E/p}{k_B \ln \left[ 1 + \left( \frac{g_2 k_{\text{nr}}(0)}{k_{r,1}} \right)^{1/(p-1)} \right]}. \quad (\text{A3.2})$$

Solving this for  $k_{r,1}$  gives

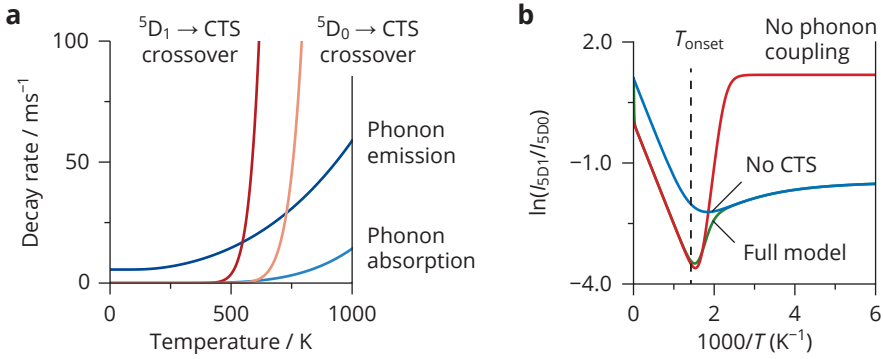
$$k_{r,1} = k_{\text{nr}}(0) g_2 n^{p-1}, \quad (\text{A3.3})$$

which implies that the intensity ratio reaches a minimum when the absorption rate of the higher-order phonons  $p-1$  is equal to  $k_{r,1}$ .

#### The fast and the slow decay component.



**Figure A3.1.** Luminescence decay of  $\text{Y}_2\text{O}_3:\text{Eu}^{3+}(0.05\%)$  at 523 K. Decay curves of the  ${}^5\text{D}_1$  and  ${}^5\text{D}_0$  emission were recorded upon excitation into  ${}^5\text{D}_1$ . The experimental data was fitted to bi-exponential decay. Both the rates of the fast components and the rates of the slow components match, which is clear signature of thermal coupling (but not yet thermal equilibrium for which single exponential decay with the same decay time for  ${}^5\text{D}_1$  and  ${}^5\text{D}_0$  emission is observed).

**Nonradiative coupling via phonons and via the charge-transfer state.**


**Figure A3.2.** Nonradiative coupling between  ${}^5\text{D}_1$  and  ${}^5\text{D}_0$  in  $\text{Y}_2\text{O}_2\text{S}:\text{Eu}^{3+}$ . **(a)** Decay rates of crossover and phonon coupling from  ${}^5\text{D}_1$  and  ${}^5\text{D}_0$ . **(b)** Calculated intensity ratios between  ${}^5\text{D}_1$  and  ${}^5\text{D}_0$  from Eq. 3.8 (green), without phonon coupling terms (red), and without crossover rates.

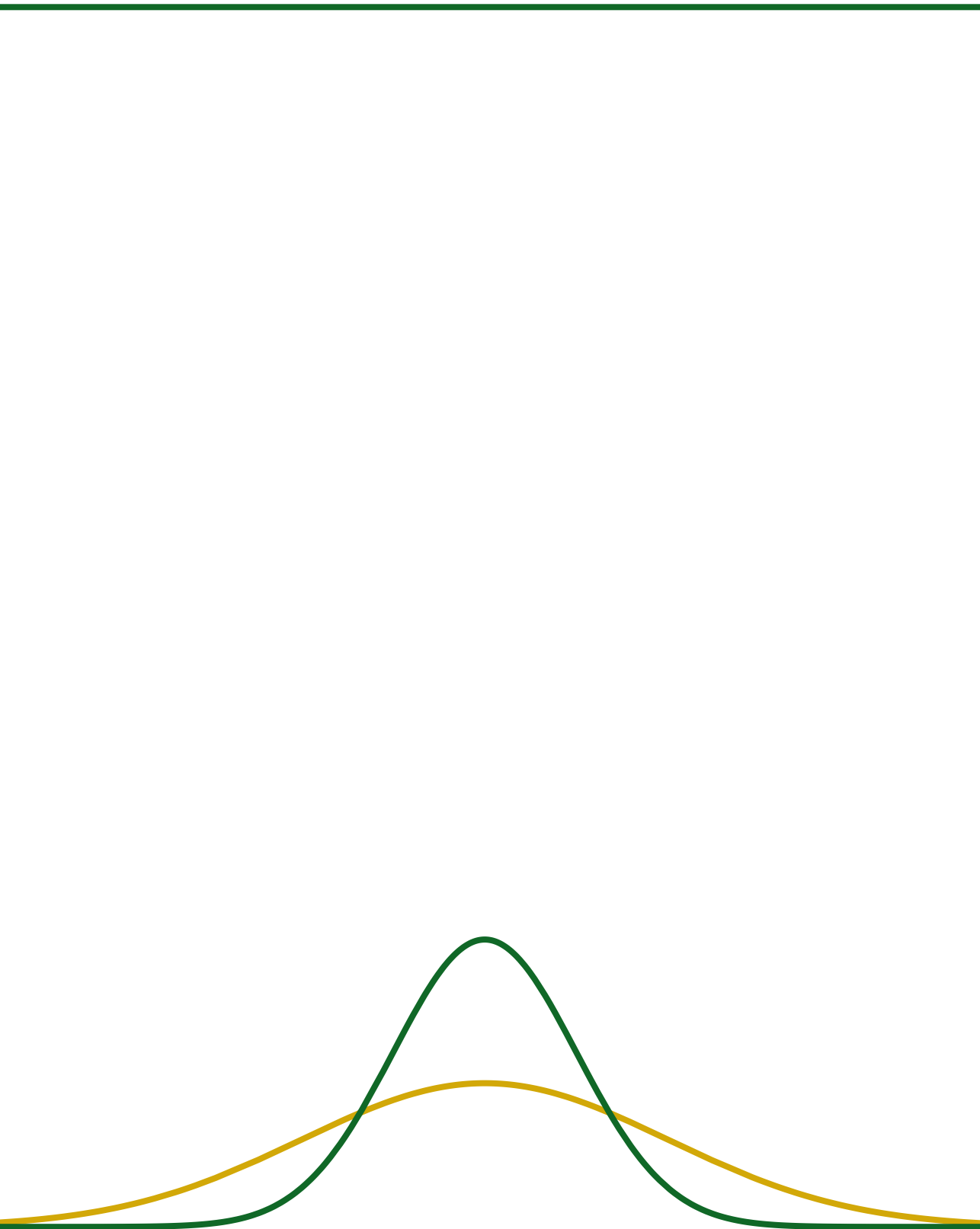
**Nonradiative coupling via phonons and via the charge-transfer state.**

**Table A3.1.** Experimental parameters of the thermally coupled  ${}^5\text{D}_1$  and  ${}^5\text{D}_0$  levels of  $\text{Eu}^{3+}$  in different host lattices. The decay rates  $k_{r,1}$ ,  $k_{r,2}$ , and  $k_{nr}(0)$  were obtained from luminescence measurements at 7 K or 78 K. Fitting procedures of the decay rates and intensity ratios to our analytical models yielded the energies of phonon modes, feeding factor  $a$ , pre-factor  $C$ , and rate constant  $k_{CT}$ . The onset of thermal equilibrium  $T_{\text{onset}}$  was calculated at the temperature, for which the phonon absorption rate is equal to the radiative rate from the lower thermally coupled state.

Material	$k_{r,1} / \text{ms}^{-1}$	$k_{r,2} / \text{ms}^{-1}$	$k_{nr}(0) / \text{ms}^{-1}$	$a$	$C$	$T_{\text{onset}} / \text{K}$	Phonon modes / $\text{cm}^{-1}$ (number $\rho$ )	$k_{CT} / \text{ms}^{-1}$
$\text{LaBO}_3:\text{Eu}^{3+}(0.5\%)$	0.98*	0.10	74	1.0	0.24	402	1467 (1), 212 (1.3)	-
$\text{LaPO}_4:\text{Eu}^{3+}(0.5\%)$	0.28	0.16	25	1.0	0.61	396	1252 (1), 286 (1.7)	-
$\text{Y}_2\text{O}_3:\text{Eu}^{3+}(0.05\%)$	0.98	0.50	8.0	1.0	0.16	559	472 (3.7)	-
$\text{NaLuF}_4:\text{Eu}^{3+}(0.5\%)$	0.18	0.11	0.18	0.76	0.57	720	414 (4.2)	-
$\text{NaYF}_4:\text{Eu}^{3+}(0.4\%)$	0.16	0.11	0.12	0.75	0.57	758	414 (4.2)	-
$\text{NaLaF}_4:\text{Eu}^{3+}(0.5\%)$	0.18	0.10	0.08	0.83	0.57	828	414 (4.2)	-
$\text{NaYF}_4:\text{Dy}^{3+}(0.4\%)$	1.3	-	$2.0 \times 10^{2**}$	-	-	174	417 (2.3)	-
$\text{NaYF}_4:\text{Er}^{3+}(0.1\%)$	1.4	-	$1.9 \times 10^{5**}$	-	-	75	417 (1.8)	-
$\text{Y}_2\text{O}_2\text{S}:\text{Eu}^{3+}(0.1\%)$	2.3	1.0	5.6	0.87	0.59	707	498 (3.5)	$1.6 \times 10^8$

\* The decay curve of the  ${}^5\text{D}_0$  emission is multi-exponential. We determined the average decay rate from a fit of the data to tri-exponential decay.

\*\* Emission from the higher thermally coupled state was very weak, which made integration of the spectral line unreliable.  $k_{nr}(0)$  was determined directly from the decay rate of this emission.



# Chapter 4

## A Ho<sup>3+</sup>-based luminescent thermometer for sensitive sensing over a wide temperature range

### Abstract

Luminescence thermometry is used in a variety of research fields for non-invasive temperature sensing. Lanthanide-doped micro-/nanocrystals are exceptionally suitable for this. The popular concept of luminescence-intensity-ratio (*LIR*) thermometry is based on emission from thermally coupled levels in a single lanthanide ion, following Boltzmann's law. These thermometers can measure temperature with low uncertainty, but only in a limited temperature range. In this Chapter, we present and quantitatively model a Ho<sup>3+</sup>-based thermometer with sustained low temperature uncertainty from room temperature up to 873 K. Our thermometer shows bright green and red luminescence with a strong and opposite dependence on temperature and Ho<sup>3+</sup> concentration. This is the result of temperature-dependent competition between multi-phonon relaxation and energy transfer, feeding the green- and red-emitting levels, respectively, following excitation with blue light. Our simple and quantitative model of this competition predicts the output spectrum over a wide range of temperatures (300–873 K) and Ho<sup>3+</sup> concentrations (0.1–30%). We can thus determine the optimum Ho<sup>3+</sup> concentration for reliable measurements over any temperature range of interest. Quantitative modeling as presented here is crucial to optimally benefit from the potential of energy-transfer thermometers to achieve low measurement uncertainties over a wide temperature range.

### Based on:

T.P. van Swieten, D. Yu, T. Yu, S.J.W. Vonk, M. Suta, Q. Zhang, A., Meijerink and F.T. Rabouw, A Ho<sup>3+</sup>-Based Luminescent Thermometer for Sensitive Sensing over a Wide Temperature Range, *Advanced Optical Materials* **9**, 2001518 (2021).

## 4.1 Introduction

In many research fields, ranging from cell biology to catalysis, the size and invasiveness of conventional thermometers hinders accurate temperature sensing.<sup>34,94</sup> Remote temperature sensing based on luminescence thermometry offers an alternative that is capable of measuring heat generation and diffusion on the microscopic scale.<sup>95</sup> Among the various choices of luminescent systems,<sup>96–101</sup> crystals doped with lanthanide ( $\text{Ln}^{3+}$ ) ions represent a particularly promising class of luminescent thermometers, because their dimensions can be tuned from a few nanometers to several micrometers and their photoluminescence spectrum is sensitive to temperature. A characteristic feature of  $\text{Ln}^{3+}$  ions is their rich energy level structure, which results in emission spectra with well-separated lines. Typically, the luminescence intensity ratio (*LIR*) between two of these emission lines is used as a sensitive measure for the temperature of the  $\text{Ln}^{3+}$ -doped crystal. After insertion of these ratiometric thermometers into a system of interest, remote operation simply involves excitation by light and detection of the luminescence with standard spectroscopic equipment.

The performance of a ratiometric thermometer is determined by how sensitively the *LIR* reacts to temperature. In general, the performance at a given temperature ( $T$ ) is quantified in terms of the relative sensitivity (Eq. 1.3). A high relative sensitivity allows for accurate probing of small temperature differences.<sup>102</sup> In addition, a reliable temperature measurement requires high precision, which depends on the signal-to-noise ratio of the measurement.<sup>103,104</sup> The precision improves with longer acquisition time and higher brightness of the thermometer. The multitude of temperature-dependent emission lines from  $\text{Ln}^{3+}$  ions offers many possibilities to optimize sensitivity and precision for the temperature range of interest. The search for superior accuracies have already led to the development of a large variety of ratiometric thermometers.<sup>102</sup>

A popular class of ratiometric thermometers relies on thermal coupling between two excited states of individual  $\text{Ln}^{3+}$  dopants. The *LIR* of the emission lines from the two states follows Boltzmann statistics, as long as thermal coupling between them is much faster than radiative decay.<sup>71</sup> The relative sensitivity for such “Boltzmann thermometers” follows a simple analytical dependence on temperature of  $S_r = \Delta E/k_B T^2$ , where  $\Delta E$  is the energy separation between the coupled states. This relation reveals a fundamental limitation of the Boltzmann thermometer: they offer low relative sensitivities at high temperatures ( $k_B T > \Delta E$ ) because the Boltzmann populations of the two coupled states are nearly equal. On the other hand, the measurement precision is low at lower temperatures ( $k_B T < \Delta E$ ) because the population of the upper level is negligible. Accurate and precise temperature sensing over a wide range thus requires a ratiometric thermometer with an alternative working mechanism.<sup>105,106</sup>

Alternative ratiometric thermometers typically consist of a material doped with different  $\text{Ln}^{3+}$  ions, e.g.  $\text{Eu}^{3+}$  and  $\text{Tb}^{3+}$ , that are connected by energy-transfer pathways with a strong temperature dependence.<sup>54,107,108</sup> This operating mechanism does not lead to a thermal equilibrium of excited-state populations, which makes higher relative sensitivities with yet appreciable luminescence intensities from the different ions possible.<sup>49,109</sup> Recently, Ximendes *et al.* reported a



similar concept using LaF<sub>3</sub> nanoparticles doped with high concentrations of Tm<sup>3+</sup>, which showed cross-relaxation (*i.e.* partial energy transfer between two identical ions).<sup>110</sup> However, the working mechanism of energy-transfer thermometers is complicated because it does not only depend on relaxation processes within an ion but also involves interactions between different ions. Consequently, it has not yet been possible to develop a quantitative method that predicts the accuracy and the precision of energy-transfer thermometers.

In this Chapter, we introduce a Ho<sup>3+</sup>-based cross-relaxation thermometer, measure its temperature-dependent luminescence, and quantitatively model its performance. Our thermometer operates via the competition between a temperature- and a doping-concentration-dependent decay pathway that lead to green and red emission, respectively. We construct a quantitative model for the rates and efficiencies of the complex set of decay pathways involved as a function of temperature and Ho<sup>3+</sup> concentration. This model successfully predicts the red-to-green *LIR* as well as the accuracy and the precision of temperature measurements. It can thus serve as a design tool to calculate the Ho<sup>3+</sup> concentration that enables the most reliable temperature measurements for any temperature regime of interest. Our method of thermometer evaluation is an important step for the design of new energy-transfer thermometers focused on and optimized for the desired application.

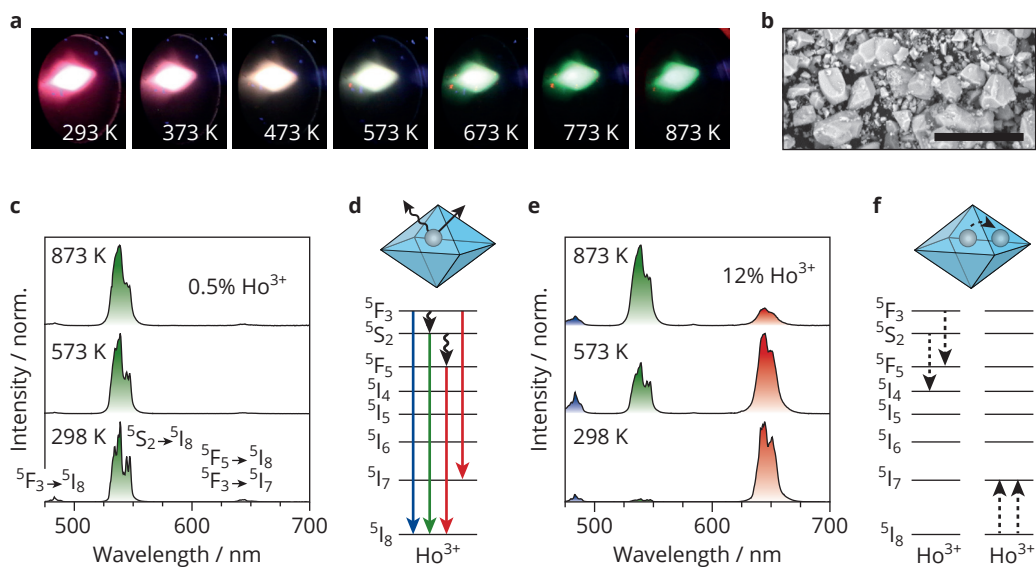
## 4.2 Results

Fig. 4.1a demonstrates the potential of our Ho<sup>3+</sup>-based thermometer, reflected by the strong color shift with increasing temperature going from red through white to green.<sup>111-114</sup> Specifically, we prepared microcrystalline fluoride compounds doped with different concentrations of Ho<sup>3+</sup>, *i.e.*  $\beta$ -NaY<sub>0.75-x</sub>Gd<sub>0.25</sub>Ho<sub>x</sub>F<sub>4</sub> (Fig. 4.1b).<sup>115</sup> Excitation of these samples with 450 nm light results in a blue, a green, and a red emission band, which are due to the  $^5F_3 \rightarrow ^5I_8$ ,  $^5S_2 \rightarrow ^5I_8 + ^5F_4 \rightarrow ^5I_8$ , and  $^5F_5 \rightarrow ^5I_8 + ^5F_3 \rightarrow ^5I_7$  radiative transitions, respectively.<sup>116</sup> Competition between different temperature-dependent decay pathways of an excited Ho<sup>3+</sup> ion, including energy-transfer pathways between neighboring Ho<sup>3+</sup> ions, controls the relative intensity of these emission lines. To quantitatively understand and predict the performance of our Ho<sup>3+</sup>-based thermometer, we performed a systematic analysis of these various decay pathways and their temperature dependence.

First, we analyze the luminescence at low Ho<sup>3+</sup> concentration, at which the ion-to-ion distances in the crystal are large and energy-transfer interactions between ions are thus negligible. In this concentration regime ( $\leq 0.5\%$ ), relaxation from the blue- ( $^5F_3$ ), green- ( $^5F_4 + ^5S_2$ ), and red-emitting ( $^5F_5$ ) levels of Ho<sup>3+</sup> takes place only via radiative decay or multi-phonon relaxation, *i.e.* coupling to phonons of the host lattice to bridge the energy gap between levels. Phonon-mode occupations increase with increasing temperature, which results in faster multi-phonon relaxation. In the emission spectra of the 0.5%-doped Ho<sup>3+</sup> sample following excitation at 450 nm (Fig. 4.1c) we observe intense luminescence at 540 nm, indicating that multi-phonon relaxation to the green-emitting level followed by radiative decay is the dominant relaxation process (Fig. 4.1d).

The small energy gap  $\Delta E$  between the blue- and the green-emitting level ( $2000\text{ cm}^{-1}$ ) already suggested that emission of only 4–6 phonons in a hexagonal fluoride host can effectively bridge this gap.<sup>80,117,118</sup> Besides a weak blue emission, we notice a weak red emission that results from a combination of multi-phonon relaxation from the green- to the red-emitting level over a larger  $3000\text{ cm}^{-1}$  energy gap, cross-relaxation from the blue- to the red-emitting level, and red emission from the blue-emitting level to the first excited  $\text{Ho}^{3+}$  level  $^5\text{I}_7$  (Ref. 113; Fig. A4.2). Increasing temperature causes only a slight change of the luminescence spectrum (Fig. 4.1c), reflecting poor thermometer performance at low  $\text{Ho}^{3+}$  concentration. At the same time, this confirms that our thermometer is stable at elevated temperatures up to 873 K, as changes of the host crystal structure would affect emission peak positions and line shapes.

An increase of the  $\text{Ho}^{3+}$  concentration decreases the distance between ions and thus makes ion–ion interactions such as cross-relaxation more likely. The red color in the photographs of



**Figure 4.1.**  $\text{Ho}^{3+}$  as a thermometer based on cross-relaxation. **(a)** Photographs of the  $\text{Na}(\text{Y,Gd})\text{F}_4$  thermometer material doped with 12%-doped  $\text{Ho}^{3+}$  sample at various temperatures upon excitation with 358 nm. **(b)** Scanning electron micrographs of the 12%-doped  $\text{Ho}^{3+}$  sample. The scale bar corresponds to 10  $\mu\text{m}$ . **(c)** Emission spectra of the 0.5%-doped  $\text{Ho}^{3+}$  sample at various temperatures upon excitation with a 450 nm laser. The dominant green luminescence around 540 nm is due to the  $^5\text{S}_2 \rightarrow ^5\text{I}_8 + ^5\text{F}_4 \rightarrow ^5\text{I}_8$  transition. The blue emission around 485 nm is due to  $^5\text{F}_3 \rightarrow ^5\text{I}_8$  transition and the red emission centered around 640 nm is due to the overlapping  $^5\text{F}_5 \rightarrow ^5\text{I}_8 + ^5\text{F}_3 \rightarrow ^5\text{I}_7$  transitions. **(d)** Energy level diagram of a single  $\text{Ho}^{3+}$  ion.<sup>80</sup> The wavy arrows represent multi-phonon relaxation and the straight arrows correspond to radiative decay (see Fig. A4.1 for more details on the energy level structure of  $\text{Ho}^{3+}$  in  $\text{Na}(\text{Y,Gd})\text{F}_4$ , including the energy gaps between the different levels). **(e)** Emission spectra of the 12%-doped  $\text{Ho}^{3+}$  sample at various temperatures. **(f)** Energy level diagram of an excited and a ground-state  $\text{Ho}^{3+}$  ion. The dashed arrows represent cross-relaxation from the blue- or the green-emitting level of an excited  $\text{Ho}^{3+}$  ion, populating the  $^5\text{I}_7$  level in a nearby  $\text{Ho}^{3+}$  ion that was initially in the  $^5\text{I}_8$  ground state.

the 12%-doped Ho<sup>3+</sup> sample at room temperature (Fig. 4.1a) already hinted towards an efficient pathway to populate the red-emitting level in samples with higher Ho<sup>3+</sup> concentrations. Instead of a dominant green luminescence observed at low Ho<sup>3+</sup> concentrations (Fig. 4.1c), the emission spectra of the 12%-doped Ho<sup>3+</sup> sample (Fig. 4.1e) indeed show a strong red emission as compared to the blue and green emissions, at low temperature. Based on the energy level structure of Ho<sup>3+</sup> (Fig. 4.1f),<sup>119</sup> cross-relaxation from the blue- to the red-emitting level can explain the strong red emission. The drastic increase of the green luminescence at elevated temperatures is due to faster blue-to-green multi-phonon relaxation competing with temperature-independent cross-relaxation that feeds the red-emitting level, as we quantify in detail below (Fig. 4.2). Such a temperature-dependent change of the dominant decay pathways is beneficial for a high relative sensitivity of the thermometer. An increase of the Ho<sup>3+</sup> concentration from 12% to 30% further changes the luminescence and its response to temperature (Fig. A4.3). Overall, these observations clearly indicate that the Ho<sup>3+</sup> concentration is the key parameter to optimize the thermometer performance for the temperature range of interest.

Rational optimization of the Ho<sup>3+</sup> concentration for a specific temperature range requires a quantitative model that accounts for the efficiencies of radiative decay, multi-phonon relaxation, and cross-relaxation. Our first step in the development of such a model was to analyze the effect of temperature on the decay pathways in isolated ions, *i.e.* radiative decay and multi-phonon relaxation. Figs. 4.2a–4.2c show decay curves at a Ho<sup>3+</sup> concentration of 0.1% for the red-, the green-, and the blue-emitting level, respectively. The curves follow single-exponential decay at all temperatures. This is a clear indication for the absence of interactions between Ho<sup>3+</sup> ions, since this would lead to multi-exponential decay. The total decay rate  $k$  depends on the radiative rate  $k_r$ , which is assumed constant with temperature, and on the nonradiative contribution  $k_{nr}(1+n)^{\Delta E/\hbar\omega}$ , where  $k_{nr}$  is the zero-temperature multi-phonon relaxation rate and  $n$  is the occupation number of the involved phonons with effective energy  $\hbar\omega$  (Eq. 1.1 and Eq. 3.1).<sup>120–122</sup> In the inset of Fig. 4.2a, we fit the temperature dependence of the decay rates from the red-emitting level to Eq. A4.1. The fit matches the data well, yielding a fitted phonon energy of 360 cm<sup>-1</sup>, which corresponds well to the expected value for hexagonal fluoride lattices.<sup>117</sup> Notably, we included a decay measurement at 4 K in the fitting procedure to ensure reliable values for  $k_r$  and  $k_{nr}$ . Similar procedures yield models for radiative decay and multi-phonon relaxation from the green- and the blue-emitting levels (Figs. 4.2b–4.2c and Eqs. A4.2–A4.3).<sup>71,82,121</sup> Multi-phonon relaxation from the blue- and from the red-emitting level are both fast. Multi-phonon relaxation from the green-emitting level is slower, sets in at higher temperature, and shows a sharper onset than multi-phonon relaxation from the blue- and red-emitting level. This difference is caused by the larger energy gap that the green-emitting level must bridge in multi-phonon relaxation and explains the dominant green luminescence in samples with a low Ho<sup>3+</sup> concentration (Fig. 4.1c). Besides this qualitative observation, our analysis also enabled a quantitative description of the temperature-dependent decay pathways in individual Ho<sup>3+</sup> ions.

The next step is the quantification of cross-relaxation in samples with higher Ho<sup>3+</sup> concentration. In general, cross-relaxation is a type of Förster resonance energy transfer via electric dipole to

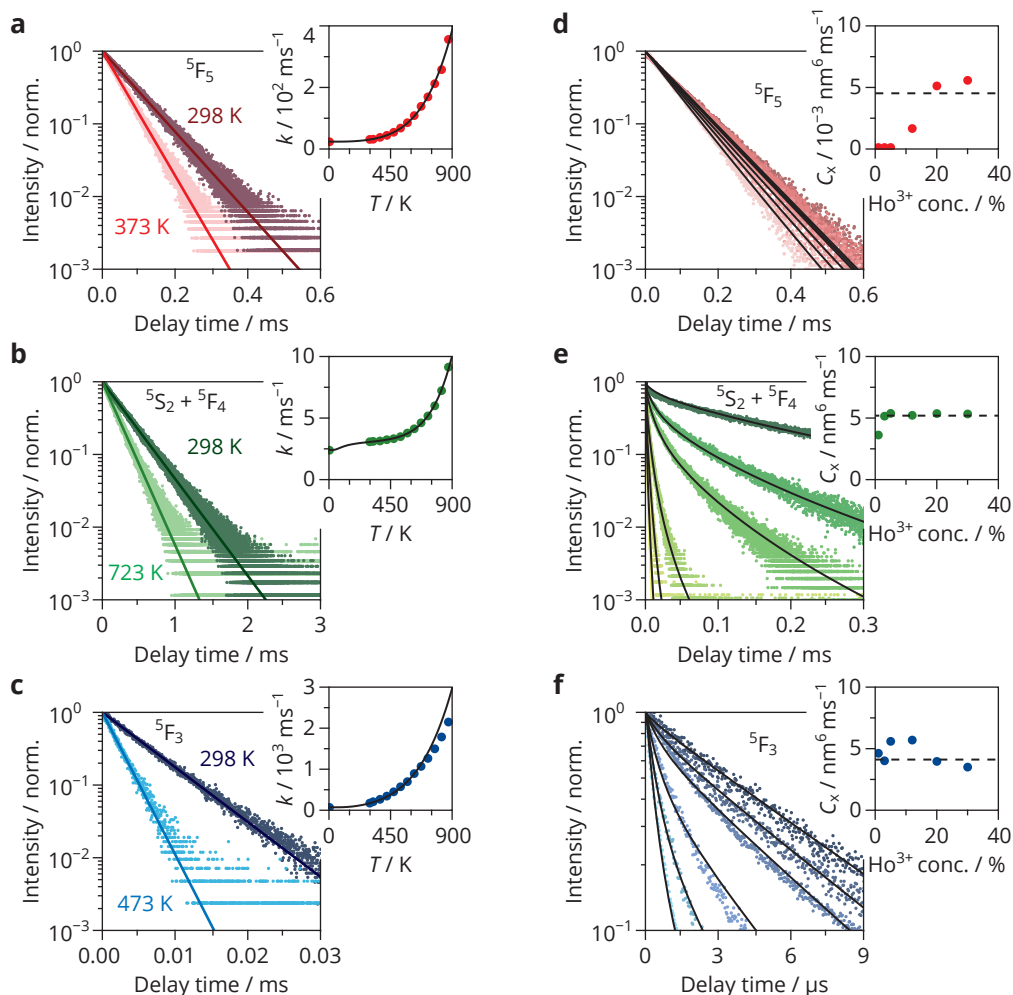


**Figure 4.2.** Quantification of radiative decay, multi-phonon relaxation, and cross-relaxation. **(a)** Decay curves of the red-emitting level ( $^5\text{F}_5$ ) measured at 645 nm upon resonant excitation at 638 nm of the 0.1%-doped  $\text{Ho}^{3+}$  sample, at two different temperatures chosen to illustrate the effect of multi-phonon relaxation. The solid lines are fits to a model of single-exponential decay. The inset shows the decay rates obtained from the fits at various temperatures. The black line is a fit to a model of temperature-dependent multi-phonon relaxation. **(b)** Same as in panel **(a)** but for the green-emitting level ( $^5\text{S}_2 + ^5\text{F}_4$ ) measured at 542 nm upon excitation at 535 nm. The black line is a fit to a model of temperature-dependent multi-phonon relaxation and thermal equilibrium between  $^5\text{S}_2$  and  $^5\text{F}_4$  populations. **(c)** Same as in panel **(b)** but for the blue-emitting level ( $^3\text{F}_3$ ) measured at 487 nm upon excitation at 447 nm and with thermal equilibrium between the  $^5\text{F}_3$ ,  $^5\text{F}_2$ , and  $^3\text{K}_8$  populations. **(d)** Decay curves of the red-emitting level measured at room temperature upon resonant excitation of samples with different  $\text{Ho}^{3+}$  concentrations (1%, 3%, 5%, 12%, 20%, and 30% with decreasing darkness of the color). The solid lines show the results of a global fit of all decay curves to a model of cross-relaxation providing one value for the “cross-relaxation strength”  $C_x$  (dashed line in the inset). The  $C_x$  values in the inset are the result of fits of the individual decay curves to the cross-relaxation model. **(e)** Same as in panel **(d)** but for the green-emitting level. **(f)** Same as in panel **(d)** but for the blue-emitting level.

electric dipole coupling. The cross-relaxation rate  $k_x$  scales with the distance  $R$  between an excited Ho<sup>3+</sup> donor ion and a ground-state Ho<sup>3+</sup> acceptor ion as  $k_x = C_x R^{-6}$ . Herein  $C_x$  is the “cross-relaxation strength” that depends, among other parameters, on the spectral overlap between the donor and acceptor transitions.<sup>120</sup> Figs. 4.2d–4.2f show the effect of cross-relaxation on the decay dynamics from the red-, green-, and blue-emitting levels, respectively. At a fixed temperature (298 K), decay becomes faster with increasing Ho<sup>3+</sup> concentration. The decay curves of the green- and blue-emitting levels are multi-exponential at high concentrations, which is a signature of ion–ion interactions over a distribution of distances  $R$ . While these observations are a clear demonstration of cross-relaxation, the strength of cross-relaxation is different for the three levels. Specifically, the decay of the green- and blue-emitting levels (Figs. 4.2e–4.2f) accelerates much more strongly with increasing Ho<sup>3+</sup> concentration than that of the red-emitting level (Fig. 4.2d). Close resonance of the <sup>5</sup>I<sub>8</sub> → <sup>5</sup>I<sub>7</sub> acceptor transition with donor transitions from the green- and blue-emitting levels (Fig. 4.1f) explains this observation. No such resonance is present for cross-relaxation from the red emitting level resulting in a  $\sim 10^3$  times lower value of  $C_x$ .

To model cross-relaxation quantitatively, we explicitly account for the distribution of discrete ion-to-ion distances  $R$  that occur when Ho<sup>3+</sup> ions randomly occupy lattice sites of the host crystal at a certain doping concentration using our shell model (Eqs. A4.4–A4.5 and Fig. A4.4).<sup>27,68,123</sup> The only free parameter in our model is the cross-relaxation strength  $C_x$ , the value of which we determine by fitting the experimental data for varying Ho<sup>3+</sup> concentration (Figs. 4.2d–4.2f). The photoluminescence decay curves of the blue-emitting level contain a weak slow component that we excluded from the fitting procedure (Fig. A4.5). For our analysis, we first fitted the individual curves separately, which resulted in a separate estimate for  $C_x$  for each Ho<sup>3+</sup> concentration. In the insets of Figs. 4.2d–4.2f, we compare these separate estimates for  $C_x$  with a global fitting procedure that includes all decay curves at different Ho<sup>3+</sup> concentrations, yielding a single value for  $C_x$ . The solid black lines through the decay curves show the results of the global fits. Our model captures how cross-relaxation causes faster decay for increasing Ho<sup>3+</sup> concentration. A similar analysis at elevated temperatures indicates that the rates of cross-relaxation from the three levels are insensitive to temperature (Fig. A4.6). Therefore, we use the  $C_x$  values from the global fits to describe cross-relaxation interactions between Ho<sup>3+</sup> ions at all temperatures.

Our cross-relaxation thermometer relies on the effect of temperature on the blue, the green, and the red luminescence intensities (Fig 4.3a and Fig. A4.7). The analysis of the decay dynamics showed that the blue-emitting level undergoes fast depopulation by two competing processes. One of them is multi-phonon relaxation to the green-emitting level, which is sensitive to temperature. The other process is cross-relaxation to the red-emitting level, which depends on the Ho<sup>3+</sup> concentration. The green-emitting level is relatively unaffected by multi-phonon relaxation but experiences fast decay via cross-relaxation to the <sup>5</sup>I<sub>4</sub> level.<sup>119</sup> However, this does not influence the population of the blue- or the red-emitting level. The red-emitting level is only weakly affected by multi-phonon relaxation and cross-relaxation. Competition between multi-phonon relaxation and cross-relaxation from the blue-emitting level is thus the most important contribution to color changes with temperature and Ho<sup>3+</sup> concentration (Fig. A4.8). This determines the working me-

chanism of our thermometer.

To evaluate the performance of our thermometer we first construct a model that calculates the relative emission intensities of the blue-, green-, and red-emitting level. This model takes all relevant decay pathways into account (Fig. 4.3a) to determine the efficiencies of radiative decay and combines these with the branching ratios of the transitions to the ground state ( $^5I_8$ ). These efficiencies depend on the rates of radiative decay, temperature-dependent multi-phonon relaxation, and the  $\text{Ho}^{3+}$ -concentration-dependent cross-relaxation. We obtained these parameters, which we need as an input for our model, from the analysis of Fig. 4.2 (Eqs. A4.6–A4.12).<sup>124</sup> In this way, we are able to predict the emission color of our thermometer for any arbitrary temperature and

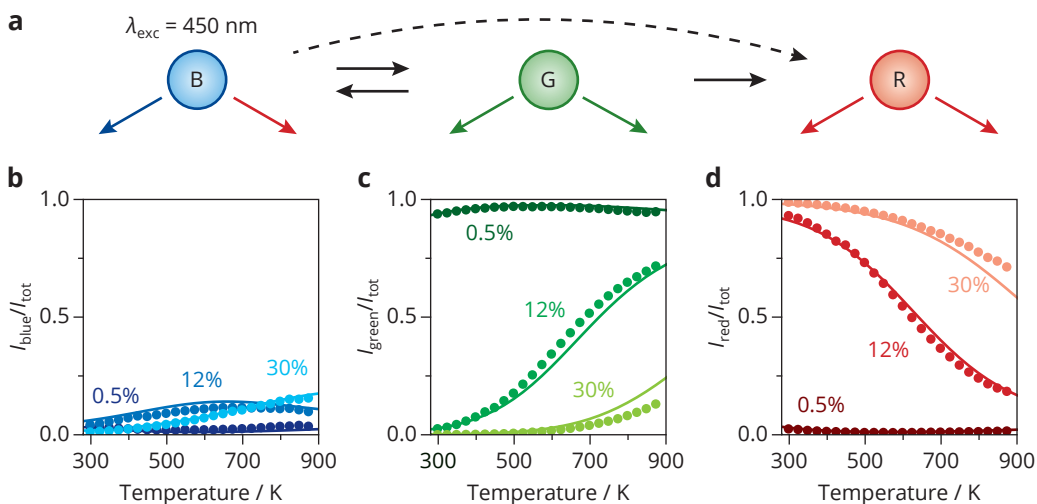


**Figure 4.3.** Comparison of the calculated and the experimental emission intensities. (a) A simplified schematic of the relevant feeding mechanisms to calculate the efficiency of radiative decay (solid colored arrows) from  $^5F_3$  (B),  $^5S_2 + ^5F_4$  (G), and  $^5F_5$  (R) levels. Multi-phonon relaxation (solid black arrow) and cross-relaxation (dashed black arrow) connect these levels (see Fig. A4.7 for the complete scheme). Comparison of the experimentally measured (dots) and the calculated (lines) relative intensities of (b) the blue, (c) the green, and (d) the red emissions as a function of temperature for three different  $\text{Ho}^{3+}$  concentrations. The experimental relative intensities were determined by integrating the emission spectra between 460–500 nm, 515–575 nm, and 625–670 nm, respectively. (e) The CIE 1931 diagram plotted with the experimentally measured (dots) and the calculated (lines) color coordinates at various temperatures for three different  $\text{Ho}^{3+}$  concentrations.

Ho<sup>3+</sup> concentration.

As a test of our model, Figs 4.3b–4.3e compare the calculated blue, green, and red emission intensities with the experimentally measured intensities. We observe an overall match between the calculated and the measured intensities, which validates this model as a basis for quantitative thermometer evaluation. As observed in the experimental spectra (Figs. 4.1c, 4.1e, and A4.3), the blue intensity is weak over the whole temperature range and for all concentrations due to strong competition of multi-phonon relaxation and cross-relaxation with radiative decay. The effect of temperature and concentration is more pronounced for the green and the red intensity—they even follow opposite trends. At low temperatures, high Ho<sup>3+</sup> concentrations cause a weak green emission and a strong red emission, because cross-relaxation dominates over multi-phonon relaxation within the blue level. Elevated temperatures compensate this effect, since they enhance multi-phonon relaxation leading to an increase of the green intensity and a decrease of the red intensity. We attribute the small difference between the measured and calculated intensities for the 30%-doped Ho<sup>3+</sup> sample to an overestimation of multi-phonon relaxation from the blue-emitting level in the model (Fig. 4.2c). In addition, thermal excitation of the <sup>5</sup>I<sub>4</sub> population might also lead to an increase of the red emission. Using the sensitivity curves of the human eye, we convert each combination of red, green, and blue intensity to a coordinate in the CIE diagram (Fig. 4.3e), which shows a similar match between model and experiment.<sup>125</sup>

Based on the models of the blue, green, and red intensities (Fig. 4.3), we can calculate the relative sensitivities of our thermometer as a function of temperature and Ho<sup>3+</sup> concentration. The *LIR* between the red and the green emission has the largest potential for achieving a high sensitivity, since these two emissions show a strong and opposite temperature dependence at higher Ho<sup>3+</sup> concentrations (Figs. 4.3c–4.3d). The potential of the red-to-green *LIR* becomes evident when we plot it against temperature (Fig. 4.4a). For high Ho<sup>3+</sup> concentrations, this *LIR* changes by approximately two orders of magnitude in the evaluated temperature range, corresponding to a relative sensitivity (Eq. 1.3) of  $S_r = 1.0\% \text{ K}^{-1}$  at 300 K.<sup>49,109</sup> Comparison of the calculated and the experimental ratios again confirms that our model predicts the effect of temperature and dopant concentration well with only a limited number of input parameters.

Fig. 4.4b shows that our Ho<sup>3+</sup>-based cross-relaxation thermometers offer the highest relative sensitivities at high Ho<sup>3+</sup> concentrations. In fact, we achieve a superior relative sensitivity over a much wider temperature range compared to the typical Boltzmann thermometer  $\beta\text{-NaYF}_4\text{:Er}^{3+}$ .<sup>43,126</sup> Arguably more importantly than a high sensitivity, reliable temperature measurements require high precision, *i.e.* low temperature uncertainty (Eq. 1.2 and Eq. A4.13–A4.14).<sup>102</sup> Fig. 4.4c demonstrates how the Ho<sup>3+</sup> concentration affects the temperature uncertainty. While the relative sensitivity consistently increases with increasing Ho<sup>3+</sup> concentration (Fig. 4.4b), the lowest temperature uncertainty is achieved at different Ho<sup>3+</sup> concentrations depending on the temperature. The trend in temperature uncertainty of our cross-relaxation thermometers becomes clearer in the color map of Fig. 4.4d. This figure can serve as a clear guide to achieve an optimized performance of the Ho<sup>3+</sup>-based luminescent thermometer over a range of 300–

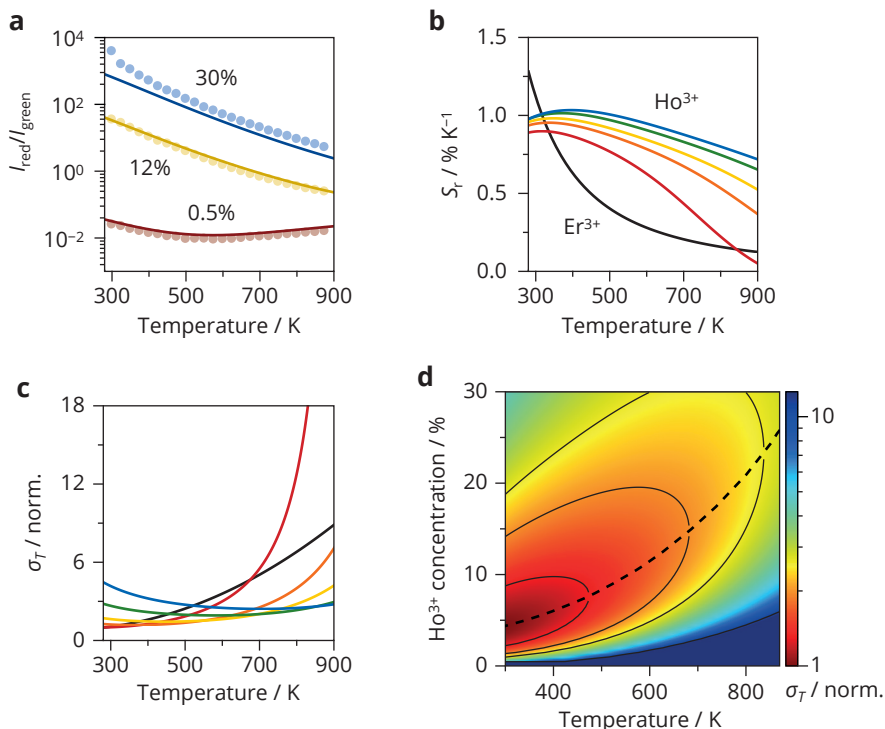


**Figure 4.4.** Evaluating thermometer performance. **(a)** Temperature dependence of the experimentally measured (dots) and the calculated (lines) red-to-green *LIR* for different concentrations. The experimental red-to-green *LIR* was determined using the same integration boundaries as in Figs. 4.3c–4.3d. **(b)** Calculated relative sensitivities for a  $\text{Ho}^{3+}$  concentration of 4% (red), 8% (orange), 12% (yellow), 20% (green), and 30% (blue), as a function of temperature. The black solid line is the relative sensitivity of the widely used Boltzmann thermometer, based on the  $^4\text{S}_{3/2}$  and  $^2\text{H}_{11/2}$  levels of  $\text{Er}^{3+}$  ions in the  $\beta\text{-NaYF}_4$  host. **(c)** Calculated temperature uncertainties ( $\sigma_T$ ). The same color scheme applies as in **(b)**. All  $\sigma_T$  values were normalized to the minimum of the curve referring to 4%  $\text{Ho}^{3+}$ . While comparing thermometers with different  $\text{Ho}^{3+}$  concentration, we account for the higher emission intensity per amount of thermometer material at higher  $\text{Ho}^{3+}$  concentrations (Eq. A4.14). **(d)** 3D plot of the normalized temperature uncertainty for the  $\text{Ho}^{3+}$  fractions and temperatures within the range of this study. The dashed line traces the minimum achievable  $\sigma_T$  as a function of temperature. The contour lines correspond to normalized  $\sigma_T$  values of 1.3, 1.9, 2.5, and 10.

873 K. Around 300 K, the lowest temperature uncertainties are achieved at a  $\text{Ho}^{3+}$  concentration of 4%. At higher temperatures, a minimum temperature uncertainty requires higher  $\text{Ho}^{3+}$  concentrations, increasing by approximately 1% for every 30-K step in temperature. Importantly, by choosing the optimal  $\text{Ho}^{3+}$  concentration for the temperature regime of interest, our cross-relaxation thermometers can cover the temperature range between 300 and 900 K with a consistently low temperature uncertainty, increasing by no more than a factor 2.5 over the entire range. This is a clear advantage of our temperature-sensing concept compared to Boltzmann thermometers like  $\beta\text{-NaYF}_4\text{:Er}^{3+}$ , for which the temperature uncertainty increases by as much as a factor 8.5 over



this temperature range.

### 4.3 Conclusions

Our results have revealed that quantitative modelling of the decay pathways is a unique and powerful tool to evaluate the performance of luminescent thermometers based on cross-relaxation. An understanding of their concentration-dependent luminescent properties helps to adjust the design of such thermometers to the temperature regime of interest for minimum temperature uncertainty. While this Chapter focused on cross-relaxation between Ho<sup>3+</sup>, our type of modelling provides a universal tool to quantify, predict, and tune the performance of many other types of energy-transfer thermometers. This enables the rational design of new Ln<sup>3+</sup>-based thermometers, but it is also indispensable in the optimization of existing energy-transfer couples.

### 4.4 Methods

**Chemicals.** YF<sub>3</sub> (99.99%), HoF<sub>3</sub> (99.9%), and GdF<sub>3</sub> (99.99%) were purchased from ChemPUR. NaF (≥ 98%) and NH<sub>4</sub>F (≥ 98%) were purchased from Sigma-Aldrich. All chemicals were dried in the oven and used without further purification.

**Sample preparation.** The solid-state procedure of Aarts *et al.*<sup>115</sup> was adjusted for the synthesis of NaY<sub>0.75-x</sub>Gd<sub>0.25</sub>Ho<sub>x</sub>F<sub>4</sub>. As starting materials, 0.25 eq. GdF<sub>3</sub>, 0.75-x eq. YF<sub>3</sub>, x eq. HoF<sub>3</sub>, 1 eq. NH<sub>4</sub>F, and 1.2 eq. NaF were mixed with a pestle and mortar. The ground mixture was added to an alumina crucible and placed in a tube oven, which was fired in N<sub>2</sub> atmosphere in an excess of NH<sub>4</sub>F. The mixture was first heated to 300 °C for 2 hours followed by an additional 10 hours at 600 °C. After cooling the samples to room temperature, the powders were crushed.

**Structural characterization.** XRD patterns were recorded with a Philips PW1700 X-ray powder diffractometer using Cu K<sub>α1</sub> (λ = 1.5418 Å) radiation. The measurement range in terms of 2θ was 10° to 80° with a step size of 0.02°. Using the XRD patterns, the sole presence of the hexagonal phase in the samples was confirmed and the lattice parameters (*a* = *b* = 0.5973 nm, *c* = 0.3549 nm) were extracted (Fig. 4.5). Only minor variations in the lattice parameters were observed for samples with different Ho<sup>3+</sup> concentrations. Scanning electron microscopy images were obtained using a Phenom ProX microscope with an acceleration voltage of 10 kV.

**Spectroscopy experiments.** Emission spectra were measured with an Edinburgh Instruments FLS920 spectrophotometer equipped with TMS300 monochromators, a R928 photomultiplier tube (PMT), and a 450 nm CW laser (1 W) or a Xe lamp (450 W) as excitation source. All emission spectra were corrected for the spectral response of the detector, monochromator, and long-

pass filter. Photoluminescence decay curves were recorded using an Ekspla NT342B OPO laser (10 Hz), a Triax 550 monochromator, and a Hamamatsu R928 PMT. Depending on the decay rate, the average count rate was kept at 1–50 counts per pulse to prevent detector saturation. Heating and cooling of the samples was achieved with a Linkam THMS600 microscope stage and a liquid He cooled cryostat, respectively.

## 4.5 Appendix

**Analysis of the decay dynamics.** All luminescence decay curves from the 0.1%-doped  $\text{Ho}^{3+}$  samples were fitted to a model of single-exponential decay to obtain decay rates at 4 K and 300–873 K. The experimental background was included in this model. The temperature dependence of the decay rates of the red level (R,  $^5\text{F}_5$ ), blue level (B,  $^5\text{F}_3$ ), and green level (G,  $^5\text{S}_2 + ^5\text{F}_4$ ) was fitted to three different multi-phonon relaxation models assuming coupling to a single effective phonon mode.

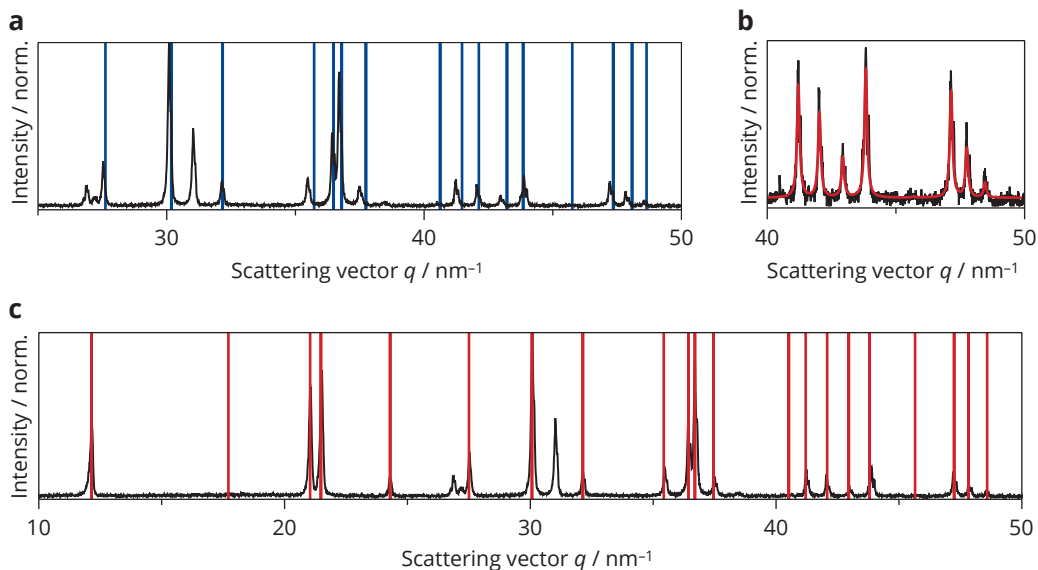


**Figure 4.5.** XRD patterns of  $\beta\text{-NaY}_{0.72}\text{Gd}_{0.25}\text{Ho}_{0.03}\text{F}_4$ . **(a)** The blue vertical lines mark the positions of the Bragg reflections from a reference pattern of  $\beta\text{-NaYF}_4$ . The significant deviation between the reflections in the reference and the measured pattern indicate that the lattice parameters  $a$  and  $c$  in this case are different from  $\beta\text{-NaYF}_4$ . We want to plug the actual lattice parameters  $a$  and  $c$  into our shell model for energy transfer. **(b)** The red line shows a fit of the measured diffraction pattern to a model that relates the reflections in a diffraction pattern to the lattice parameters of a hexagonal crystal structure. The reflections between  $40 \text{ nm}^{-1}$  and  $50 \text{ nm}^{-1}$  are used for fitting, since their positions show the strongest dependence on the crystal structure. **(c)** The red vertical lines mark the peak positions that were calculated from the fitted lattice parameters of  $a = 0.5973 \text{ nm}$ , and  $c = 0.3549 \text{ nm}$  found in **(b)**.

$$k_R(T) = k_{r-R} + k_{nr-R}[1 + n(T)]^{\Delta E_R/\hbar\omega_{\text{vib}}}, \quad (\text{A4.1})$$

$$k_B(T) = \frac{g_{B1} \left\{ k_{r-B} + k_{nr-B} \left( [1 + n(T)]^{\Delta E_{B1}/\hbar\omega_{\text{vib}}} + \frac{g_{B1}}{g_{G2}} n(T)^{\Delta E_{B1}/\hbar\omega_{\text{vib}}} \right) \right\}}{g_{B1} + g_{B2} e^{-\Delta E_{B2}/k_B T} + g_{B3} e^{-(\Delta E_{B2} + \Delta E_{B3})/k_B T}}, \quad (\text{A4.2})$$

$$k_G(T) = \frac{g_{G1} (k_{r-G1} + k_{nr-G} [1 + n(T)]^{\Delta E_{G1}/\hbar\omega_{\text{vib}}}) + g_{G2} k_{r-G2} e^{-\Delta E_{G2}/k_B T} + g_{B1} k_{r-B} e^{-(\Delta E_{G2} + \Delta E_{B1})/k_B T}}{g_{G1} + g_{G2} e^{-\Delta E_{G2}/k_B T} + g_{B1} e^{-(\Delta E_{G2} + \Delta E_{B1})/k_B T}}. \quad (\text{A4.3})$$

In the above equations,  $k_{r-R,G,B}$  is the radiative decay rate from the red, green, or blue level. Following similar definitions,  $k_{nr-R,G,B}$  is the zero-temperature rate of multi-phonon relaxation from these levels to the level below. The Boltzmann constant is  $k_B$  and  $T$  is the absolute temperature. The gap between energy level  $i$  and the first lower lying level is defined as  $\Delta E_i$ . Each  $g_i$  term denotes the degeneracies of the level  $i$ , where  $i = R, G1, G2, B1, B2,$  or  $B3$  for  ${}^5F_5, {}^5S_2, {}^5F_4, {}^5F_3, {}^5F_2,$  or  ${}^3K_8$ , respectively (Fig. A4.1). In all fitting and color-modelling procedures,  $g_i, \Delta E_{B2}, \Delta E_{B3}, \Delta E_{G2},$  and  $\Delta E_R$  were fixed.<sup>80</sup>

For decay from the red level, we can use the simplest model (Eq. A4.1), since thermal excitation from the red level to the next-higher-energy level ( ${}^5S_2$ ) is negligible because of the large energy gap ( $3000 \text{ cm}^{-1}$ ).<sup>80,118</sup> Following the same reasoning, we neglect thermal equilibrium between  ${}^5I_4$  and  ${}^5F_5$ . The only nonradiative decay pathways from the red-emitting level are thus spontaneous and stimulated phonon emission, for which the  $[1 + n(T)]^{\Delta E_R/\hbar\omega_{\text{vib}}}$  term accounts. The values that we find from this procedure are  $k_{r-R} = 1.6 \text{ ms}^{-1}$ ,  $k_{nr-R} = 3.5 \text{ ms}^{-1}$ , and  $\hbar\omega_{\text{vib}} = 360 \text{ cm}^{-1}$ . The latter is fixed in following fitting procedures.

Unlike the red level, decay from the blue level is influenced by occupation of higher lying

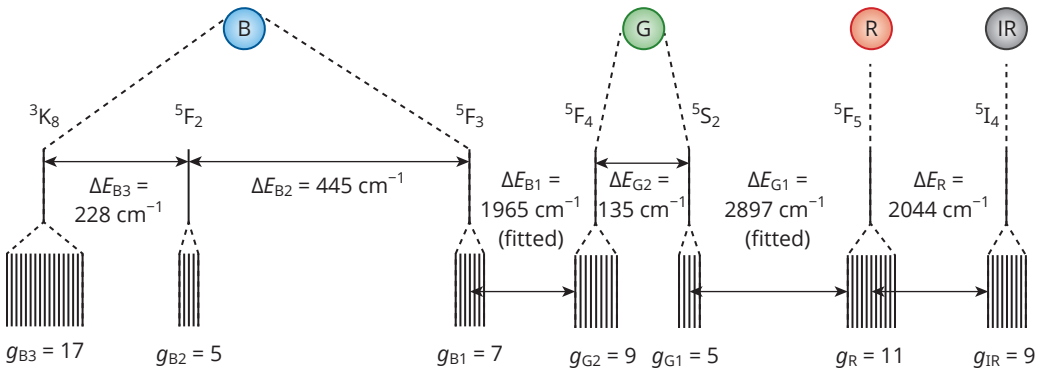


**Figure A4.1.** Energy level diagram of Ho<sup>3+</sup> that defines the mathematical notations of the relevant parameters and gives the values of the fixed parameters. The values of  $\Delta E_{G1}$  and  $\Delta E_{B1}$  are obtained using Eqs. A4.2–A4.3.

levels ( ${}^5F_2$  and  ${}^3K_8$ ). According to the work of Sytsma *et al.*, the decay rate from  ${}^5F_3$  then becomes a Boltzmann-weighted average of the decay rates from  ${}^5F_3$ ,  ${}^5F_2$ , and  ${}^3K_8$ .<sup>121</sup> Decay from these levels is dominated by multi-phonon relaxation from  ${}^5F_3$ , so we approximate that the decay rate from  ${}^5F_2$  and  ${}^3K_8$  are negligible (Eq. A4.2). We also include thermal equilibrium between  ${}^5F_3$  and  ${}^5F_4$ . Following the rate-equation solution of two thermally coupled excited levels with similar radiative decay rates, we add a stimulated phonon absorption term  $n(T)^{\Delta E_B/\hbar\omega_{\text{vib}}}$  accounting for thermal excitation from  ${}^5F_4$  to  ${}^5F_3$ .<sup>71,82</sup> The effect of this thermal equilibrium is only minor on the decay rate of  ${}^5F_3$ . However, these subtle differences are important for correct color modeling, since competition between multi-phonon relaxation and cross-relaxation from this level

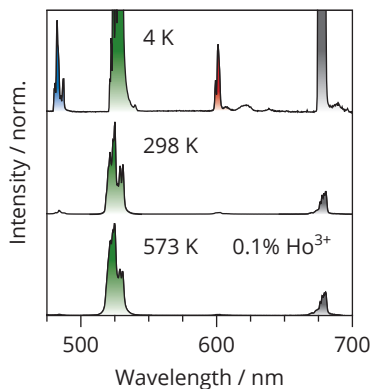


**Figure A4.2.** Emission spectra of the 0.1%-doped  $\text{Ho}^{3+}$  sample at various temperatures upon excitation at 450 nm. Division of the integrated intensity of the blue- and red-shaded area by the total integral for the measurement at 4 K provides the ratio between radiative decay and multi-phonon relaxation from the blue level. The red integral was corrected for emission from the  ${}^5F_5$  level following multi-phonon relaxation from the green level. Multiplication of this ratio with the decay rate of the blue level at 4 K ( $69.6 \text{ ms}^{-1}$ ) gives the radiative decay rate from the blue level ( $k_{r-B} = 4.17 \text{ ms}^{-1}$ ). Division of the integrated intensity of the blue-shaded area by the sum of the blue and red area for the measurement at 4 K provides the branching ratios of blue emission from the blue level ( $\beta_{B-B} = 0.65$ ). Similar analyses give the branching ratio of red emission from the blue level ( $\beta_{B-R} = 0.35$ ) and the branching ratio of green emission from the green level ( $\beta_{G-G} = 0.85$ ), which showed insensitivity towards temperature in the range 298–873 K. A value of  $\beta_{R-R} = 0.80$  was estimated based on a literature value for a similar host material.<sup>118</sup> At 298 K and 0.1%  $\text{Ho}^{3+}$ , we calculate that 77% of the red emission originates from the  ${}^5F_3$  level and only 23% from the  ${}^5F_5$  level.

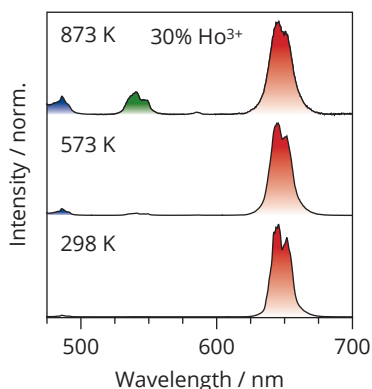


**Figure A4.3.** Emission spectra of the 30%-doped  $\text{Ho}^{3+}$  sample at various temperatures upon excitation with a 450-nm laser.

predominantly determines the emission color. Fitting the temperature dependence of the blue decay rates to Eq. A4.2 is performed with fixed  $k_{r-B}$  determined from the emission spectrum at 4 K ( $k_{r-B} = 4.17 \text{ ms}^{-1}$ , Fig. A4.2). The values that we find from this procedure are  $k_{nr-B} = 68.6 \text{ ms}^{-1}$ , and  $\Delta E_{B1} = 1965 \text{ cm}^{-1}$ . The latter is fixed in following fitting procedures.

The decay rate from the green level is affected by the thermal populations of the two close energy levels  $^5S_2$  and  $^5F_4$ , as well as thermal occupation of the blue-emitting  $^5F_3$  level at higher temperatures. Multi-phonon relaxation to the red-emitting  $^5F_5$  level is relatively slow, so the total decay rate is in large part determined by the Boltzmann-weighted radiative decay rate. Our fitting function for the decay rate from the green-emitting level, Eq. A4.3, explicitly accounts for this Boltzmann weighting of the radiative decay rates of the  $^5S_2$  ( $k_{r-G1}$ ),  $^5F_4$  ( $k_{r-G2}$ ), and  $^5F_3$  ( $k_{r-B}$ ) levels. The values that we find from this procedure are  $k_{r-G1} = 2.4 \text{ ms}^{-1}$ ,  $k_{r-G2} = 3.7 \text{ ms}^{-1}$ ,  $k_{nr-G} = 2.3 \times 10^{-2} \text{ ms}^{-1}$ , and  $\Delta E_{G1} = 2897 \text{ cm}^{-1}$ .

**Cross-Relaxation.** To analyze cross-relaxation between Ho<sup>3+</sup> ions in the hexagonal  $\beta$ -NaREF<sub>4</sub> lattice ( $RE = Y, Gd, Ho$ ), we can use our previously presented shell model that separates decay processes in isolated ions [described as exponential contribution  $e^{-k_{x-R,G,B}(T)t}$  to the decay] from decay due to interactions between ion [described as a non-exponential contribution  $X(t)$ ].

$$I(t) = X(C_{x-R,G,B}, \varphi, t) e^{-k_{x-R,G,B}(T)t}. \quad (\text{A4.4})$$

Here,  $X(C_{x-R,G,B}, \varphi, t)$  accounts for the distribution of cross-relaxation rates ( $k_{x-R,G,B}$ ) between a central donor Ho<sup>3+</sup> ion and all nearby acceptor Ho<sup>3+</sup> ions for the red-, green-, or blue-emitting level. These rates depend on the distance  $R$  between an excited Ho<sup>3+</sup> donor ion and a ground-state Ho<sup>3+</sup> acceptor ion as  $k_{x-R,G,B} = C_{x-R,G,B} R^{-6}$ . Here,  $C_{x-R,G,B}$  is the ‘‘cross-relaxation strength’’, which is a constant independent of the fraction of Ho<sup>3+</sup> dopants ( $\varphi$ ). Before quantifying  $C_x$ , we first calculate the distances between a central donor and all rare-earth cationic sites using the crystal structure and lattice parameters of NaY<sub>0.75-x</sub>Gd<sub>0.25</sub>Ho<sub>x</sub>F<sub>4</sub> obtained from the XRD analysis in Fig. 4.5.

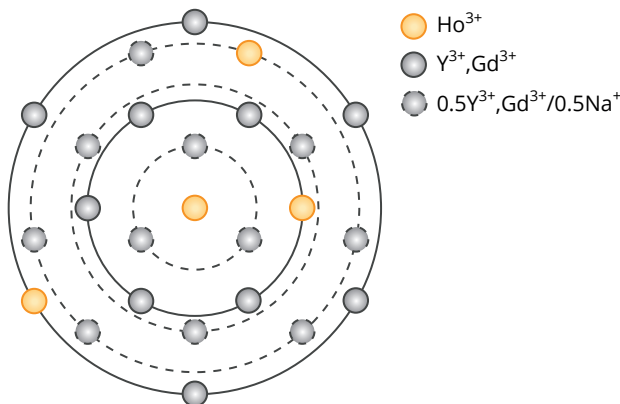


**Figure A4.4.** 2D representation of the hexagonal  $\beta$ -Na(Y,Gd)F<sub>4</sub> lattice. Multiple cationic sites surround a central Ho<sup>3+</sup> ion with equal interion distances. Occupation of Y<sup>3+</sup> and Gd<sup>3+</sup> sites by Ho<sup>3+</sup> ions depends on the Ho<sup>3+</sup> concentration.

The periodic nature of this lattice makes only a discrete set of donor–acceptor distances possible, forming a shell-like structure (Fig. A4.4). Assuming a statistical distribution of dopant ions, the expression for  $X(C_{x-R,G,B}, \varphi, t)$  can be written as:<sup>68</sup>

$$X(C_{x-R,G,B}, \varphi, t) = \frac{2}{3} \prod_i \left(1 - \varphi + \varphi e^{-C_{x-R,G,B}t/R_i^6}\right)^{n_i} \times \prod_i \left(1 - \varphi/2 + \varphi/2 e^{-C_{x-R,G,B}t/R_i^{*6}}\right)^{n_i^*} + \frac{1}{3} \prod_i \left(1 - \varphi/2 + \varphi/2 e^{-C_{x-R,G,B}t/R_i^6}\right)^{n_i} \times \prod_i \left(1 - \varphi + \varphi e^{-C_{x-R,G,B}t/R_i^{*6}}\right)^{n_i^*}, \quad (\text{A4.5})$$

where  $n_i$  is the number of acceptor ions in shell  $i$  surrounding a donor ion with a distance  $R_i$ . Half of the unit cells in a hexagonal  $\beta$ -NaREF<sub>4</sub> crystal contains one RE site that is filled by Na<sup>+</sup>. The expression for  $X(C_{x-R,G,B}, \varphi, t)$  includes four terms to account for this complex structure.

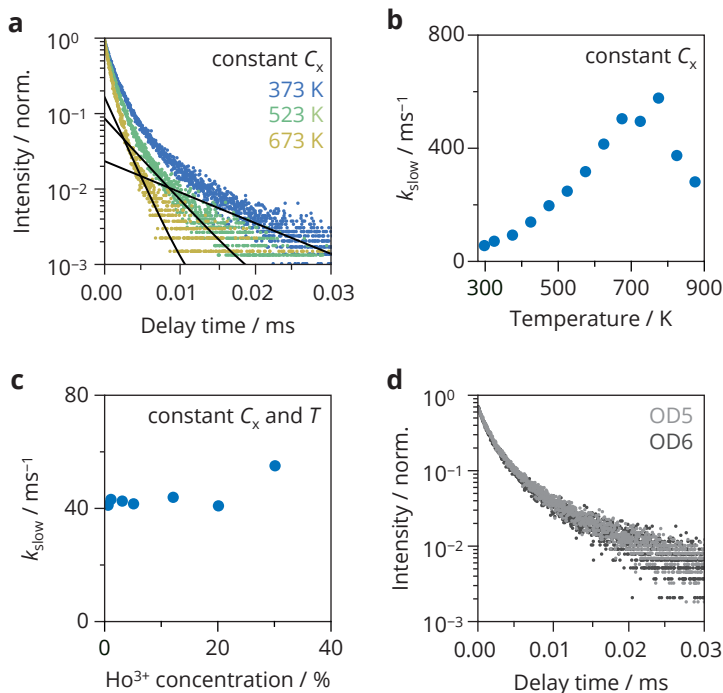


**Figure A4.5.** (a) Luminescence decay curves from the blue level in the 12%-doped Ho<sup>3+</sup> sample for various temperatures. The data is fitted to the cross-relaxation model with an additional decay component included and with a constant cross-relaxation strength obtained by the global fitting procedure at 298 K. The solid black line shows the fit of the additional decay component. (b) The decay rates of the additional component for the analysis of (a). (c) The decay rates of the additional component for various Ho<sup>3+</sup> concentrations at room temperature. (d) Decay curves from the blue level in the 12%-doped Ho<sup>3+</sup> sample for different excitation powers. Neutral density filters with an optical density (OD) of 5 and 6 provided control over the excitation power.

With a global-fit procedure of Eq. A4.4 to the decay curves measured at constant temperature (298 K) and various concentrations (0.1%, 1%, 3%, 5%, 12%, 20%, and 30%), we extracted the values of  $C_{x-R,G,B}$ . The  $R_i^{-6}$  dependence of the cross-relaxation rate allowed us to only include acceptor ions within 2.2 nm from the donor ion. The intrinsic single-ion decay rates  $k_{R,G,B}(T)$  were first fixed based on a single-exponential fit to the decay curves of the 0.1%-doped sample. The decay curves of the blue level contain a slow component (Fig. A4.5), which we excluded from the fitting procedure. At the end of this section, we will discuss the possible origin of the slow component in more detail. Besides an amplitude and a background level (only for the red and the green level) for each decay curve, the only free variable in our global fit procedure was  $C_{x-R,G,B}$ , since the dopant fraction and the distances between the donor and the rare-earth cations are known. In addition to the global-fit procedure, we fitted each individual decay curve to Eq. A4.4 and obtained independent values for  $C_{x-R,G,B}$  from each decay curve. The comparison between global fit (dashed line) and individual fits (points) is included in Figs. 4.2d–4.2f as insets. Finally, an effect of temperature

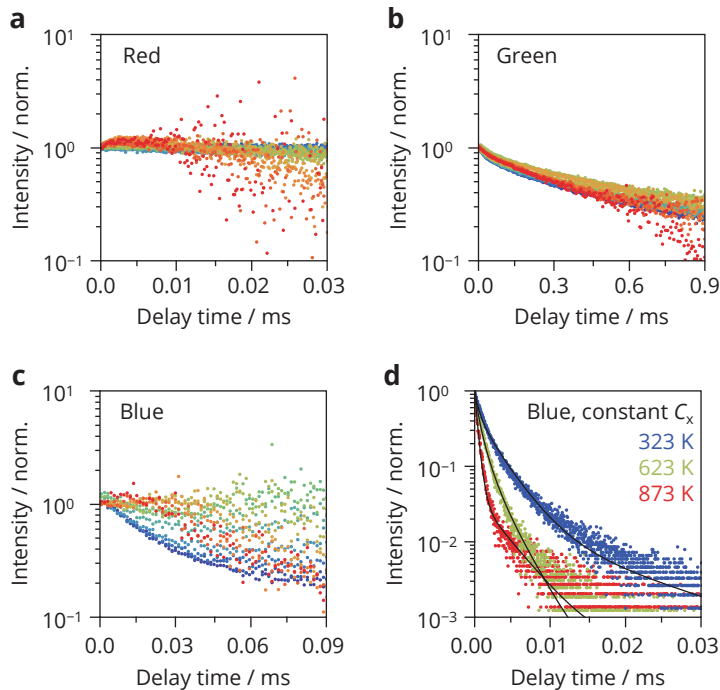


**Figure A4.6.** (a) Division of the luminescence decay from the red level for the 12%-doped  $\text{Ho}^{3+}$  sample by the decay at 0.1%  $\text{Ho}^{3+}$  for equal temperatures shows the contribution of cross-relaxation to the total decay. Plotting this for temperatures between 293 K (blue) and 873 K (red) reveals the absence of a temperature-dependent effect on cross-relaxation. (b) Same as in (a) but for the green level and the 1%-doped sample. (c) Same as in (a) but for the blue level. From this analysis, the effect of temperature on cross-relaxation is less evident for the blue level due to the additional decay component. (d) Fitting the decay to the cross-relaxation model with a constant  $C_x$  indicates that temperature has no effect on cross-relaxation from the blue level.

on cross-relaxation was excluded by the analysis in Fig. A4.6.

The slow component in the decay curves of the blue level can have multiple origins. First, we analyzed the temperature dependence of this slow component (Figs. A4.5a–A4.5b) and observed an increase of its rate with temperature. Geitenbeek *et al.* also observed biexponential decay from the  $^5D_1$  level of  $\text{Eu}^{3+}$  in  $\text{NaYF}_4$ . Here, the fast component was ascribed to a combination of radiative decay and multi-phonon relaxation to the lower-lying  $^5D_0$  level, while the slow component was due to thermal back-excitation from  $^5D_0$ . The slow decay component of the blue emission may have a similar origin. Another possible origin of the slow component would be upconversion excitation followed by slow nonradiative relaxation from a level above the blue level. This would cause a change in the decay dynamics for different  $\text{Ho}^{3+}$  concentrations or excitation powers, but we do not observe this in Figs. A4.5c–A4.5d.

**Color modelling.** A model based on the decay rates was constructed to calculate the efficiencies of blue, green, and red emission under 450 nm excitation (Fig. A4.7). For the red- and blue-emitting levels, the internal efficiencies of radiative decay ( $\eta_{r-i}$ ), multi-phonon relaxation ( $\eta_{nr-i}$ ), and cross-relaxation ( $\eta_{x-i}$ ) are easily calculated by integrating the theoretical decay curves provided by our model:<sup>124</sup>

$$\begin{aligned}\eta_{r-i} &= k_{r-i} \int_0^\infty X(C_{x-i}, \varphi, t) e^{-k_i(T)t} dt \\ \eta_{nr-i} &= [k_i(T) - k_{r-i}] \int_0^\infty X(C_{x-i}, \varphi, t) e^{-k_i(T)t} dt \\ \eta_{x-i} &= 1 - \eta_{nr-i} - \eta_{r-i},\end{aligned}\tag{A4.6}$$

where  $i = \text{R}$  or  $\text{B}$ . Next, the non-negligible thermal coupling between the blue- and green-emitting levels (Eq. A4.3) has to be taken into account. In line with the procedures of Eq. A4.6, we calculate the efficiencies of different radiative decay processes  $j$  from the green/blue thermally equilibrated

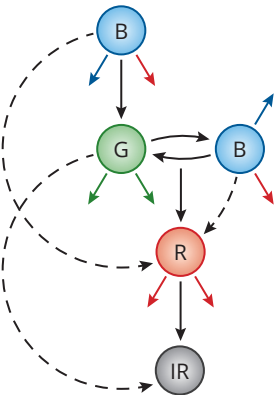


**Figure A4.7.** Schematic of the decay channels in  $\text{Ho}^{3+}$ -doped materials. Radiative decay (solid colored arrows) occurs to the ground state ( $^5I_8$ ) or to the level above the ground state ( $^5I_7$ ). Cross-relaxation (dashed black arrows) and multi-phonon relaxation (solid black arrows) enable transitions between the energy levels.



states as

$$\eta_{r-j}^{\text{BG}} = B_j(T) k_{r-j} \int_0^\infty X(C_{x-\text{BG}}, \varphi, t) e^{-k_G(T)t} dt \quad (\text{A4.7})$$

where  $j = \text{G1, G2, or B1}$  and  $B_j(T)$  is the Boltzmann factor with  $\Delta E_j = 0$ ,  $\Delta E_{\text{G2}}$ , or  $\Delta E_{\text{G2}} + \Delta E_{\text{B1}}$ , respectively:

$$B_j(T) = \frac{g_j e^{-\Delta E_j/k_B T}}{g_{\text{G1}} + g_{\text{G2}} e^{-\Delta E_{\text{G2}}/k_B T} + g_{\text{B1}} e^{-(\Delta E_{\text{G2}} + \Delta E_{\text{B1}})/k_B T}}. \quad (\text{A4.8})$$

Using these factors, we also calculated the cross-relaxation strength from the green/blue thermally equilibrated states ( $C_{x-\text{BG}}$ ):

$$C_{x-\text{BG}} = [B_{\text{G1}}(T) + B_{\text{G2}}(T)]C_{x-\text{G}} + B_{\text{B1}}(T)C_{x-\text{B}} \quad (\text{A4.9})$$

The efficiency of multi-phonon relaxation from the green/blue thermally equilibrated states to the red-emitting level is calculated as

$$\eta_{\text{nr}}^{\text{BG}} = [k_G + B_{\text{G1}}(T)k_{r-\text{G1}} + B_{\text{G2}}(T)k_{r-\text{G2}} + B_{\text{B1}}(T)k_{r-\text{B}}] \int_0^\infty X(C_{x-\text{BG}}, \varphi, t) e^{-k_G(T)t} dt \quad (\text{A4.10})$$

Finally, we determine the efficiency of cross-relaxation from the blue-emitting level <sup>5</sup>F<sub>3</sub>. This also depends on temperature via a Boltzmann factor:

$$\eta_{x-\text{B}}^{\text{BG}} = \frac{B_{\text{B1}}(T) C_{x-\text{B}}}{[B_{\text{G1}}(T) + B_{\text{G2}}(T)] C_{x-\text{G}} + B_{\text{B1}}(T) C_{x-\text{B}}} (1 - \eta_{r-\text{G1}}^{\text{BG}} - \eta_{r-\text{G2}}^{\text{BG}} - \eta_{r-\text{B}}^{\text{BG}} - \eta_{\text{nr}}^{\text{BG}}). \quad (\text{A4.11})$$

Next, from the internal efficiencies of the different levels we obtain expressions for the normalized luminescence intensities of red, green, and blue emissions  $I_{\text{R,G,B}}$ . These are the probabilities that excitation of Ho<sup>3+</sup> at 450 nm results in emission of a red, green, or blue photon, respectively. We use that the intensity emitted due to a set of sequential decay steps (Fig. A4.7) is proportional to the product of the individual efficiencies. We also take into account the branching ratios of the visible emissions. Importantly, the blue-emitting level emits both blue (<sup>5</sup>F<sub>3</sub> → <sup>5</sup>I<sub>8</sub>) and red (<sup>5</sup>F<sub>3</sub> → <sup>5</sup>I<sub>7</sub>) photons, with branching ratios  $\beta_{\text{B-B}}$  and  $\beta_{\text{B-R}}$ , respectively, determined from Fig. A4.2:

$$\begin{aligned} I_{\text{B}} &= \beta_{\text{B-B}} (\eta_{r-\text{B}} + \eta_{\text{nr-B}} \eta_{r-\text{B}}^{\text{BG}}) \\ I_{\text{G}} &= \beta_{\text{G-G}} \eta_{\text{nr-B}} (\eta_{r-\text{G1}}^{\text{BG}} + \eta_{r-\text{G2}}^{\text{BG}}) \\ I_{\text{R}} &= \beta_{\text{R-R}} \eta_{r-\text{R}} [\eta_{x-\text{B}} + \eta_{\text{nr-B}} (\eta_{\text{nr}}^{\text{BG}} + \eta_{x-\text{B}}^{\text{BG}})] + I_{\text{B}} (\beta_{\text{B-R}} / \beta_{\text{B-B}}). \end{aligned} \quad (\text{A4.12})$$

Using Eq. A4.12, the luminescence intensities were numerically calculated from 280 to 900 K for  $\text{Ho}^{3+}$  concentrations between 0% and 30%. Dividing each of these calculated intensities by the sum of the all three intensities, yields the calculated relative intensity as a function of temperature and  $\text{Ho}^{3+}$  concentration. We determine the experimentally measured relative intensities by integrating the emission spectra with the following integration boundaries: 460–500 nm, 515–575 nm, and 625–670 nm for the blue, the green, and the red intensity, respectively.

The coordinates in the 1931 CIE color diagram were determined at every 25 K in the 298–873 K temperature range. This is a straightforward procedure for the experimentally measured spectra, since it only requires multiplication of the spectrum with the sensitivity curves of the human eye, followed by integration.<sup>125</sup> It is slightly more complex to obtain the CIE coordinates from the calculated intensities, since our model does not predict the full shape of the emission spectrum explicitly. For each temperature, the blue, green, and red peak shapes were therefore extracted from the emission spectrum using the above integration boundaries. The peak shapes were scaled according to the calculated intensities (Eq. A4.12) to obtain calculated spectra, which were then converted into the CIE coordinates. Moreover, we calculate the quantum yield by summing the blue, green, and red emission intensities. For the 0.5%-, 12%-, and 30%-doped sample, this results in quantum yields of 49.5%, 7.8%, and 8.1% at 298 K, which decrease to 22%, 0.8%, and 0.3% at 873 K, respectively.

### The temperature uncertainty of a $\text{Ho}^{3+}$ -based thermometer. The calculated intensities of

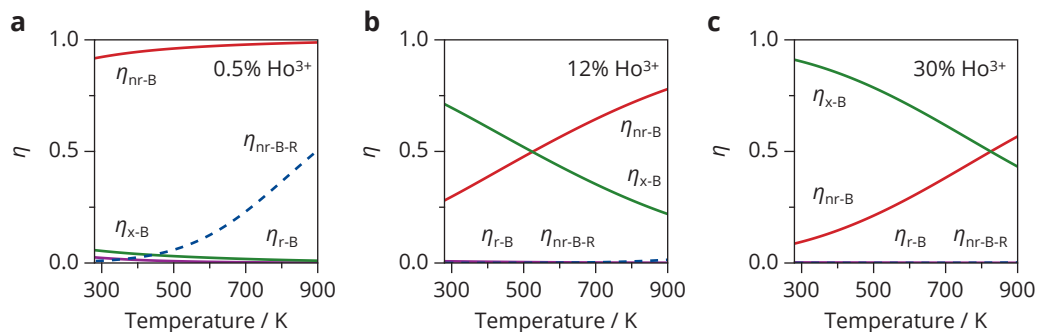


**Figure A4.8.** The efficiencies of radiative decay ( $\eta_{r-B}$ ), multi-phonon relaxation ( $\eta_{nr-B}$ ), and cross-relaxation ( $\eta_{x-B}$ ) from the blue-emitting level. Multi-phonon relaxation from the blue- to the green-emitting level can be followed by a second multi-photon relaxation step to the red-emitting level. The probability of this two-step process is denoted as  $\eta_{nr-B-R}$ . Panel (a) shows these efficiencies for the 0.5%-doped, panel (b) for the 12%-doped sample, and panel (c) for the 30%-doped  $\text{Ho}^{3+}$  sample. These plots illustrate the working mechanism of our thermometer: cross-relaxation ( $\eta_{x-B}$ ) from the blue to the red level is strong at high  $\text{Ho}^{3+}$  concentration and low temperature, while multi-phonon relaxation ( $\eta_{nr-B}$ ) is dominant at high temperature or low  $\text{Ho}^{3+}$  concentration. Note that the rate of cross-relaxation is constant with temperature (Fig. A4.6) but the efficiency of cross-relaxation goes down with increasing temperature, as a result of the accelerating rates of multi-phonon relaxation (Figs. 4.2a–4.2c).

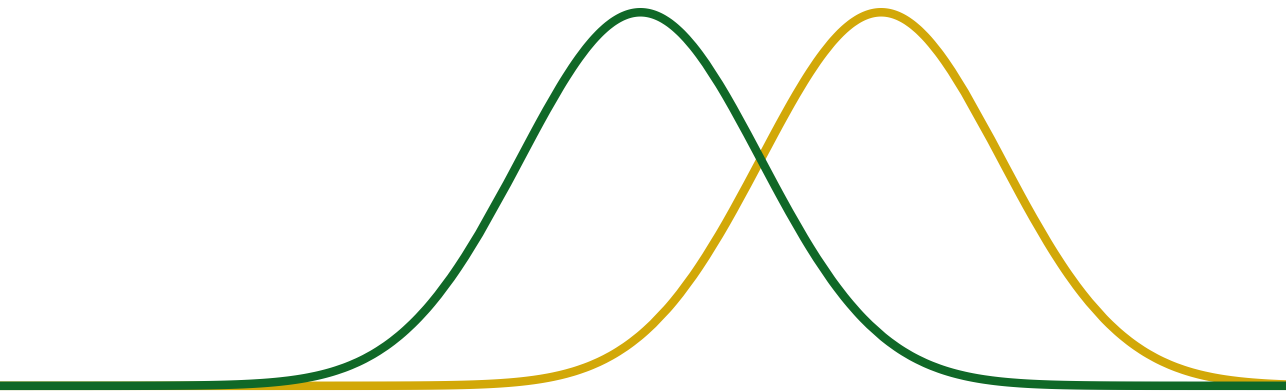
green and red luminescence were translated to relative sensitivities and temperature uncertainties. The derivative of the red-to-green  $LIR$  with respect to temperature was calculated numerically and used to obtain the theoretical relative sensitivity  $S_r$  as a function of temperature and Ho<sup>3+</sup> concentration, using Eq. 1.3. The temperature uncertainty  $\sigma_T$  then follows from  $S_r$  and the statistical uncertainty  $\sigma_{LIR}$  on the  $LIR$ . We assume that the uncertainty on the green ( $\sigma_G$ ) and red intensity ( $\sigma_R$ ) is only due to the shot noise of the detector. This means that the errors  $\sigma_G$  and  $\sigma_R$  directly follow from Poissonian statistics, which states that  $\sigma_{G,R} = \sqrt{I_{G,R}}$ . We thus obtain a lower limit for the statistical temperature uncertainty:

$$\sigma_{LIR} = \sqrt{\left| \frac{dLIR}{dI_R} \right|^2 \sigma_R^2 + \left| \frac{dLIR}{dI_G} \right|^2 \sigma_G^2} = \frac{I_R}{I_G} \sqrt{\frac{1}{I_R} + \frac{1}{I_G}} \quad (\text{A4.13})$$

$$\sigma_T = \left| \frac{dT}{dLIR} \right| \sigma_{LIR} = \frac{1}{S_r} \frac{\sigma_{LIR}}{LIR} = \frac{\sqrt{\frac{1}{I_R} + \frac{1}{I_G}}}{S_r}.$$

Eq. A4.13 shows that variation of the Ho<sup>3+</sup> concentration not only changes  $\sigma_T$  via the red-to-green ratio, but also via the absolute intensity of the green and red emission. We thus need to include a term in the expression for the temperature uncertainty that accounts for the increased number of Ho<sup>3+</sup> ions in the excitation spot, assuming that the excitation fluence and spot size are constant for different Ho<sup>3+</sup> concentrations.

$$\sigma_T(\varphi) = \frac{\sqrt{\frac{1}{\varphi I_R} + \frac{1}{\varphi I_G}}}{S_r} = \frac{\sigma_T}{\sqrt{\varphi}} \quad (\text{A4.14})$$



---

# Chapter 5

## Mapping elevated temperatures with a micrometer resolution using the luminescence of chemically stable upconversion nanoparticles

### Abstract

The temperature-sensitive luminescence of nanoparticles enables their application as remote thermometers. The size of these nanothermometers makes them ideal to map temperatures with a high spatial resolution. However, high-spatial-resolution mapping of temperatures above 373 K has remained challenging. In this Chapter, we realize nanothermometry with high spatial resolutions at elevated temperatures using chemically stable upconversion nanoparticles and confocal microscopy. We test this method on a microelectromechanical heater and study the temperature homogeneity. Our experiments reveal distortions in the luminescence spectra that are intrinsic to high-resolution measurements of samples with nanoscale photonic inhomogeneities. Specifically, the spectra are affected by the high-power excitation as well as by scattering and reflection of the emitted light. The latter effect has an increasing impact at elevated temperatures. We present a procedure to correct for these distortions. As a result, we extend the range of high-resolution nanothermometry beyond 500 K with a precision of 1–4 K. This work will improve the accuracy of nanothermometry, not only in micro- and nanoelectronics, but also in other fields with photonic inhomogeneous substrates.

### Based on:

T.P. van Swieten, T. van Omme, D.J. van den Heuvel, S.J.W. Vonk, R.G. Spruit, F. Meirer, H.H. Pérez Garza, B.M. Weckhuysen, A. Meijerink, F.T. Rabouw and R.G. Geitenbeek, Mapping elevated temperatures with a micrometer resolution using the luminescence of chemically stable upconversion nanoparticles. *ACS Appl. Nano Mater.* **4**, 4208–4215 (2021).

---

## 5.1 Introduction

Thermometry on the microscopic scale is an essential characterization tool for the development of nano- and microelectronic devices.<sup>127–130</sup> However, conventional thermometers like thermocouples are often unable to reliably measure the temperature on this length scale due to their size. An additional drawback is the requirement of direct contact between the sensing element and the temperature-registration instrument. The development of remote temperature sensing by optical thermometry techniques partially solved this issue. These techniques rely on temperature-dependent blackbody radiation (infrared thermography),<sup>131</sup> Raman scattering,<sup>132,133</sup> reflectance,<sup>134</sup> luminescence,<sup>102</sup> or other optical properties.<sup>135</sup> Thermometry based on luminescence is particularly interesting since it is easily implemented, requiring only the deposition of a luminescent material in or on a sample of interest and the detection of its luminescence. The development of bottom-up synthesis methods for luminescent materials with nanoscale dimensions opened the field of luminescence nanothermometry with dramatically enhanced spatial resolution.<sup>97</sup> Luminescence nanothermometry is therefore currently developing into the method of choice for temperature measurements in microscopy.<sup>34,42,136–138</sup>

Several luminescence properties of a nanothermometer can serve as a measure for temperature. The luminescence intensity ratio (*LIR*) between two emission bands is a popular choice, because it is generally considered insensitive to experimental parameters such as excitation intensity, alignment, or the amount of deposited thermometer material. Typical nanothermometers used in *LIR* thermometry consist of an inorganic host crystal doped with lanthanide ( $\text{Ln}^{3+}$ ) ions, which are luminescent due to  $4f-4f$  transitions. The minor spectral overlap between these transitions and their narrow linewidth prevent systematic errors and allow high accuracy in determination of the *LIR*. An additional advantage of  $\text{Ln}^{3+}$ -doped nanocrystals is the possibility to efficiently generate upconversion luminescence, *i.e.* the emission of one high-energy photon after the absorption of at least two low-energy photons.<sup>43,139</sup> Via this process infrared excitation can lead to visible luminescence. While detection of visible luminescence is straightforward with a standard camera or photodiode, excitation with infrared light prevents background fluorescence, a common issue of conventional down-shifting luminescence, *i.e.* excitation with one high-energy photon resulting in the emission of one low-energy photon. These properties of upconversion nanoparticles guarantee accurate determination of the *LIR* and thus reliable temperature measurements.

Typical applications of upconversion nanoparticles in thermometry on the microscopic scale are in cell biology and microelectronics. Upconversion luminescence from  $\text{Er}^{3+}/\text{Yb}^{3+}$ -doped nanoparticles is well-known for temperature mapping in these fields,<sup>34,42,138</sup> but  $\text{Eu}^{3+}/\text{Tb}^{3+}$ - and  $\text{Eu}^{3+}/\text{Sm}^{3+}$ -doped systems have also been used.<sup>136,137</sup> With these nanoparticles a high spatial resolution is achieved by spatially mapping the *LIR* using either wide-field or confocal microscopy. Thermometry via wide-field microscopy is a fast technique, as it directly images the intensity maps of two emission bands using bandpass filters. Dividing the two images yields the spatially resolved *LIR*, which easily translates to a temperature map. Confocal microscopy is a slower technique, as a laser spot scans the sample to construct an image. However, it can provide a spectrum for every

pixel enabling a more reliable determination of the *LIR*. Both techniques are mainly used to probe temperatures up to  $\sim 350$  K. Recent work from our group demonstrated that it is possible to extend the temperature range to 873 K using luminescent microcrystals.<sup>129</sup> In this Chapter, deposition of the microcrystals on a microheater designed for *in situ* transmission electron microscopy (TEM) experiments revealed the temperature profile with a spatial resolution of roughly  $10\ \mu\text{m}$ . However, these microheaters and other microelectromechanical systems (MEMS) contain structures with dimensions smaller than  $1\ \mu\text{m}$ .<sup>140</sup> A higher spatial resolution of luminescence thermometry at elevated temperatures is thus crucial for its implementation in MEMS technology.

In this Chapter, we develop a combined microscopy and data-analysis approach to map elevated temperatures with high spatial resolution. Specifically, we measure the local temperatures on a MEMS-based microheater using confocal-microscopy mapping of the two green emission bands of  $\text{NaYF}_4:\text{Er}^{3+}, \text{Yb}^{3+}$  upconversion nanoparticles. The demand for a high spatial resolution comes with intrinsic challenges due to the higher excitation powers necessary to obtain sufficient signal<sup>30,40</sup> and due to inhomogeneities of the optical environment of nanothermometers. We characterize both phenomena and develop data analysis procedures to correct for them. This enables a quantitative study of the temperature profile generated by the microheater at elevated temperatures up to 523 K.

## 5.2 Results

The microheater consists of a spiral-shaped metal that is embedded between two layers of silicon nitride that form a membrane (Fig. 5.1a–5.1b).<sup>141</sup> A silicon substrate supports the membrane

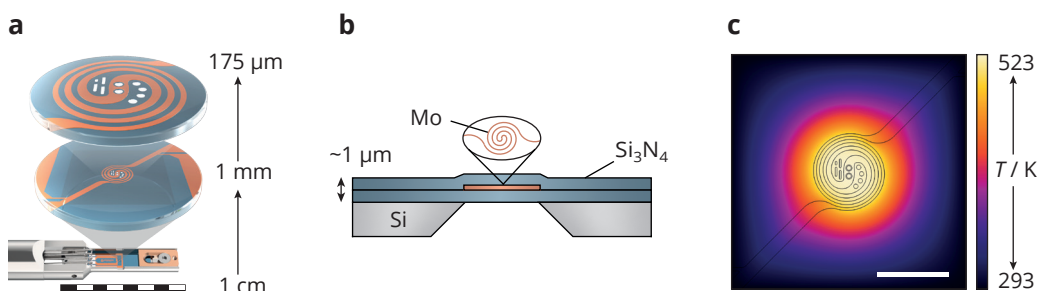


**Figure 5.1.** The microheater for *in situ* TEM. **(a)** Magnification of the microheater design. The metal heating spiral (orange) is embedded in a silicon nitride membrane (blue). Electron microscopy users place their samples on the electron-transparent silicon-nitride windows in the center of the heater. The scale bar represents 1 cm, 1 mm, and  $175\ \mu\text{m}$  for the bottom, middle, and top magnification, respectively. **(b)** Side view of the microheater. A silicon substrate supports the silicon nitride membrane, with the encapsulated molybdenum heating spiral. Due to its low thermal conductivity, the silicon nitride acts as a thermal insulator between the heater and the silicon substrate. This way a steep temperature gradient is realized between the edge of the heating spiral and the  $400\ \mu\text{m}$  thick silicon substrate, which remains at room temperature. **(c)** Temperature profile across the membrane and microheater for a center temperature of 523 K simulated with finite element analysis. The scale bar represents  $175\ \mu\text{m}$ .

with the microheater and enables loading into a dedicated TEM holder. Four metal needles connect the holder with the metal contacts of the microheater. By applying a voltage across two of the contacts, a current flows, which induces Joule heating. The two other contacts are used to measure the resistance. The metal has a linear relationship between resistance and temperature, which is exploited to measure and control the temperature. Fig. 5.1c shows the temperature profile at a center temperature of 523 K as predicted by a finite element model.<sup>141</sup> The geometry of the metal spiral was designed to generate a homogeneous temperature in the center area where the electron microscopy users place their samples. Outside this area, over a distance of 175  $\mu\text{m}$  between the heater spiral and the silicon substrate, the temperature shows a steep gradient to room temperature at the edges of the membrane. This is explained by the low thermal conductivity of the silicon nitride, which minimizes heat loss through the membrane. The much higher thermal conductivity of the silicon substrate ensures that the substrate remains at room temperature. Measuring the gradient requires a thermometry technique with a high spatial resolution.

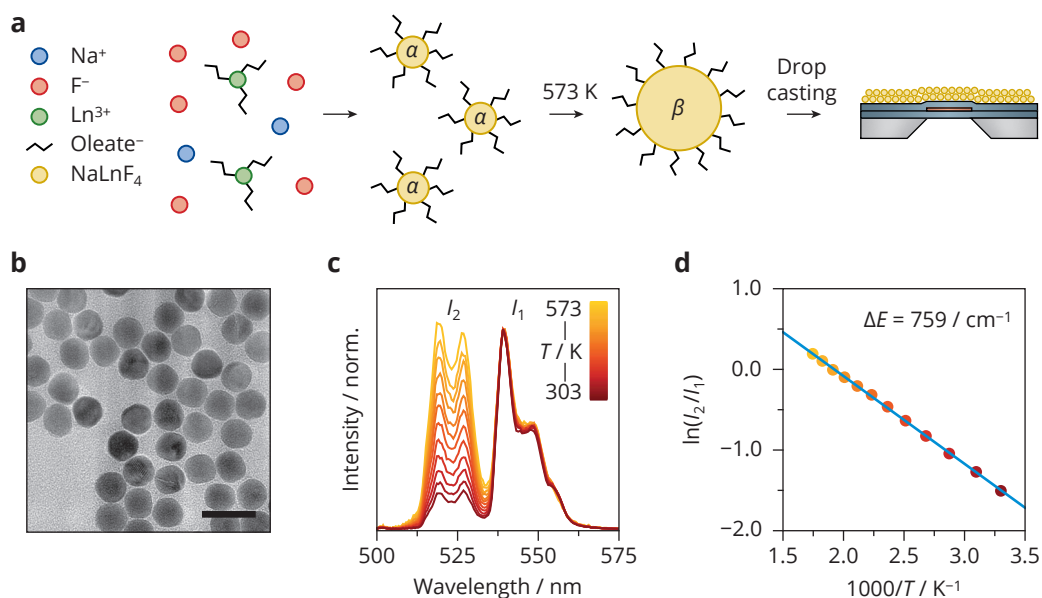


**Figure 5.2.** Upconversion nanoparticles: their fabrication and luminescence. **(a)** Schematic of the two-step synthesis of the nanoparticles: small cubic  $\alpha$ - $\text{NaLnF}_4$  ( $\text{Ln}^{3+} = \text{Y}^{3+}$ ,  $\text{Er}^{3+}$ , or  $\text{Yb}^{3+}$ ) particles form at room temperature followed by growth to larger  $\beta$ - $\text{NaLnF}_4$  particles at 573 K. These particles are deposited on the microheater by drop-casting. **(b)** TEM image of  $\text{NaYF}_4:\text{Er}^{3+}(2\%),\text{Yb}^{3+}(18\%)$  nanoparticles with a diameter of  $32 \pm 1$  nm. The scale bar represents 50 nm. **(c)** Green upconversion luminescence of the nanoparticles upon 980 nm excitation ( $1.0 \text{ kW cm}^{-2}$ ) at various temperatures ranging from 303 K (dark red) to 573 K (yellow). **(d)** The logarithm of the ratio between the integrated intensities from **(c)** versus the reciprocal temperature (colored dots). The integration boundaries for the  ${}^2\text{H}_{11/2}$  and  ${}^4\text{S}_{3/2}$  emissions are 510–530 nm and 537–560 nm, respectively. The blue line is a fit of the experimental ratios to the Boltzmann model of Eq. 5.1.



Calibrating the resistance–temperature relation of the heater is currently done using Raman spectroscopy. Silicon particles are deposited on the microheater, which is inserted into a vacuum chamber to imitate the conditions of an electron microscopy experiment. The position of the silicon peak in the Raman spectrum around  $520\text{ cm}^{-1}$  is used as a measure for temperature.<sup>132,142</sup> Although the size of the Raman laser spot ( $1\text{ }\mu\text{m}$ ) guarantees a high spatial resolution, the temperature uncertainty can be as high as  $13\text{ K}$  at  $523\text{ K}$ .<sup>141</sup> The aim of our luminescence thermometry technique is thus to measure temperature with a similar spatial resolution but a lower temperature uncertainty.

The discussion of our technique starts with the characterization of the luminescent thermometers. We use hexagonal  $\text{NaYF}_4$  nanoparticles doped with  $2\%$   $\text{Er}^{3+}$  and  $18\%$   $\text{Yb}^{3+}$ . The choice for this specific composition is motivated by its relatively high upconversion quantum yield.<sup>143</sup> Using a colloidal synthesis procedure,<sup>43</sup> we first produce cubic  $\alpha\text{-NaYF}_4\text{:Er}^{3+}(2\%),\text{Yb}^{3+}(18\%)$  nanoparticles and further heat these to  $573\text{ K}$  to obtain hexagonal  $\beta\text{-NaYF}_4\text{:Er}^{3+}(2%),\text{Yb}^{3+}(18\%)$

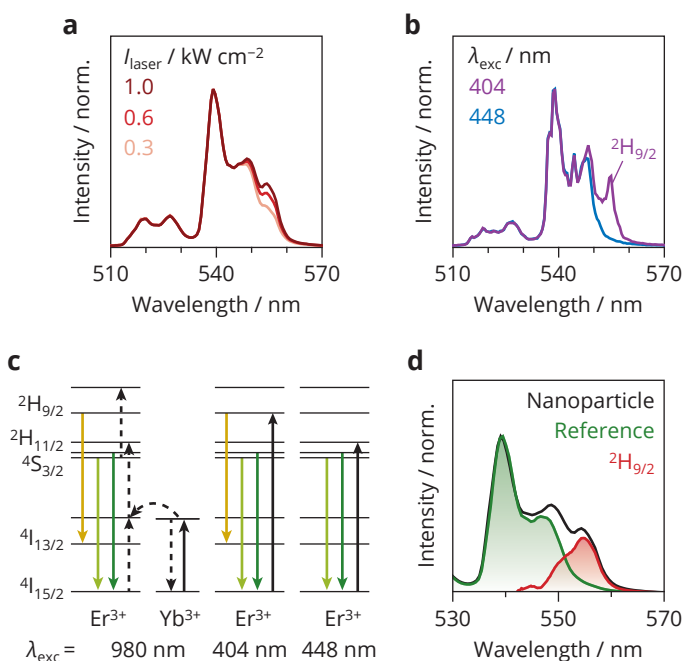


**Figure 5.3.** Multi-photon upconversion. **(a)** Green upconversion luminescence of the nanoparticles at different excitation intensities of the 980 nm laser. **(b)** Emission spectra of microcrystalline  $\text{NaYF}_4\text{:Er}^{3+}(2\%),\text{Yb}^{3+}(18\%)$  at different excitation wavelengths recorded with a high spectral resolution using a spectrofluorometer. **(c)** Simplified energy level diagrams for three different excitation wavelengths with the absorption, emission, and energy-transfer transitions indicated by solid black, solid colored, and dashed black arrows, respectively. **(d)** Emission spectra of the upconversion nanoparticles (measured) and a microcrystalline  $\text{NaYF}_4\text{:Er}^{3+}(2\%),\text{Yb}^{3+}(18\%)$  sample (reference). Subtracting the reference spectrum from the nanoparticle spectrum gives the difference spectrum revealing the spectral shape of the <sup>2</sup>H<sub>9/2</sub> emission.

nanoparticles with a diameter of  $32 \pm 1$  nm (Fig. 5.2a–5.2b). Excitation with 980 nm light yields bright green upconversion emission due to the radiative transitions in  $\text{Er}^{3+}$  from the thermally coupled  ${}^2\text{H}_{11/2}$  and  ${}^4\text{S}_{3/2}$  levels to the  ${}^4\text{I}_{15/2}$  ground state (Fig. 5.2c). Thermal coupling between these levels leads to stronger luminescence from the higher-excited level upon a temperature ( $T$ ) increase, following Boltzmann statistics (Eq. 2.4):<sup>29</sup>

$$\frac{I_2}{I_1} = \frac{A_2 g_2}{A_1 g_1} \exp\left(-\frac{\Delta E}{k_B T}\right) = C \exp\left(-\frac{\Delta E}{k_B T}\right), \quad (5.1)$$

where  $k_B$  is the Boltzmann constant and  $\Delta E$  is the energy difference between the thermally coupled levels.  $I_i$  and  $A_i$  are the integrated luminescence intensity and the spontaneous emission rate from excited state  $i$  to the ground state with degeneracy  $g_i$ , respectively. If  $\Delta E$  is known (e.g. from literature), one could extract the exponential pre-factor  $C$  from the intensity ratio in an emission spectrum. However, such a ‘calibration-free’ procedure introduces an additional error. We therefore fit the *LIR* between the  ${}^2\text{H}_{11/2}$  and  ${}^4\text{S}_{3/2}$  emissions at various temperatures to the Boltzmann model in Eq. 5.1 and find a  $\Delta E$  of  $759 \text{ cm}^{-1}$  (Fig. 5.2d), which is in agreement with  $\Delta E$  values from literature.<sup>43</sup> This model can thus serve as a calibration for our thermometers to accurately measure temperature.

As nanothermometry requires high excitation intensities to obtain sufficient signal, we must understand how not only temperature but also intense excitation changes the upconversion emission spectrum (Fig. 5.3a). We observe an upconversion emission band at 555 nm that becomes stronger with increasing excitation intensity. With reference measurements, exciting into (404 nm) or just below (448 nm) the  ${}^2\text{H}_{9/2}$  state of  $\text{Er}^{3+}$  (Fig. 5.3b), we can show that the 555-nm emission must be due to radiative relaxation from the  ${}^2\text{H}_{9/2}$  state to the first-excited state ( ${}^4\text{I}_{13/2}$ ) of  $\text{Er}^{3+}$ . The  ${}^2\text{H}_{9/2}$  emission becomes stronger in the upconversion spectrum at higher excitation intensity. This is consistent with a  ${}^2\text{H}_{9/2}$  population mechanism requiring upconversion of three 980-nm photons, compared to the two photons that were needed to populate the  ${}^4\text{S}_{3/2}$  and  ${}^2\text{H}_{11/2}$  levels (Figs. 5.3c and A5.2). As the  ${}^2\text{H}_{9/2} \rightarrow {}^4\text{I}_{13/2}$  upconversion emission partially overlaps with the emission from the  ${}^4\text{S}_{3/2}$  state, we must take care when integrating the spectral bands to determine the *LIR*. If we naively integrated between the wavelength boundaries of the  ${}^2\text{H}_{11/2}$  and  ${}^4\text{S}_{3/2}$  emissions (Fig. 5.2d), we would overestimate the  ${}^4\text{S}_{3/2}$  intensity at higher excitation powers and therefore, via Eq. 5.1, underestimate the temperature. A possible solution would be to only integrate the part of the  ${}^4\text{S}_{3/2}$  band without overlap with the  ${}^2\text{H}_{9/2}$  emission, effectively excluding data points. As the relative error on a measurement of photon counts reduces with higher total counts,<sup>29</sup> a narrow integration boundary would thus result in a larger relative error on the *LIR*, leading to a higher temperature uncertainty. To maintain a low uncertainty on the measured temperature we design a correction procedure that removes the  ${}^2\text{H}_{9/2}$  emission.

The first step of this correction procedure is to separate the shapes of the  ${}^2\text{H}_{11/2} + {}^4\text{S}_{3/2}$  and the  ${}^2\text{H}_{9/2}$  emission via a similar approach as presented in the recent work of Rühl *et al.*<sup>40</sup> Here, we use a microcrystalline  $\text{NaYF}_4:\text{Er}^{3+}(2\%),\text{Yb}^{3+}(18\%)$  as a reference. This sample shows negligible

$^2\text{H}_{9/2}$  emission upon 980 nm excitation at an intensity of  $0.3 \text{ kW cm}^{-2}$  (Fig. 5.3d),<sup>67</sup> because the surface-to-volume ratio is much smaller compared to the nanoparticle samples. This results in weaker coupling of  $^4\text{S}_{3/2}$  with vibrations in surface species, which leads to a reduced population of  $^4\text{F}_{9/2}$  and thereby results in less upconversion from  $^4\text{F}_{9/2}$  to  $^2\text{H}_{9/2}$ .<sup>144</sup> The spectral difference between the reference and the luminescence that is measured from the nanoparticles then gives the shape of the  $^2\text{H}_{9/2}$  emission. Using these spectral shapes, we fit a linear combination of  $^4\text{S}_{3/2}$  emission and  $^2\text{H}_{9/2}$  intensity to each experimental spectrum of a confocal map. Here, we used the same spectral range for the  $^4\text{S}_{3/2}$  and  $^2\text{H}_{9/2}$  emission. Finally, we integrate the  $^2\text{H}_{11/2} + ^4\text{S}_{3/2}$  emission between the appropriate boundaries to determinate the *LIR*. We record reference spectra at various temperatures to apply this procedure to the calibration spectra (Fig. A5.1) and all spectra of the temperature mapping experiments. Noticing and correcting this effect of the excitation intensity is straightforward with confocal microscopy, since a measurement provides a spectrum per pixel. This is less straightforward with wide-field techniques, as it would require a very narrow and selective bandpass filter for the  $^4\text{S}_{3/2}$  emission.

To acquire temperature-dependent luminescence from the microheater we cover it with a layer of upconversion nanoparticles. Using a confocal microscope, we scan a 980-nm excitation laser over the microheater to acquire an array of emission spectra, which we correct using the above procedure. Integration of the  $^2\text{H}_{11/2} + ^4\text{S}_{3/2}$  emission at each pixel yields an intensity map at a set temperature of  $T_{\text{set}} = 303 \text{ K}$  (Fig. 5.4a). Notably, the integrated luminescence is stronger on the heating spiral, indicating that the collection and/or excitation efficiency of the luminescence is higher on the metal due to its higher reflectivity. The objective used has a relatively low numerical aperture (NA) of 0.3, corresponding to a poor detection efficiency. However, its long working distance makes a large number of measurement geometries possible, including measurements on a microheater inserted into a vacuum chamber (Figs. A5.3a–A5.3b). To demonstrate the complete potential of this setup we mapped the center of a microheater at 523 K in vacuum with a high pixel density (Fig. A5.3c). In this intensity map, we can clearly distinguish the edges of

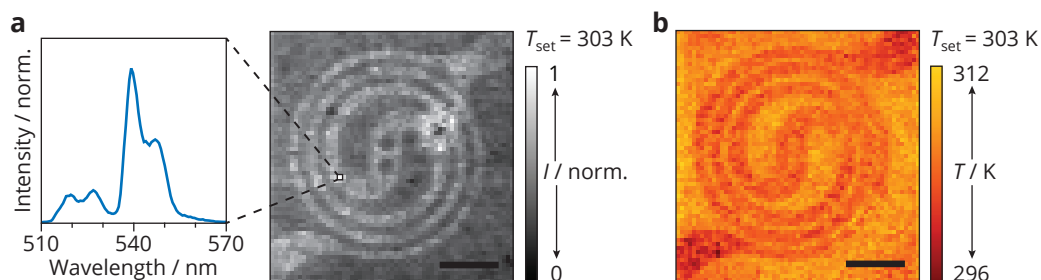


**Figure 5.4.** Temperature mapping. (a) Map of the integrated green luminescence from a microheater coated with upconversion nanoparticles at a set temperature of 303 K measured in ambient atmosphere. The intensity of the 980 nm excitation light was  $1.0 \text{ kW cm}^{-2}$ . The measurement provides a spectrum for every pixel. The scale bar represents  $50 \mu\text{m}$ . (b) Converting the ratio of the emission peaks using the calibration of Fig. A5.1d yields a temperature map.

the silicon-nitride windows with an accuracy of  $\sim 1 \mu\text{m}$ .

Next, we convert the *LIR* from each corrected emission spectrum to construct a temperature map (Fig. 5.4b). At first sight, the temperature values in the map seem in agreement with the set temperature. However, we notice a systematic deviation of the readout temperature on the heating spiral—it is approximately 4 K lower. This likely is an artefact of our nanothermometry technique, because the heating element cannot be colder than its surroundings. We exclude the correction procedure for multi-photon upconversion as potential origin, since the uncorrected temperature

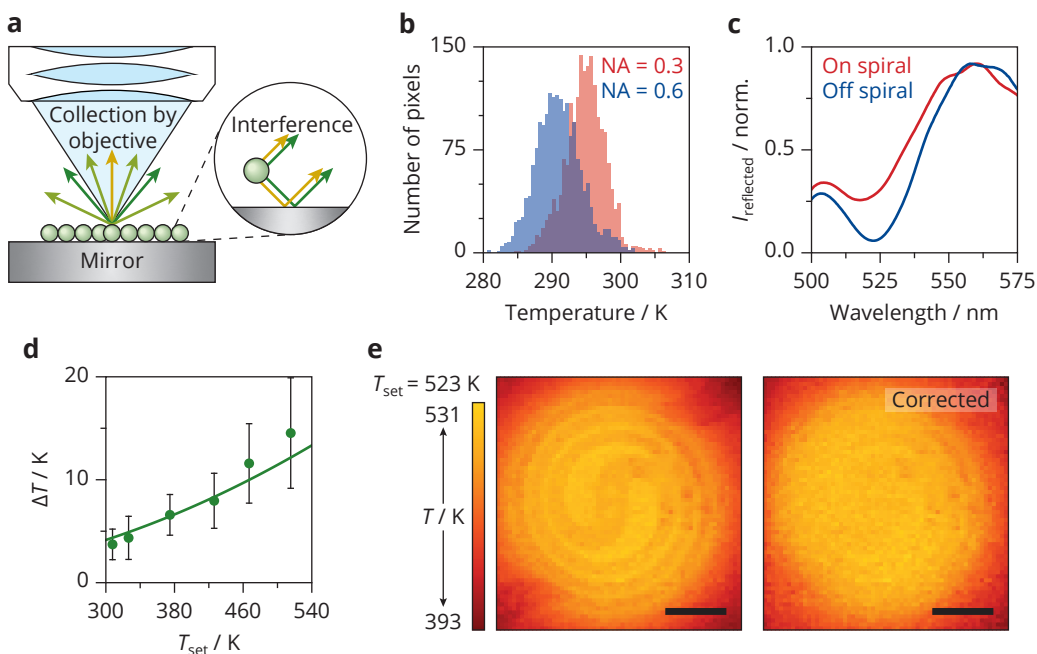


**Figure 5.5.** Artefacts in luminescence thermometry on the microscopic scale. **(a)** Schematic of  $\text{Er}^{3+}$ -doped nanoparticles on a mirror. Interference of the direct and the reflected  ${}^2\text{H}_{11/2}$  (green) and  ${}^4\text{S}_{3/2}$  (yellow) emission changes the spectrum that is collected by the microscopy objective. **(b)** Histograms of the measured temperatures from 1849 pixels in the center of temperature maps that were obtained with numerical apertures of 0.3 and 0.6 at room temperature (Fig. A5.6). **(c)** Intensity of the reflected light from a halogen lamp that illuminated a location on and off the spiral of a bare microheater. The spectra were recorded with an NA of 0.75. **(d)** Temperature difference between locations on and off the spiral ( $\Delta T$ ), as a function of the set temperature. The green dots show the average of the experimental  $\Delta T$  values, determined from 40 pixels both on spiral and off spiral. The bars indicate the propagated errors on  $\Delta T$  values, determined from the standard deviation of the average readout temperatures on and off the spiral. The solid line is a fit of the experimental  $\Delta T$  values to a model that calculates the temperature-dependence of the temperature error  $\Delta T(T)$  from Boltzmann thermometers due to the photonic environment (Eq. 5.2). **(e)** Temperature map of the microheater at a set temperature of 523 K measured in ambient atmosphere (left). The intensity of the 980 nm excitation light was  $1.0 \text{ kW cm}^{-2}$ . Correction of the left map using Eq. 5.2 yields the temperature map on the right. The scale bars represent  $50 \mu\text{m}$ .

maps show a similar trend (Fig. A5.4). In addition, the readout temperature did not change at different excitation intensities (Fig. A5.5). Laser heating could therefore not be the cause of the lower readout temperature on the heating spiral. This phenomenon thus requires further investigation to allow for reliable temperature mapping.

We propose that the systematic deviation of the readout temperature between the spiral and the membrane is an intrinsic challenge of nanothermometry, related to inhomogeneities of the photonic environment of the nanothermometers at the nanoscale.<sup>31</sup> Drexhage was the first to demonstrate how the emission of fluorescent molecules depended on the photonic environment, in particular on the vicinity of a reflective mirror at a distance of up to a few times the emission wavelength.<sup>21,145</sup> This dependence can be explained as interference of the reflected emission with direct emission of the molecules, affecting the emission pattern (*i.e.* the directions into which emission is strongest) and the overall spontaneous emission rate.<sup>146</sup> The same interference phenomenon must affect the readout temperatures in our system. Indeed, the thickness of both the nanoparticle layer (a few  $\mu\text{m}$ ) and the silicon nitride membrane are on the order of the emission wavelength and the microheater can act as a mirror.<sup>20</sup> The emission wavelengths of  $^4\text{S}_{3/2}$  and  $^2\text{H}_{11/2}$  are slightly different, so interference affects the emission patterns in different ways. This changes the *LIR* of the emission collected by our objective (Fig. 5.5a). The different components of the microheater (metal spiral versus silicon nitride membrane) have different reflectivities, explaining why the interference effect depends on the location of the nanoparticles on the microheater.

The effect of the photonic environment becomes evident when we compare luminescence spectra acquired using objectives with different numerical apertures. We measure temperature maps of the same sample using microscopy objectives with a NA of 0.3 and 0.6. Fig. 5.5b shows histograms of the readout temperatures in the center of these maps, both recorded at room temperature. For a NA of 0.3, the center of the histogram is at 296 K. This completely changes when we collect emission over a wider angle with a NA of 0.6, showing a shift to 290 K. Clearly, the dependence of the readout temperature distributions on the NA confirms modification of the luminescence spectrum by the photonic environment.

Further evidence of the irregular photonic environment on the microheater follows from reflectance measurements. Here, we study a bare microheater by separately illuminating the heating spiral and a location next to it. The intensity of the reflected light is roughly 2 times higher on the heating spiral (Fig. A5.7), which is consistent with the observations in Fig. 5.4a. In addition, normalization demonstrates a higher relative reflectivity on the heating spiral in the range of the  $^2\text{H}_{11/2}$  emission, *i.e.* 510–535 nm (Fig. 5.5c). Interference between reflected and direct  $^2\text{H}_{11/2}$  emission is thus stronger on the heating spiral than off spiral.

Finally, we examine how the temperature error due to the photonic environment depends on the actual temperature in a pixel. We first determine the difference in readout temperature between locations on and off spiral ( $\Delta T$ ) and observe an increase at higher temperatures (Fig. 5.5d). The relation between the readout temperature and the spontaneous emission rates explains this observation (Eq. 5.1). For the nanoparticles on the microheater, we must interpret the sponta-

neous emission rates  $A_i$  in Eq. 5.1 as the rates of spontaneous emission under angles that can be collected by our instrumentation. This specification requires no special attention if the emission is approximately isotropic, such as in thermometry on the millimeter scale where any photonic effects average out. However, nanoscale photonic heterogeneities lead to a locally different ratio  $A_2/A_1$ . The constant  $C$  of Eq. 5.1 should therefore be multiplied by a correction factor  $C_p$  that accounts for the effect of the photonic environment on the emission rates. The readout temperature  $T_p$  of a nanothermometer with anisotropic emission depends on its actual temperature  $T$  as well as on this correction factor  $C_p$ . This yields a temperature error of (Eqs. A5.1–A5.4):

$$\Delta T = T - T_p = T - \frac{\Delta E}{\Delta E/T + k_B \ln(C_p)}. \quad (5.2)$$

Higher actual temperatures thus lead to an increase of  $\Delta T$  for  $C_p < 1$ , which matches the trend in Fig. 5.5d. We further confirm this by fitting the experimental  $\Delta T$  values to Eq. 5.2. This gives us a method to correct for the systematic deviation in measured temperatures on the microheater.

This second correction starts with the determination of  $C_p$  for each location on the microheater. Here, we assume that the temperature distribution is homogeneous for the map recorded at a set-temperature of 303 K (Figs. 5.4b and A5.8). For every pixel,  $C_p$  is then the only unknown in Eq. 5.2, which makes it possible to construct a map of  $C_p$  values. In this case, this ‘calibration-free’ procedure is necessary to correct for the position-dependent photonic effects. We find values around 0.95 on the spiral, while  $C_p$  is around 1 off the spiral. Indeed, the photonic effects on  $A_2/A_1$  are expected to be subtle as the  ${}^2\text{H}_{11/2}$  and  ${}^4\text{S}_{3/2}$  emissions have nearly the same wavelength. To correct the maps at elevated temperatures we plug these values and the readout temperatures off the spiral into Eq. 5.2 to obtain the actual temperatures. The average temperature in the center of the heating spiral was lower at elevated set temperatures, up to approximately 10 K at 523 K. We attribute this deviation to a temperature gradient through the layer of nanothermometers, leading to a lower temperature near the nanothermometer–air interface than on the surface of the microheater. A potential origin of this gradient is the poor thermal conductivity of the nanothermometer layer compared to Si particles that were used for calibration of the microheater.<sup>147</sup> A thinner layer of nanothermometers would reduce this gradient, but resulted in incomplete coverage of the microheater and it thereby complicated the analysis of the temperature homogeneity. To correct for the photonic artefact, we use the readout temperature in the center of the heating spiral as input for the physical temperature in Eq. 5.2. After correction (Fig. 5.5e), the microheater shows a homogeneous temperature distribution at elevated set temperatures, which matches the simulations presented in Fig. 5.1c. This clearly demonstrates the effectiveness of our correction procedure in removing temperature artefacts due to the photonic environment.

Finally, we use the fully corrected temperature maps to study the temperature homogeneity of the microheater. Fig. 5.6 shows horizontal traces through the center of these maps. The temperature is nearly constant in the center of these traces, followed by a decrease at the edges. We compare this with temperature profiles simulated using the finite element model (Fig. 5.1c). As in-

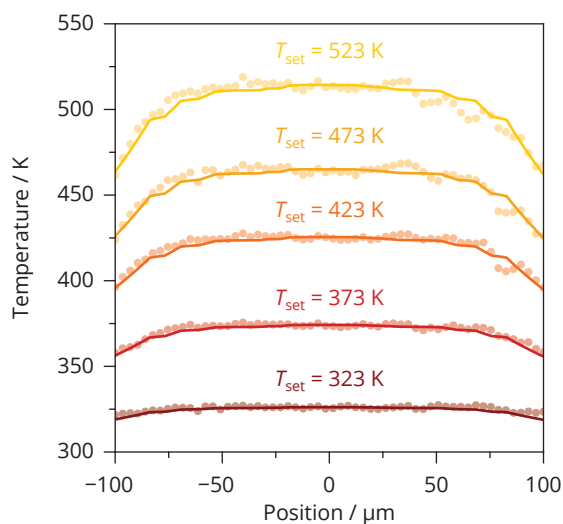


**Figure 5.6.** Mapping elevated temperatures. The dots show the average of seven horizontal line traces through the center of the temperature maps at elevated temperatures. The lines represent the temperature profiles as simulated using the finite element model.

put for the simulation, we use the measured temperature at the center of the fully corrected maps. The simulated temperature profiles (lines) show an excellent match with the experimental traces (dots). We determine the standard deviation of the temperature in the center to quantify the accuracy of this thermometry method and find values of 1 K at 323 K increasing to only 4 K at 513 K. This confirms both the reliability of finite element analysis as design tool and the strength of our temperature mapping technique as a characterization tool, achieving a high accuracy and a spatial resolution of  $\sim 1 \mu\text{m}$ . This makes nanothermometry using confocal luminescence spectroscopy a promising method to map temperature profiles in other fields such as biology<sup>34</sup> and catalysis,<sup>148</sup> where temperature variations are important but hard to monitor with conventional methods.

### 5.3 Conclusions

We have mapped the luminescence of upconversion nanoparticles and designed an analysis procedure to accurately measure the temperature profile of a MEMS-based microheater. To ensure high temperature accuracy it is crucial to correct each emission spectrum for complications that are inherent to luminescence nanothermometry (but often ignored): additional emission lines at high excitation intensity and spectral variations induced by the photonic environment of the nanoparticles. A reliable correction procedure was developed and enabled the experimental assessment of the temperature homogeneity at the surface of the microheater. The combination of luminescence thermometry and confocal microscopy not only allows for temperature mapping of this specific microheater, but can also be applied to visualize temperature variations with micrometer resolution and superior accuracy up to high temperatures in many other fields. This makes our thermometry technique a valuable new tool in characterizing temperature distributions on the micrometer scale, which becomes increasingly important with the ongoing trend towards

further miniaturization of devices.

## 5.4 Methods

**Sample preparation.** The synthesis procedure of Geitenbeek *et al.* was used to obtain multiple batches of  $\text{NaYF}_4:\text{Er}^{3+}(2\%),\text{Yb}^{3+}(18\%)$  nanoparticles dispersed in cyclohexane.<sup>43</sup> Deposition of the nanoparticles was achieved by drop casting on the microheater (Wildfire Nano-Chips, commercially available from DENSsolutions). The thickness of the dried nanoparticle layer (a few micrometer) was estimated using the concentration of the nanoparticle dispersion. Microcrystalline  $\text{NaYF}_4:\text{Er}^{3+}(2\%),\text{Yb}^{3+}(18\%)$  was obtained following the procedure of Kramer *et al.*<sup>67</sup>

**Spectroscopy experiments.** The particle size and morphology were investigated with a FEI Tecnai 12 transmission electron microscope operating at 120 keV. Samples were prepared by drying the diluted nanoparticle dispersion onto carbon-coated copper grids. The luminescence of the dried nanoparticle layer was mapped using a Nikon TE2000-S inverted microscope fitted with a C1si confocal scanner.<sup>149</sup> A 980 nm laser diode was connected to the confocal scanner-head via a single-mode fiber. The laser light was reflected by a 680 nm short-pass dichroic mirror and focused on the nanoparticle layer using a 10× CFI Plan Fluor (NA = 0.3) air objective or a 40× CFI S Plan Fluor ELWD (NA = 0.6) air objective. The luminescence was directed back into the confocal scanner head via the same objective, passed through the dichroic, coupled into a 50 μm multi-mode fiber, passed through a 680 nm shortpass filter, dispersed by an equilateral SF10-glass prism (Linos) and finally detected using a back illuminated CDD (Princeton Instruments, NTE/CCD-1340). All maps were obtained with a pixel dwell time of 100 ms. For the calibration of the luminescence a powder of dried nanoparticles was heated with a Linkam THMS600 microscope stage. Selective excitation of the microcrystalline  $\text{NaYF}_4:\text{Er}^{3+}(2\%),\text{Yb}^{3+}(18\%)$  sample with 404 and 448 nm light was achieved with an Edinburgh Instruments FLS920 spectrofluorometer equipped with TMS300 monochromators, a R928 photomultiplier tube, and a Xe lamp (450 W). The reflection measurements were performed on a Nikon Ti-U inverted microscope. The microheater was illuminated in wide-field with a broad-spectrum LED (Lumencor Sola) through a 40× Nikon CFI Plan Fluor (NA = 0.75) air objective. The reflected light was collected through the same objective and collimated outside of the microscope using a relay lens system. The light was focused on a mechanical slit at the entrance of a spectrometer Andor Kymera 193i and dispersed with a 150 lines/mm grating on an Andor iXon EMCCD.

**Simulation.** Finite Element simulations were carried out using COMSOL Multiphysics. The electric currents and heat transfer modules were two-way coupled to include the temperature-dependent resistivity. The model assumes a vacuum environment. Convective heat transfer through air is not taken into account, but radiation is included. The validity of the model was shown in our previous work.<sup>141</sup>



## 5.5 Appendix

## Temperature-dependence of the upconversion luminescence.

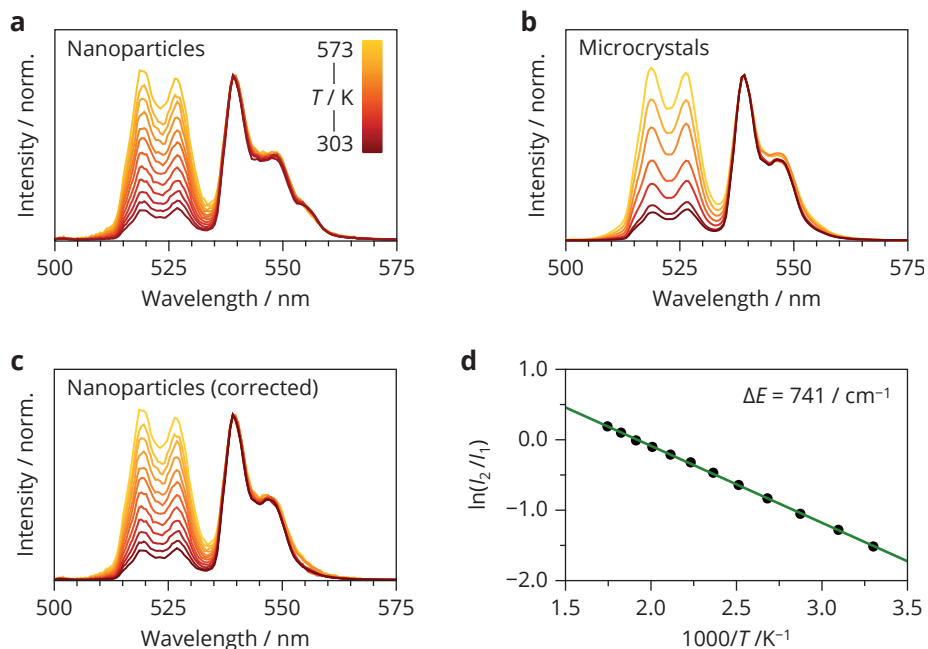


**Figure A5.1.** (a) Copy of Fig. 5.2c : Upconversion luminescence of NaYF<sub>4</sub>:Er<sup>3+</sup>(2%),Yb<sup>3+</sup>(18%) nanoparticles upon 980 nm excitation measured at various temperatures and an excitation intensity of 1.0 kW cm<sup>-2</sup>. (b) Same as in (a) but for microcrystalline NaYF<sub>4</sub>:Er<sup>3+</sup>(2%),Yb<sup>3+</sup>(18%) and an excitation intensity of 0.3 kW cm<sup>-2</sup>. (c) Same as in (a), but each spectrum is corrected for the <sup>2</sup>H<sub>9/2</sub> emission via the procedure that is depicted in Fig. 5.3d using the spectra in (b). (d) The logarithm of the ratio between the integrated intensities from (c) versus the reciprocal temperature (black dots). The integration boundaries for the <sup>2</sup>H<sub>11/2</sub> and <sup>4</sup>S<sub>3/2</sub> emissions are 510–530 nm and 537–560 nm, respectively. The green line is a fit of the experimental ratios to the Boltzmann model of Eq. 5.1. The  $\Delta E$  value obtained from the fit is slightly lower compared to the fit of the uncorrected data. We can explain this difference with temperature-dependent multi-phonon relaxation from <sup>2</sup>H<sub>9/2</sub>. Faster multi-phonon relaxation at higher temperatures reduces the contribution of the <sup>2</sup>H<sub>9/2</sub> emission (overlapping with <sup>4</sup>S<sub>3/2</sub>) giving an apparent faster decrease of the relative intensity of the <sup>4</sup>S<sub>3/2</sub> emission, which translates into a higher  $\Delta E$  than the actual  $\Delta E$  determined from the spectra after correction.

### Excitation-intensity dependence of the upconversion luminescence.

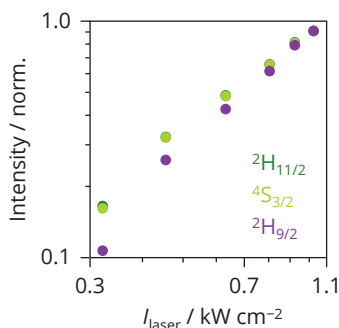


**Figure A5.2.** Peak intensities of the  ${}^2\text{H}_{11/2}$ ,  ${}^4\text{S}_{3/2}$ , and  ${}^2\text{H}_{9/2}$  emissions for various excitation intensities determined at 527 nm, 540 nm, and 550 nm, respectively.

### Possible applications of the temperature-mapping technique.

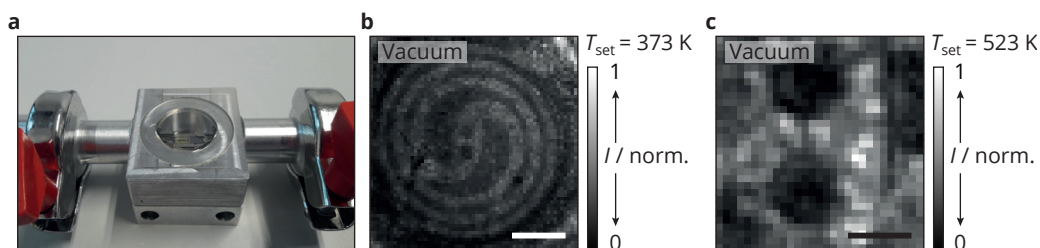


**Figure A5.3.** (a) Photograph of the set-up that was used for measurements at reduced pressure ( $10^{-5}$  mbar). The set-up consists of two metal tubes attached to a vacuum chamber containing a transparent window. One end of the metal tube is connected to a vacuum pump, while a microheater loaded into an electron-microscopy holder is inserted through the other end. The distance between the window and the microheater is large (more than 5 mm). This demonstrates the need for long-working distance objectives in some applications, inevitably leading to a lower NA. (b) Map of the integrated green luminescence from a microheater coated with upconversion nanoparticles at a set temperature of 373 K and a pressure of  $10^{-5}$  mbar. The intensity of the 980 nm excitation light was  $1.0 \text{ kW cm}^{-2}$ . The scale bar represents 50  $\mu\text{m}$ . (c) Same as in (b) but recorded with smaller a field-of-view, higher pixel density, and at a set temperature of 523 K. The scale bar represents 10  $\mu\text{m}$ .

### Correction for multi-photon upconversion.

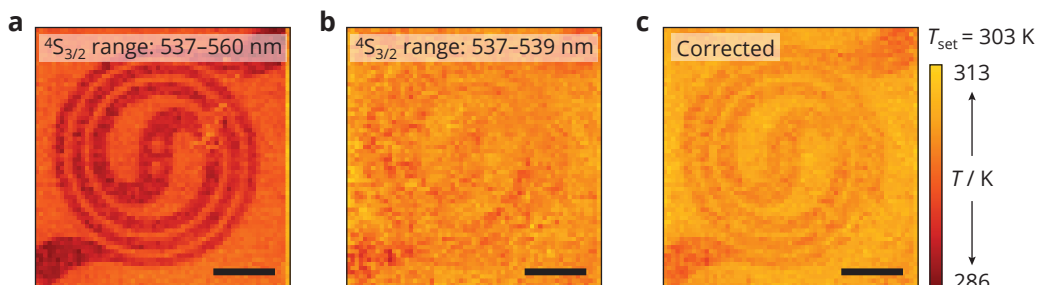


**Figure A5.4.** Temperature map of the microheater at a set temperature of 303 K (same data as Fig. 5.4b). The integration ranges of the  ${}^4\text{S}_{3/2}$  emission are 537–560 nm for (a) and (c) and 537–539 nm for (b). The data of panel (c) was corrected for multi-photon upconversion. The scale bars represent 50  $\mu\text{m}$

## Mapping temperature at different excitation intensities.

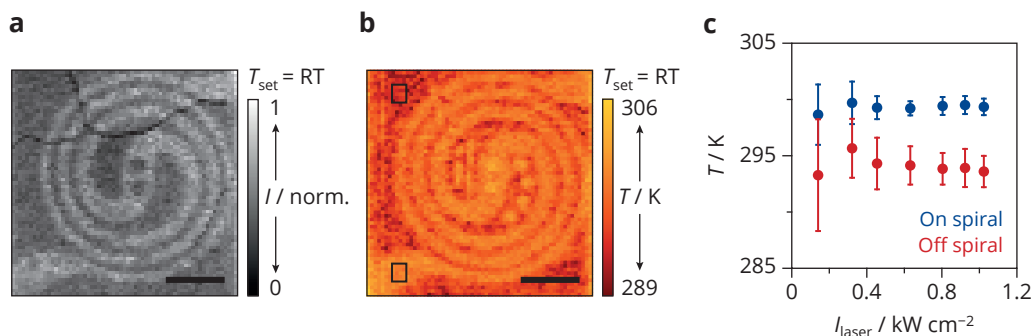


**Figure A5.5.** (a) Map of the integrated green luminescence from a microheater coated with upconversion nanoparticles, recorded at an excitation intensity of  $1.0 \text{ kW cm}^{-2}$  and a set temperature of  $303 \text{ K}$  measured in ambient atmosphere. The scale bar represents  $50 \mu\text{m}$ . (b) Converting the ratio of the emission peaks using the calibration of Fig. A5.1d yields a temperature map. Notably, the readout temperature on the heating spiral is higher than on the membrane, while Fig. 5.4b and Fig. A5.4 showed the opposite trend. We attribute this to a subtle difference in the thickness of the membrane that covers the microheater. (c) Average temperature on and off the heating spiral for various intensities of the  $980 \text{ nm}$  laser. The average temperature was determined from the pixels inside the black rectangles in (b).

## Temperature maps corresponding to the histograms of Fig. 5.5b.

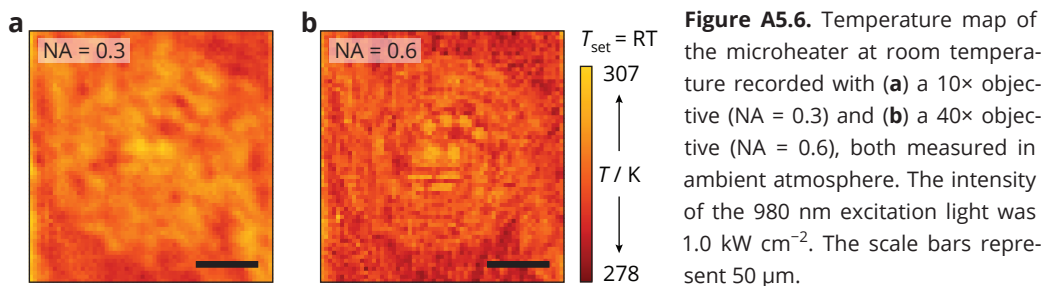


**Figure A5.6.** Temperature map of the microheater at room temperature recorded with (a) a  $10\times$  objective (NA = 0.3) and (b) a  $40\times$  objective (NA = 0.6), both measured in ambient atmosphere. The intensity of the  $980 \text{ nm}$  excitation light was  $1.0 \text{ kW cm}^{-2}$ . The scale bars represent  $50 \mu\text{m}$ .

## Non-normalized reflectivity.

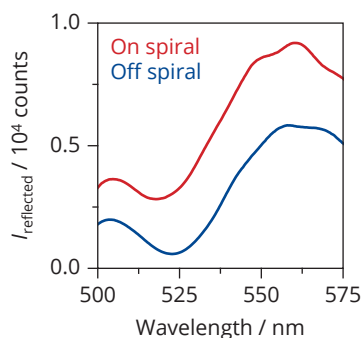


**Figure A5.7.** Non-normalized intensity of the reflected light from a halogen lamp that illuminated a location on and off the spiral of a bare microheater.

### Temperature profile at a set temperature of 303 K.

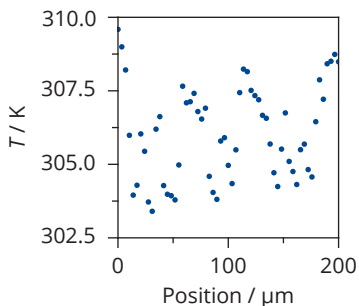


**Figure A5.8.** Horizontal line trace through the center of Fig. 5.4b. The measured temperatures in the center and on the sides of the heater are approximately similar, which enables determination of  $C_p$  for every pixel using the map in Fig. 5.4b.

**The photonic correction factor.** For a nanoparticle that experiences a different photonic environment than during the calibration, Eq. 5.1 is written as:

$$\frac{I_2}{I_1} = CC_p \exp\left(-\frac{\Delta E}{k_B T_p}\right). \quad (\text{A5.1})$$

Here,  $C$  is obtained with the calibration and  $C_p$  is a correction term that accounts for a variation in collection efficiencies of the two emission lines due to the photonic environment. We can re-arrange the above equation to find an expression for  $T_p$ .

$$T_p = -\frac{\Delta E/k_B}{\ln(I_2/I_1) - \ln(CC_p)}. \quad (\text{A5.2})$$

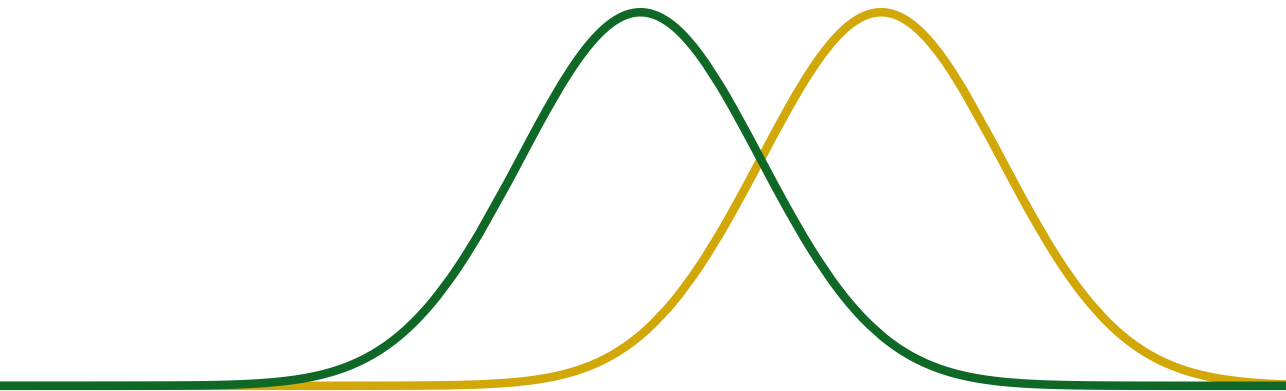
From Eq. 5.1 we know that

$$\ln(I_2/I_1) - \ln(C) = -\Delta E/k_B T, \quad (\text{A5.3})$$

and therefore

$$T_p = -\frac{\Delta E}{k_B(-\Delta E/k_B T) - k_B \ln(C_p)} = \frac{\Delta E}{\Delta E/T + k_B \ln(C_p)}. \quad (\text{A5.4})$$





---

# Chapter 6

## Enormous photonic artifacts in luminescence nanothermometry

### Abstract

In this Chapter, we experimentally demonstrate enormous systematic errors for luminescence thermometry in nanostructured environments. We place lanthanide-based luminescent nanothermometers at controlled distances up to 600 nm from a Au surface. Although this geometry supports no absorption nor scattering resonances, distortion of the emission spectra of the thermometers due to the modified density of optical states results in temperature readout errors of up to 100 K. Our simple analytical model explains the effects of thermometer emission frequencies, experimental equipment, and sample properties on the magnitude of the errors and inspires strategies to correct for them.

### Based on:

T.P. van Swieten, S.J.W. Vonk, A. Cocina and F.T. Rabouw, Enormous photonic artifacts in luminescence nanothermometry, *submitted*

---

## 6.1 Introduction

The emission of nanocrystals is often sensitive to temperature, which makes them ideal as remote thermometers. Recent applications in physics, chemistry, and biology exploit this to measure heat generation and thermal diffusion, for instance, during laser absorption in nanoplasmonics or exposure of living cells to photothermal therapy.<sup>34,147,150</sup> In most cases, the temperature is extracted from the emission spectrum of semiconductor, noble metal, or lanthanide-doped nanocrystals.<sup>151</sup> However, the community has recently come to realize that the recorded emission spectrum may be distorted by wavelength-dependent transmission by the sample or wavelength-dependent self-absorption by the thermometer material.<sup>31,33,152</sup>

More generally, the effect of the local density of optical states (LDOS) on luminescence thermometry has not yet been investigated. This is somewhat surprising, as the entire field of nanophotonics revolves around modulating light–matter interaction using the LDOS. For instance, photonic structures that guide, reflect, or scatter light, shape the LDOS at the position of an emitter and thereby steer spontaneous emission in certain directions.<sup>21,153,154</sup> The strongest light–matter interactions are achieved with structures that have a resonant response at the electromagnetic frequency of interest. For instance, cavities enable strong localization of light and antennas direct light of specific wavelengths.<sup>155–157</sup> Many sensing methods, including surface-enhanced Raman scattering and cavity-based immunoassays, rely on these resonances to improve the signal-to-noise ratio and measure small amounts of analyte molecules.<sup>158–160</sup> Placing an emitter or scatterer in the hotspot of a resonant photonic structure also modifies its output spectrum. This modification is intentional in some cases, such as for the suppression of phonon sidebands in the nitrogen-vacancy emission of diamond, but can also be an undesired distortion.<sup>161,162</sup> Lin *et al.* recently demonstrated how to correct for photonic distortions in plasmon-enhanced Raman scattering using the background fluorescence of plasmonic particles.<sup>159</sup> One should expect any inhomogeneous optical environment, *i.e.* a sample containing materials with different refractive indices, to feature a wavelength- and position-dependent LDOS that affects the signal from an embedded sensor. Indeed, our recent temperature-sensing experiments on a nonresonant microelectronic heater have shown temperature readout errors of more than 10 K (Chapter 5).<sup>35</sup> The potential impact of an inhomogeneous optical environment on sensing is often however neglected.<sup>30,152,163–166</sup>

This Chapter studies luminescent nanothermometers in different optical environments and quantifies photonic artifacts in the temperature readout. Specifically, we place a monolayer of Er<sup>3+</sup>- and Ho<sup>3+</sup>-doped nanocrystals at controlled distances from a planar Au mirror. This creates an open nonresonant geometry with no absorbing material between the nanothermometers and the detector, but the LDOS experienced by the emitters varies. The recorded emission spectra, from which the temperature is determined, depends strongly on the distance from the Au. This leads to errors in the temperature readout of up to 100 K using the Er<sup>3+</sup>-based thermometer and up to 250 K using the Ho<sup>3+</sup>-based thermometer, at a constant set temperature of 373 K. A simple self-interference model reproduces the experiment and explains the difference in readout error



between  $\text{Er}^{3+}$  and  $\text{Ho}^{3+}$  from the energy separation of their emission lines. The model further shows how the magnitude of the errors depend on the thermometer sensitivity, the numerical aperture (NA) of the microscope objective used, and on the sample properties. These insights can guide the optimized selection of the luminescent probe and the experimental setup to minimize photonic artifacts in luminescence thermometry and other optical sensing methods.

## 6.2 Results

We prepared lanthanide-doped colloidal nanocrystals as thermally and photo-stable sources of temperature-sensitive emission. The nanocrystals consist of crystalline  $\text{NaYF}_4$ , in which a fraction of the  $\text{Y}^{3+}$  ions is substituted by either 2%  $\text{Er}^{3+}$  and 18%  $\text{Yb}^{3+}$  or by 13.1%  $\text{Ho}^{3+}$  (Fig. A6.1). Fluoride-based materials are a popular choice due to their low vibrational energy, resulting in slow nonradiative relaxation and therefore high luminescence quantum yields.<sup>143</sup> In the  $\text{Er}^{3+}$ -doped nanocrystals, the luminescence is generated via an upconversion mechanism, where the  $\text{Yb}^{3+}$  ions transfer multiple 980-nm excitations to nearby  $\text{Er}^{3+}$  ions populating states that emit in the visible (Fig. 6.1a). The emission spectra of the nanocrystals in homogeneous optical environment show green emissions at 520 nm and 540 nm, which are due to radiative decay from the excited  ${}^2\text{H}_{11/2}$

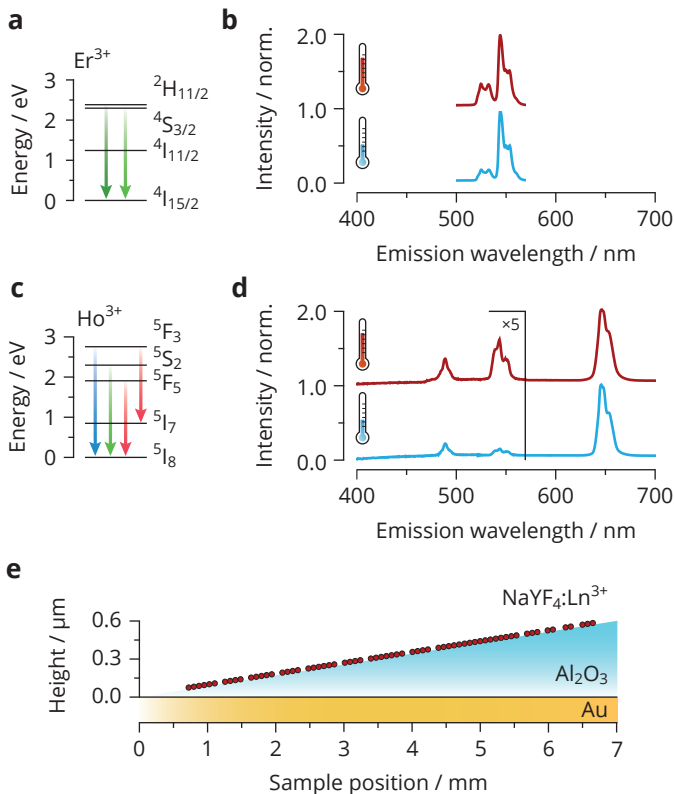


**Figure 6.1.** (a) Energy level diagram of  $\text{Er}^{3+}$  with the relevant emissions as colored arrows. (b) Luminescence spectrum of the  $\text{NaYF}_4:\text{Er}^{3+}(2\%),\text{Yb}^{3+}(18\%)$  nanocrystals excited at 980 nm in homogeneous environment. At elevated temperature, the relative intensity of the  ${}^2\text{H}_{11/2} \rightarrow 4\text{I}_{15/2}$  emission increases. (c) Same as in (a) but for  $\text{Ho}^{3+}$ . (d) Same experimental procedure as in (b), but for the  $\text{NaYF}_4:\text{Ho}^{3+}(13.1\%)$  nanocrystals excited at 445 nm. The blue and green emission lines are magnified by a factor 5. At elevated temperature, the red-to-green ratio decreases. (e) Schematic illustration of the substrate with controlled photonic environment. The ramped alumina spacer ( $\text{Al}_2\text{O}_3$ ) systematically varies the distance between the Au mirror and a sub-monolayer of nanocrystals doped with lanthanide ions ( $\text{Ln}^{3+}$ ).

and  $^4S_{3/2}$  states, respectively (Fig. 6.1b). Boltzmann-type coupling between these states changes the luminescence intensity ratio (*LIR*) with temperature, making it a useful measure for temperature. We excite the  $\text{Ho}^{3+}$ -doped nanocrystals with 445-nm light to obtain blue, green, and red emissions (Figs 6.1c–6.1d). The luminescence intensity ratio between green emission from the  $^5S_2$  state and red emission from the  $^5F_5$  and  $^5F_3$  states is determined by the competition between temperature-sensitive multi-phonon relaxation and temperature-independent Förster resonance energy-transfer.<sup>77</sup> We calibrate the thermal response of the  $\text{Er}^{3+}$  and  $\text{Ho}^{3+}$  luminescence in homogeneous optical environment using an external temperature controller (Fig. A6.2).

We deposited the lanthanide-doped nanocrystals on a Au mirror that is covered by an alumina spacer of variable thickness to create a continuous range of emitter–mirror distances (Figs. 6.1e and A6.3). The sputter-coated alumina spacer has a thickness increasing from 0 to 600 nm over a distance of 7 mm<sup>167</sup> and is covered with a monolayer of nanocrystals by spin-coating a dilute dispersion. A 40× air objective (NA = 0.75) was used to focus the excitation light and collect the luminescence of the nanocrystals at several locations on the substrate, corresponding to 10–15 nm steps in the emitter–mirror distance. The substrate was loaded on a heating stage for the measurements at controlled elevated temperatures.

Figs. 6.2a–6.2b compare the  $\text{Er}^{3+}$  emission spectra recorded from nanothermometers at room temperature and placed at two distances  $d$  from the planar Au mirror. Clearly, the spectra are different from each other and from the room-temperature emission spectrum of nanothermometers in a homogeneous environment (dashed lines; reproduced from Fig. 6.1b). The luminescence intensity ratio  $^2H_{11/2}/^4S_{3/2}$  is higher at  $d = 310$  nm (Fig. 6.2a) resembling a temperature higher than room temperature, and lower at  $d = 450$  nm (Fig. 6.2b) resembling a lower temperature.

The distortions in the recorded spectra can be understood in terms of the LDOS at the location of the nanothermometers. We model the  $\text{Er}^{3+}$  ions as sources of isotropic electric-dipole emission in a planar-mirror geometry with an alumina spacer of variable thickness  $d$  (Eqs. A6.1–A6.10).<sup>20,168–170</sup> In the nanocrystals of this study, the excited-state dynamics that populate the emitting excited states are much faster than radiative decay, which makes the relative populations of these states almost independent of the optical environment.<sup>29,77</sup> Hence, the photon emission rate into direction  $\Omega$  is directly proportional to the differential LDOS  $d\rho/d\Omega$ —*i.e.* the density of states propagating into direction  $\Omega$ —at the relevant photon energy. Fig. 6.2c presents calculated emission patterns for the green emissions of  $\text{Er}^{3+}$ . The patterns overlap differently with the range of collection angles, that is the NA, of our microscope objective (yellow cone). We define the density of photon modes within this range as the collected LDOS,

$$\rho_{\text{col}}(d, \omega) = \int_{\text{col}} \frac{\partial \rho}{\partial \Omega} d\Omega, \quad (6.1)$$

where the integration runs over the NA of our microscope objective. We then predict the recorded luminescence spectrum  $I(d, \omega)$  at distance  $d$  from the Au mirror by scaling the reference

spectrum of emitters in homogeneous optical environment  $I(\infty, \omega)$  with the calculated collected LDOS:

$$I(d, \omega) = I(\infty, \omega) \rho_{\text{col}}(d, \omega). \quad (6.2)$$

This expression holds only approximately if the LDOS affects feeding of the emitting levels (Eqs. A6.1–A6.5).

Fig. 6.2d shows the experimental intensity ratios between the two green  $\text{Er}^{3+}$  emission lines as a function of the emitter–mirror distance  $d$ , obtained by integrating the experimental spectra. The intensity ratio oscillates with  $d$  and the amplitude increases as a function of  $d$ . Qualitatively, this is explained by the collected LDOS at the individual emission energies that oscillate with slightly different periodicities, producing a beating wave for the recorded intensity ratio. We convert the ratios to readout temperatures using the calibration based on the Boltzmann model

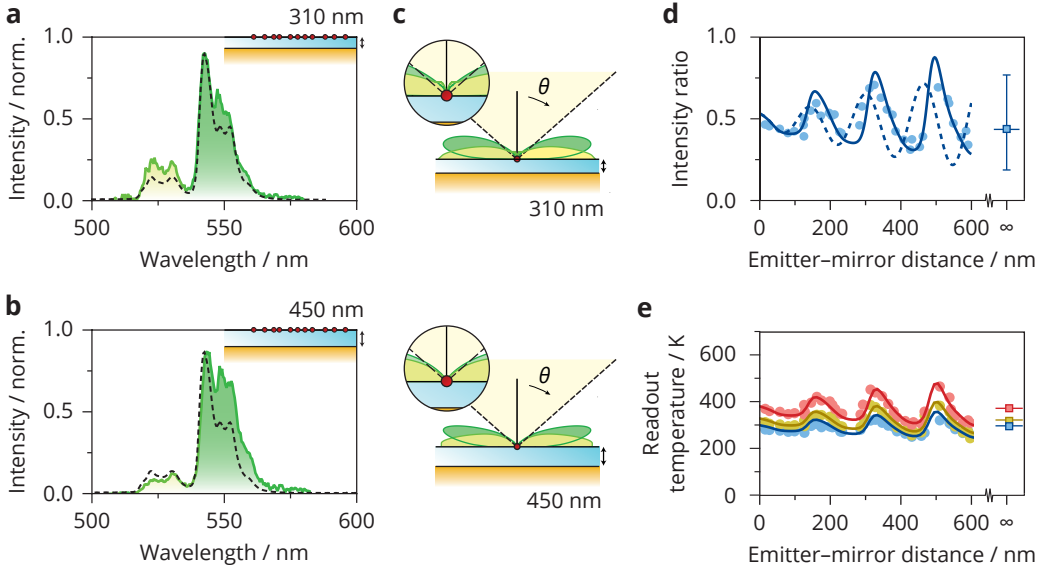


**Figure 6.2.** (a) Luminescence of the  $\text{Er}^{3+}$ -doped nanocrystals at an emitter–mirror distance of  $d = 310$  nm, recorded using focused 980-nm excitation. The dashed line is the reference spectrum recorded from a homogeneous environment. (b) Same as in (a) but for  $d = 450$  nm. (c) Calculated radiation patterns of emissions at 520 nm (dark green) and 540 nm (light green), for  $d = 310$  nm (top) and  $d = 450$  nm (bottom). The objective collects the fraction of the pattern that is within the NA (yellow area). (d) Experimental ratios between the  ${}^2\text{H}_{11/2}$  and  ${}^4\text{S}_{3/2}$  intensities, integrated between 519–537 nm and 537–544 nm, respectively, as a function of  $d$  (blue dots). Solid lines: intensity ratios calculated from the collected LDOS averaged over the emission lines (Eqs. A6.1–A6.10). Blue square at  $d = \infty$ : intensity ratio in homogeneous environment. Dashed: intensity ratio calculated using our simplified model (Eq. A6.17). The bars at  $d = \infty$  are the maximum distortions encountered in the experiments. (e) Experimental readout temperatures of the  $\text{Er}^{3+}$ -doped nanocrystals as a function of  $d$  measured at set temperatures of 298 K (blue dots), 323 K (orange dots), and 373 K (red dots). The colored solid lines are the readout temperatures calculated using the collected LDOS and the calibration based on the Boltzmann model.

(Figs. 6.2e and A6.2a). Readout errors are as large as 50 K when the substrate is at room temperature. Heating the substrate to 373 K increases the errors to up to 100 K as a result of the reduced sensitivity of Boltzmann thermometers at elevated temperatures (Eq. A6.31). The calculated intensity ratios based on Eq. 6.2 (solid line in Fig. 6.2d) match the experimental ratios. Converting them to expected readout temperatures using the calibration (solid lines in Fig. 6.2e) reproduces the experimental temperature errors. Our analysis thus demonstrates how the LDOS in a nonresonant optical environment can distort the emission spectrum of nanothermometers, translating into significant errors in temperature readout.

To investigate the impact of the emission energies we measure the luminescence of  $\text{Ho}^{3+}$ -doped nanocrystals on the ramped reflector. Compared to  $\text{Er}^{3+}$ , the energy difference between the temperature-sensitive emission lines of  $\text{Ho}^{3+}$  is larger by a factor seven. Figs. 6.3a–6.3b show that this causes a stronger modification of the emission spectrum. The radiation patterns presented in Fig. 6.3c further illustrate how the completely different collection of the green and red emissions distorts the spectrum. Consequently, the experimental red-to-green intensity ratios heavily oscillate with emitter–mirror distance (Fig. 6.3d; note the logarithmic  $y$ -scale). Translating the ratios to temperatures produces readout errors of more than 250 K (Fig. 6.3e and Fig. A6.2b). Remarkably, readout is impossible at the minima of the oscillations, because here the recorded intensity ratio is lower than possible in a homogeneous environment at any temperature. Conveniently, the green-to-green ratio of  $\text{Er}^{3+}$  and the red-to-green ratio of  $\text{Ho}^{3+}$  have a similar sensitivity to temperature.<sup>77</sup> This allows us to identify the energy of the two emission lines as one of the key parameters that determines the photonic distortions.

What is the relevance of our experiments for luminescence (nano)thermometry in applications? The large errors we found, in excess of 10% in absolute temperature, are unacceptable in most cases. Similar errors may be encountered for relevant samples with highly reflective interfaces, such as microelectronic devices. Smaller errors may be expected for dielectric or biological samples with lower reflectivities. To predict the magnitude of photonic distortions in different sample environments we consider the following simple geometry: a source of isotropic electric-dipole emission in a homogeneous medium at a distance  $d$  from an interface with reflectivity  $R$  that is independent of polarization, incidence angle, or energy of the emission (Eqs. A6.11–A6.18). Considering a microscope objective collecting all emission, the ratio of the collected LDOS at two emission lines with energy difference  $\Delta\omega$  and average energy  $\bar{\omega}$  is

$$\frac{\rho_2}{\rho_1} \approx 1 + \frac{c}{\bar{\omega}d} \frac{2\sqrt{R}}{1+R} \sin(\Delta\omega d/c) \cos(2\bar{\omega}d/c), \quad (6.3)$$

where  $c$  is the speed of light. As a function of  $d$ , the ratio behaves as a beating wave with envelope periodicity  $\Delta\omega$  and carrier-wave periodicity  $2\bar{\omega}$ . Eq. 6.3 can be adapted slightly to account for a finite NA in the experiment (Eq. A6.17). Figs. 6.2d and 6.3d compare the experimental luminescence intensity ratios (dots) with the ratios of our simplified model (dashed lines), which gives approximately matching maximum distortions. We therefore use this model to estimate the

maximum errors in temperature readout near an interface with arbitrary reflectivity  $R$ :

$$\Delta T_{\max} \approx \frac{1}{S_r} \frac{\Delta\omega}{\bar{\omega}} \frac{2\sqrt{R}}{1+R} \frac{1+\cos^3\theta_m}{1-\cos\theta_m}. \quad (6.4)$$

Here  $S_r$  is the relative sensitivity of the thermometer and  $\theta_m$  is the highest collection angle of the microscope objective. The weak dependence of  $\Delta T_{\max}$  on interface reflectivity, due to the factor  $2\sqrt{R}/(1+R)$  in Eq. 6.4, indicates that photonic artifacts are important even for samples with minor refractive-index contrasts. For example, thermometry in biological samples near a water–glass interface ( $R = 0.004$ ) would show maximum readout errors as large as 12% of those we found here near a mirror ( $R \approx 1$ ).<sup>171</sup> Eq. 6.4 further shows that thermometers with high  $\Delta\omega/\bar{\omega}$  are

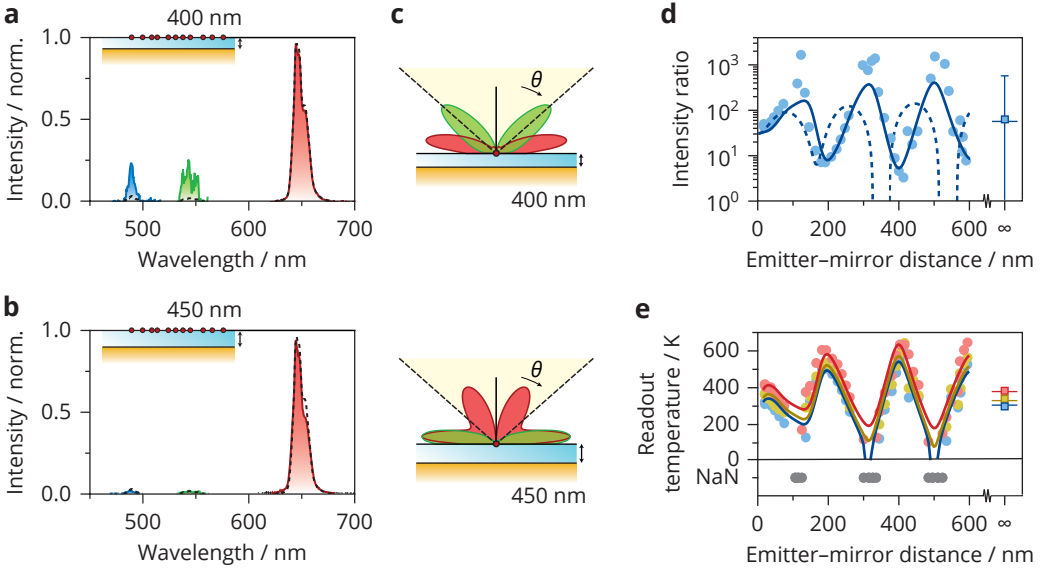


**Figure 6.3.** (a) Luminescence of the  $\text{Ho}^{3+}$ -doped nanocrystals at an emitter–mirror distance of  $d = 400$  nm, recorded using focused 445-nm excitation. (b) Same as in (a) but for  $d = 450$  nm. The dashed line is the reference spectrum recorded from a homogeneous environment. (c) Calculated radiation patterns of emissions at 535 nm (green) and 650 nm (red), for  $d = 400$  nm, (top) and  $d = 450$  nm (bottom). The objective collects the fraction of the pattern that is within the NA (yellow area). (d) Experimental ratios of the red-to-green intensities, integrated between 632–670 nm and 532–560 nm, respectively, as a function of  $d$  (blue dots). Solid lines: intensity ratio as a function of  $d$  calculated using the collected LDOS averaged over the emission lines (Eqs. A6.1–A6.10). Blue square at  $d = \infty$ : intensity ratio in a homogeneous environment ( $d = \infty$ ). Dashed line: approximate intensity ratio using a simplified model (Eq. A6.17). The bars at  $d = \infty$  represent the maximum distortions found experimentally. (e) Experimental readout temperatures of the  $\text{Ho}^{3+}$ -doped nanocrystals for various emitter–mirror distances measured at set temperatures of 298 K (blue dots), 323 K (orange dots), and 373 K (red dots). Solid lines: readout temperatures calculated using the collected LDOS and the shell model for a  $\text{Ho}^{3+}$  concentration of 13.1%.

particularly vulnerable to photonic artifacts. Infrared-emitting thermometers with small  $\bar{\omega}$ , which are the preferred choice in biological systems because of the large penetration depth of near-infrared light,<sup>33,152,172</sup> may thus not be the ideal choice when it comes to minimizing photonic artifacts. Our model predicts lower readout errors if a high-NA microscope objective ( $\theta_m$ ) collects the luminescence. Careful selection of the thermometer and the experimental equipment could thus minimize the distortions that are inherently induced by reflective interfaces in the sample.

Other practically relevant samples could contain metallic or dielectric scattering particles with dimensions on the nano- to micrometer scale instead flat reflective surfaces.<sup>151</sup> If the two emission lines of the thermometer have a different overlap with the frequency-dependent polarizability of the particle, scattering can distort the recorded intensity ratio and therefore cause readout errors. To further understand this we consider an electric-dipole emitter on the surface of a particle with a polarizability that is given by the Lorentz oscillator model (Eqs. A6.19–A6.28). We find that a strongly polarizable particle with a resonance close to the emission energies also causes temperature errors scaling linearly with  $\Delta\omega/\bar{\omega}$ , similar to a reflective interface. Fig. 6.4 plots the predicted maximum readout errors for the three discussed samples geometries. This highlights that various photonic structures encountered in thermometry experiments can cause errors of at least a few kelvin.

### 6.3 Discussion and conclusions

Our experimental observations and theoretical derivations show that photonic distortions in the spectrum of luminescent thermometers have serious implications for the accuracy of temperature measurements. These effects can be minimized by tuning the emission energies of the thermometer to low  $\Delta\omega/\bar{\omega}$  values or by collecting the luminescence with a high-NA microscope objective (Eqs. 6.3–6.4). However, even with an optimized experimental design the errors in temperature readout inevitably amount to a few kelvin (Fig. 6.4). A simple solution would be to quantify the frequency-dependent collected LDOS inside the sample environment, for instance with a reference measurement at room temperature, and use this to correct the recorded spectrum.<sup>35</sup> However, this solution would work only in static samples, because changes in the optical environment during the actual experiment would otherwise affect the LDOS dynamically. A strategy applicable to dynamic samples is the acquisition of real-time information of the LDOS at the position of the thermometer, as Lin *et al.* previously demonstrated for plasmon-enhanced Raman spectroscopy.<sup>159</sup> Applied to luminescence thermometry, this would require embedding a reference emitter with a broad and temperature-insensitive emission spectrum into the sample, whose spectrum would provide real-time information on the LDOS during the experiment.<sup>151</sup> Strategies such as these make sample preparation, experiments, and analysis more cumbersome, but enhance the accuracy of luminescence thermometry.

Our work highlights the pitfalls of luminescence (nano)thermometry that are induced by inhomogeneous optical environments, and it provides strategies to minimize them. The conclusions

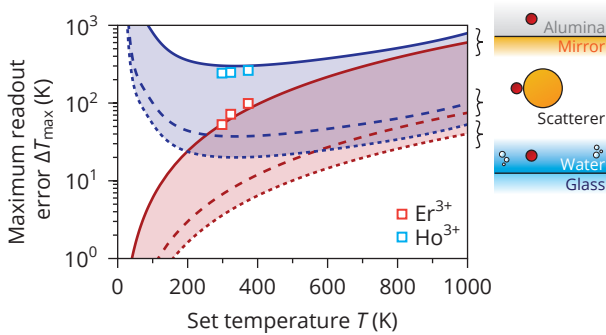


**Figure 6.4.** (a) Readout errors of the  $\text{Er}^{3+}$ - and  $\text{Ho}^{3+}$ -doped thermometers located in alumina near a perfect reflector (thin solid lines), on the surface of a strongly polarizable particle (thick dashed lines), and in water near a slab of glass (thin dashed lines) for an NA of 0.75. The squares are the experimental readout errors.

are not only relevant for thermometry but are also important for other optical sensing methods.

## 6.4 Methods

**Sample preparation.** A four-inch Si wafer was diced into  $1 \times 1 \text{ cm}^2$  chips. Each chip was cleaned by ultrasonication for 2 minutes in acetone and in isopropylalcohol, and blown dry with  $\text{N}_2$ . Then, a layer of 280-nm-thick positive electron-beam resist (Allresist, CSAR AR-P 6200.09) was spincoated on the chip. Reference marks were etched using electron-beam lithography. After electron-beam exposure (Vistec Lithography, EBPG 5200+), the resist was developed (Allresist, AR 600-546) for 1 minute. The marks were etched into Si using a HBr-based inductively-coupled-plasma reactive-ion etching procedure. The resist was removed by exposing the surface to an oxygen plasma (PVA TePla, GIGAbatch 310M) at 600 W for 5 minutes. Finally, the chip was cleaned in a piranha solution, consisting of a 1:1 mix of sulfuric acid (Sigma-Aldrich, 95.0–97.0%) and hydrogen peroxide (VWR Chemicals, 30%), for 15 minutes.

The silicon substrates were loaded into a thermal evaporator (Kurt J. Lesker, Nano 36). Approximately 200 nm of Au (Umicore pellets) was evaporated onto the substrate at a rate of  $1 \text{ nm s}^{-1}$ . The sample consisting of a Si substrate coated with Au layer was then transferred to the vacuum chamber of a magnetron sputterer (PVD75, Kurt Lesker) and mounted on a four-inch rotating holder for deposition of  $\text{Al}_2\text{O}_3$ . The evaporator chamber was evacuated to a pressure below  $8 \times 10^{-6}$  Torr. A custom-built metallic shadow mask was then mounted on a non-rotating support at close distance from the substrate, partially covering the sample from the sputtered material.  $\text{Al}_2\text{O}_3$  was deposited via reaction of Al sputtered from an Al target (2.00 inch diameter  $\times$  0.125 inch thick, 99.999% purity, Kurt Lesker) and partial  $\text{O}_2$  injection in addition to Ar during the deposition. The volumetric flow ratio  $\text{O}_2/\text{Ar}$  was kept to 20%, which gave an overall  $\text{Al}_2\text{O}_3$  evaporation rate of  $7 \text{ nm min}^{-1}$ . By rotating the holder with respect to the fixed shadow mask during deposition, the area of the sample covered by the mask was gradually decreased such to expose fresh Au areas to the material flux. The sample holder was rotated during the deposition every 8 minutes by 0.6 degrees for 14 times.

The procedure of Geitenbeek *et al.* was used to prepare lanthanide-doped nanocrystals.<sup>43</sup> A

monolayer of nanocrystals was deposited on the ramped reflector by spincoating from a diluted dispersion (concentration  $\sim 5 \text{ mg mL}^{-1}$ ).

**Spectroscopy experiments.** All photoluminescence measurements were performed using a home-built optical setup based on a Nikon Ti-U inverted microscope body. For the upconversion  $\text{NaYF}_4:\text{Er}^{3+}(2\%),\text{Yb}^{3+}(18\%)$  nanocrystals, a 980-nm laser (OBIS LX 980 nm) was guided to the sample by a 50/50 beamsplitter (Thorlabs, BSW26R) and focused by a 40 $\times$  Nikon CFI Plan Fluor (NA = 0.75) air objective. The  ${}^2\text{H}_{11/2} + {}^4\text{S}_{3/2} \rightarrow {}^4\text{I}_{15/2}$  emission lines were selected using a band-pass filter (Chroma, ET535/70M). For the  $\text{NaYF}_4:\text{Ho}^{3+}(13.1\%)$  nanocrystals, a 445-nm laser (OBIS LX 445 nm FC) was guided to the sample by a long-pass dichroic (Semrock, FF01-468/SP-25) in combination with a short-pass filter (Semrock, FF01-468/SP-25) to reject the long-wavelength tail of the laser line. A long-pass filter (Semrock, BLP01-458R-25) was used to block the reflected excitation light.

All lanthanide emission was collected by the same objective and collimated outside of the microscope using a relay lens system and subsequently focused on a mechanical slit (200  $\mu\text{m}$ ) at the entrance of an Andor Kymera 193i spectrometer and dispersed with a 150 lines/mm grating blazed at 500 nm on an Andor iXon EMCCD. All emission spectra were corrected for the wavelength-dependent collection and detection efficiency using an Ocean Optics HL-3 calibration lamp.

## 6.5 Appendix

**LDOS-dependence of the luminescence intensity ratio.** In this work, we characterize the influence of the photonic environment on the *LIR* of two emission lines from a luminescence thermometer. We will show that there is a fundamental but subtle difference of the LDOS dependence on the *LIR* for Boltzmann thermometers and energy-transfer thermometers.

We start by considering a Boltzmann thermometer with energy levels A and B. B is higher in energy than A by an amount  $\Delta E$ . If the population exchange between the two levels by phonon absorption/emission is much faster than decay from the levels, then their fractional populations  $p_A, p_B$  are in a quasi-Boltzmann equilibrium. We approximate in our work that the  $\text{Er}^{3+}$ -based thermometer remains a Boltzmann thermometer in all photonic environments since the LDOS

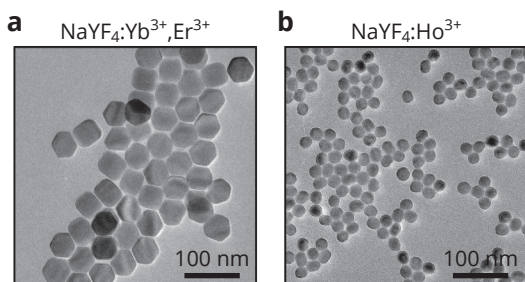


**Figure A6.1.** (a) Electron-microscopy image of  $\text{NaYF}_4:\text{Er}^{3+}(2\%),\text{Yb}^{3+}(18\%)$  nanoparticles. The particles have a diameter of  $46.3 \pm 3.3 \text{ nm}$  (mean  $\pm$  standard deviation). (b) Same as (a), but for  $\text{Ho}^{3+}$ -doped nanocrystals with a diameter of  $22.4 \pm 1.8 \text{ nm}$  (mean  $\pm$  standard deviation). The electron microscopy images were acquired with a Tecnai 20 transmission electron microscope.



does not boost the radiative decay rate to values comparable with (or faster than) the nonradiative coupling rate between the levels. The total photon emission rate  $k_{\text{tot},i}$  from level  $i$  is then given by

$$k_{\text{tot},i}(\omega_i, T) = p_i(T) \rho_{\text{tot}}(\omega_i) k_{r,i}, \quad (\text{A6.1})$$

where the rate constant for radiative decay in a homogeneous environment  $k_{r,i}$  is distorted by the photonic environment via the total LDOS  $\rho_{\text{tot},i}$  (normalized to the LDOS in a homogeneous environment) at the emission frequency  $\omega_i$ .

In an experiment, not all photon modes can be collected by the microscope objective. The collected photon emission rate

$$k_{\text{col},i}(\omega_i, T) = p_i(T) \rho_{\text{col}}(\omega_i) k_{r,i} \quad (\text{A6.2})$$

accounts for the experimental collection efficiency  $\rho_{\text{col}}/\rho_{\text{tot}}$  at the emission frequency  $\omega_i$  and is proportional to the recorded signal strength at frequency  $\omega_i$ . The *LIR* of a Boltzmann thermometer with two infinitely narrow emission lines equals the ratio of collected photon emission rates of the lines:

$$Y_{\text{BM}}(T) = \frac{k_{\text{col},B}(\omega_B, T)}{k_{\text{col},A}(\omega_A, T)} = \frac{k_{r,B} \rho_{\text{col}}(\omega_B)}{k_{r,A} \rho_{\text{col}}(\omega_A)} e^{-\Delta E/k_B T}, \quad (\text{A6.3})$$

which only depends on  $\rho_{\text{col}}$  at the two emission frequencies, not on  $\rho_{\text{tot}}$ .

Next, we consider an energy-transfer thermometer with energy levels A and B where the populations are fed from some higher energy level on a time scale comparable to radiative decay from A and B. Here, the population of the energy levels is, in general, determined by competition between temperature-dependent nonradiative processes, temperature-independent nonradiative processes, and LDOS-dependent radiative processes. Following the same derivation as for the Boltzmann thermometer, but with LDOS-dependent fractional populations of the energy levels, we obtain a general expression for the *LIR* from a thermometer with infinitely narrow emission lines:

$$Y_{\text{ET}}(T) = \frac{p_B[\rho_{\text{tot}}(\omega_B) k_{r,B}; T]}{p_A[\rho_{\text{tot}}(\omega_A) k_{r,A}; \rho_{\text{tot}}(\omega_B) k_{r,B}; T]} \frac{k_{r,B} \rho_{\text{col}}(\omega_B)}{k_{r,A} \rho_{\text{col}}(\omega_A)}. \quad (\text{A6.4})$$

We describe here that the populations of the levels depend on the total LDOS at the emission frequencies  $\omega_A$  and  $\omega_B$  and the *LIR*, additionally, on the collected LDOS. However, in the limit that radiative processes are slow compared to nonradiative processes, the dependence on total LDOS drops out and we can approximate that

$$Y_{\text{ET}}(T) \approx \frac{p_B(T) k_{r,B} \rho_{\text{col}}(\omega_B)}{p_A(T) k_{r,A} \rho_{\text{col}}(\omega_A)}. \quad (\text{A6.5})$$

**Modelling the intensity ratio from a self-interference model.** To calculate the luminescence intensity ratio of the lanthanide-doped nanoparticles in our experiments, we model our sample as a four-layer mirror geometry (Fig. 6.1e). All optical transitions of  $\text{Er}^{3+}$  and  $\text{Ho}^{3+}$  studied in this work are electric-dipole transitions.<sup>173</sup> In our model, layer 1 is the central layer containing the emitters with constant thickness  $h$ , layer 2 is the top semi-infinite layer with dielectric constant  $\varepsilon_2$ , layer 3 is the layer below the emitter with variable thickness  $d$  and dielectric constant  $\varepsilon_3$ , and layer 4 is the semi-infinite bottom layer. We assume a fixed distance between the emitters and the top layer  $s_{12} = h$  such that the emitters are located on the interface between layers 1 and 3 and the separation between the emitters and interface 3/4 is varied with the thickness  $d$  of the spacer layer 3. In this geometry, the polarization-averaged LDOS for an electric-dipole transition is given by:<sup>168</sup>

$$\frac{\rho}{\rho_0} = \int_0^{u_m} \text{Im} \left\{ \left[ \frac{(1 + r_s^{12} e^{-2k_0 \sqrt{\varepsilon_1} l_1 s_{12}})(1 + r_s^{134})}{1 - r_s^{12} r_s^{134} e^{-2k_0 \sqrt{\varepsilon_1} l_1 s_{12}}} \right. \right. \\ \left. \left. + \frac{(1 + r_p^{12} e^{-2k_0 \sqrt{\varepsilon_1} l_1 s_{12}})(1 + r_p^{134}) - 2u^2 (r_p^{12} e^{-2k_0 \sqrt{\varepsilon_1} l_1 s_{12}} + r_p^{134})}{1 - r_p^{12} r_p^{134} e^{-2k_0 \sqrt{\varepsilon_1} l_1 s_{12}}} \right] \frac{u}{l_1} \right\} du, \quad (\text{A6.6})$$

where  $\rho_0$  is the radiative transition rate of the nanocrystal in a homogeneous optical environment with dielectric constant  $\varepsilon_1$ ,  $k_0 = 2\pi/\lambda$  is the vacuum wave vector,  $l_j = -i\sqrt{\varepsilon_j/\varepsilon_1 - u^2}$ , and  $u = k_{\parallel}/k$  the fractional in-plane momentum of electromagnetic radiation. From this expression we can calculate the total LDOS  $\rho_{\text{tot}}$  using  $u_m = \infty$  and the collected LDOS  $\rho_{\text{tot}}$  using  $u_m = \text{NA}/\sqrt{\varepsilon_1}$ , where NA is the numerical aperture of the microscope objective. The collected LDOS is dependent on the spacer thickness  $d$  via the three-layer Fresnel coefficients  $r_{s,p}^{134}$ , given by

$$r_{s,p}^{134} = \frac{r_{s,p}^{13} + r_{s,p}^{34} e^{-2k_0 \sqrt{\varepsilon_1} l_3 d}}{1 + r_{s,p}^{13} r_{s,p}^{34} e^{-2k_0 \sqrt{\varepsilon_1} l_3 d}}, \quad (\text{A6.7})$$

where  $r_{s,p}^{13}$  and  $r_{s,p}^{34}$  are the Fresnel coefficients for reflection of s- and p-polarized light on the interface between layers 1/3 and 3/4, respectively. The Fresnel coefficient for the interface between medium  $i$  and  $j$  is given in terms of the dielectric constants  $\varepsilon_i$  and the emission direction  $u$  by:

$$r_s^{ij} = \frac{l_i - l_j}{l_i + l_j}, r_p^{ij} = \frac{\varepsilon_j l_i - \varepsilon_i l_j}{\varepsilon_j l_i + \varepsilon_i l_j}. \quad (\text{A6.8})$$

In our experiments, layer 1 consists of  $\text{NaYF}_4$  nanoparticles ( $\varepsilon_1 = 2.2$ )<sup>169</sup> with fixed thickness  $s_{12} = h = 20$  nm, layer 2 is air with dielectric constant  $\varepsilon_2 = 1$ , layer 3 is an  $\text{Al}_2\text{O}_3$  spacer with variable thickness  $d$  ( $\varepsilon_3 = 2.78$ ) and the bottom layer 4 is a reflective Au surface (wavelength-dependent dielectric constant  $\varepsilon_4$  obtained from McPeak *et al.*)<sup>170</sup>

In a homogeneous optical environment, all lanthanide ions in a nanocrystal have the same

emission spectrum. Most emission peaks in the spectrum of a lanthanide are due to a set of transitions between the excited-state multiplet and the ground-state multiplet. Both multiplets can be split by the crystal field of the host lattice, which gives rise to the distinct lineshape of lanthanide emission. The splitting of the excited-state multiplet due to the crystal field is typically much smaller than the thermal energy, and thermal population exchange is therefore much faster than radiative decay. The population distribution within a crystal-field-split multiplet is therefore unaffected by the total LDOS. The population distribution between different multiplets relevant for thermometry may or may not depend on LDOS, as discussed above (Eqs A6.1–A6.5).

$\text{Er}^{3+}$  used in this work acts as a Boltzmann thermometer and the multiplet populations are independent of LDOS. The emission spectrum  $I(d, \omega)$  collected from nanocrystals at a distance  $d$  from the reflector is easily calculated from the emission spectrum in a homogeneous environment  $I(\infty, \omega)$  and the collected LDOS  $\rho_{\text{col}}(d, \omega)$  (Eq. 6.1). We measured the homogeneous emission spectrum  $I(\infty, \omega)$  of a film of nanocrystals embedded between a glass coverslip and PMMA (all

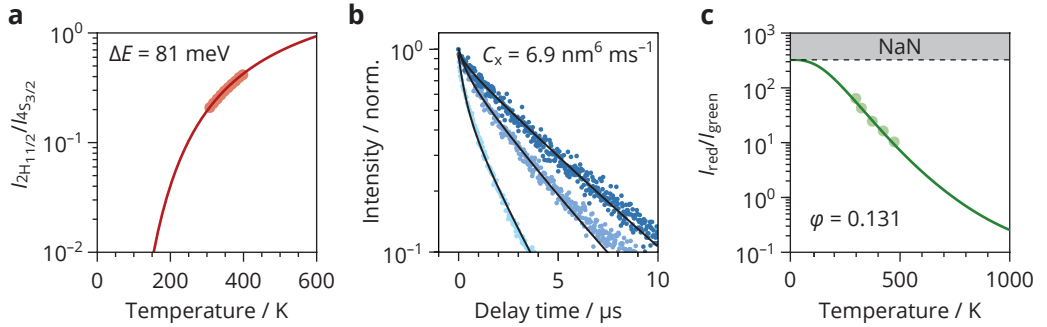


**Figure A6.2.** Calibration of the luminescence thermometers. **(a)** Intensity ratio of  ${}^2\text{H}_{11/2}$  and  ${}^4\text{S}_{3/2}$  emission lines (red dots) of the  $\text{NaYF}_4:\text{Er}^{3+},\text{Yb}^{3+}$  nanocrystals in a homogeneous optical environment (film of nanocrystals embedded between PMMA and glass coverslip) for set temperatures between 303 K and 393 K. We fit the data points using the Boltzmann model in homogeneous optical environment (red solid line, Eq. 5.1), which yielded  $\Delta E = 81$  meV. We use the fitted line to convert the measured intensity ratio  $Y$  on the ramped reflector to readout temperatures  $T'$  in Fig. 6.2e. **(b)** Photoluminescence decay curves of the blue energy level (445 nm excitation) of  $\text{Ho}^{3+}$ -doped microcrystalline  $\text{NaYF}_4$ . The  $\text{Ho}^{3+}$  concentration in the studied samples is 0.1% (dark blue), 5% (blue), and 12% (light blue). We use a global-fitting procedure based on a microscopic cross-relaxation model and find a cross-relaxation constant  $C_x = 6.9 \text{ nm}^6 \text{ ms}^{-1}$ . **(c)** Same as **(a)**, but for the  $\text{Ho}^{3+}$ -doped nanocrystals. The solid red line is an analytical calculation of the red-to-green intensity ratio as a function of temperature using the radiative rates, energy-transfer rates, multi-phonon relaxation rates of the energy levels in the visible and a statistical distribution of local-ion environments in  $\text{NaYF}_4$  (doping concentration 13.1%).<sup>77</sup> We adapted the cross-relaxation constant of the blue energy level **(b)** to account for a slighter higher intensity ratio  $Y$  over the entire temperature range for doped  $\text{NaY}_{1-x}\text{Ho}_x\text{F}_4$  (this work) versus  $\text{NaY}_{0.75-x}\text{Gd}_{0.25}\text{Ho}_x\text{F}_4$ . Again, the solid line is used to convert the intensity ratio  $Y$  measured on the ramped reflector to a readout temperature in Fig. 6.3e. We observe that intensity ratios  $Y > 160$  are unphysical since they exceed the highest possible red-to-green ratio in a homogeneous optical environment posed by the radiative decay rates and the steady-state populations of the emitting levels at zero kelvin.

refractive indices  $n \sim 1.5$ ). We then calculate the expected intensity ratio  $Y$  between the two emission lines of the  $\text{Er}^{3+}$ -based thermometer (Fig. 6.2d) as a function of emitter–mirror separation  $d$  by integrating Eq. 6.1 over the emission lines:

$$Y(d) = \frac{C_R \int_{\omega_R} I(\infty, \omega) \rho_{\text{col}}(d, \omega) d\omega}{C_G \int_{\omega_G} I(\infty, \omega) \rho_{\text{col}}(d, \omega) d\omega}. \quad (\text{A6.9})$$

where  $\omega_{G1}$  and  $\omega_{G2}$  denote the range of emission frequencies corresponding to the two transitions.

For  $\text{Ho}^{3+}$ , Eq. A6.9 holds only approximately, because  $\text{Ho}^{3+}$  is an energy-transfer thermometer and the populations of the multiplets emitting green, and red light depend weakly on  $\rho_{\text{tot}}$ . We account for this with correction factors  $C_R$  and  $C_G$  in the calculation of expected intensity ratio  $Y$  from the experimental spectrum  $I(\infty, \omega)$  in the homogeneous environment:

$$Y(d) = \frac{C_R \int_{\omega_R} I(\infty, \omega) \rho_{\text{col}}(d, \omega) d\omega}{C_G \int_{\omega_G} I(\infty, \omega) \rho_{\text{col}}(d, \omega) d\omega}. \quad (\text{A6.10})$$

To calculate  $C_R$  and  $C_G$ , we use the full model for the excited-state dynamics of the  $\text{Ho}^{3+}$ -based thermometer,<sup>77</sup> but with increased/decreased radiative rates  $k_{r,i} \rightarrow \rho_{\text{tot}}(\omega_i)k_{r,i}$  depending on the thermometer–reflector separation  $d$ . Here  $\rho_{\text{tot}}$  is calculated at the center emission frequencies of the  $\text{Ho}^{3+}$  emission lines:  $\{2\pi c/\omega_B, 2\pi c/\omega_G, 2\pi c/\omega_R\} = \{485, 540, 650\}$  nm. The altered radiative decay rates change the photon emission yields from the red- and green-emitting levels by an amount  $C_R$  and  $C_G$ , respectively. Both correction factors are approximately equal to unity for all values of  $d$ , so the photonic distortions of the  $\text{Ho}^{3+}$  can still be understood conceptionally from the simple Eq. 6.1.

**Intensity-ratio distortions for emitters near reflective surfaces.** Here, we derive a simplified model for the photonic artifacts in luminescence thermometry to gain insights into the effects of various experimental parameters.

We consider an isotropic electric-dipole source in a homogeneous medium with dielectric

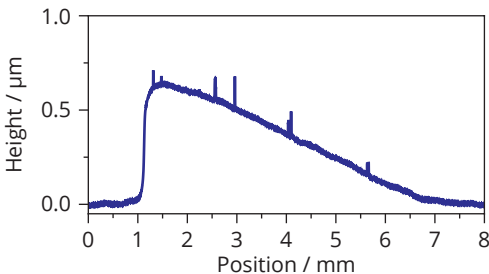


**Figure A6.3.** Measurements of the  $\text{Al}_2\text{O}_3$  ramp on the silicon–Au sample using a stylus profilometer (DektakXT, Bruker). The distance between the starting position of the profile scan and an engraved marking on the sample was measured to determine the spacer thickness for all optical measurements at different positions.

constant  $\varepsilon_1$  with  $z$ -coordinate  $z = d$  above a reflective 2D interface at  $z = 0$  (Fig. A6.4a). By reciprocity, the electric-field strength of light emitted into direction  $(\theta, \varphi)$  is proportional to the electric-field strength of a plane wave coming from  $(\theta, \varphi)$  on the position of the emitter. This is equal to

$$\mathbf{E}_{p,s} = \mathbf{E}_{p,s}^0 + \mathbf{r}^{p,s} \odot \mathbf{E}_{p,s}^0 e^{2ikd \cos\theta}, \quad (\text{A6.11})$$

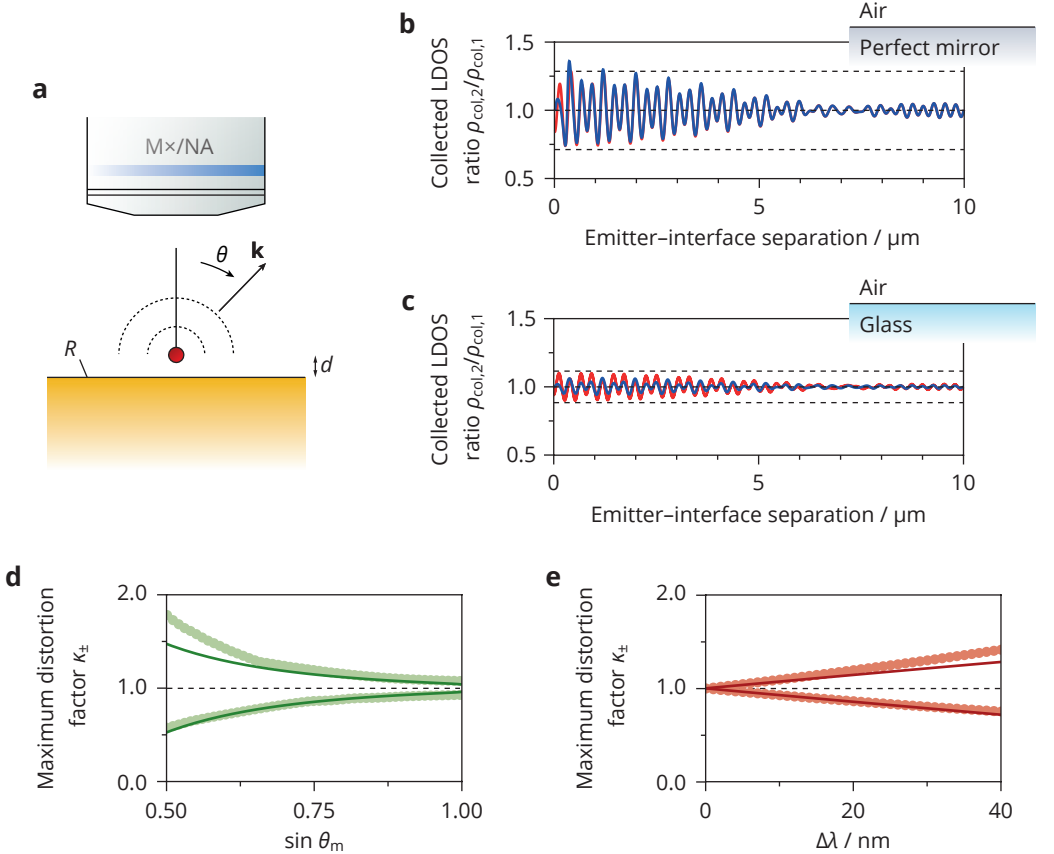


**Figure A6.4.** Intensity-ratio oscillations near an interface. (a) Source of electric-dipole radiation in medium 1 with permittivity  $\varepsilon_1$  at distance  $d$  from an interface with reflectivity  $R$ . (b) Collected intensity ratio versus emitter-interface separation for two emission lines at 520 nm and 540 nm near a perfect mirror ( $R = 1$ ) for the analytical model (blue line, Eq. A6.17) and the approximation (red line, Eq. A6.18) for a numerical aperture  $\text{NA} = 0.75$ . The dashed lines show the maximum distortion factors  $\kappa_{\pm}$  calculated with reflectivity  $R = 1$ , numerical aperture  $\text{NA} = 0.75$ , and relative frequency difference  $\Delta\omega/\bar{\omega} = 0.038$ . (c) Same as (b), but for a glass-air interface ( $R = 0.04$ ). The amplitude of the oscillations is approximately 40% of the amplitude for the perfect mirror. (d) Maximum distortion factor  $\kappa_{\pm}$  versus  $\text{NA} = \sin \theta_m$  for two emission lines at 520 nm and 540 nm from the analytical model (Eq. A6.17, dots) and the approximation (Eq. A6.18, solid lines). (e) Maximum distortion factor  $\kappa_{\pm}$  for an emission line at 520 nm and a redshifted emission line with wavelength difference  $\Delta\lambda$ , from numerically optimizing the analytical model (Eq. A6.17, dots) and evaluating the approximation (Eq. A6.18, solid lines).

for s and p-polarized light, where  $k = \sqrt{\epsilon_1} 2\pi/\lambda$ . Here,  $\mathbf{E}_{p,s}^0$  are electric-field vectors for s/p-polarized plane waves coming from  $(\theta, \varphi)$ , and  $\mathbf{r}_{p,s}$  takes into account the amplitude and direction of the electric field of the reflected plane wave given by

$$\mathbf{E}_p^0 = \begin{pmatrix} \cos\theta \cos\varphi \\ \cos\theta \sin\varphi \\ \sin\theta \end{pmatrix}, \mathbf{E}_s^0 = \begin{pmatrix} -\sin\varphi \\ \cos\varphi \\ 0 \end{pmatrix}, \mathbf{r}_p = r_p \begin{pmatrix} 1 \\ 1 \\ -1 \end{pmatrix}, \text{ and } \mathbf{r}_s = r_s \begin{pmatrix} 1 \\ 1 \\ 1 \end{pmatrix}. \quad (\text{A6.12})$$

We will make the approximation that the Fresnel coefficients are angle- and polarization-independent,  $r_s(\theta) = r_p(\theta) = r$ , and purely real. The emission intensity  $I_{\text{tot}}$  into a direction  $(\theta, \varphi)$ , equal to the incoherent sum of s- and p-polarized light, is given then by

$$I_{\text{tot}}(\theta) = \frac{1}{2} \left( |\mathbf{E}_p|^2 + |\mathbf{E}_s|^2 \right) = 1 + R + 2r(1 - u^2) \cos(2kd \cos\theta), \quad (\text{A6.13})$$

We can calculate the maximum collected LDOS  $\rho_{\text{col,max}}$ , achieved in the limit that the microscope objective collects all light propagating in the positive  $z$ -direction, by integrating the emission intensity  $I_{\text{tot}}$  over all possible emission angles  $\theta \in [0, \pi/2]$  into the half-space of the microscope objective

$$\rho_{\text{col,max}} = \int_0^{\pi/2} I_{\text{tot}}(\theta) \sin\theta d\theta \approx 1 + R + \frac{r}{kd} \sin(2kd), \quad (\text{A6.14})$$

where in the second step we have neglected terms of order  $kd^{-2}$  and higher since these terms do not significantly contribute in our experiments ( $kd > 1$  for 540-nm emission and emitter–mirror separations  $> 100$  nm). We observe that the maximum collected LDOS has a constant offset and term that oscillates with emitter–interface separation  $d$  at a frequency  $2k$ . At large  $kd$ , the amplitude of the oscillation is small with respect to the constant offset.

We can account for the finite NA of microscope objectives by integrating Eq. A6.14 over the range of emission angles  $\theta \in [0, \theta_m]$  that can be collected. We obtain a modified expression for the collected LDOS

$$\rho_{\text{col}} \approx (1 + R)(1 - \cos\theta_m) + \frac{r}{kd} \left[ \sin(2kd) - \cos\theta_m \sin(2kd \cos\theta_m) \right], \quad (\text{A6.15})$$

where again we neglected terms of order  $kd^{-2}$  and higher. We see that  $\rho_{\text{col}}$  now has two terms that oscillate with  $d$  at slightly different frequencies  $2k$  and  $2k \cos\theta_m$ . At large  $kd$ , the amplitude of the oscillation is still small with respect to the constant offset.

To illustrate the effect of reflectivity  $R$ , NA, and frequency difference  $\Delta\omega$  on the intensity-ratio distortions, we calculate the collected LDOS ratio  $\rho_{\text{col},2}/\rho_{\text{col},1}$  between two emission lines at frequencies  $\omega_1 = k_1c$  and  $\omega_2 = k_2c$ . We use that, for large values of  $d$ , the amplitude of the oscillating

terms in  $\rho_{\text{col}}$  (Eq. A6.15) is much smaller than the constant offset. This allows us to expand  $\rho_{\text{col},1}^{-1} = [a + f(kd)]^{-1} = a^{-1} + a^{-2}f(kd) + \mathcal{O}[f(kd)^2]$ , where  $a$  and  $f(kd)$  denote the constant and oscillating terms in  $\rho_{\text{col},1}$ . We arrive at the expression

$$\frac{\rho_{\text{col},2}}{\rho_{\text{col},1}} \approx 1 + \frac{c}{\bar{\omega}d} \frac{2\sqrt{R}}{1+R} \left[ \frac{\cos(2\bar{\omega}d/c) \sin(\Delta\omega d/c) - \cos^2\theta_m \cos(2\bar{\omega}d \cos\theta_m/c) \sin(\Delta\omega d \cos\theta_m/c)}{1 - \cos\theta_m} \right], \quad (\text{A6.16})$$

using  $\sin(2\omega_1 d/c) - \sin(2\omega_2 d/c) = 2 \cos(2\bar{\omega}d/c) \sin[(\omega_1 - \omega_2)d/c]$  to express the sum of sines as a beating wave with envelope frequency  $\Delta\omega = \omega_1 - \omega_2$  and modulation frequency  $2\bar{\omega} \approx \omega_1 + \omega_2$ , and similarly for the terms containing  $\cos\theta_m$ .

The function  $\rho_{\text{col},2}/\rho_{\text{col},1}$  oscillates rapidly with  $d$  within an envelop function that varies more slowly. We obtain an expression for the envelope of  $[\rho_{\text{col},2}/\rho_{\text{col},1}]_{\text{env}}$  by setting the value of the two rapidly oscillating cosine factors at  $\pm 1$ :

$$\left[ \frac{\rho_{\text{col},2}}{\rho_{\text{col},1}} \right]_{\text{env}} \approx 1 \pm \frac{c}{\bar{\omega}d} \frac{2\sqrt{R}}{1+R} \left[ \frac{\sin(\Delta\omega d/c) + \cos^2\theta_m \sin(\Delta\omega d \cos\theta_m/c)}{1 - \cos\theta_m} \right]. \quad (\text{A6.17})$$

This slowly oscillating function approaches unity for  $d \rightarrow \infty$ , corresponding to an effectively homogeneous optical environment. The extreme point, deviating maximally from unity, is at  $d \rightarrow 0$ . At this point, we define the maximum possible distortion factor  $\kappa_{\pm}$

$$\kappa_{\pm} = 1 \pm \frac{\Delta\omega}{\bar{\omega}} \frac{2\sqrt{R}}{1+R} \frac{1 + \cos^3\theta_m}{1 - \cos\theta_m}, \quad (\text{A6.18})$$

which depends on the relative frequency difference  $\Delta\omega$ , the reflectivity  $R$  of the interface, and the  $\text{NA} = \sin\theta_m$  of the microscope objective.

To visualize the effect of the reflectivity on the intensity-ratio distortions of the two emission lines  $\rho_{\text{col},2}/\rho_{\text{col},1}$ , we calculate the distortions as a function of emitter–interface separation for a mirror–air (Fig. A6.4b,  $R = 1$ ) and a glass–air interface (Fig. A6.4c,  $R = 0.04$ ) using a  $\text{NA} = 0.75$  and for emission lines at  $2\pi c/\omega_2 = 520$  nm and  $2\pi c/\omega_1 = 540$  nm (approximately the two emission lines of  $\text{Er}^{3+}$ ). We observe that evaluating the full model (blue lines, Eq. A6.15) and the simplified model (red lines, Eq. A6.16) give approximately the same collected LDOS ratio as a function of emitter–interface separation. Also, the dashed lines in Figs. A6.4b–c show that Eq. A6.18 approximately gives the maximum distortions of the intensity ratio.

Perhaps surprisingly, we observe that the maximum distortion factor  $\kappa_{\pm}$  due to a glass–air interface ( $R = 0.04$ ) is as high as 40% of the distortion factor due to a perfect mirror ( $R = 1$ ), while

the reflectivity  $R$  is smaller by a factor 25. This can be understood from Eq. A6.18, which shows a weaker than square-root dependence of the distortion factor on  $R$ . This highlights that reliable temperature readout is difficult, even near interfaces that are barely reflective, such as in biological environments. Fig. A6.4d shows the maximum distortion factor  $\kappa_{\pm}$  as a function of the NA =  $\sin\theta_m$  by numerically optimizing the analytical model  $\rho_{\text{col},2}/\rho_{\text{col},1}$  (dots, Eq. A6.15) and evaluating the approximation (solid lines, Eq. A6.18) near a mirror–air interface. The distortions diverge for  $\theta_m \rightarrow 0$ , which shows the importance of maximizing the collection angle  $\theta_m$  to minimize distortions. In Fig. A6.4e, we investigated the distortions for one emission line at 520 nm and a redshifted emission line 520 nm +  $\Delta\lambda$  near a mirror–air interface (NA = 0.75) for the analytical model (dots) and the approximation (solid lines). We observe that the maximum distortion factors increase/decrease approximately linearly with the wavelength shift  $\Delta\lambda$ .

**Readout temperature for emitters on a polarizable particle.** We consider an isotropic emitter in medium 1 with dielectric constant  $\epsilon_1$  directly on a polarizable particle with polarizability  $\alpha$  and radius  $a$  that sits in the origin of the coordinate system (Fig. A6.5a). The emitter is located between the objective and the polarizable particle. By reciprocity, the electric-field strength of the light emitted by the emitter into direction  $(\theta, \varphi)$  is proportional to the electric-field strength of a

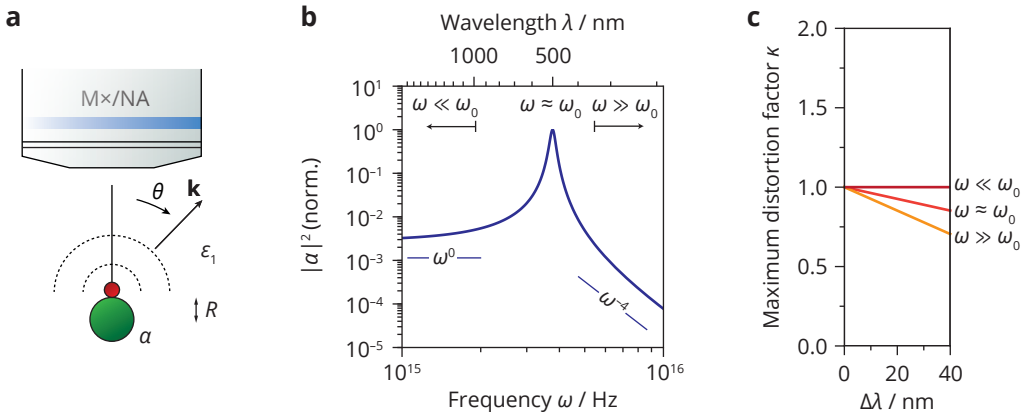


**Figure A6.5.** Intensity-ratio distortions on a polarizable particle. (a) We consider an isotropic emitter in medium 1 ( $\epsilon_1$ ) on a polarizable particle with polarizability  $\alpha$  and radius  $R$ . (b)  $|\alpha|^2$  from a simple Lorentz oscillator model with resonance wavelength  $2\pi c/\omega_0 = 500$  nm and a damping rate  $\gamma$  of  $10^{14}$  Hz. For low emission frequencies with respect to the resonance frequency  $\omega \ll \omega_0$ ,  $|\alpha|^2$  is frequency independent and photonic artifacts on the emission spectrum of the thermometer of emitter are absent. For high emission frequencies compared to the resonance frequency  $\omega \gg \omega_0$ ,  $|\alpha|^2$  decreases rapidly with frequency  $\omega^{-4}$ . (c) Maximum distortion factor  $\kappa$  of the luminescence intensity ratio between one emission line at 520 nm and one redshifted emission line at 520 nm +  $\Delta\lambda$  far red-detuned from the particle resonance (dark red line, Eq. A6.26), at the resonance frequency (red line, Eq. A6.27), and blue-detuned emission frequencies from the particle resonance (orange line, Eq. A6.28).



plane wave coming from the  $z$ -direction on position  $\mathbf{r} = a(\sin \theta \cos \varphi, \sin \theta \sin \varphi, \cos \theta)^\top$ . Here, we model the particle as a polarizable dipole source driven by the plane wave. For  $x$ - and  $y$ -polarized light the total electric field on the position of the emitter is given by

$$\begin{aligned}\mathbf{E}_{(x)} &= \mathbf{E}_{(x)}^0 e^{ikz} + \vec{\mathbf{G}}_{\text{NF}} \cdot \left( \alpha \mathbf{E}_{(x)}^0 \right) \\ \mathbf{E}_{(y)} &= \mathbf{E}_{(y)}^0 e^{ikz} + \vec{\mathbf{G}}_{\text{NF}} \cdot \left( \alpha \mathbf{E}_{(y)}^0 \right)\end{aligned}\tag{A6.19}$$

where we use the near-field Green's function

$$\vec{\mathbf{G}}_{\text{NF}} = \frac{e^{ika}}{4\pi\epsilon_0\epsilon_1 a^3} \left[ 3 \left( \frac{\mathbf{r} \otimes \mathbf{r}}{a^2} \right) - \vec{\mathbf{I}} \right]\tag{A6.20}$$

to calculate the electric-field strength on the position of the emitter in the near field of the polarizable particle. Using reciprocity, we calculate the intensity of isotropic emission into  $(\theta, \varphi)$  by the incoherent sum of  $x$ - and  $y$ -polarized light intensities on the position of the emitter. The maximum collected LDOS  $\rho_{\text{col,max}}$  is equal to the total intensity integrated over all emission angles  $\theta \in [0, \pi/2]$  into the half-space of the microscope objective:

$$\rho_{\text{col,max}} = \frac{1}{2|\mathbf{E}_0|^2} \int_0^{\pi/2} \left( |\mathbf{E}_{(x)}|^2 + |\mathbf{E}_{(y)}|^2 \right) \sin\theta \, d\theta,\tag{A6.21}$$

which can be evaluated analytically to

$$\begin{aligned}\rho_{\text{col,max}} &= 1 + \frac{|\alpha|^2}{8\pi^2\epsilon_0^2\epsilon_1^2 a^6} - \\ &\text{Re}(\alpha) \left[ \frac{6ka - (6 + k^2 a^2) \text{sinka}}{4\pi\epsilon_0\epsilon_1 k^3 a^6} \right] + \text{Im}(\alpha) \left[ \frac{2(k^2 a^2 - 3) - (6 + k^2 a^2) \text{coska}}{4\pi\epsilon_0\epsilon_1 k^3 a^6} \right].\end{aligned}\tag{A6.22}$$

We use a simple Lorentz oscillator model for the frequency-dependence of polarizability  $\alpha$  of a particle with resonance frequency  $\omega_0$ :

$$\alpha = \frac{\alpha_0}{(\omega^2 - \omega_0^2) + i\gamma\omega},\tag{A6.23}$$

where  $\gamma$  is the damping rate and  $\alpha_0$  is a prefactor. **Fig. A6.5b** shows  $|\alpha|^2$  for resonance wavelength  $2\pi c/\omega_0 = 500 \text{ nm}$  and  $\gamma = 10^{14} \text{ Hz}$ . We consider the limit of strong polarizability

$\alpha \gg 4\pi\epsilon_0 R^3$ , where the  $|\alpha|^2$  term of Eq. A6.24 dominates. In this limit, the maximum distortion factor  $\kappa = [\rho_{\text{col,max},2}/\rho_{\text{col,max},1}]_{\text{max}}$  can be simplified for two emission lines of the thermometer centered around  $\bar{\omega}$ , at  $\omega_{1,2} = \bar{\omega}(1 \pm \Delta/2)$  with relative frequency difference  $\Delta = \Delta\omega/\bar{\omega}$  to

$$\kappa(\bar{\omega}) = \frac{|\alpha[\bar{\omega}(1 + \Delta/2)]|^2}{|\alpha[\bar{\omega}(1 - \Delta/2)]|^2}. \quad (\text{A6.24})$$

To investigate the dependence of the maximum distortion factor  $\kappa$  on the relative frequency difference  $\Delta$ , we expand Eq. A6.24 around  $\Delta = 0$  up to first order

$$\kappa(\bar{\omega}) = 1 + \frac{2\bar{\omega}}{|\alpha(\bar{\omega})|} \left( \frac{d|\alpha|}{d\omega} \right)_{\omega=\bar{\omega}} \Delta + \mathcal{O}(\Delta^2). \quad (\text{A6.25})$$

For thermometer emission strongly red-detuned from the particle resonance  $\bar{\omega} \ll \omega_0$ ,  $|\alpha|^2$  is frequency-independent (Fig. A6.5b) and the maximum distortion factor  $\kappa$  is unity (Fig. A6.5c)

$$\lim_{\bar{\omega} \rightarrow 0} \kappa(\bar{\omega}) \approx 1. \quad (\text{A6.26})$$

For two emission lines with average frequency  $\bar{\omega}$  very close to the resonance frequency  $\omega_0$ , we find

$$\lim_{\bar{\omega} \rightarrow \omega_0} \kappa(\bar{\omega}) \approx 1 - 2 \frac{\Delta\omega}{\bar{\omega}}, \quad (\text{A6.27})$$

which gives a linearly increasing/decreasing distortion factor  $\kappa$  as a function of the relative frequency difference  $\Delta\omega/\bar{\omega}$  (Fig. A6.5c). Lastly, we investigate the regime where the average emission frequency of a thermometer is strongly blue-detuned from the resonance frequency  $\bar{\omega} \gg \omega_0$ . Here,  $|\alpha|^2$  scales very strongly with frequency  $\omega^{-4}$  (Fig. A6.5b). In this limit, we find a distortion factor

$$\lim_{\bar{\omega} \rightarrow \infty} \kappa(\bar{\omega}) \approx 1 - 4 \frac{\Delta\omega}{\bar{\omega}}, \quad (\text{A6.28})$$

which also gives a linearly increasing/decreasing distortion factor  $\kappa$  (Fig. A6.5c), but with a larger pre-factor compared to the resonant regime.

**Readout errors for an arbitrary intensity-ratio near a reflective surface.** We can calculate the readout temperature  $T'$  near a reflector at temperature  $T$  with absolute distortion on the intensity ratio  $Y(\kappa_{\pm} - 1)$ . To first order, the readout temperature  $T'$  is given by

$$T' \approx T + Y(\kappa_{\pm} - 1) \frac{dT}{dY}. \quad (\text{A6.29})$$

Using the definition of relative sensitivity  $S_r = Y^{-1} dT/dY$ , which is a commonly accepted parameter to characterize thermometer performance, and filling in Eq. A6.18, we obtain

$$\Delta T_{\max} \approx \frac{1}{S_r} \frac{\Delta\omega}{\bar{\omega}} \frac{2\sqrt{R}}{1+R} \frac{1 + \cos^3\theta_m}{1 - \cos\theta_m} \quad (\text{A6.30})$$

for the maximum temperature error  $\Delta T = T' - T$  due to photonic effects of a reflective surface. We see that the readout temperature differences are minimized by minimizing the relative frequency difference between the emission lines  $\Delta\omega/\bar{\omega}$  and the reflectivity  $R$  of the nearby reflective surface, and maximizing the NA (small  $\cos\theta_m$ ). For a Boltzmann thermometer, we can calculate the readout error analytically using the expression for the relative sensitivity  $S_r = \Delta E/k_B T^2$

$$\Delta T_{\max} \approx \frac{k_B T^2}{\hbar\bar{\omega}} \frac{2\sqrt{R}}{1+R} \frac{1 + \cos^3\theta_m}{1 - \cos\theta_m}. \quad (\text{A6.31})$$

We observe the quadratic temperature dependence of the temperature error  $\Delta T$  on the set temperature  $T$ , which explains the larger temperature error of the Boltzmann thermometer in Fig. 6.2 at elevated set temperatures.



---

# Chapter 7

## Summary and outlook

## Summary and outlook

Materials with temperature-sensitive luminescence are becoming the desired probes for thermometry experiments in many research disciplines. Unlike conventional techniques that rely on physical contact between temperature probe and readout instrument, luminescent thermometers can be operated remotely, requiring only an excitation source, a light dispersion element, and a photodetector. An additional advantage is that modern synthesis procedures can control the size of luminescent materials from several micrometers to a few nanometers. Luminescent materials are therefore readily inserted into microscopic systems, like living organisms, catalyst particles, and electronic devices, and enable temperature measurements with high spatial resolutions.

As described in **Chapter 1**, several characteristics of the luminescence can serve as a measure for temperature. The luminescence intensity ratio (*LIR*) between two emission lines is however the most popular metric, because it is generally insensitive to sample alignment, excitation intensity, and other experimental parameters. Materials based on trivalent lanthanide ions are exceptionally suited as ratiometric thermometers due to their narrow emission lines that reduce systematic errors caused by spectral overlap of the two relevant emissions. An important metric to quantify the performance of ratiometric thermometers is the relative sensitivity, which quantifies how strongly the *LIR* responds to temperature variations. However, the reliability of a thermometry experiment not only depends on the relative sensitivity, but also on the signal-to-noise ratio in the emission spectrum and on the susceptibility to systematic errors. In this thesis, we have investigated the parameters that determine the performance of luminescent thermometers in the actual application and, based on our results, propose guidelines to optimize thermometer design.

In **Chapter 2**, we have studied how different sources of noise in photon detection experiments translate to the uncertainty of temperature readout. We characterized the noise on the recorded luminescence signal at various background levels and in different photon counting modes of the CCD detector. As expected, the probability distribution of photon detection before conversion to photoelectrons follows Poisson statistics, but the detector adds various types of noise, depending on the settings. Furthermore, background signal introduces additional photon and detection noise, which even after background subtraction cannot be removed and increases the temperature uncertainty. We showed that such experimental factors strongly affect the temperature uncertainty and the uncertainty is therefore an undesired parameter to compare the performance of luminescent thermometers. Instead, we find that the relative sensitivity and the brightness of the thermometer are more meaningful figure of merits, because those are intrinsic thermometer properties that are independent of experimental conditions. The relative sensitivity is easily measured. However, the brightness is determined by the absorption cross section and the photoluminescence quantum yield (at a specific dopant concentration and excitation intensity), which are still unknown for most thermometer materials. While the absorption cross section is an invariable material property, the quantum yield heavily relies on the synthesis procedure. Extensive work has already optimized the quantum yield of nanocrystals using core-shell structures.<sup>56</sup> Similar strategies would enhance the brightness of existing and new thermometer materials.

In **Chapter 3**, we have focused on the design of the most common luminescent thermometer, the Boltzmann thermometer, which relies on energy levels in thermal equilibrium. As long as thermal equilibrium is established, the *LIR* follows Boltzmann statistics serving as a convenient calibration model. However, the dynamic temperature range of Boltzmann thermometers, in which accurate measurements can be performed, is limited. At elevated temperatures, the relative sensitivity rapidly decreases with  $\Delta E/k_B T^2$ , which shows that the upper limit of the dynamic range is fixed by the energy gap. Therefore, the only way to increase the upper limit is the selection of a thermometer with a different energy gap. In contrast, it is possible to reduce the lower limit by increasing the nonradiative coupling rates, because this shifts the onset of thermal equilibrium to lower temperatures. To investigate how the onset temperature can be reduced we prepared a series of microcrystalline  $\text{Eu}^{3+}$ -doped materials and we studied the luminescence of the  ${}^5\text{D}_0$  and  ${}^5\text{D}_1$  levels. Our experimental results reveal that the onset temperature decreases with a lower number of required phonons to bridge the energy gap and a shorter lanthanide–ligand distance. We additionally showed that selection rules dictate intrinsically low nonradiative coupling rates for transitions with magnetic-dipole character compared to those with electric-dipole character. These findings are important guidelines for the design of thermometers with wide dynamic temperature ranges.

A future strategy for the development of thermometers that are suited for both low and high temperatures could be directed towards unexplored pairs of thermally coupled levels with electric-dipole transitions and a wide energy gap. For example, the  ${}^2\text{P}_{3/2}$ – ${}^2\text{K}_{13/2}$  pair of  $\text{Er}^{3+}$  is an interesting candidate, because the energy gap of  $\sim 1300\text{ cm}^{-1}$  leads to higher sensitivities at elevated temperatures and, in addition, the luminescence can be excited via upconversion of infrared or visible light.<sup>174,175</sup> Alternatively, thermal equilibrium with a third level could be included to obtain higher sensitivities, which was recently demonstrated for the  ${}^6\text{P}_{7/2-3/2}$  levels of  $\text{Gd}^{3+}$ .<sup>176</sup> Other strategies could search for materials that do not rely on thermal equilibrium but have a different mechanism for temperature-dependent luminescence. This has driven the design of thermometers based on energy-transfer between lanthanide ions that allow for tuning of the sensitivity and precision via the dopant concentrations. Materials that are co-doped with  $\text{Eu}^{3+}$  and  $\text{Tb}^{3+}$  are well-known for concentration-dependent thermometer performance, although, for example,  $\text{Tm}^{3+}$ -doped or  $\text{Nd}^{3+}/\text{Yb}^{3+}$ -co-doped materials show similar behavior.<sup>54,107,108,110,177,178</sup> The temperature-dependent mechanisms of energy-transfer thermometers are however complex, which impedes determination of the optimum dopant concentrations.

In **Chapter 4**, we have designed a quantitative model to predict the luminescence of energy-transfer thermometers. We applied this model to  $\text{Ho}^{3+}$ -doped  $\text{NaYF}_4$  microcrystals with temperature-dependent green and red emissions. The working mechanism of this thermometer is the competition between temperature-independent cross-relaxation and temperature-dependent multi-phonon relaxation. To obtain the input parameters for our model we carefully measured the excited-state dynamics of all relevant emissions, which made it possible to determine the optimum sensitivity and precision in a wide range of dopant concentrations and temperatures. Our model is not only applicable to this  $\text{Ho}^{3+}$ -based thermometer, but it is also important for the

understanding and development of other energy-transfer thermometers.

When luminescent thermometers are used in the actual application, other factors, besides the sensitivity and the signal-to-noise ratio, should additionally be considered for reliable temperature readout. Excitation of the luminescence could, for example, induce heating of the thermometer, which modifies the temperature of the sample.<sup>30</sup> Furthermore, background fluorescence or blackbody radiation could overlap with the luminescence of the thermometer or the thermometer could be vulnerable to wavelength-dependent absorption, scattering or reflection by the medium between thermometer and detector.<sup>31,33,152</sup> In both cases, the luminescence spectrum is distorted, which causes systematic errors in temperature readout.

In **Chapter 5**, we mapped the temperature of a microheater coated with  $\text{Er}^{3+}/\text{Yb}^{3+}$ -doped nanocrystals and demonstrated that thermometry experiments at high spatial resolutions face two other types of readout errors. The luminescence of the nanocrystals is generated via upconversion of two 980 nm excitations that are transferred from  $\text{Yb}^{3+}$  to  $\text{Er}^{3+}$  to obtain the typical green luminescence. At the high excitation intensities needed for experiments on the microscopic scale, the temperature-dependent green luminescence of  $\text{Er}^{3+}$  is distorted by an additional emission from a higher energy level that is populated via a three-photon upconversion mechanism. This introduces a systematic error in temperature readout. We were however able to identify the higher excited state and determine the spectral shape using carefully recorded reference spectra. To map the temperature distribution on the microheater we acquired the luminescence of the nanocrystals using a confocal microscope and removed the additional emission from each spectrum. Remarkably, the temperature maps still showed systematic deviations at the metal components of the heater that have a higher reflectivity than the support membrane. Using experiments with different microscope objectives, we discovered that these deviations are caused by self-interference of the direct and reflected emission. This modifies the wavelength-dependent angular distribution of luminescence and creates photonic artifacts in the temperature maps. In our static sample environment, a map recorded at known (room) temperature fortunately makes it possible to correct for this artifact, but this procedure would no longer work in dynamic samples.

In **Chapter 6**, we obtained further understanding of these photonic artifacts using substrates that provided better control over the optical environment of the thermometers. We fabricated Au mirrors coated with an alumina spacer of variable thickness, on which we deposited  $\text{Er}^{3+}/\text{Yb}^{3+}$ -doped or  $\text{Ho}^{3+}$ -doped nanocrystals. Both thermometers have temperature-dependent emissions in the visible, but the difference in emission energy is 7 times larger for  $\text{Ho}^{3+}$ . We observed a strong dependence of the luminescence on the separation between the nanocrystals and the mirror, which translated into enormous readout errors of 100 K for  $\text{Er}^{3+}$  and of 250 K for  $\text{Ho}^{3+}$ . Our simple self-interference model explained these results and revealed that the photonic artifacts are minimized by sample geometries with poorly reflective interfaces and by a high numerical aperture of the microscope objective. More importantly, a thermometer is less susceptible to photonic artifacts when it has a low value of the ratio between the difference in emission energies  $\Delta\omega$  and the average emission energy  $\bar{\omega}$  ( $\Delta\omega/\bar{\omega}$ ). While it is often impossible to change the geometry



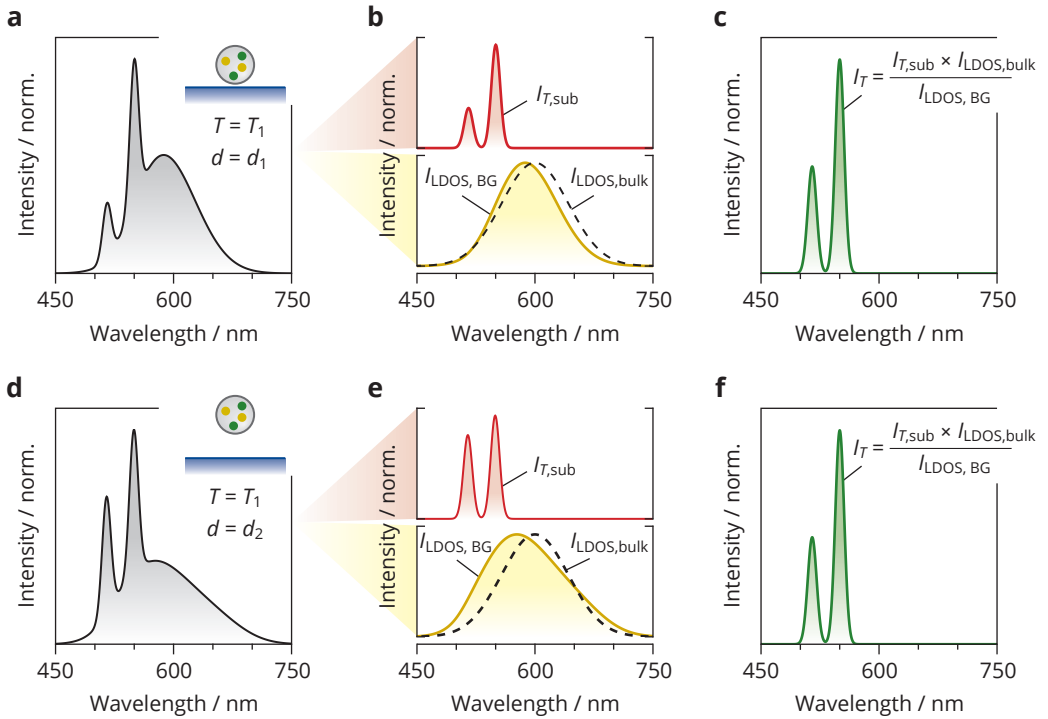


**Figure 7.1.** Bifunctional luminescent materials to correct for photonic distortions. **(a)** Simulated luminescence spectrum of bifunctional nanocrystals that are co-doped with thermometer ions having two narrow Gaussian emissions and with LDOS-sensing ions having a single broad Gaussian emission. The inset schematically shows the bifunctional nanocrystals at a distance  $d_1$  from a reflector at temperature  $T_1$ . A self-interference model was used to simulate the distortion of the input emissions in this geometry. **(b)** Distorted emission of the thermometer ions (red,  $I_{T,\text{sub}}$ ) and the LDOS-sensing ions (yellow,  $I_{\text{LDOS,BG}}$ ) after background subtraction. The black dashed line shows the broad-band emission of the bulk sample. **(c)** Thermometer emissions after correction for photonic distortions. **(d-f)** Same as in **(a-c)** but for a geometry with distance  $d_2$  between the reflector and the nanocrystals. The corrected thermometer emissions ( $I_T$ ) exactly match. This figure explains the procedure that was reported by Lin *et al.* to correct for photonic artifacts in surface-enhanced Raman scattering experiments.<sup>159</sup>

of the sample, optimization of the microscope objective and the emission energies of the thermometer could be an effective strategy to achieve higher measurement accuracies.

These results suggest that Boltzmann thermometers are ideal for the minimization of photonic artifacts due to their small difference in emission energy. Boltzmann thermometers that also have high emission energies  $\bar{\omega}$ , like  $\text{Gd}^{3+}$ , further reduce photonic artifacts—the difference with infrared-emitting thermometers like  $\text{Nd}^{3+}$  is more than a factor 5. However, even when  $\Delta\omega/\bar{\omega}$  is optimized, the optical environment of luminescent thermometers can still cause readout errors of a few kelvin, which might be acceptable for some applications, such as high-temperature catalysis, but are unacceptable for others, like *in vivo* experiments. Correcting for photonic artifacts

in such dynamic sample environments would require real-time information of the LDOS. Luminescent probes with a broad temperature-independent emission band at the emission frequencies of the thermometer could provide this information.<sup>159</sup> Here, the broad-band emitter acts as a LDOS-sensor that experiences the same photonic distortions as the thermometer but is unaffected by temperature. To correct the luminescence of such bifunctional materials in unknown optical environment, the broad background should first be subtracted from the raw spectrum. The ratio between the subtracted broad-band background and the bulk broad-band emission then gives the information of the LDOS that is necessary to retrieve the luminescence of the thermometer without photonic distortions. Ideally, the LDOS sensors are incorporated into the thermometer material to probe exactly the same optical environment. This could be achieved, for example, by co-doping YAG:Er<sup>3+</sup> with Ce<sup>3+</sup>, which shows a broad 5d–4f emission at 450–750 nm that overlaps with the green luminescence of the Er<sup>3+</sup> (Fig. 7.1).<sup>179</sup> Although the design of these bifunctional thermometers brings additional challenges, such as energy transfer between the LDOS- and temperature-sensing ions and slight temperature-dependence in the emission and absorption spectrum of the LDOS sensor, successful implementation would give much more freedom in the design and application of luminescent thermometers.





---

## References

## References

1. L. Michalski, K. Eckersdorf, J. Kucharski and J. McGhee, *Temperature measurement*, John Wiley & Sons (2001).
2. K.M. McCabe and M. Hernandez, *Pediatr. Res.* **67**, 469–475 (2010).
3. H. Preston-Thomas, *Metrologia* **27**, 3–10 (1990).
4. A.W. van Herwaarden and P.M. Sarro, *Sensors and Actuators* **10**, 321–346 (1986).
5. G.K. White and S.B. Woods, *Rev. Sci. Instrum.* **28**, 638–641 (1957).
6. S. Gomès, A. Assy and P.O. Chapuis, *Phys. Status Solidi A* **212**, 477–494 (2015).
7. A. Balčytis, M. Ryu, S. Juodkazis and J. Morikawa, *Sci. Rep.* **8**, 6324 (2018).
8. W. Tian, C. Wang, J. Wang, Q. Chen, J. Sun, C. Li, X. Wang and N. Gu, *Nanotechnology* **26**, 355501 (2015).
9. F. Menges, P. Mensch, H. Schmid, H. Riel, A. Stemmer and B. Gotsmann, *Nat. Commun.* **7**, 10874 (2016).
10. S. Sadat, E. Meyhofer and P. Reddy, *Rev. Sci. Instrum.* **83**, 084902 (2012).
11. S. Sadat, A. Tan, Y.J. Chua and P. Reddy, *Nano Lett.* **10**, 2613–2617 (2010).
12. R. Usamentiaga, P. Venegas, J. Guerediaga, L. Vega, J. Molleda and F.G. Bulnes, *Sensors* **14**, 12305–12348 (2014).
13. C.D.S. Brites, S. Balabhadra and L.D. Carlos, *Adv. Opt. Mater.* **7**, 1801239 (2019).
14. G.H. Dieke and H.M. Crosswhite, *Appl. Opt.* **2**, 675–686 (1963).
15. M. Krośnicki, A. Kędzierski, L. Seijo and Z. Barandiarán, *J. Phys. Chem. A* **118**, 358–368 (2014).
16. G. Blasse, A. Brill and W.C. Nieuwpoort, *J. Phys. Chem. Solids* **27**, 1587–1592 (1966).
17. J. Ueda and S. Tanabe, *Opt. Mater. X* **1**, 100018 (2019).
18. P. Atkins and T. Overton, *Shriver and Atkins' Inorganic Chemistry*, Oxford University Press (2010).
19. T. Senden, F.T. Rabouw and A. Meijerink, *ACS Nano* **9**, 1801–1808 (2015).
20. F.T. Rabouw, P.T. Prins and D.J. Norris, *Nano Lett.* **16**, 7254–7260 (2016).
21. K.H. Drexhage, *J. Lumin.* **1**, 693–701 (1970).
22. W.L. Barnes, S.A.R. Horsley and W.L. Vos, *J. Opt.* **22**, 073501 (2020).
23. M. Pelton, *Nat. Photon.* **9**, 427–435 (2015).
24. W.L. Barnes, *J. Mod. Opt.* **45**, 661–699 (1998).
25. T. Förster, *Ann. Phys.* **437**, 55–75 (1948).
26. P. Vergeer, T.J.H. Vlugt, M.H.F. Kox, M.I. Den Hertog, J.P.J.M. van Der Herden and A. Meijerink, *Phys. Rev. B* **71**, 014119 (2005).
27. F.T. Rabouw, S. A. Den Hartog, T. Senden and A. Meijerink, *Nat. Commun.* **5**, 3610 (2014).
28. S.A. Egorov and J.L. Skinner, *J. Chem. Phys.* **103**, 1533–1543 (1995).
29. M. Suta and A. Meijerink, *Adv. Theory Simul.* **3**, 2000176 (2020).
30. A. D. Pickel, A. Teitelboim, E.M. Chan, N.J. Borys, P.J. Schuck and C. Dames, *Nat. Commun.* **9**, 4907 (2018).
31. J. Zhou, B. Del Rosal, D. Jaque, S. Uchiyama and D. Jin, *Nat. Methods* **17**, 967–980 (2020).
32. A. Bednarkiewicz, L. Marciniak, L.D. Carlos and D. Jaque, *Nanoscale* **12**, 14405–14421 (2020).
33. Y. Shen, J. Lifante, N. Fernandez, D. Jaque and E. Ximendes, *ACS Nano* **14**, 4122–4133 (2020).
34. X. Zhu, J. Li, X. Qiu, Y. Liu, W. Feng and F. Li, *Nat. Commun.* **9**, 2176 (2018).
35. T.P. van Swieten, T. van Omme, D.J. van den Heuvel, S.J.W. Vonk, R.G. Spruit, F. Meirer, H.H. Pérez Garza, B.M. Weckhuysen, A. Meijerink, F.T. Rabouw and R.G. Geitenbeek, *ACS Appl. Nano Mater.* **4**, 4208–4215 (2021).
36. T. Hartman, R.G. Geitenbeek, C.S. Wondergem, W. van der Stam and B.M. Weckhuysen, *ACS Nano* **14**, 3725–3735 (2020).

37. F.E. Maturi, C.D.S. Brites, E.C. Ximendes, C. Mills, B. Olsen, D. Jaque, S.J.L. Ribeiro and L.D. Carlos, *Laser Photon. Rev.* **15**, 2100301 (2021).
38. C.D.S. Brites, M.C. Fuertes, P.C. Angelome, E.D. Martínez, P.P. Lima, G. J.A.A. Soler-Illia and L.D. Carlos, *Nano Lett.* **17**, 4746–4752 (2017).
39. M. Back, E. Trave, J. Ueda and S. Tanabe, *Chem. Mater.* **28**, 8347–8356 (2016).
40. P. Rühl, D. Wang, F. Garwe, R. Müller, M. Haase, K. W. Krämer, W. Paa, R. Heintzmann, S.H. Heinemann and H. Stafast, *J. Lumin.* **232**, 117860 (2020).
41. C.D.S. Brites, A. Millán and L.D. Carlos, in *Handbook on the Physics and Chemistry of Rare Earths*, Elsevier, pp. 339–427 (2016).
42. F. Vetrone, R. Naccache, A. Zamarrón, A. Juarranz de la Fuente, F. Sanz-Rodriguez, L. Martinez Maestro, E. Martin Rodriguez, D. Jaque, J. Garcia Solé and J. A. Capobianco, *ACS Nano* **4**, 3254–3258 (2010).
43. R.G. Geitenbeek, P.T. Prins, W. Albrecht, A. van Blaaderen, B.M. Weckhuysen and A. Meijerink, *J. Phys. Chem. C* **121**, 3503–3510 (2017).
44. M. Jia, Z. Sun, M. Zhang, H. Xu and Z. Fu, *Nanoscale* **12**, 20776–20785 (2020).
45. K.B.W. Harpsøe, M.I. Andersen and P. Kjægaard, *Astron. Astrophys.* **537**, A50 (2012).
46. M. Hirsch, R.J. Wareham, M.L. Martin-Fernandez, M.P. Hobson and D.J. Rolfe, *PLoS One* **8**, e53671 (2013).
47. J.C. Mullikin, L.J. van Vliet, H. Netten, F.R. Boddeke, G. der Feltz and I.T. Young, in *Image Acquisition and Scientific Imaging Systems*, pp. 73–84 (1994).
48. U. Rocha, C. Jacinto, K. U. Kumar, F.J. Lopez, D. Bravo, J.G. Solé and D. Jaque, *J. Lumin.* **175**, 149–157 (2016).
49. M. Runowski, P. Woźny, N. Stopikowska, I.R. Martin, V. Lavin and S. Lis, *ACS Appl. Mater. Interfaces* **12**, 43933–43941 (2020).
50. Z. Wang, J. Christiansen, D. Wezendonk, X. Xie, M.A. Van Huis and A. Meijerink, *Nanoscale* **11**, 12188–12197 (2019).
51. P. Löw, B. Kim, N. Takama and C. Bergaud, *Small* **4**, 908–914 (2008).
52. M. Xu, X. Zou, Q. Su, W. Yuan, C. Cao, Q. Wang, X. Zhu, W. Feng and F. Li, *Nat. Commun.* **9**, 2698 (2018).
53. F. LaPlant, G. Laurence and D. Ben-Amotz, *Appl. Spectrosc.* **50**, 1034–1038 (1996).
54. X. Liu, S. Akerboom, M. de Jong, I. Mutikainen, S. Tanase, A. Meijerink and E. Bouwman, *Inorg. Chem.* **54**, 11323–11329 (2015).
55. E.J. McLaurin, L.R. Bradshaw and D.R. Gamelin, *Chem. Mater.* **25**, 1283–1292 (2013).
56. C. Homann, L. Krukewitt, F. Frenzel, B. Grauel, C. Würth, U. Resch-Genger and M. Haase, *Angew. Chemie Int. Ed.* **57**, 8765–8769 (2018).
57. C.A. Leatherdale, W.-K. Woo, F.V. Mikulec and M.G. Bawendi, *J. Phys. Chem. B* **106**, 7619–7622 (2002).
58. J. De Roo, M. Ibáñez, P. Geiregat, G. Nedelcu, W. Walravens, J. Maes, J. C. Martins, I. van Driessche, M. V Kovalenko and Z. Hens, *ACS Nano* **10**, 2071–2081 (2016).
59. C. Xia, W. Wu, T. Yu, X. Xie, C. van Oversteeg, H. C. Gerritsen and C. de Mello Donega, *ACS Nano* **12**, 8350–8361 (2018).
60. D.S. Reig, B. Grauel, V.A. Konyushkin, A.N. Nakladov, P.P. Fedorov, D. Busko, I.A. Howard, B.S. Richards, U. Resch-Genger, S.V. Kuznetsov and C. Würth, *J. Mater. Chem. C* **8**, 4093–4101 (2020).
61. R.H. Page, K.I. Schaffers, P.A. Waide, J.B. Tassano, S.A. Payne, W.F. Krupke and W.K. Bischel, *JOSA B* **15**, 996–1008 (1998).
62. M.Y. Hossan, A. Hor, Q. Luu, S.J. Smith, P.S. May and M.T. Berry, *J. Phys. Chem. C* **121**, 16592–16606 (2017).

63. G. Sui, B. Chen, X. Zhang, X. Li, J. Zhang, S. Xu, J. Sun, Y. Cao, X. Wang, Y. Zhang, Y. Zhang and X. Zhang, *J. Alloys Compd.* **834**, 155242 (2020).
64. Y. Zhang, B. Chen, S. Xu, X. Li, J. Zhang, J. Sun, X. Zhang, H. Xia and R. Hua, *Phys. Chem. Chem. Phys.* **20**, 15876–15883 (2018).
65. J. Nanda, S. A. Ivanov, H. Htoon, I. Bezel, A. Piryatinski, S. Tretiak and V.I. Klimov, *J. Appl. Phys.* **99**, 34309 (2006).
66. M.A. van de Haar, M. Tachikirt, A.C. Berends, M.R. Krames, A. Meijerink and F.T. Rabouw, *ACS Photonics* **8**, 1784–1793 (2021).
67. K.W. Krämer, D. Biner, G. Frei, H.U. Güdel, M.P. Hehlen and S.R. Lüthi, *Chem. Mater.* **16**, 1244–1251 (2004).
68. F.T. Rabouw, P.T. Prins, P. Villanueva-Delgado, M. Castelijns, R.G. Geitenbeek and A. Meijerink, *ACS Nano* **12**, 4812–4823 (2018).
69. B. Terlingen, R. Oord, M. Ahr, E. Hutter, C. van Lare and B.M. Weckhuysen, *ACS Catal.* **11**, 10574–10588 (2021).
70. M. Suta, Ž. Antić, V. Dordjević, S. Kuzman, M.D. Dramićanin and A. Meijerink, *Nanomaterials* **10**, 543 (2020).
71. R.G. Geitenbeek, H.W. de Wijn and A. Meijerink, *Phys. Rev. Appl.* **10**, 64006 (2018).
72. G. Gao, A. Turshatov, I.A. Howard, D. Busko, R. Joseph, D. Hudry and B.S. Richards, *Adv. Sustain. Syst.* **1**, 1600033 (2017).
73. E.B. Sveshnikova and V.L. Ermolaev, *Opt. Spectrosc.* **111**, 34–50 (2011).
74. J.M.F. van Dijk and M.F.H. Schuurmans, *J. Chem. Phys.* **78**, 5317–5323 (1983).
75. L.A. Riseberg and H.W. Moos, *Phys. Rev. Lett.* **19**, 1423 (1967).
76. V.L. Ermolaev and E.B. Sveshnikova, *J. Lumin.* **20**, 387–395 (1979).
77. T.P. van Swieten, D. Yu, T. Yu, S.J.W. Vonk, M. Suta, Q. Zhang, A. Meijerink and F.T. Rabouw, *Adv. Opt. Mater.* **9**, 2001518 (2021).
78. X. Li, D. Chen, F. Huang, G. Chang, J. Zhao, X. Qiao, X. Xu, J. Du and M. Yin, *Laser Photon. Rev.* **12**, 1800030 (2018).
79. R. Shi, C.D.S. Brites and L.D. Carlos, *Nanoscale* **13**, 19771–19782 (2021).
80. W.T. Carnall, H. Crosswhite and H.M. Crosswhite, *Energy Level Structure and Transition Probabilities of the Trivalent Lanthanides in LaF<sub>3</sub>*, Argonne National Laboratory (1977).
81. Y. An, A. Duhaime and P.S. May, *J. Lumin.* **111**, 131–138 (2005).
82. K.R. German and A. Kiel, *Phys. Rev. B* **8**, 1846 (1973).
83. C.K. Asawa, *Phys. Rev.* **173**, 869 (1968).
84. P. Netzsch, M. Hämmer, E. Turgunbajew, T.P. van Swieten, A. Meijerink, H.A. Höppe and M. Suta, *Adv. Opt. Mater.* **10**, 2200059 (2022).
85. J.A. Capobianco, P. Kabro, F.S. Ermeneux, R. Moncorge, M. Bettinelli and E. Cavalli, *Chem. Phys.* **214**, 329–340 (1997).
86. A. Ellens, H. Andres, M.L.H. ter Heerdt, R.T. Wegh, A. Meijerink and G. Blasse, *J. Lumin.* **66**, 240–243 (1995).
87. T. Senden, R.J.A. van Dijk-Moes and A. Meijerink, *Light Sci. Appl.* **7**, 8 (2018).
88. C.W. Struck and W.H. Fonger, *J. Lumin.* **1**, 456–469 (1970).
89. B. Bendel and M. Suta, *J. Mater. Chem. C* **10**, 13805–13814 (2022).
90. F.A. Kröger, W. Hoogenstraaten, M. Bottema and T.P.J. Botden, *Physica* **14**, 81–96 (1948).
91. B.M. Walsh, in *Advances in spectroscopy for lasers and sensing*, Springer, pp. 403–433 (2006).
92. W.H. Fonger and C.W. Struck, *J. Chem. Phys.* **52**, 6364–6372 (1970).
93. T.P. van Swieten, A. Meijerink and F.T. Rabouw, *ACS Photonics* **9**, 1366–1374 (2022).
94. T. Hartman, R.G. Geitenbeek, G.T. Whiting and B.M. Weckhuysen, *Nat. Catal.* **2**, 986–996 (2019).



95. C.D.S. Brites, X. Xie, M.L. Debasu, X. Qin, R. Chen, W. Huang, J. Rocha, X. Liu and L.D. Carlos, *Nat. Nanotechnol.* **11**, 851–856 (2016).
96. D. Ruiz, B. del Rosal, M. Acebrón, C. Palencia, C. Sun, J. Cabanillas-González, M. López-Haro, A.B. Hungria, D. Jaque and B.H. Juárez, *Adv. Funct. Mater.* **27**, 1604629 (2017).
97. S. Heer, K. Kömpe, H.U. Güdel and M. Haase, *Adv. Mater.* **16**, 2102–2105 (2004).
98. M. Back, J. Ueda, J. Xu, K. Asami, M. G. Brik and S. Tanabe, *Adv. Opt. Mater.* **8**, 2000124 (2020).
99. M.D. Dramićanin, B. Milićević, V. Đorđević, Z. Ristić, J. Zhou, D. Milivojević, J. Papan, M.G. Brik, C.-G. Ma, A.M. Srivastava and M. Wu, *ChemistrySelect* **4**, 7067–7075 (2019).
100. M. Sekulić, V. Đorđević, Z. Ristić, M. Medić and M.D. Dramićanin, *Adv. Opt. Mater.* **6**, 1800552 (2018).
101. E.N. Cerón, D.H. Ortgies, B. del Rosal, F. Ren, A. Benayas, F. Vetrone, D. Ma, F. Sanz-Rodríguez, J.G. Solé, D. Jaque and E.M. Rodríguez, *Adv. Mater.* **27**, 4781–4787 (2015).
102. C.D.S. Brites, S. Balabhadra and L.D. Carlos, *Adv. Opt. Mater.* **7**, 1801239 (2019).
103. B. Fond, C. Abram, M. Pougin and F. Beyrau, *Opt. Mater.* **89**, 615–622 (2019).
104. A. A. Alaulamie, *Nanoscale Temperature Measurement of Phase Transition in Water Using Novel Optical Thermometry Techniques*, College of Arts and Sciences of Ohio University, (2017).
105. A.S. Souza, L.A.O. Nunes, I.G.N. Silva, F.A.M. Oliveira, L.L. da Luz, H.F. Brito, M.C.F.C. Felinto, R.A.S. Ferreira, S.A. Júnior, L.D. Carlos and O.L. Malta, *Nanoscale* **8**, 5327–5333 (2016).
106. K. Trejgis, A. Bednarkiewicz and L. Marciniak, *Nanoscale* **12**, 4667–4675 (2020).
107. C.D.S. Brites, P.P. Lima, N.J.O. Silva, A. Millán, V.S. Amaral, F. Palacio and L.D. Carlos, *Adv. Mater.* **22**, 4499–4504 (2010).
108. D. Jaque, M.O. Ramirez, L. E. Bausá, J. G. Solé, E. Cavalli, A. Speghini and M. Bettinelli, *Phys. Rev. B* **68**, 35118 (2003).
109. C.D.S. Brites, K. Fiaczyk, J.F.C.B. Ramalho, M. Sójka, L.D. Carlos and E. Zych, *Adv. Opt. Mater.* **6**, 1701318 (2018).
110. E.C. Ximendes, A.F. Pereira, U. Rocha, W.F. Silva, D. Jaque and C. Jacinto, *Nanoscale* **11**, 8864–8869 (2019).
111. Z. Cao, X. Wei, L. Zhao, Y. Chen and M. Yin, *ACS Appl. Mater. Interfaces* **8**, 34546–34551 (2016).
112. B. Chen, Y. Liu, Y. Xiao, X. Chen, Y. Li, M. Li, X. Qiao, X. Fan and F. Wang, *J. Phys. Chem. Lett.* **7**, 4916–4921 (2016).
113. H. Zou, B. Chen, Y. Hu, Q. Zhang, X. Wang and F. Wang, *J. Phys. Chem. Lett.* **11**, 3020–3024 (2020).
114. Y. Hu, Q. Shao, X. Deng and J. Jiang, *Nanophotonics* **9**, 2879–2885 (2020).
115. L. Aarts, B.M. der Ende and A. Meijerink, *J. Appl. Phys.* **106**, 23522 (2009).
116. R.S. Quimby, N.J. Condon, S.P. O'Connor and S.R. Bowman, *Opt. Mater.* **34**, 1603–1609 (2012).
117. J.F. Suyver, J. Grimm, M.K. van Veen, D. Biner, K.W. Krämer and H.U. Güdel, *J. Lumin.* **117**, 1–12 (2006).
118. B.M. Walsh, G.W. Grew and N.P. Barnes, *J. Phys. Condens. Matter* **17**, 7643 (2005).
119. M. Malinowski, R. Piramidowicz, Z. Frukacz, G. Chadeyron, R. Mahiou and M.F. Joubert, *Opt. Mater.* **12**, 409–423 (1999).
120. B. Henderson and G.F. Imbusch, *Optical spectroscopy of inorganic solids*, Oxford Univ. Press (2006).
121. J. Sytsma, G.F. Imbusch and G. Blasse, *J. Phys. Condens. Matter* **2**, 5171 (1990).
122. D. Yu, J. Ballato and R. E. Riman, *J. Phys. Chem. C* **120**, 9958–9964 (2016).
123. D.C. Yu, F.T. Rabouw, W. Q. Boon, T. Kieboom, S. Ye, Q.Y. Zhang and A. Meijerink, *Phys. Rev. B* **90**, 165126 (2014).
124. X. Huang, S. Han, W. Huang and X. Liu, *Chem. Soc. Rev.* **42**, 173–201 (2013).
125. M.D. Fairchild, *Color Appearance Models*, John Wiley & Sons (2013).
126. G. Yao, C. Lin, Q. Meng, P.S. May and M.T. Berry, *J. Lumin.* **160**, 276–281 (2015).
127. R.G. Geitenbeek, J.C. Vollenbroek, H.M.H. Weijgertze, C.B.M. Tregouet, A.E. Nieuwelink, C.L. Kennedy, B.M. Weck-

- huysen, D. Lohse, A. van Blaaderen, A. van Den Berg, M. Odijk and A. Meijerink, *Lab Chip* **19**, 1236–1246 (2019).
128. Q. Cheng, S. Rajauria, E. Schreck, R. Smith, N. Wang, J. Reiner, Q. Dai and D. Bogy, *Sci. Rep.* **10**, 20087 (2020).
129. I.K. van Ravenhorst, R.G. Geitenbeek, M.J. van der Eerden, J. Tijn van Omme, H.H. Pérez Garza, F. Meirer, A. Meijerink and B.M. Weckhuysen, *ChemCatChem* **11**, 5505–5512 (2019).
130. S. Yakunin, B.M. Benin, Y. Shynkarenko, O. Nazarenko, M. I. Bodnarchuk, D. N. Dirin, C. Hofer, S. Cattaneo and M.V. Kovalenko, *Nat. Mater.* **18**, 846–852 (2019).
131. A. Sarua, H. Ji, M. Kuball, M.J. Uren, T. Martín, K.P. Hilton and R.S. Balmer, *IEEE Trans. Electron Devices* **53**, 2438–2447 (2006).
132. R. Tsu and J.G. Hernandez, *Appl. Phys. Lett.* **41**, 1016–1018 (1982).
133. E.L. Keller and R.R. Frontiera, *ACS Nano* **12**, 5848–5855 (2018).
134. P. Jiang, X. Qian and R. Yang, *Rev. Sci. Instrum.* **88**, 74901 (2017).
135. C.D.S. Brites, P.P. Lima, N. J.O. Silva, A. Millán, V.S. Amaral, F. Palacio and L.D. Carlos, *Nanoscale* **4**, 4799–4829 (2012).
136. R. Piñol, J. Zeler, C.D.S. Brites, Y. Gu, P. Téllez, A.N. Carneiro Neto, T.E. da Silva, R. Moreno-Loshuertos, P. Fernandez-Silva, A.I. Gallego, L. Martinez-Lostao, A. Martinez, L.D. Carlos and A. Millan, *Nano Lett.* **20**, 6466–6472 (2020).
137. C. Brites, P. Pereira, N. João, A. Millán, V. Amaral, F. Palacio and L.A.D. Carlos, *Front. Chem.* **1**, 9 (2013).
138. E. Saïdi, N. Babinet, L. Lalouat, J. Lesueur, L. Aigouy, S. Volz, J. Labéguerie-Egée and M. Mortier, *Small* **7**, 259–264 (2011).
139. F. Auzel, *Chem. Rev.* **104**, 139–174 (2004).
140. S. Kumar, P. Bhushan, M. Pandey and S. Bhattacharya, *J. Micromanufacturing* **2**, 175–197 (2019).
141. J.T. van Omme, M. Zakhozheva, R.G. Spruit, M. Sholkina and H.H. Pérez Garza, *Ultramicroscopy* **192**, 14–20 (2018).
142. C. B. Saltonstall, J. Serrano, P.M. Norris, P.E. Hopkins and T.E. Beechem, *Rev. Sci. Instrum.* **84**, 064903 (2013).
143. C. Renero-Lecuna, R. Martín-Rodríguez, R. Valiente, J. González, F. Rodríguez, K.W. Krämer and H.U. Güdel, *Chem. Mater.* **23**, 3442–3448 (2011).
144. R.B. Anderson, S.J. Smith, P.S. May and M.T. Berry, *J. Phys. Chem. Lett.* **5**, 36–42 (2014).
145. R. Brechbühler, F.T. Rabouw, P. Rohner, B. le Feber, D. Poulikakos and D.J. Norris, *Phys. Rev. Lett.* **121**, 113601 (2018).
146. G.W. Ford and W.H. Weber, *Phys. Rep.* **113**, 195–287 (1984).
147. A. Rafiei Miandashti, L. Khosravi Khorashad, A.O. Govorov, M.E. Kordesch and H.H. Richardson, *J. Phys. Chem. C* **123**, 3770–3780 (2019).
148. R.G. Geitenbeek, A.E. Nieuwelink, T.S. Jacobs, B.B.V. Salzmänn, J. Goetze, A. Meijerink and B.M. Weckhuysen, *ACS Catal.* **8**, 2397–2401 (2018).
149. P. Frederix, M.A.H. Asselbergs, W. Van Sark, D.J. den Heuvel, W. Hamelink, E.L. De Beer and H.C. Gerritsen, *Appl. Spectrosc.* **55**, 1005–1012 (2001).
150. G. Baffou, C. Girard and R. Quidant, *Phys. Rev. Lett.* **104**, 136805 (2010).
151. G. Baffou, *ACS Nano* **15**, 5785–5792 (2021).
152. L. Labrador-Páez, M. Pedroni, A. Speghini, J. García-Solé, P. Haro-González and D. Jaque, *Nanoscale* **10**, 22319–22328 (2018).
153. P. Anger, P. Bharadwaj and L. Novotny, *Phys. Rev. Lett.* **96**, 113002 (2006).
154. M. Pelton, *Nat. Photon.* **9**, 427–435 (2015).
155. T. Shibanuma, T. Matsui, T. Roschuk, J. Wojcik, P. Mascher, P. Albella and S.A. Maier, *ACS Photonics* **4**, 489–494 (2017).

156. R. Kullock, M. Ochs, P. Grimm, M. Emmerling and B. Hecht, *Nat. Commun.* **11**, 115 (2020).
157. H.M. Doeleman, C.D. Dieleman, C. Mennes, B. Ehrler and A.F. Koenderink, *ACS Nano* **14**, 12027–12036 (2020).
158. J. Langer, *et al.*, *ACS Nano* **14**, 28–117 (2019).
159. K.-Q. Lin, J. Yi, J.-H. Zhong, S. Hu, B.-J. Liu, J.-Y. Liu, C. Zong, Z.-C. Lei, X. Wang, J. Aizpuru, R. Esteban and B. Ren, *Nat. Commun.* **8**, 14891 (2017).
160. C. Chen and J. Wang, *Analyst* **145**, 1605–1628 (2020).
161. A. Faraon, P.E. Barclay, C. Santori, K.M.C. Fu and R.G. Beausoleil, *Nat. Photon.* **5**, 301–305 (2011).
162. H.-Q. Zhao, M. Fujiwara and S. Takeuchi, *Opt. Express* **20**, 15628 (2012).
163. H. Ahn, J. Hong, S.Y. Kim, I. Choi and M.J. Park, *ACS Appl. Mater. Interfaces* **7**, 704–712 (2015).
164. T. Zheng, M. Sójka, M. Runowski, P. Woźny, S. Lis and E. Zych, *Adv. Opt. Mater.* **9**, 2101507 (2021).
165. L. Chen, J.-W. Ye, H.-P. Wang, M. Pan, S.-Y. Yin, Z.-W. Wei, L.-Y. Zhang, K. Wu, Y.-N. Fan and C.-Y. Su, *Nat. Commun.* **8**, 15985 (2017).
166. J.R. Casar, C.A. McLellan, C. Siefe and J.A. Dionne, *ACS Photonics* **8**, 3–17 (2021).
167. A. Cocina, R. Brechbühler, S.J.W. Vonk, J. Cui, A.A. Rossinelli, H. Rojo, F.T. Rabouw and D.J. Norris, *J. Phys. Chem. Lett.*, 2022, **13**, 4145–4151.
168. S. Karaveli and R. Zia, *Phys. Rev. Lett.*, 2011, **106**, 193004.
169. V.I. Sokolov, A.V. Zvyagin, S.M. Igumnov, S.I. Molchanova, M. M. Nazarov, A.V. Nechaev, A.G. Savelyev, A.A. Tyutyunov, E.V. Khaydukov and V.Y. Panchenko, *Opt. Spectrosc.* **118**, 609–613 (2015).
170. K.M. McPeak, S.V. Jayanti, S.J.P. Kress, S. Meyer, S. Iotti, A. Rossinelli and D.J. Norris, *ACS Photonics* **2**, 326–333 (2015).
171. R. Khan, B. Gul, S. Khan, H. Nisar and I. Ahmad, *Photodiagnosis Photodyn. Ther.* **33**, 102192 (2021).
172. A.M. Smith, M.C. Mancini and S. Nie, *Nat. Nanotechnol.* **4**, 710–711 (2009).
173. C.M. Dodson and R. Zia, *Phys. Rev. B* **86**, 125102 (2012).
174. H. Xu and Z. Jiang, *Chem. Phys.* **287**, 155–159 (2003).
175. K. Zheng, D. Zhao, D. Zhang, N. Liu and W. Qin, *Opt. Lett.* **35**, 2442 (2010).
176. D. Yu, H. Li, D. Zhang, Q. Zhang, A. Meijerink and M. Suta, *Light Sci. Appl.* **10**, 236 (2021).
177. V. Trannoy, A.N. Carneiro Neto, C.D.S. Brites, L.D. Carlos and H. Serier-Brault, *Adv. Opt. Mater.* **9**, 2001938 (2021).
178. M.S. Pudovkin, A.K. Ginkel and E.V. Lukinova, *Opt. Mater.* **119**, 111328 (2021).
179. J. Zhou, Y. Teng, X. Liu, S. Ye, Z. Ma and J. Qiu, *Phys. Chem. Chem. Phys.* **12**, 13759–13762 (2010).



---

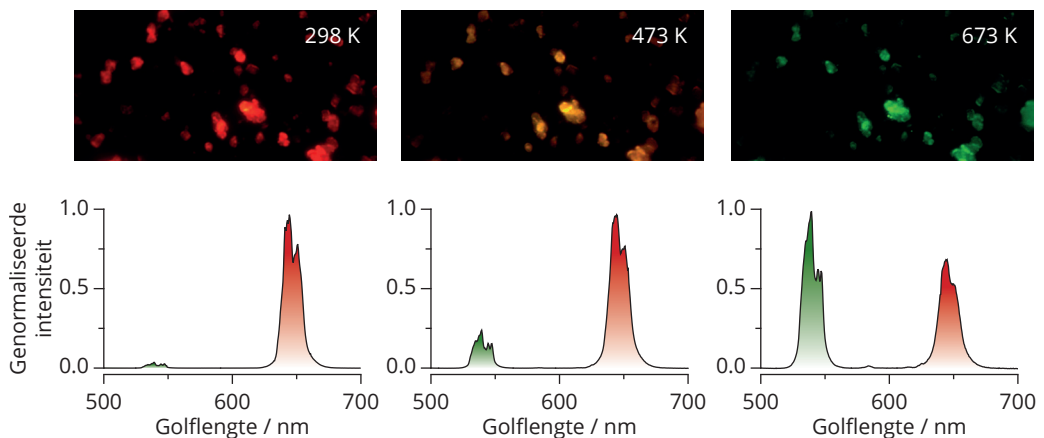
# Appendix

---

## Samenvatting in het Nederlands

Luminescente materialen kunnen licht van de ene kleur absorberen om vervolgens licht van een andere kleur uit te zenden. In het dagelijks leven zien we dit proces bijvoorbeeld terug in de flits van een mobiele telefoon, die bestaat uit een blauwe *light-emitting diode* (LED) waarop een materiaal met gele luminescentie is geplakt. Menging van het blauwe en het gele licht zorgt dat we helderwit licht waarnemen. In dit proefschrift onderzoeken we materialen waarvan de kleur van de luminescentie verandert als de temperatuur verandert, waardoor ze als thermometer gebruikt kunnen worden (Fig. 7.2). Als we de kleur van de luminescentie namelijk nauwkeurig bepalen, kunnen we afleiden wat de temperatuur van het materiaal is geweest op het moment van de meting. Het waarnemen van de luminescentie vindt plaats door middel van een fotodetector wat als voordeel heeft dat er geen fysiek contact nodig is tussen de thermometer en het apparaat dat de temperatuur uitleest, in tegenstelling tot bijvoorbeeld een thermokoppel. Verder kunnen moderne synthesprocedures luminescente materialen produceren met afmetingen op de nanometer- tot micrometerschaal; dit is 10 tot 10000 keer kleiner dan de dikte van een haar. Zulke kleine thermometers kunnen makkelijk worden ingebracht in microscopische systemen, zoals levende biologische cellen of katalysatordeeltjes voor chemische reacties. Dit stelt wetenschappers in staat om temperatuurmetingen uit te voeren, die voorheen niet of moeilijk mogelijk waren.

Luminescentie kan op verschillende manieren gemeten worden, hoewel in thermometrie het gebruikelijk is om een spectrum op te nemen en de intensiteitsverhouding tussen twee emissiebanden als maat voor de temperatuur te nemen (Fig. 7.2). De intensiteitsverhouding is namelijk onafhankelijk van experimentele factoren zoals de hoeveelheid thermometermateriaal en de belichtingsintensiteit. Veel thermometermaterialen bestaan uit anorganische kristallen waarin een



**Figuur 7.2.** Microkristallen van  $\text{Na(Y,Gd)F}_4$  gedoteerd met 12%  $\text{Ho}^{3+}$ . De bovenste rij panelen laat foto's zien die zijn opgenomen met een CCD-camera verbonden aan een fluorescentiemicroscop. De luminescentie van de microkristallen werd opgewekt door bestraling met blauw licht (445 nm). De afmetingen van de foto's corresponderen met een werkelijke grootte van  $110 \mu\text{m}$  bij  $45 \mu\text{m}$ . De onderste rij panelen toont de emissiespectra, die zijn gemeten bij de temperatuur van het bovenliggende paneel.

fractie van de kationen is vervangen door lanthanide-ionen—een procedure die “dotering” wordt genoemd. De nauwe emissiebanden van de lanthanide-ionen overlappen vaak nauwelijks wat de fouten in het bepalen van de intensiteitsverhouding beperkt en de nauwkeurigheid van de temperatuurmetingen ten goede komt. Twee soorten meetfouten kunnen van elkaar worden onderscheiden: systematische fouten en stochastische, oftewel *random*, fouten. In thermometrie zorgen systematische fouten bij elke meting voor dezelfde afwijking van de werkelijke temperatuur. Dit is vaak het gevolg van imperfecties in het experiment, zoals opwarming van de thermometer door belichting. Stochastische fouten daarentegen worden veroorzaakt door kans, bijvoorbeeld door de kans dat de fotodetector de luminescentie omzet in een signaal. Stochastische fouten zijn in het spectrum terug te zien als ruis. Dit proefschrift bestudeert hoe systematische en stochastische fouten de betrouwbaarheid van luminescente thermometers beïnvloeden en formuleert richtlijnen om de ontwikkeling van thermometers te optimaliseren.

In **Hoofdstuk 2** hebben we onderzocht hoe de statistiek van fotodetectie zich vertaalt naar de stochastische fouten van luminescentiethermometrie, oftewel de temperatuuronzekerheid. Hier toe maten we series van emissiespectra om experimenteel de temperatuuronzekerheid te bepalen, waarbij de metingen werden blootgesteld aan verschillende bronnen van ruis door de instellingen van de fotodetector te variëren en achtergrondsignaal te introduceren. We ontwikkelden statistische modellen om de temperatuuronzekerheid te voorspellen en bevestigden deze met experimentele resultaten. Dit werk heeft ons geleerd dat de temperatuuronzekerheid sterk afhankelijk is van de meetomstandigheden en daardoor een ongeschikte parameter is om thermometers met elkaar te vergelijken. De gevoeligheid van de luminescentie voor temperatuurverandering en de emissie-intensiteit van de thermometer zijn echter wel geschikt, omdat deze parameters niet bepaald worden door de meetomstandigheden. Hoewel de gevoeligheid van nieuwe thermometermaterialen al vaak wordt gerapporteerd, zijn er minder methodes bekend om de emissie-intensiteit te verbeteren. Hierin is nog veel winst te behalen bij de optimalisatie van nieuwe en bestaande thermometers.

De meest gebruikte luminescente thermometer berust op thermisch evenwicht tussen twee elektronische toestanden in één enkel lanthanide-ion. In thermisch evenwicht wisselt de bezetting van de twee toestanden veel sneller dan de tijdschaal waarop emissie van luminescentie plaatsvindt. Hierdoor volgt de intensiteitsverhouding van deze toestanden een eenvoudig fysisch model, wat erg nuttig is voor de kalibratie van de thermometers. Bij lage temperaturen geldt thermisch evenwicht echter niet meer, omdat de twee toestanden minder snel wisselen van bezetting. Dit beperkt het temperatuurbereik waarin het simpele kalibratiemodel gebruikt kan worden. In **Hoofdstuk 3** hebben we thermisch evenwicht onder de loep genomen en naar manieren gezocht om het startpunt van thermisch evenwicht naar lagere temperaturen te verschuiven. Onze experimenten aan europium-gedoteerde materialen toonden aan dat het kristalrooster van het lanthanide-ion een sterke invloed heeft op de starttemperatuur van thermisch evenwicht. Daarnaast toonden we aan dat de elektronische eigenschappen van het lanthanide-ion zelf van groot belang zijn. Deze resultaten kunnen helpen dit populaire type thermometer toepasbaar te maken in een breder temperatuurbereik.

In **Hoofdstuk 4** ontwikkelden we een nieuwe thermometer die gebaseerd is op de luminescentie van het lanthanide-ion holmium (Fig. 7.2). Het bijzondere van deze thermometer is dat er na de absorptie van licht energie-overdracht kan plaatsvinden tussen de holmium-ionen. De snelheid van energie-overdracht is sterk afhankelijk van de afstand tussen ionen en daardoor van de holmiumconcentratie. Tegelijkertijd vindt er temperatuur-afhankelijk niet-stralend verval binnenin de ionen plaats, waardoor de luminescentie ook afhangt van de temperatuur. We hebben de dynamiek van alle elektronische processen zorgvuldig gemeten en hebben de resultaten ingevoerd in een model dat de prestaties van deze thermometer voorspelt in een breed bereik van holmiumconcentraties en temperaturen. Ons model is niet alleen toepasbaar op deze holmium-gebaseerde thermometer, maar het is ook belangrijk voor het begrip en de ontwikkeling van andere energie-overdracht-thermometers.

Luminescente thermometers worden vaak gekarakteriseerd in ideale meetomstandigheden (zo ook de twee bovengenoemden). Wanneer de thermometers daadwerkelijk worden toegepast, zal, naast de gevoeligheid en de emissie-intensiteit, de invloed van systematische fouten een belangrijke rol spelen. **Hoofdstuk 5** liet zien dat temperatuurmetingen op de microscopische schaal kwetsbaar zijn voor twee bijzondere soorten systematische fouten. We merkten dit op tijdens onze temperatuurmetingen aan een spiraalvormige verwarmers met micrometer-afmetingen. Voor dit experiment hebben we een laag thermometerkristallen op de microverwarmer aangebracht, waarna we een microscoop gebruikten om de kristallen te belichten en de luminescentie op te vangen. Op deze manier kunnen warmteverdelingen met micrometerresolutie in kaart worden gebracht. Temperatuurmetingen met een microscoop vereisen alleen erg hoge belichtingsintensiteiten. Onze experimenten toonden aan dat, bij hoge belichtingsintensiteiten, emissie vanuit hogere elektronische toestanden van de thermometer het spectrum kan verstoren. Dit introduceert een systematische fout. Verder namen we systematische afwijkingen in de temperatuur waar voor thermometers die zich op het reflecterende metaal van de microverwarmer bevonden. We schreven dit toe aan “zelf-interferentie” tussen directe en gereflecteerde emissie van de thermometers, waardoor de luminescentie-intensiteit in sommige richtingen wordt versterkt en in andere richtingen wordt gedempt. Zelf-interferentie wordt sterk bepaald door de golflengte van de emissie en de lokale omgeving van de thermometer. Hierdoor kan, afhankelijk van de locatie van de thermometer, de gedetecteerde luminescentie-intensiteit bij elke golflengte in het spectrum veranderen, wat ook weer resulteert in een systematische fout. Gelukkig was het mogelijk bij onze experimenten aan de onbeweeglijke microverwarmer om voor beide systematische fouten te corrigeren, maar dit zal lastiger zijn voor samples met bewegende componenten.

In **Hoofdstuk 6**, hebben we een beter begrip gekregen van zelf-interferentie door thermometers op vaste afstanden van een spiegel te plaatsen. Op deze manier konden we systematisch bestuderen hoe de luminescentie, en dus de gemeten temperatuur, wordt beïnvloed door de lokale omgeving van de thermometer. We hebben deze experimenten uitgevoerd met twee verschillende thermometers: de ene heeft twee groene emissiebanden en de andere heeft een groene en een rode emissieband. De fouten in de gemeten temperatuur waren 100 K bij de groene thermometer en ze waren zelfs 250 K bij de groen-rode thermometer. Ons model om zelf-interferentie te beschrijven



verklaarde deze bevindingen en het toonde aan dat niet alleen de luminescentiekleur de fouten in de gemeten temperatuur bepaalt, maar ook de geometrie van het monster en de collectie van de luminescentie door het microscopieobjectief. Hoewel het vaak niet mogelijk en niet wenselijk is om de geometrie van het monster te veranderen, zou de betrouwbaarheid van toekomstige metingen baat kunnen hebben bij optimalisatie van het microscopieobjectief en van de luminescentiekleur van de thermometers.

## Acknowledgements

Vier jaar geleden begon ik met mijn promotieonderzoek. Ik had niet gedacht er nu met zoveel plezier op terug te kijken. Ik heb tijdens mijn onderzoek alle vrijheid gehad om mezelf te ontwikkelen op veel verschillende vlakken. Dit was niet mogelijk geweest zonder de hulp en het advies van jullie—collega's, vrienden en familie. Ik ben dan ook blij dat ik me in de laatste pagina's van dit proefschrift tot jullie kan richten.

Ik begin bij jou, **Andries**. Het werken in jouw groep heb ik als ontzettend prettig ervaren. Je bent altijd erg betrokken geweest bij alle aspecten van mijn onderzoek. Hiermee motiveerde je me om nieuwe experimenten uit te voeren en analyses te verbeteren. Dit zorgde voor een goede vaart in mijn onderzoeksprojecten. Verder was er een luchtige en ontspannen sfeer in de groep. Dit hield je actief in stand door vanuit Avifauna selfies met een papegaai op je hoofd naar me te sturen. Dit is slechts één van de vele momenten dat ik hard om je heb moeten lachen. Waar nodig, wist je deze informele sfeer goed af te wisselen voor harde maar eerlijke kritiek op wetenschappelijk gebied. Ik heb dit erg gewaardeerd en ik heb veel van je geleerd. Bedankt voor alles.

**Bert**, ik weet nog goed dat je me tijdens mijn MSc-onderzoek hebt aangespoord een toekomstplan te maken en na te denken over het doen van promotieonderzoek. Je hebt hiermee een belangrijke rol gespeeld in mijn keuze dit daadwerkelijk te gaan doen. Hiervoor wil ik je graag bedanken. Verder vond ik het leuk hoe mijn connectie met de katalysegroep in stand bleef doordat jij mijn promotor was. Hier zijn denk ik een aantal interessante samenwerkingen uit voortgevloeid.

In de eerste weken van mijn onderzoek liep ik nog ietwat onhandig rond over de chemische en optische laboratoria. Het was in deze periode dat jij naar me toekwam, **Freddy**, en vroeg of ik het interessant vond om wat modelleerwerk te doen in een lopend project (**Hoofdstuk 4**). Ik was al snel enthousiast, maar nog wel onwetend. Jij bent naast me gaan zitten achter mijn computer en hebt mij in talloze sessies de wiskunde en programeervaardigheden geleerd, die nodig waren voor dit project. Met hetzelfde geduld heb je vervolgens me uitgelegd hoe ik duidelijke figuren van de resultaten kon maken en hoe ik er daarna een helder verhaal omheen kon bouwen. Dit proces herhaalde zich bij al mijn volgende projecten. Ik ben je erg dankbaar voor al je hulp. Hoewel wij in het begin 'niks' van elkaar waren, ben ik blij dat ik je nu mijn copromotor mag noemen. Ook nadat je officieel mijn copromotor werd, was er gelukkig nog genoeg ruimte om te klieren. Ik weet niet hoeveel promovendi kunnen zeggen dat ze ethanol uit een laboratoriumfles op hun copromotor hebben gespoten en daarna niet zijn ontslagen. Tot slot heb ik veel plezier gehad in onze activiteiten buiten de wetenschap, zoals wielrennen en daarna pannenkoeken eten. Hopelijk blijven we dit de komende jaren doen.

**Robin**, ik mocht jou opvolgen in het onderzoek naar luminescentiethermometrie bij CMI. Doordat jij je werk zo goed had gedaan kon mijn onderzoek soepel van start gaan. Het was erg prettig hoe je in de overgangsfase mij alle vrijheid gaf om zelf mijn weg te vinden in de laboratoria, maar wel altijd paraat stond voor hulp en advies. Die vrijheid bleef je geven toen je verder ging met het thermometrieonderzoek in de katalysegroep. Bedankt hiervoor.

De collega-promovendus met wie ik het meest heb samengewerkt ben jij zonder enige twijfel, **Sander**. Al tijdens onze studie merkte ik dat we veel interesses op zowel wetenschappelijk als sportief gebied delen. Je vaardigheden op het gebied van optische microscopie en je kennis van de nanofotonica zijn bewonderingswaardig. Hiermee heb je belangrijk werk gedaan in onze vele gedeelde publicaties, bedankt voor de goede samenwerking. Daarnaast houden we allebei van wielrennen. Ik zal niet snel onze fietstocht van Enschede naar Utrecht vergeten. Het heeft de hele rit van 144 km geregend, maar we vertikten het allebei om het hazenpad te kiezen en de trein te pakken.

**Markus**, al vroeg in mijn promotieonderzoek kwam je werken bij CMI om een postdoc te doen in luminescentiethermometrie. Hierdoor was ik gelukkig niet meer de enige in onze groep die actief was binnen dit onderzoeksveld. Ik kon altijd bij je terecht voor vragen en wetenschappelijke discussies, waarvoor ik je graag wil bedanken. Verder is je kennis op het gebied van anorganische syntheses ongeëvenaard. Dit heeft enorm geholpen bij het tot stand komen van **Hoofdstuk 3**. Ik was blij om te zien dat we goed contact konden houden nadat je een positie als professor in Düsseldorf kreeg.

**Dave**, binnen het Debye instituut heb jij een van de grootste verzameling microscopen en lasers in beheer. Je bent altijd bereid om te kijken hoe je met deze apparatuur de experimenten van anderen kan verbeteren. Met jouw hulp lukte het al na een paar maanden om een belangrijk onderdeel van mijn promotieonderzoek—het in kaart brengen van temperatuur met hoge ruimtelijke resolutie—te volbrengen. Ik heb altijd erg veel plezier gehad in onze dagen achter de microscoop dankzij jouw enthousiaste en eigenzinnige werkwijze. Bedankt voor de fijne samenwerking.

**Tijn, Ronald en Hugo**, de samenwerking met jullie bedrijf DENSsolutions heb ik altijd enorm interessant gevonden. De bezoeken aan jullie kantoor in Delft lieten mij zien hoe je met wetenschappelijke innovaties daadwerkelijk commercieel succes kan behalen. Hopelijk lukt het met onze experimentele resultaten uit **Hoofdstuk 5** nog beter om jullie klanten te laten zien dat jullie microverwarmers geweldig goed werken. Bedankt voor jullie grote betrokkenheid bij mijn onderzoek.

At the end of my PhD, we finally got to meet each other in person, **Ario**. This was a nice change after all those videocalls. I would like to thank you for the smooth collaboration. The substrates that you prepared for Sander and me helped us a lot to quantify an important source of systematic errors in luminescence thermometry (**Chapter 6**).

Already in the first weeks of my PhD, our collaboration started, **Dechao**. You and **Ting** had performed experiments on a new material with very interesting temperature-dependent luminescence. You allowed me to do the modelling work to better understand this temperature-dependence (**Chapter 4**). I am very grateful to you for giving me this opportunity.

**Bas en Tjom**, een paar dagen voor het schrijven van dit dankwoord kregen we goed nieuws van *Angewandte Chemie*. Het is erg fijn dat jullie experimenten aan luminescente katalysatordeeltjes in zo'n mooi tijdschrift zijn gepubliceerd. Bedankt dat jullie me hebben betrokken bij dit

project.

Tijdens mijn onderzoek ben ik ook veel geholpen door de studenten waarmee ik samenwerkte. **Auke, Jesse, Ravi** en **Sam**, jullie experimenten aan Boltzmann thermometers hebben ons veel nieuwe inzichten verschaft. Ik ben erg blij dat we jullie harde werk hebben kunnen bundelen tot **Hoofdstuk 3** van dit proefschrift. Bedankt voor jullie inspanningen. Ik wil ook graag jullie bedanken, **Martijn, Mitchell**, en **Mike**. Jullie werk heeft onze kennis van luminescentiethermometrie verbreedt en verdiept. Dat is erg waardevol. Ayla, jouw onderzoek naar diffusie van lanthanide-ionen is veelbelovend. Jouw gedrevenheid en optimisme maakten het een feest om je te begeleiden. Bedankt voor de prettige samenwerking.

Verder wil ik graag iedereen van **CMI** bedanken voor alle gezelligheid. In het bijzonder wil ik mijn kantoorgenoten bedanken. **Naud**, gedurende mijn hele promotieonderzoek zijn wij kantoorgenoten geweest, dus ik begin bij jou. Het duurde even voordat ik je goed leerde kennen, maar ik ben je de afgelopen jaren erg gaan waarderen. Onze gedeelde liefde voor muziek, van Britney Spears tot Chopin, maakt ons kantoor elke dag (en dan vooral de vrijdag) de gezelligste plek in het Ornsteinlaboratorium. Verder heb ik denk ik nog nooit iemand ontmoet die zoveel zelfspot heeft en die zo hard lacht om mijn (en zijn eigen) grappen. Bedankt voor de goede tijd. **Jur**, jij bent een van de weinigen binnen CMI die de charme van de Ekspla-kamer begrijpt en het duurde dus ook niet lang voordat we hier een nieuwe opstelling gingen bouwen voor jouw onderzoek. De samenwerking beviel erg goed. Toen wij erachter kwamen dat het kantoor met daarin een grote bank vrijkwam, hadden we al snel besloten dat we moesten verhuizen. Als kantoorgenoot heb ik je scherpe gevoel voor humor leren kennen en ik kan dan ook erg met je lachen. Onze gedeelde passie voor activiteiten in de bergen heeft ons in Wałbrzych (de uitspraak gaat nog steeds niet lekker) in een benarde situatie gebracht toen de band van mijn mountainbike lek ging. Ik zal niet snel vergeten hoe jij al fietsend twee mountainbikes terug hebt weten te krijgen terwijl ik hardlopend achter je aan kwam. Bedankt voor de mooie ervaringen. **Atul**, we were office mates for the first two years of my PhD. I have never met someone who is so kind and so calm as you are. It was really great to be office mates with you. Thank you for the nice time. **Vasya**, you are a funny guy. The main memory I have of you as an office mate is that you were having a lot of telephone conversations. In the beginning I thought you must be a very important person. After not too long I figured out that you were just having a lot of casual chats with former colleagues, friends, and family. We also started having these casual chats and I enjoyed them a lot. Thank you for bringing such a nice atmosphere to our office.

Mijn promotieonderzoek heeft zich niet alleen in het Ornsteinlaboratorium afgespeeld maar deels ook in de katalysegroep **ICC**. Ik heb me altijd erg welkom gevoeld in de katalysegroep en ik wil de mensen bedanken die hieraan bijdroegen. **Thimo, Max** and **Tim**, I would like to spend some extra words on you. **Thimo**, je bent ontzettend enthousiast over het thermometrieonderzoek en wilt er graag alles over leren. Dit maakt het erg prettig om met je samen te werken. Verder was het geweldig om je erbij te hebben op de conferentie in Belgrado. Het mouserend ontbijtje op de vrijdag maakte de laatste conferentiepraatjes een stuk aangenamer. **Max**, it was one of the

first months of my PhD when we both became supervisor of our MSc student Martijn. The project was quite interdisciplinary, which was sometimes challenging. We nevertheless managed to observe interesting jumps in the catalyst temperature at the onset of chemical reaction. Thank you for the nice collaboration. **Tim**, hoewel je eerst mijn collega-promovendus was bij CMI, werk je nu voor de katalysegroep, dus daarom noem ik je in deze alinea. Je hebt altijd veel belangstelling getoond in mijn onderzoek. Dit zorgde voor interessante en leerzame discussies. Verder ken ik naast jou weinig mensen die zo enthousiast zijn over onderzoek naar nanomaterialen. Ik wil jou en **Annelies** bedanken dat ik met jullie mee mocht naar de synchrotron in Oxford. Dit was een ontzettend indrukwekkende ervaring.

I would also like to thank all members of the **MCEC** consortium. **Luca** and **Marvin**, I enjoyed collaborating with you and learning the details of your projects. **Mark**, onze samenwerking ging direct goed van start toen we samen Mitchell mochten begeleiden bij zijn MSc onderzoek. We zaten vaak op één lijn op educatief en wetenschappelijk vlak, wat zorgde voor een soepele communicatie. Verder was ik altijd blij als ik hoorde dat je meeging naar een van de vele MCEC evenementen. Door ons geklier bij de koffieautomaat kon ik na een minder interessant praatje weer met frisse zin deelnemen aan de rest van het wetenschappelijk programma. Hiervoor wil ik je graag bedanken.

Daarnaast zijn er nog een hoop vrienden, die ik wil bedanken voor de goede tijd naast het onderzoek. **Huize Breedstraat**, de deur stond bij jullie altijd open en de wijn had precies de goede temperatuur. Ik wil jullie graag bedanken voor jullie gastvrijheid. **Mexers**, als oud-studiegenoten kon ik goed met jullie praten over alle frustraties, die promotieonderzoek met zich meebrengt. Bedankt voor jullie goede raad, de gezellige borrels en de mooie vakanties. Vrienden van **de jaarclub**, bedankt voor alle gezelligheid en de mooie vakanties. Na een weekje skiën met jullie kon ik weer met hernieuwde motivatie verdergaan met mijn onderzoek. **Anneke**, **Daan** en alle vrienden buiten bovenstaande groepen, ook bedankt voor het aanhoren van alle verhalen over mijn onderzoek.

Mijn paranimfen, **Martijn** en **Stijn**, wil ik graag in het bijzonder bedanken. Jullie wisten de problemen in mijn promotieonderzoek altijd goed te relativeren en gaven me nuttig advies wanneer ik daarom vroeg.

Ik heb ook veel te danken aan mijn familie. **Papa**, **mama**, **Roos**, **Laura**, **Sweder**, **Lise**, **Demi**, **Peer** en **Marleen**, jullie luisterden naar alle verhalen over mijn onderzoek en steunden me waar nodig. Bedankt hiervoor.

Tot slot wil ik jou graag bedanken, **Anne**. Er is niemand die mij zo goed begrijpt als jij en ik bewonder je grote inlevingsvermogen. Zo weet je me op precies de goede momenten op te vrolijken met een taartje of een andere verrassing. Je bent me heel erg dierbaar.

## List of publications in this thesis

- 1. A Ho<sup>3+</sup>-based luminescent thermometer for sensitive sensing over a wide temperature range.**  
T.P. van Swieten, D. Yu, T. Yu, S.J.W. Vonk, M. Suta, Q. Zhang, A., Meijerink and F.T. Rabouw, *Adv. Opt. Mater.* **9**, 2001518 (2021).
- 2. Mapping elevated temperatures with a micrometer resolution using the luminescence of chemically stable upconversion nanoparticles.**  
T.P. van Swieten, T. van Omme, D.J. van den Heuvel, S.J.W. Vonk, R.G. Spruit, F. Meirer, H.H. Pérez Garza, B.M. Weckhuysen, A. Meijerink, F.T. Rabouw and R.G. Geitenbeek, *ACS Appl. Nano Mater.* **4**, 4208–4215 (2021).
- 3. Impact of noise and background on measurement uncertainties in luminescence thermometry.**  
T.P. van Swieten, A. Meijerink and F.T. Rabouw, *ACS Photonics* **9**, 1366–1374 (2022).
- 4. Extending the dynamic temperature range of Boltzmann thermometers.**  
T.P. van Swieten, J.M. Steenhoff, A. Vlasblom, R. de Berg, S.P. Mattern, F.T. Rabouw, M. Suta and A. Meijerink, *Light Sci. Appl.*, *accepted*.
- 5. Enormous photonic artifacts in luminescence nanothermometry.**  
T.P. van Swieten, S.J.W. Vonk, A. Cocina and F.T. Rabouw, submitted.

## List of other publications

- 1. Variation of the conduction band edge of (LuGd)<sub>3</sub>(Ga, Al)<sub>5</sub>O<sub>12</sub>:Ce garnets studied by thermally stimulated luminescence.**  
V. Khanin, I. Venevtsev, K. Chernenko, P. Rodnyi, T.P. van Swieten, S. Spoor, J. Boerekamp, H. Wiczorek, I. Vrubel, A. Meijerink and C. Ronda, *J. Lumin.* **211**, 48–53 (2019).
- 2. Extending surface-enhanced Raman spectroscopy to liquids using shell-isolated plasmonic superstructures.**  
C.S. Wondergem, T.P. van Swieten, R.G. Geitenbeek, B.H. Ern e and B.M. Weckhuysen, *Chem. Eur. J.* **25**, 1–8 (2019).
- 3. Trapping and detrapping in colloidal perovskite nanoplatelets: elucidation and prevention of nonradiative processes through chemical treatment.**  
S.J.W. Vonk, M.B. Fridriksson, S.O.M. Hinterding, M.J.J. Mangnus, T.P. van Swieten, F.C. Grozema, F.T. Rabouw and W. van der Stam, *J. Phys. Chem. C* **124**, 8047–8054 (2020).

- 4. High temperature (nano)thermometers based on  $\text{LiLuF}_4:\text{Er}^{3+}, \text{Yb}^{3+}$  nano- and microcrystals. Confounded results for core-shell nanocrystals.**  
A.M. Kaczmarek, M. Suta, H. Rijckaert, T.P. van Swieten, I. van Driessche, M.K. Kaczmarek, and A. Meijerink, *J. Mater. Chem. C* **9**, 3589 (2021).
- 5. Exciton interaction with  $\text{Ce}^{3+}$  and  $\text{Ce}^{4+}$  ions in  $(\text{LuGd})_3(\text{Ga, Al})_5\text{O}_{12}$  ceramics.**  
V. Khanin, I. Venevtsev, K. Chernenko, V. Pankratov, K. Klementiev, T.P. van Swieten, A.J. van Bunningen, I. Vrabel, R. Shendrik, C. Ronda, P. Rodnyi and A. Meijerink, *J. Lumin.* **237**, 118150 (2021).
- 6. Beyond the energy gap law: the influence of selection rules and host compound effects on nonradiative transition rates in Boltzmann thermometers.**  
P. Netzsch, M. Hämmer, E. Turgunbajew, T.P. van Swieten, A. Meijerink, H.A. Höpfe and M. Suta, *Adv. Opt. Mater.* **10**, 2200059 (2022).
- 7. Europium oxychloride as catalytic material and operando thermometer in an exothermic chemical reaction.**  
B. Terlingen, T. Arens, T.P. van Swieten, F.T. Rabouw, M.M. de Beer, A. Meijerink, M. Ahr, E.M. Hutter, C. van Lare and B.M. Weckhuysen, *Angew. Chem. Int. Ed.*, *accepted*.

## List of presentations

- 1. High-resolution temperature mapping using confocal microscopy and nanothermometry.**  
Nanax 9, Hamburg, Germany, September 2019 (poster presentation).
- 2. Temperature mapping on the microscopic level.**  
MCEC annual meeting, Eindhoven, The Netherlands, April 2020 (oral presentation).
- 3. A new  $\text{Ho}^{3+}$ -based luminescent thermometer for sensitive sensing over a wide temperature range.**  
The 2nd international conference on phosphor thermometry, online, July 2020 (oral presentation).
- 4. In luminescence thermometry we trust. Can we?**  
NanoTBtech webinar, online, June 2021 (oral presentation given together with Freddy Rabouw).
- 5. A  $\text{Ho}^{3+}$ -based luminescent thermometer for sensitive sensing over a wide temperature range.**  
The 19th international conference on luminescence, online, July 2021 (oral presentation).

- 6. High-resolution temperature mapping using luminescent nanoparticles.**  
NWO CHAINS 2021, online, December 2021 (oral presentation).
- 7. High-resolution temperature mapping using luminescent nanoparticles.**  
NWO Physics@Veldhoven 2022, online, January 2022 (poster presentation).
- 8. Photonic artifacts in luminescence nanothermometry.**  
Debye lunch lecture, Utrecht, The Netherlands, April 2022 (oral presentation).
- 9. Enormous photonic artifacts in luminescence nanothermometry.**  
The 6th international conference on the physics of optical materials and devices & the 5th international workshop of persistent and photostimulable phosphors (IWPPP-5), Belgrade, Serbia, August 2022 (oral presentation).
- 10. Extending the dynamic temperature range of Boltzmann thermometers.**  
21st international conference on dynamical processes in excited states of solids, Wroclaw, Poland, September 2022 (oral presentation).







## Curriculum vitae

### **2018–2022      PhD candidate, Utrecht University, Utrecht, the Netherlands.**

- Performed spectroscopy experiments and designed analytical models to understand measurement errors in luminescence thermometry
- Collaborated with a diverse group of fellow scientists with backgrounds in chemistry, physics, and engineering.
- Received the *Most Interactive Student Award* on the Winter School on Luminescent Nanothermometry for Biomedical Applications in Madrid.
- Supervised 4 MSc students and 3 BSc students during their research projects.
- Gave tutorials in spectroscopy to first and second year BSc students.
- Was a member of the Debye PhD committee to represent students of the Debye Institute of Nanomaterials Science of Utrecht University.

### **2016–2018      MSc Nanomaterials: Chemistry and Physics, Utrecht University, Utrecht, the Netherlands.**

- Graduated *cum laude*.
- Wrote a thesis in the group of Bert Weckhuysen on the plasmonic properties of gold nanoparticles and their application in catalyst characterization.
- Worked as an intern at Philips Lighting to investigate fluorescent materials for high-power lighting applications.

### **2012–2016      BSc Chemistry, Utrecht University, Utrecht, the Netherlands.**

- Wrote a thesis in the group of Daniel Vanmaekelbergh on the luminescence and morphology of CdSe quantum dots.

### **2006–2012      Secondary school, Erasmiaans Gymnasium, Rotterdam, the Netherlands.**